

**DEVELOPMENT OF INJECTABLE BONE CEMENTS
FOR TISSUE HEALING AND THERAPEUTIC
APPLICATIONS**

SANDHYA S.

Ph.D THESIS

2018



**SREE CHITRA TIRUNAL INSTITUTE
FOR
MEDICAL SCIENCES AND TECHNOLOGY
THIRUVANANTHAPURAM
INDIA**

**DEVELOPMENT OF INJECTABLE BONE CEMENTS
FOR TISSUE HEALING AND THERAPEUTIC
APPLICATIONS**

A THESIS PRESENTED BY
SANDHYA S.

TO
SREE CHITRA TIRUNAL INSTITUTE FOR
MEDICAL SCIENCES AND TECHNOLOGY,
THIRUVANANTHAPURAM



IN PARTIAL FULFILMENT OF THE REQUIREMENTS
FOR THE AWARD OF
DOCTOR OF PHILOSOPHY
2018

DECLARATION

I, **Sandhya S.**, hereby certify that I had personally carried out the work depicted in the thesis entitled, “*Development of Injectable Bone Cements for Tissue Healing and Therapeutic Applications*”, except where due acknowledgment has been made in the text. No part of the thesis has been submitted for the award of any other degree or diploma prior to this date.

Thiruvananthapuram

10.01.2018

Sandhya S.

Reg.No: 2012/PhD/03

SREE CHITRA TIRUNAL INSTITUTE FOR MEDICAL SCIENCES & TECHNOLOGY
BIOMEDICAL TECHNOLOGY WING, POOJAPPURA
THIRUVANANTHAPURAM – 695011, INDIA
(An Institute of National Importance under Govt. of India)
Phone-(91)0471-2520220 Fax-(91)0471-2341814 www.sctimst.ac.in



Dr. P.R.Harikrishna Varma
Scientist G (Division of Bioceramics,
Department of Biomaterial Sciences and Technology)
&Head Biomedical Technology Wing
BMT Wing, SCTIMST
email: varma@sctimst.ac.in

This is to certify that **Ms. Sandhya S**, in the Bioceramics Laboratory, Biomaterials Science and Technology of this Institute has fulfilled the requirements prescribed for the Ph. D degree of the Sree Chitra Tirunal Institute for Medical Sciences and Technology, Thiruvananthapuram. The thesis entitled, “*Development of Injectable Bone Cements for Tissue Healing and Therapeutic Applications*” was carried out under my direct supervision. No part of the thesis was submitted for the award of any degree or diploma prior to this date.

* Clearance was obtained from the Institutional Ethics Committee/ Institutional Animal Ethics Committee for carrying out the study.

Thiruvananthapuram
10.01.2018

Dr. P.R. Harikrishna Varma
(Research Supervisor)

The thesis entitled

**“DEVELOPMENT OF INJECTABLE BONE CEMENTS
FOR TISSUE HEALING AND THERAPEUTIC
APPLICATIONS”**

Submitted by
SANDHYA S.

for the degree of
Doctor of Philosophy
of

**SREE CHITRA TIRUNAL INSTITUTE
FOR
MEDICAL SCIENCES AND TECHNOLOGY, TRIVANDRUM**

Is evaluated and approved by

.....
Dr. P.R.Harikrishna Varma
(Research Supervisor)

.....
(Thesis examiner)

Dedicated to

MY FAMILY AND TEACHERS

ACKNOWLEDGEMENTS

It is with deep sense of gratitude, satisfaction and with the divine blessings of God that I submit this dissertation. I take this opportunity with much pleasure to thank all who have contributed in many ways for the success of this study.

*I have no words to express my deepest sense of gratitude and respect to my research supervisor **Dr. P.R. Harikrishna Varma** (Scientist G, Bioceramics Lab and Head, Biomedical Technology Wing) who offered continuous advice and encouragement throughout the course of my study. I thank him for the systematic guidance and support which motivated me always for achieving the targets of the study. He was always accessible willing to help with his advice and took significant effort for the successful completion of this endeavour.*

*I am fortunate in having **Dr. Manoj Komath** (Scientist G, Scientist in Charge of Bioceramics Laboratory) as my co-guide who always monitor the output of the work and give timely suggestions and put great effort to train me in the scientific field, for facilitating all the requirement for testing, preparing the manuscript and finally the thesis. He was always ready for discussions, put ideas to explore and give suggestions which are tremendously helpful in improving the quality of the work and leading to be in the final successful outcome.*

*I pay my allegiance to the members of doctoral advisory committee, **Dr. P. Ramesh** (Division of Polymeric Medical Devices), **Dr. P.P. Lissymol** (Division of Dental Products) and **Dr. U.S. Hareesh** (Division of Material Science and Technology, National Institute for Interdisciplinary Science and Technology) of SCTIMST for spending their valuable time in patient hearing of my long presentations, for the constructive comments, valuable suggestions and feedback given to me, from time to time.*

*I am grateful to the **Director of SCTIMST** and the **Head, BMT Wing** for all the support provided during the course of my work. I also thank for **SCTIMST INSTITUTE FELLOWSHIP 2012** in chemical sciences stream which provide fund for the research work and attending conferences.*

*I am thankful to the Dean **Dr. V. Kalliyana Krishnan** & Associate Dean **Dr. Roy Joseph** for their support during the course. I am also acknowledging **Dr. Santhosh Kumar B.**, the Deputy Registrar and all members of academic division for their assistance.*

*I am very much grateful to **Dr. T.V. Kumary, Dr. P.R. Anil Kumar, Ms. Usha Vasudev, Mr. D. Vinod., Ms. Deepa K.Raj, Dr. Eva C.Das** and staff of Tissue Culture Lab for in vitro cytocompatibility evaluation of bone cements and putting their valuable time for discussion and correcting the manuscript.*

*I am sincerely thankful to **Dr. Lissy K. Krishnan, Dr. Anughya Bhut, Mr. Ranjith Kartha** of Division of Thrombosis Research for the haemocompatibility studies of the samples. I am extremely thankful to **Dr. Mohanan P.V., Dr. Gayathri V., Dr. Remya, Mr. Shaji, Mr. Harikumar** of Toxicology Division for helping in 'in vivo' toxicological evaluation including the implantation in rabbit femoral defect model.*

*I am extremely thankful to **Dr. Sharma C.P, Dr. Rekha M.R** and **Mr. Willipaul** and all members of Biosurface Technology Division for giving me permission to conduct the UV-Visible spectrophotometric and DLS analysis.*

*I owe many thanks to **Dr. Ramesh P., Dr. Roy Joseph, Mr. Willi Paul, Ms. Jincy, Dr. Mayuri P.V., Dr. Remya** of Division of Polymeric Medical Devices for helping me in injectability, compressive strength, Raman spectroscopic and HPLC analysis. I am also thankful*

to **Dr.K. Srinivasan** and **Dr. T.V. Radha Kumari** of Laboratory for Polymer Analysis for simultaneous TG-DTA and Isothermal differential scanning calorimetric analysis.

I would like to give my earnest appreciation to **Dr. A. Sabareeswaran, Dr. Joseph Sebastian, Ms. Sulekha Baby, Dr. Manjula** and all staff of Division of Experimental Pathology for helping me in the histopathological and histomorphometric analysis. I am sincerely thankful to **Dr. V. Kalliyana Krishnan, Dr. P.P. Lizyol, Dr. Ranjith P. Nair, Dr. C. Vibha** and **Ms. Lakshmi** for the Micro-CT analysis of the cements, explant and drug delivery sample analysis.

I am sincerely and extremely grateful to **Dr. Maya Nandakumar, Mr. T.S. Pradeep Kumar** and all members of Division of Microbiology to spend their valuable time for helping me with laborious antimicrobial testing and to give valuable input for my studies and clearing my doubts.

I acknowledge **Dr. Lakshmi Varma, Mr. Pir Muhammad, Mr. Kiran** and **Ms. Sridevi** 'National Institute for Interdisciplinary Science and Technology (NIIST)' for the ^1H NMR, BET surface area, TEM and SAED pattern analysis.

I am extremely thankful to my lab mates for their help during the study. I thank **Dr. Sureshbabu** and **Mr. Vijayan S.** for giving me training in XRD, FTIR and OES-ICP analysis and valuable inputs and suggestions during discussions and willingness to help at any time we need. I thank **Mr. Nishad** for helping me in SEM and EDS analysis and **Ms. Susan Mani** for TEM analysis. I also thank **Mr. P.J. Sreekanth, Ms. Nimmy Mohan, Dr. Padmaja Vasudev, Mr. R.K. Adarsh, Ms. Anchu,** and **Dr. E.B. Ansar** for their friendship which relieved my stresses and made my days memorable.

Finally, I acknowledge the people who mean a lot to me, my parents **G. Sathyarajan & G. Subhadra** and my brother **S.S. Lallu** for showing faith in me and giving me confidence and liberty to choose what I desired. I salute you all for the selfless love, care, prayers, pain and sacrifice you

*did during these days. I am gratified to my mother-in-law **G. Subhadra** and father-in-law **P. Sivaprasad** for their support for overcoming difficult times.*

*I owe thanks to a very special person, my husband, **Sony S. Prasad** for his continued and unfailing love, support and understanding during my pursuit of Ph.D degree that made the completion of thesis possible. You were always with me for and ever for any decision I took in my life. I appreciate my baby, my little 2 year old cutie **Divena Sony** for abiding my ignorance and the patience she showed during my absence.*

TABLE OF CONTENTS

DECLARATION	i
CERTIFICATE OF THE GUIDE	ii
APPROVAL OF THE THESIS	iii
ACKNOWLEDGEMENTS	v
LIST OF FIGURES	xvi
LIST OF TABLES	xxiii
ABBREVIATIONS	xxiv
SYNOPSIS	xxvii
CHAPTER 1-INTRODUCTION	1
1.1 Need and Significance of bone grafting	1
1.2 Strategies in bone grafting	2
1.2.1 Natural bone grafts	2
1.2.2 Synthetic bone graft substitutes and de rigueur for bioactivity	3
1.2.3 Calcium phosphate bioceramics	5
1.2.4 Bone Fillers	7
1.2.4.1 <i>The need and significance of bone fillers</i>	7
1.2.4.2 <i>Inorganic self-setting bone cement systems</i>	8
(i) <i>Calcium phosphate cements (CPCs)</i>	9
(ii) <i>Calcium sulfate cements</i>	11
1.2.5 Injectable self-setting bone cements – Towards an ideal bone filler material	12
1.2.5.1 <i>Calcium phosphate cements as an injectable system</i>	13
1.2.5.2 <i>Calcium sulfate cements as an injectable system</i>	15
1.2.5.3 <i>Limitations in the existing cement systems</i>	16
1.3 Hypothesis	17
1.4 Objectives of the study	17
1.5 Brief overview of the study	18
CHAPTER 2- LITERATURE REVIEW	22
2.1 Early research on calcium phosphate bone cement	22
2.1.1 Apatitic bone cements	22
2.1.2 Brushite based bone cement formulations	23
2.1.3 Octa calcium phosphate based bone cement formulations	24
2.2 Incipient concept of injectable bioactive bone cement	25
2.2.1 Calcium phosphate based injectable bone cements	26
2.2.1.1 <i>Gelling agents in injectable CPC system</i>	28
2.2.1.2 <i>CPC system with macroporosity for tunable degradation with foaming agents</i>	30
2.2.1.3 <i>Inorganic additives or mineral components in CPC system</i>	31
2.2.2 Brushite based injectable CPC system	31

2.3 Research on calcium sulfate cement system	32
2.3.1 Calcium sulfate as bone void filler	32
2.3.2 Calcium sulfate cement in dentistry	34
2.3.2.1 <i>Guided tissue regeneration</i>	34
2.3.2.2 <i>Alveolar Ridge preservation</i>	35
2.3.2.3 <i>Sinus augmentation</i>	36
2.3.3 Calcium sulfate cement as local drug delivery system	36
2.3.4 Development of injectable CSC system	38
2.3.4.1 <i>Tailoring parameters - Injectability, resorption rate, setting time, mechanical property and bioactivity</i>	38
CHAPTER III- MATERIALS AND METHODS	40
PHASE I	40
3.1 Synthesis and characterization of low dimensional calcium sulfate dihydrate (gypsum) for the injectable bone cement formulations	40
3.1.1 Rationale for material selection	40
3.1.2 Materials	42
3.1.3 Synthesis of submicron dimensional Gypsum by drowning out wet crystallization method	42
3.1.4 Characterisation of the precipitated powder	44
3.1.4.1 <i>Phase and chemical bonding analysis</i>	44
3.1.4.2 <i>Micromorphology of the synthesised gypsum</i>	45
3.1.4.3 <i>Transmission electron microscopy and the selected area electron diffraction pattern</i>	45
3.1.5 Optimization route and parameters for selecting the current System	45
3.1.5.1 <i>ESEM analysis for particle homogeneity</i>	45
3.1.5.2 <i>Comparative solubility of Gypsum in the reaction media</i>	46
(i) <i>Dependence on the polarity of the reaction media</i>	47
(ii) <i>Dependence on the temperature difference of the reaction Media</i>	47
(iii) <i>Dependence on the concentration change of organic solvent</i>	48
3.1.6 Surface area analysis of the low dimensional gypsum with Brunauer Emmette Teller method	48
3.1.7 Heavy metal analysis by OES-ICP	48
3.1.8 In vitro screening test for the cell compatibility evaluation of synthesised gypsum	49
3.1.8.1 <i>In vitro cell culture cytotoxicity - Test on extract (ISO 10993-5, 2009)</i>	49
3.1.8.2 <i>Metabolic activity via MTT assay using mouse fibroblast cells (L929)</i>	50
3.1.9 Analysis of the chemical system and particle size control through nucleation kinetics studies	51
3.1.9.1 <i>Induction time measurements</i>	53

3.1.9.2 Equilibrium concentration from induction time variation	55
3.1.9.3 The surface energy and nucleation rate	57
3.1.9.4 Critical radius of the nucleus	58
3.1.9.5 Synthesis of gypsum nanoparticles	59
PHASE II	60
3.2 Design development of injectable bioactive bone filler cement	60
3.2.1 Optimization of thermal conversion of gypsum to bassanite	60
3.2.1.1 Structural overview of polymorphic analogues of calcium sulfate	60
3.2.1.2 Simultaneous Thermogravimetry /Differential Thermal Analysis ..	63
3.2.1.3 XRD analysis to identify the thermal conversion of gypsum	63
3.2.2 Production and characterisation of bassanite	64
3.2.3 Preparation of the cement precursor powder	65
3.2.4 Quantitative determination of injectability of the cement paste extrusion rheometry	66
3.2.5 Enthalpy of hydration of the modified cement	68
3.2.6 Effect of addition of DHPD on the phase conversion	69
3.2.7 Appending phase formation studies with elemental composition analysis	70
3.2.8 Micromorphology of the cement and evidence for the phosphate incorporation in the cement	71
3.2.9 Particle size analysis via High resolution 3D surface profilometry ...	71
3.2.10 Variation of setting time and compressive strength	72
PHASE III	
3.3. In vitro and in vivo validation of ‘BioCaS’ as an injectable bioactive bone filler cement	75
3.3.1 Materials and cell lines	75
3.3.2 In vitro aseptic degradation profile of BioCaS in Phosphate buffered saline	75
3.3.3 In vitro bioactivity through immersion in simulated body fluid	76
3.3.4 Selection of the tests and regulatory aspects	77
3.3.5 In vitro screening tests	78
3.3.5.1 In vitro cell culture cytotoxicity	78
(i) Method of test on extract using mouse fibroblast cells (L929)	78
(ii) Metabolic activity via MTT assay using mouse fibroblast cells (L929)	79
(iii) Cell viability using human osteosarcoma cells via a live/dead assay	79
(iv) Actin staining for evaluating the plastic adherence of HOS cells during the cell adhesion	81
(v) Scanning electron microscopy for the morphology of HOS cells on the surface of the cement matrix during cell adhesion	81
3.3.5.2 Haemolytic potential	81

3.3.6 Biocompatibility and evaluation of BioCaS	82
3.3.6.1 Acute systemic toxicity	82
3.3.6.2 Pyrogenicity	83
3.3.6.3 Irritation potential	84
3.3.6.4 Delayed hypersensitivity	85
3.3.6.5 In vivo implantation in rabbit model	86
(i) Implantation and histology	86
(ii) SEM with EDS of histological sections of BioCaS	89
(iii) Histomorphometry	89
(iv) Micro-CT analysis	90
PHASE IV	
3.4 Injectable ‘BioCaS’ as a local drug delivery medium	91
3.4.1 Chemicals and reagents	94
3.4.2 Theoretical frame work for drug delivery	94
3.4.3 Formulation of drug loaded BioCaS samples	96
3.4.4 Detection of gentamicin eluted from the BioCaSG cement formulation	97
3.4.5 Detection of Vancomycin eluted from the BioCaSV cement formulation	98
3.4.6 The validation of UV-Visible spectroscopic detection with HPLC analysis	98
3.4.7 Kinetics of GS release with concentration and surface area/volume ratio change	99
3.4.8 Kinetics of VH release with concentration and surface area change ..	100
3.4.9 Cementing Characteristics of the GS and VH loaded BioCaS	100
3.4.10 In vitro Antibacterial activity of the drug loaded BioCaS	101
PHASE V	
3.5 Injectable bioactive bone filler cements incorporating N,O- Carboxymethyl chitosan as gelling agent	103
3.5.1 Materials	104
3.5.2 Synthesis and characterizations of the N,O-Carboxymethyl chitosan (NOCMC)	104
3.5.3 Characterisation of the synthesised NOCMC	106
3.5.4 Preparation of the cement	107
3.5.5 Quantitative assay of the Injectability of the bone cement composition	108
3.5.6 Self setting times and compressive strength of the cement compositions	108
3.5.7 Characterizing the set cement composition	108
3.5.8 In vitro degradation study in phosphate buffered saline	109
3.5.9 In vitro bioactivity of the material	109
3.5.10 In vitro biocompatibility evaluation of the optimised composition ..	110
3.5.11 Cell adhesion study using human osteosarcoma cells by ESEM	110

3.5.12 Cell viability study by live/dead assay	111
CHAPTER 4-RESULTS	112
PHASE I	112
4.1 Synthesis and characterization of low dimensional calcium sulfate (gypsum) for the injectable bone cement formulations	112
4.1.1 Phase and chemical bonding analysis of the synthesised powder	112
4.1.2 Micromorphology of the synthesised gypsum (smCSD)- ESEM analysis.....	114
4.1.3 Particle size of the synthesised gypsum through transmission electron microscopy (TEM)	116
4.1.4 Regulation of parameters for the new chemical system.....	117
4.1.5 Validating the chemical system with the solubility parameter	119
4.1.6 BET specific surface area analysis of the synthesised gypsum	121
4.1.7 Heavy metal screening for the synthesised gypsum	122
4.1.8 In vitro tests for cytotoxicity	122
4.1.9 Nucleation kinetics parameters and synthesis of gypsum nanoparticles in the chemical system	124
4.1.9.1 Induction time measurement by turbidimetry	124
4.1.9.2 Determining the interfacial tension or surface free energy	126
4.1.9.3 Determining the nucleation rates and critical size	126
4.1.9.4 Particle size analysis of the nano gypsum	128
PHASE II	
4.2. Design development of injectable bioactive bone filler cement	130
4.2.1 Thermal conversion of phase of the synthesised gypsum (smCSD) ...	130
4.2.2 Characterisation of the bassanite or β -CSH	132
4.2.3 Effect of DHPD addition in the injectability of the cement	134
4.2.4 Enthalpy change of hydration in presence of the additive	136
4.2.5 Influence of the additive in the phase conversion of bassanite during cementing	137
4.2.6 Chemical mechanism for the formation of cement	140
4.2.7 Micromorphological variation of the set cements due to the additive	142
4.2.8 Particle size distribution of the cement from high resolution 3D surface profilometry	144
4.2.9 Appending phase formation studies with elemental analyses	145
4.2.10 Effect on the setting time and compressive strength	147
PHASE III	
4.3 In vitro and in vivo validation of ‘BioCas’ as a bone filler cement	150
4.3.1 In vitro screening tests	150
4.3.1.1 Immersion in simulated body fluid	150
4.3.1.2 In vitro degradation profile of the bone cement	157
4.3.1.3 In vitro tests for cytotoxicity	158
(i) Test on extract method	158
(ii) Metabolically active cell viability – MTT assay	158

(iii) Human osteoblast like HOS cell compatibility-Live dead assay	160
(iv) Plastic adherence of HOS cells during cell adhesion – F-actin staining	162
(v) Cell Morphology and adherence of HOS cells seeded on the bone cement using Scanning Electron Microscopy	163
4.3.1.4 Haemolytic potential	164
4.3.1.5 Biocompatibility evaluation in vivo	165
(i) Acute systemic toxicity	165
(ii) Pyrogenic potential of BioCaS	167
(iii) Intracutaneous reaction and skin sensitization	167
(iv) Efficacy evaluation of BioCaS through bone implantation	168
(a) Histology evaluation	168
(b) Elemental composition analysis in the defect site of BioCaS implant	174
(c) Histomorphometric evaluation of the implanted sections	174
(d) Micro-CT analysis	175
PHASE IV	179
4.4 Therapeutic efficacy of injectable BioCaS	179
4.4.1 Injectable BioCaS for Gentamicin (GS) loading in the BioCaS cement and in vitro elution profile	179
4.4.2 In vitro elution profile of Vancomycin loaded BioCaS	181
4.4.3 Validation of drug release pattern with HPLC	183
4.4.4 Elution profile and kinetics of VH loaded in BioCaS with concentration change	184
4.4.5 Elution profile and kinetics of VH loaded in BioCaS with S/V ratio ..	185
4.4.6 Elution profile and kinetics of GS loaded in BioCaS with concentration change	186
4.4.7 Elution profile and kinetics of GS loaded in BioCaS with surface area to volume ratio change	187
4.4.8 Injectability with concentration of the drug loaded	188
4.4.9 Setting times and mechanical property of the BioCaSG and BioCaSV group	189
4.4.10 In vitro antibacterial activity of the drug loaded BioCaS	191
PHASE V	
4.5 Injectable bioactive bone filler cements incorporating N,O-carboxy methyl chitosan as gelling agent	194
4.5.1 Phase and chemical bonding analysis of the synthesised NOCMC....	194
4.5.2 Comparison of the flow properties of the bone cement compositions	196
4.5.3 Setting times of the bone cement compositions	198
4.5.4 Comparison of the compressive strength of the compositions	199
4.5.5 Characterising the bone cement composition	200
4.5.6 Micro morphological variation of the set bone cement composition...	202
4.5.7 In vitro degradation studies of the cement composition	203

4.5.8	Invitro bioactivity of the optimised cement composition	203
4.5.9	Invitro biocompatibility studies	207
4.5.9.1	<i>Invitro cell culture cytotoxicity by test on extract method</i>	207
4.5.9.2	<i>MTT assay</i>	208
4.5.9.3	<i>Haemolytic assay</i>	209
4.5.10	Human osteoblast cell viability by live dead assay	209
4.5.11	Micromorphology of the HOS cells adhered on the surface of CS 251 and CS253 using Scanning Electron Microscopy	210
CHAPTER V – DISCUSSION		
5.1	Method of synthesis and characterisation of precursor phase for Injectable Bone Cement formulation	212
5.1.1	Optimisation of the production of low dimensional medical grade gypsum (smCSD)	212
5.1.2	Relevance of CNT in the current chemical system	216
5.2	Physicochemical mechanism for the formation of injectable bioactive bone filler cement	219
5.3	Preclinical validation of ‘BioCaS’	223
5.4	Injectable BioCaS as a local drug delivery system for minimally invasive chronic osteomyelitis management	228
5.4.1	Initial screening of BioCaS for drug holding capability and mechanism of drug loading	228
5.4.2	Elution kinetics varying the concentration of the drug loaded and S/V ratio of the matrix	229
5.4.3	Antimicrobial activity of BioCaSG3 and BioCaSV3 against the <i>E. Coli</i> and <i>S. aureus</i>	231
5.5	Injectable bioactive bone cement with NOCMC integrated Gypsum.....	232
5.6	Limitations of the study	234
5.7	Future perspective	235
CHAPTER 6 - SUMMARY AND CONCLUSION.....		
6.1.	Summary	236
6.2.	Conclusions.....	240
BIBLIOGRAPHY.....		
LIST OF PUBLICATIONS.....		
CIRRICULUM VITAE.....		

LIST OF FIGURES

Fig No.	Caption	Page No.
1	Statistical data showing the fertile market for bone graft substitutes	2
2	Phase diagram of solubility of calcium phosphates in terms of Ca ²⁺ ion concentration as function of pH	6
3	Different approaches towards the incorporation of Gelling agents in CPC system	27
4	Schema showing the precipitation of submicron dimensional gypsum powder	44
5	Schema showing the outline of nucleation kinetics study of the low dimensional gypsum formation	52
6	The chains of edge-sharing CaO ₈ polyhedra and (SO ₄) tetrahedra in anhydrite; (b) linking of chains into layers parallel to (-110) in anhydrite c) the layer of chains of edge sharing polyhedra in gypsum	61
7	(a)The structure of bassanite viewed along [001]; (b) the (CaO ₉) coordination polyhedron in bassanite.	62
8	Crystal structure of a) gypsum and b) bassanite viewed along the [001] vector	62
9	The schematic of the custom designed capillary rheometer	66
10	Custom fabricated Vicats needle type apparatus for setting time measurement	73
11	Three set of low dose drug loaded BioCaS cement samples with varying surface area to volume ratio	99
12	The schematic representation for the formation of N,O-carboxymethyl chitosan	105
13	X-Ray diffraction pattern of the precipitate obtained in 2-propanol	112
14	FTIR spectrum of the precipitated powder.	113
15	SEM image showing the micromorphology of the synthesised submicron dimensional particles of a) gypsum revealing monomodal low dimensional particle size distribution b) magnified view	114
16	SEM image a)-c) of gypsum particles formedadopting the same reaction parameters in CaCl ₂ -H ₂ SO ₄ , Ca(NO ₃) ₂ -Na ₂ SO ₄ , Ca(NO ₃) ₂ -H ₂ SO ₄ chemical systems in aqueous medium respectively d) Particles obtained in solvent exchange	115
17	a) Bright field TEM image and b) the magnified view of the precipitate revealing uniform rod-like submicron particles (c) Corresponding electron diffraction pattern	116
18	Micromorphology of the low dimensional gypsum synthesised in different reaction medium a)waer b) Methanol c) Ethanol d) 2-propanol and e) Acetone	117

19	SEM images of the synthesised gypsum with concentration of 2-propanol in reaction medium a) 1:9 b) 1:3 c) 2:3 and d) 1:1 (v/v) [20%, 50%, 80% and 100% respectively as solvent of $\text{Ca}(\text{NO}_3)_2 \cdot 4\text{H}_2\text{O}$].	118
20	Solubility of synthesised gypsum with respect to a) reaction media b) change in concentration of 2-propanol in the reaction medium c) temperature of the reaction medium	120
21	BET plot for the surface area analysis of the synthesised gypsum powder	121
22	Trace elemental analysis data of the synthesised low dimensional gypsum by OES-ICP method	122
23	L929 cells after incubating with A) negative control B) positive control and C) 50% extract of submicron dimensional gypsum	123
24	MTT assay for the metabolic activity of viable cells.	124
25	a) Representative graph demonstrating the finding of induction time induction time for the crystallization of the gypsum from the absorption kinetics b) Variation of t_{ind} with molar concentration of each of the independent reactant in the corresponding solvent (c) Relation between log induction time and inverse square of log supersaturation ratio.	125
26	Variation of a) nucleation rate and b) critical radius size with supersaturation ratio	127
27	Particle size distribution obtained in dynamic light scattering for the supersaturation ratio 2.12	128
28	TEM images of the particles formed at the supersaturation ratio 2.15 in presence of surfactant, taken at 80 kV. Regions of agglomeration could be seen in Picture A (X30,000). Magnified view of the particles are shown in Picture B (X40,000)	129
29	Simultaneous TG/DTA thermograms of smCSD showing the weight loss and transition temperature for the phase conversion.	130
30	Stacked XRD patterns of the smCSD at different calcination temperatures.	131
31	XRD pattern of the phase converted smCSD (the standard peaks of bassanite are marked, ICDD data base no. 74-2787)	132
32	FTIR spectrum of smCSD after calcination at 393K.	133
33	SEM image of the bassanite showing fine particles and lumps. At high magnification the lumps are found to be formed from the very fine particular aggregates	134
34	The variations of viscosity with time, of the cement compositions obtained from injectability study. A - smCHD0, B - smCHD1, C - smCHD2 and D - smCHD 5	135
35	Mean viscosity value of the cement pastes with varying concentrations of DHPD (from 1.5 to 10 % added in smCHD), corresponding to 98 s extrusion period	135

36	a) Smooth flow of smCHD2 cement paste through the needle during the extrusion rheometry b) Set cement paste after extrusion collected from the detachable bottom	136
37	Isothermal DSC plot of cumulative heat of hydration against time – A) smCHD0 and B) smCHD3	137
38	XRD patterns of - preset cement compositions A) Bassanite & B) DHPD and C) set cement smCHD5. The 0 2 0 peaks of smCHD5 are shown magnified and superimposed with that of the smCHD2 in the inset.	138
39	FTIR spectra of A) unmodified cement smCHD0, B) DHPD alone C) smCHD2 and D) smCHD5	139
40	Schema showing the mechanism of formulation of injectable bone cement	141
41	ESEM images of the set cement corresponding to-a smCHD0, b smCHD1, c smCHD2, d smCHD3, e smCHD4 and f smCHD5.	143
42	The growth features and aggregates observed in the set cement corresponding to – a) smCHD1, b) smCHD2, c) smCHD3, d) smCHD4 and e) smCHD5.	143
43	a) 3D surface profile b) particle size distribution profile of the surface and c) the corresponding peak count histogram of the smCHD2 obtained through Talysurf CLI100	144
44	a) 3D surface profile b) particle size distribution profile of the surface and c) the corresponding peak count histogram of the smCHD5 obtained through Talysurf CLI100.	145
45	EDS spectra corresponding to smCHD0 and smCHD5, obtained from area scan. Presence of P is seen in smCHD5.	146
46	Percentage content of P in different cement samples obtained from the spot EDS analysis	146
47	Eluted quantity of calcium (Ca), phosphorous (P) and sulfur (S) estimated through OES–ICP analysis	147
48	The variation of the initial (ti) and final (tf) setting times of the cement with DHPD concentration	148
49	SEM images of cement samples in the in vitro bioactivity test. (a) Surface of the BioCaS disc (b) after 4 days of immersion in SBF (c) Cross section showing the interface of the thickly coated apatite layer and the bulk BioCaS cement. (d) Magnified view of the area marked with an arrow in (b) showing the typical micromorphological features of the HA layer (e) Surface of unmodified CSC ie. smCHD0 after 4 days of immersion wherein the HA layer is non-uniform and discontinuous (f) Magnified view of the region in figure (e).	151
50	XRD patterns of the BioCaS and smCHD0 disc surfaces on the 2nd & 4th days of immersion in SBF.	152
51	FTIR spectrum of the BioCaS disc before and after 4 days of immersion in SBF	153

52	FTIR spectrum of the smCHD0 disc before and after 4 days of immersion in SBF	154
53	a) pH variation of SBF with immersion time (3 and 6 hours and 2, 4, 7 and 14 days) of BioCaS compared to unmodified CSC b)-d) Elemental concentration profile of a) Ca ²⁺ b) P ⁵⁺ and c) S ⁶⁺ estimated by OES-ICP with the soaking time of cements in in SBF	155
54	Degaradation profile in terms of a) percentage of degradation and b) rate of degradation of BioCaS and smCHD0	158
55	L929 cells incubated with (a) cell control and 50% extracts of (b) smCHD0 (c) 'BioCaS' (d) smCHD4 (e) smCHD5 and (f) 6.25% extract of the smCHD5.	159
56	MTT assay results of smCHD0, 'BioCaS', smCHD4 and smCHD5, normalized against the control.	159
57	Live/dead double staining of HOS cells adhered on the surface of the BioCaS and smCHD0	160
58	Z-stack confocal microscopic image of the HOS cells adhered on the BioCaS at consecutive depths of 11.2 μm from the surface.	161
59	Depth code analysis showing the cell viability on the BioCaS bone cement.	161
60	Z-stack confocal microscopic image of the HOS cells adhered on the smCHD0 at consecutive depths of 11.2μm	162
61	Depth code analysis showing the cell viability on the smCHD0 bone cement	162
62	F-actin of HOS cells, adhered on the surface of glass coverslip, BioCaS and smCHD0 stained using rhodamine-phalloidin and nuclei stained with Hoechst 33258 (magnification ×20).	163
63	SEM image of HOS cells a) on the surface of BioCaS b) the corresponding magnified view c) on the surface of smCHD0 d) the magnified view.	164
64	Potential of the BioCaS cement compared to unmodified cement and the reference material expressed as mean ±SD (n=3) ns: non-significant	165
65	Eluted elemental concentration in the intravenously administered PS extract through OES –ICP	167
66	Placement of samples in bone implantation study in rabbit femur : a) Injecting the BioCaS cement in the defect site using syringe b) BioCaS cement after setting.	168
67	Photomicrographs of stained histological sections (Stevenels' blue staining followed by counter-staining with Van Gieson's Picro-Fuchsin) of the test sample (BioCaS, (a), (c) and (e)) and the control sample (hydroxyapatite ceramic, (b), (d) and (f)) at 12 weeks.	170

68	Photomicrographs of stained histological sections (Stevenels' blue staining followed by counter-staining with Van Gieson's Picro-Fuchsin) of the test sample (BioCaS, (a), (c) and (e)) and the control sample (hydroxyapatite ceramic, (b), (d) and (f)) at 26 weeks.	172
69	Photomicrographs of stained histological sections (Stevenels' blue staining followed by counter-staining with Van Gieson's Picro-Fuchsin) of the test sample (BioCaS, (a), (c) and (e)) and the control sample (hydroxyapatite ceramic, (b), (d) and (f)) at 52 weeks.	173
70	The interface regions of implanted BioCaS A) 12 weeks after implantation B) 26 weeks after implantation and C) and D) their corresponding EDS pattern	174
71	Histomorphometrical evaluation. a) The new bone formation area b) The residual materials corresponding to HA and BioCaS after 12, 26 and 52 weeks of implantation	175
72	a) and c) Density histogram evaluation of 12 weeks implanted site depicting the bone mineralization density (in mg HA/ccm indicating milligram of HA per cubic centimeter) across the defect site including the newly formed bone (NB) and the host Bone (HB) in BioCaS and HA scaffold implanted group, respectively, derived from the corresponding 2D micro-CT slices shown in (b) and (d).	176
73	a) and c) Bone mineralization density distribution plot [mg HA/ccm indicating milligram of hydroxyapatite, HA per cubic centimeter] across the defect site in BioCaS and HA scaffold implanted group acquired from the corresponding 2D slices (b) and (d) respectiely 26 weeks post implantation	177
74	a) and b) Bone mineralization density distribution plot [mg HA/ccm indicating milligram of hydroxyapatite, HA per cubic centimeter] across the defect site in BioCaS and HA scaffold implanted group acquired from the corresponding 2D slices (c) and (d) respectiely 52 weeks post implantation	177
75	Conversion of GS to its isoindole derivative and the UV spectrum of the standard concentrations of GS showing the wavelength of absorption maximum λ_{max} at 333nm	179
76	Drug elution of GS from BioCaS bone cement a) Elution profile, b) Cumulative amount of the drug released and the c) The percentage cumulative drug release against time. d) shows the fitting in Korsmeyer- peppas model	180
77	The structure of Vancomycin hydrochloride (VH) and the UV spectrum of the standard concentrations of VH showing the wavelength of absorption maximum λ_{max} at 280 nm	181

78	Drug elution of VC from BioCaS bone cement a) Elution profile, b) Cumulative amount of the drug released and the c) The percentage cumulative amount of the drug released against time. d) shows the fitting in Korsmeyer- peppas model.	182
79	HPLC chromatogram of A) PBS B)and C) eluted samples at day 2 and 10 with the corresponding peak of vancomycin hydrochloride marked with retention time 4.5 minutes	183
80	Compiled elution plot VH obtained through HPLC and UV-Visible spectrophotometry	183
81	Elution profile b)cumulative amount of the drug release c) percentage cumulative amount of the drug release and d) Curve fitting in Korsmeyer-peppas model for the BioCaSV1, BioCaSV2 and BioCaSV3	184
82	a) Elution profile b) cumulative amount of the drug release c) percentage cumulative amount of the drug release and d) Curve fitting in Korsmeyer-peppas model for the BioCaSVS1, BioCaSVS2 and BioCaSVS3.	185
83	a) Elution profile b) cumulative amount of the drug release c) percentage cumulative amount of the drug release and d) curve fitting in Higuchi model for the BioCaSG1, BioCaSG2 and BioCaSG3	186
84	a) Elution profile b) cumulative amount of the drug release c) percentage cumulative amount of the drug release and d) curve fitting in Higuchi model for the BioCaSGS1, BioCaSGS2 and BioCaSGS3	187
85	Viscosity-time profile of the a) GS & b) VH loaded BioCaS with change in concentration of the drug loaded	188
86	a) Initial and final setting times of the BioCaS loaded with low, middle and high dose GS (ns-not significant)	189
87	a) Initial and final setting times of the BioCaS loaded with low, middle and high dose VH (ns-not significant)	189
88	Compressive strength and corresponding compressive modulus of the BioCaS loaded with low, middle and high dose antibiotic group	190
89	Growth inhibition of E.Coli and S.aureus by Gentamicin eluted from the BioCaSG3	191
90	Growth inhibition of E.Coli and S.aureus by Vancomycin eluted from the BioCaSV3	191
91	Diameter of inhibition zone of E.Coli and S.aureus by Gentamicin eluted from the BioCaSG3 injectable bone cement at days 1, 2, 3, 5,7,9,12,15 and 20 along with positive and negative control	192
92	Diameter of inhibition zone of E.Coli and S.aureus by Vancomycin eluted from the BioCaSV3 injectable bone cement at days 1, 2, 3, 5,7,9,12,15 and 20 along with positive and negative control	193

93	FTIR spectrum of a) chitosan and b) chitosan after carboxymethylation. All the major transmission peak of spectrum b) matches with N,O-Carboxymethyl chitosan	194
94	¹ H NMR spectrum of NOCMC in D ₂ O at 22.3 °C and the corresponding spectral data	195
95	Viscosity-time plot describing the flow property of the bone cement pastes with varying concentration of NOCMC a) 1.5% DHPD incorporated cement b) 2.5% DHPD incorporated cement c) 3.5% DHPD incorporated cement each with varying concentration of NOCMC d) The average viscosity at 120 sec at the three concentration of DHPD against the wt.% of NOCMC (A-1.5%DHPD, B-2.5%DHPD, C-3.5% DHPD).	197
96	Setting times of the bone cements with varying compositions of DHPD and NOCMC	198
97	a) Compressive strength and b) compressive modulus values of the bone cement with varying compositions of DHPD and NOCMC	199
98	Stacked FTIR spectrum of smCHD0, DHPD, NOCMC, CS253 and CS356	201
99	Mechanism for the formation of bone cement containing Ca ²⁺ chelated by NOCMC	201
100	The scanning electron microscopic images of a) CS151 b) CS153 c) CS156 d) CS251 e) CS253 f) CS256 g) CS351 h) CS353 i) CS356	202
101	a) the percentage of degradation and b) the rate of percentage of degradation of the CS251 and CS253 bone cement	203
102	Stacked XRD pattern of CS253 at different immersion periods in SBF	204
103	Stacked FTIR pattern of CS253 at different immersion periods in SBF	205
104	ESEM image of CS253 a) 2 days b) 4 days and c) 7 days immersion in SBF d) shows the magnified view of one of the cracked region.	206
105	a) pH variation of SBF with immersion time 3 and 6 hours and 2, 4, 7 and 14 days of BioCaS and CS253 b) Elemental concentration profile of a) Ca ²⁺ b) P ⁵⁺ and c) S ⁶⁺ estimated by OES-ICP with the soaking time of CS253 and BioCaS in SBF	207
106	L929 cells after incubating with (a) positive control (b) negative control and 50% extract of (c) CS251 and (d) CS253	208
107	MTT assay for the metabolic activity of viable cells in the physiological saline extract of the CS251 and CS253	209
108	Live–dead double staining of HOS cells adhered on the surface of CS251 and CS253 showing high cell viability	210
109	Scanning electron micrographs showing attachment and adhesion of Human osteoblasts like HOS cells on the surface of (a and b) CS251 and (d and e) CS253 and (c) and (f) corresponding magnified view	211

LIST OF TABLES

Table No.	Title	Page No.
1	Sample code of the set cement with preset additive composition	107
2	Compressive strength and compressive modulus variation of the set cement as a function of weight percentage of DHPD	148
3	Clinical observation data sheet for acute systemic toxicity RE-respiratory, MO-motor, CO-convulsions, RE-reflexes, OC-ocular signs, CA-cardiovascular signs, SA-salivation, PI-piloerection, AN-analgesis, MT-muscle tone, GI-gastrointestinal, SK-skin.	166

ABBREVIATIONS

ACP	: Amorphous Calcium Phosphate
ASTM	: American Society for Testing and Materials
BET	: Brunauer Emmette Teller
BG	: Bioactive Glass
BMPs	: Bone Morphogenic Proteins
CaS	: Calcium Sulfate
CDHA	: Calcium Deficient Hydroxyapatite
CPCs	: Calcium Phosphate Cements
CSCs	: Calcium Sulfate Cements
CSH	: Calcium Sulfate Hemihydrate
DBM	: Demineralized Bone Matrix
DCPA	: Dicalcium Phosphate Anhydrous
DCPD	: Dicalcium Phosphate Dihydrate
DD	: Deionised Distilled
DHPD	: Disodium hydrogenorthophosphate Dihydrate
DLS	: Dynamic Light Scattering
DTA	: Differential Thermal Analysis
EDS	: Energy Dispersive Spectroscopy
ESEM	: Environmental Scanning Electron Microscopy
FDA	: Fluorescein Diacetate
FGF	: Fibroblast Growth Factor
FTIR	: Fourier Transform Infrared Spectroscopy
GBR	: Guided Bone Regeneration
GDFs	: Growth Differentiation Factor
GS	: Gentamicin Sulfate
HA	: Hydroxyapatite

HOS	: Human Osteosarcoma Cell lines
IBC	: Injectable Bone Cements
ISO	: International Standard Organisation.
MCPM	: Monocalcium Phosphate Monohydrate
MRSA	: Methicillin-resistant Staphylococcus Aureus
NOCMC	: N,O-carboxymethylchitosan
OCP	: Octacalcium phosphate
OES-ICP	: Inductively Coupled Plasma-Optical Emission Spectroscopy
OPA	: O-Phthalaldehyde
PBS	: Phosphate Buffered Saline
PDGF	: Platelet Derived Growth Factor
PI	: Propidium Iodide
PMMA	: Polymethyl Methacrylate
PRP	: Platelet Rich Plasma
rh-BMP	: Recombinant Human Bone Morphogenetic Protein
SAED	: Selected Area Electron Diffraction
SBF	: Simulated Body Fluid
SEM	: Scanning Electron Microscopy
smCSD	: Submicron Dimensional Gypsum
TCP	: Tricalcium Phosphate
TEM	: Transmission Electron Microscopy
TG	: Thermogravimetry
TGF- β	: Transforming Growth Factor- β
TTCP	: Tetra Calcium Phosphate
UHMWPE	: Ultrahigh Molecular Weight Polyethylene
UTM	: Universal Testing Machine

VH : Vancomycin Hydrochloride
XRD : X-ray Diffraction
ZOI : Zone of Inhibition

SYNOPSIS

Bone fillers refer to the class of biomaterials which are bioactive and resorbable, intended to fill bony voids or gaps caused by trauma or surgery. They are useful in appending or augmenting bone grafts so as to avoid gaps facilitating the migration of osteoblast cells and thereby to achieve faster healing. Self-setting calcium salt compositions, based on calcium sulfates and phosphates, have successfully been used as bone fillers.

In the recent years, researchers are actively working on the development of ‘injectable’ bioactive bone filler cements for the minimally invasive bone defect management. An ideal injectable bioactive bone filler cement should be affordable, biocompatible to ensure systemic safety, bioactive to help local bone remodeling. It should have clinically acceptable setting parameters, appropriate resorption *in vivo* and preferably should have the ability of controlled drug release to manage bone diseases. None of the existing compositions satisfy these ideal requirements. The major challenge is that conventional calcium salt based cements are inherently lack flow properties. Gelling agents could be used to induce viscosity but they may hamper the setting and biocompatibility. Some of the compositions have fast resorption and some are not suitable for drug delivery.

The main goal of the study was set towards the development of an injectable bioactive bone filler cement useful for bone grafting procedures, as well as for local drug delivery in bone diseases. The work plan consisted of developing methods for the synthesis of basic precursor moieties, design and optimization of the cement formulation and its biocompatibility and efficacy evaluation. Also the study on drug

delivery action and further scope of modification using biocompatible additives were included.

On the basis of the current knowledge, the following hypotheses were arrived at : (i) *The physico-chemical properties of the bone cements depend on the morphology and size of the precursor phase and can be tailored for flowability and mechanical property by synthesizing the crystals of low dimension and high purity* (ii) *Appropriate choice of the chemical additives, particularly the phosphate group addition, can impart the required bioactivity and osteoconductivity* (iii) *The cement formulation can incorporate higher quantity of drug and enable sustainable controlled delivery greater than minimum inhibitory concentration without the loss of biofunctionality.*

In order to prove the hypotheses, the major objectives of the current study were defined:

- To synthesise calcium based inorganic salt precursor compounds with uniform low dimensional crystal size and high level of purity, through viable chemical methods.
- To develop bone filler cement formulation, to optimise the injectability, setting time and compressive strength corresponding to clinical requirement, and to explore the physico-chemical mechanism leading to injectability.
- To conduct *in vitro* screening tests and *in vivo* biocompatibility evaluation of the optimized cement formulation based on the international standard guidelines.

- To conduct efficacy of the optimized cement formulation in defect healing through animal bone implantation study.
- To evaluate the performance of the bone cement as a drug delivery medium for bone infections.
- To explore further scope of modification of the bone filler cement with biocompatible additives.

The study is presented in the thesis in six chapters. The background and introduction to the work are presented in Chapter 1. It covers the need and significance of bone grafting, available strategies for the same, need for bone fillers, bone cement systems and finally the importance of injectable bioactive bone filler cements (IBCs). Current strategies available, limitations of the existing IBCs and the major challenges in designing them are discussed.

In Chapter 2, literature is reviewed to understand the current status of bioactive bone filler cement compositions. The topics reviewed include the concept of injectable bone cements, the methods to impart injectability via gelling agent, imparting macro-porosity and controlling degradation rate and use of additives for achieving appropriate setting and compressive strength. Early history of gypsum bone void filler, potential areas of application of cement system and the regaining research interest in nowadays are presented. Lastly the development of injectable gypsum based system and tailoring the injectability, resorption rate, setting time, mechanical property and bioactivity has been reviewed.

In Chapter 3, experimental design of the proposed study is elaborated. It includes detailed description of the materials used, synthesis methods, experimental protocols

and instruments employed for the present study. In the phase 1, a novel method was developed for the synthesis of submicron dimensional gypsum (smCSD) to obtain the precursor phase. The relevance of classical nucleation theory in the system analysing the nucleation kinetics parameters through turbidimetry, validating its purity as medical grade were also described. Phase purity (SAED), heavy metal content (OES-ICP), specific surface area (BET method), has been assessed and preliminary biocompatibility screening (MTT assay and hemolytic assay) was done. Phase 2 describes the design development of injectable bioactive bone filler cement with smCSD where the set cement comprises the phosphate-containing gypsum. Method for assessing the physico-chemical mechanism during cementing (using TG, DTA, XRD, FTIR), enthalpy of hydration (Isothermal DSC), particles size (TEM, 3D surface profilometry), micromorphology features (ESEM), elemental composition (EDS and OES-ICP) were described. Quantitative estimation of injectability done with custom made capillary rheometer for scaled down Extrusion rheometry was explained. Particle size distribution of the cement with 3D surface profilometry and cementing parameters, setting time with custom fabricated Vicat needle type apparatus and compressive strength evaluation with UTM are also given. Phase 3 comprises the *in vitro* assays for bioactivity, degradation, cytotoxicity, hemolysis and *in vivo* assays for the interaction with the biological system. Protocol for bioactivity evaluation through SBF immersion, HOS cell viability with Live-Dead Assay and plastic adherence property with F-actin staining are described. *In vivo* biocompatibility evaluation including an acute systemic toxicity test (in mice), an intracutaneous reactivity test (in rabbits), pyrogen test (in rabbits) and a maximization sensitization test (in guinea pigs) are explained. Implantation

procedure in rabbit femoral defect with HA ceramic scaffold as control, histological and histomorphometric evaluation procedures, density profile of the explant with Micro-CT are described. In phase 4, potential of the optimised cement 'BioCaS' to act as local drug delivery system for osteomyelitic management has been explained with drug elution kinetics and invitro anti-bacterial activity [Kirbi-Bauer disc diffusion susceptibility test for growth inhibition of gram positive *Escherichia coli* (ATCC25922) and *Staphylococcus aureus* (ATCC 25923)]. The scope for enhancing the injectability and mechanical property with gelling agent N,O Carboxymethyl chitosan (NOCMC) was studied and explored the mechanism of cementing as described in section 5. Assessing the formation of water soluble NOCMC and calcium cross linking via chelation in the cement matrix with PMR and FTIR respectively were given.

Chapter 4 includes results presented in the form of figures, images, tables and graphs. Medical grade submicron dimensional gypsum of 3-5 μ m length and < 500 nm width were produced by novel drowning out wet chemical method involving the lowest *surface free energy* reported compared by regulating the parameters. Prioritizing full injectability with low and constant viscosity without compromising the cementing parameters, IBC named 'BioCaS' comprising the phosphate integrated gypsum crystal lattices were developed where the preset formulation comprises the bassanite obtained from the smCSD modified with Disodium hydrogen orthophosphate dihydrate (DHPD). The integrated phosphate attributed to the higher bioactivity and low degradation rate. The interaction of the cement with the biological tissue were analysed *in vitro* and *in vivo* established the safety profile.

Bone implantation study revealed BioCaS to be osteoconductive and its efficacy of healing the experimental bone defects in rabbit femora is on a par with that of hydroxyapatite ceramic. The material resorbed at a pace matching that of new bone formation. This property of osteotransductivity will help the defect to heal and gain strength faster. From microbiological study, The optimised drug loaded cement matrix, the higher dose gentamicin loaded BioCaS (BioCaSG3) showed potential inhibition of *E.coli* up to 15 days and of *S. aureus* up to the 20 days (under the 20 day study period). Higher dose vancomycin loaded BioCaS (BioCaSV3) was effective against *S. aureus* up to 20 days and it even showed considerable inhibition of gram negative pathogen *E. coli* up to 5 days. It was found that both NOCMC and DHPD has compiled role in enhancing the injectability during the formulation of cements with gelling agent. The optimised cements with 2.5w/w% DHPD and 0.15% w/v of NOCMC (CS251) and 2.5w/w% DHPD and 0.30% w/v of NOCMC (CS253) showed higher compressive strength than BioCaS. In vitro degradation percentage was found to be less than BioCaS and the gelling agent not hampered the bioactivity but the thick layer of HA formation got delayed while immersion in SBF. The modified cement passed the *in vitro* screening test for biocompatibility and proved the osteoconductive nature from the cell adhesion study.

Chapter 5 comprises the results discussed and analyzed on the basis of current literature. It is shown that injectable bone cements with bone cell compatibility, bioactivity and osteotransductivity with clinically acceptable setting and mechanical strength could act as an effective bone filler for skeletal or bone defect repair in load bearing application. Paste consistency helps to incorporate more drug than sintered

ceramic and hence become an effective sustained and controlled local drug delivery system. The importance of the present work is also highlighted.

Chapter 6 includes the summary and conclusions drawn from the present study. Considering its physicochemical and biological properties, it can be concluded that BioCaS is on a par with other bioactive self-setting cements, particularly CPC. None of the injectable CSC system has reported the bioresorption greater than 8 weeks and hence BioCaS is unique without compromising clinically acceptable parameters. The BioCaS G3 and BioCaSV3 showed biofunctionality greater than 14 days against both *E.coli* & *S.aureus* and *S.aureus* respectively. Cement systems with higher mechanical properties viz. CS251 and CS253 with even low degradation rate than BioCaS were also developed with gelling agent. The limitations of the current study have been identified and future perspective to enhance the injectability of BioCaSG3 and BioCaSV3 and its preclinical validity testing in osteomyelitic animal defect model for efficacy assessment for minimally invasive bone defect management in diabetic patients were included. The regeneration efficacy variation for CS251 and CS253 compared with BioCaS has to be further carried out.

The conclusion shows that the objectives of the study are met. The Citations are listed in the bibliographic section.

CHAPTER 1

INTRODUCTION

1.1 Need and significance of bone grafting

Bone tissues have remarkable ability to combat injuries by self-repair and regeneration. However massive bone defects that encounter in trauma, surgical resection for tumor and revision of failed joint prosthesis, fail to heal naturally, while pathologic, metabolic and oncological disorders may hamper the regain of original function. Reconstructive surgeries and routine fracture reduction (where the surgical parts are aligned with fixation devices like plates, screws, rods and wires) often require the bone grafting to compensate for the missing bone which gets managed with natural bone grafts and/or synthetic bone graft substitutes.

The requirement of bone graft and synthetic substitutes often arises in clinical practices: (i) to compensate the lost bone in the fracture, (ii) to fill the gap left out in surgical resection site, (iii) surgical correction of skeletal deformities like maxillofacial orthognathic surgery and (iv) for augmentation like sinus lift. Approximately 3.5 million bone graft procedures are performed every year (Nich et al., 2011) and considering the global significance, the World Health Organisation had declared the period 2000 -10 as the “bone and joint decade”. This was for conscientizing about the major threats and burden of musculoskeletal disorders/injuries on the society, and for high level financing of research for its prevention, diagnosis and high quality therapy (Baroli et al., 2009). It was predicted that the number of victims would double by 2020 due to the ageing population and

“democratization of high risk sports” (Dorozhkin, 2010). As per the report of Global industry analysts in USA, the global market for the bone graft substitutes is anticipated to reach 3.2 billion US dollars by 2022 (Figure 1).

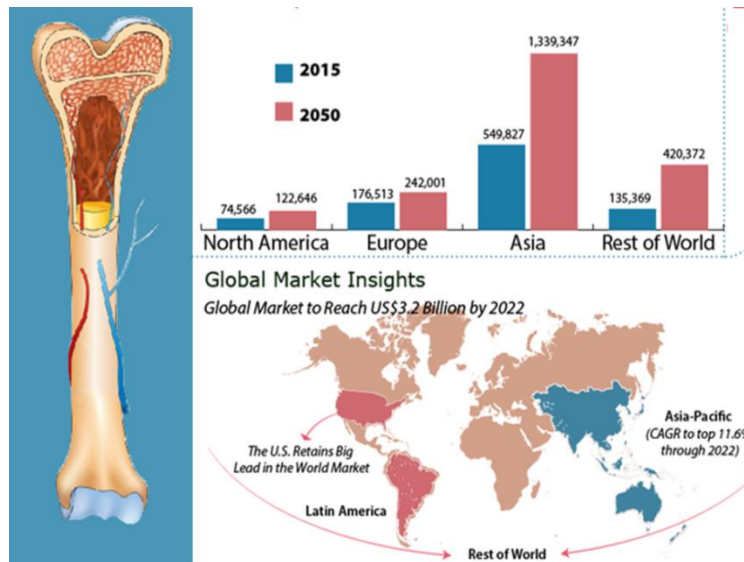


Figure 1: Statistical data showing the fertile market for bone graft substitutes Ref: <http://www.strategyr.com/MarketResearch/infographTemplate.asp?code=MCP-1637>

1.2 Strategies in bone grafting

1.2.1 Natural bone grafts

Autogenous graft, harvested usually from the rib or iliac crest of the patients themselves, is considered as the ‘gold standard’. It comprises four primary components of an ideal bone graft : (a) an osteoconductive matrix, to host the osteoblast and osteoprogenitor cells, (b) osteoinductive factors like bone morphogenic proteins to stimulate the mitogenesis of undifferentiated and pluripotent stromal cells into osteoprogenitor cells, (c) osteogenic metabolically viable cells, capable of differentiation in to bone forming cell-lineage, and (d) osteointegrative porous surface to form direct anchorage with host bone through chemical bond

without an intervening fibrous layer (Kheirallah *et al.*, 2016). However, this approach has drawbacks since it necessitates additional surgery and may cause donor site morbidity, risk of infection, scarring and blood loss. Also the availability of autogenous bone is limited especially in pediatric patients and the elderly (Bovan *et al.*, 2011).

The ‘allograft’ derived from a cadaver or human donors are the other alternative. In developed countries, they are readily available banked in frozen, freeze-dried or demineralised forms in a variety of sizes and shapes. However allografts lack osteogenicity and possess high risk of immune rejection and disease transmission (Graham *et al.*, 2010). Xenografts derived from other species (mainly bovine) are also used owing to the easy availability. Yet they require processing to eliminate antigenic epitopes which alter the properties and function and lessen the efficacy (Szpalski *et al.*, 2011).

Bone derived components such as collagen, demineralized bone matrix (DBM), deproteinated bone, coralline derivatives and growth factors (Bone Morphogenic Proteins or BMPs), Transforming Growth Factor (TGF- β), Platelet Derived Growth Factor (PDGF), Growth Differentiation Factor (GDFs), Fibroblast Growth Factor (FGF) etc were also explored. Despite being osteoinductive, they were reported to have complications due to immunogenic response, under or overproduction of bone, quick resorption rate and lack of mechanical strength are the associated complications (Campana *et al.*, 2014).

1.2.2 Synthetic bone graft substitutes and de rigueur for bioactivity

The inherent shortcomings of the biological grafts prompted for the development of synthetic bone graft substitutes. There are several materials used in orthopedics for

skeletal repair, mainly for fracture reduction and joint replacements. Synthetic bone graft substitutes used in early times were designed to match the physical and mechanical properties of the bone. Examples are substitutes made of (a) alloys (stainless steel, cobalt base alloys with Cr, Ni, Mo and N, Ti based alloys Ti-6Al-4V, Ti-6Al-7Nb and Ti-12Mo-6Zr-2Fe) (b) ceramics (alumina, zirconia) and (c) polymers (UHMWPE, PMMA, Polypropylene, Poly urethanes, Polyetheretherketones (PEEK), Silicone) etc (Kapanen *et al.*, 2001). These materials are not 'bioactive', that is they do not impart natural bone repair and remodeling; further they tend to form a fibrous connective tissue encapsulation at the host bone-material interface.

With the advent of bioceramics based on the hydroxyapatite (HA), the class of bioactive synthetic graft materials for bone regeneration has been introduced. The bioactive materials trigger chemical changes at the interface of the material when implanted, undergoes time dependent changes and generates a biologically active carbonated apatite layer *in vivo* quite similar to mineral component of the bone (ISO/FDIS 23317:2014(E)). Bioactive materials provide binding sites for the newly forming/repairing tissue and the stable interface helps to withstand the tensile and shear stress which are favourable for remodeling. The family of bioactive materials consists of calcium orthophosphates, bioactive glass and bioactive glass ceramics. Several commercial synthetic bone graft products based on bioactive materials are available in the market. These synthetic bone grafts are available in custom fabricated design offering abundant off the-shelf supply, low risk of disease transmission and immunogenicity and lesser surgical complications.

1.2.3 Calcium phosphate bioceramics

Calcium phosphate bioceramics comprises the mineral salts of calcium orthophosphate synthesised by wet chemical, sol gel or hydrothermal, electrodeposition methods and subsequently sintered at temperatures 1000-1200°C. The calcium orthophosphate ceramics that are predominantly used presently are (i) dihydrated and anhydrous forms of dicalcium phosphate, namely brushite ($\text{CaHPO}_4 \cdot 2\text{H}_2\text{O}$) and monetite (CaHPO_4) where brushite is metastable converts to monetite at $\text{pH} < 6$ and found in fracture callus and hence reported sometimes as a precursor of HA in the bone, (ii) α and β crystallographic forms of tricalcium phosphate [$\text{Ca}_3(\text{PO}_4)_2$, α and β -TCP] with α -TCP more degradable than β -TCP and readily transforms in to CDHA with Ca/P ratio 1.5, (iii) octacalcium phosphate [OCP, $\text{Ca}_8\text{H}_2(\text{PO}_4)_6 \cdot 5\text{H}_2\text{O}$], a metastable precursor of apatitic calcium phosphate in teeth and bone that readily transforms in to HA *in vivo*, (iv) calcium hydroxyapatite [HA, $(\text{Ca}_{10}(\text{PO}_4)_6(\text{OH})_2)$], most crystalline and stable which is identical to bone mineral, (v) amorphous calcium phosphate $\text{Ca}_x\text{H}_y(\text{PO}_4)_z \cdot n\text{H}_2\text{O}$ where $n = 3-4.5$ having same chemical property of TCP but lack long range order and (vi) non-stoichiometric calcium deficient hydroxyapatite with low crystallinity [$\text{Ca}_{(10-x)}(\text{HPO}_4)_x(\text{PO}_4)_{(6-x)}(\text{OH})_{(2-x)}$, $1.5 < \text{Ca/P} < 1.67$].

The correlation between solubility of Ca^{2+} in various calcium phosphate compounds and the pH calculated from their solubility products (Figure 2), predicts their stability in various pH range and are found to be critical during their production. The apatite is the most thermodynamically stable phase at neutral and alkaline regions and brushite at regions of 4.3 or less. The most widely used calcium

phosphate compounds are the hydroxyapatite (Ca/P ratio 1.67) and tricalcium phosphate (Ca/P ratio 1.50) which are implanted in sintered porous, compact or granular ceramic forms.

The inorganic part of the mammalian calcified tissue is composed of ‘biological apatite’, the apatitic calcium phosphate non-stoichiometrically substituted with carbonate and trace amount of Na, K, Mg, Cl and F (Chernousova *et al.*, 2014, Bohner *et al.*, 2000). Synthetic Hydroxyapatite ceramics have chemical and crystallographic similarity to bone mineral and due to high stability in physiological pH (Figure 2), the complete degradation may takes several years.

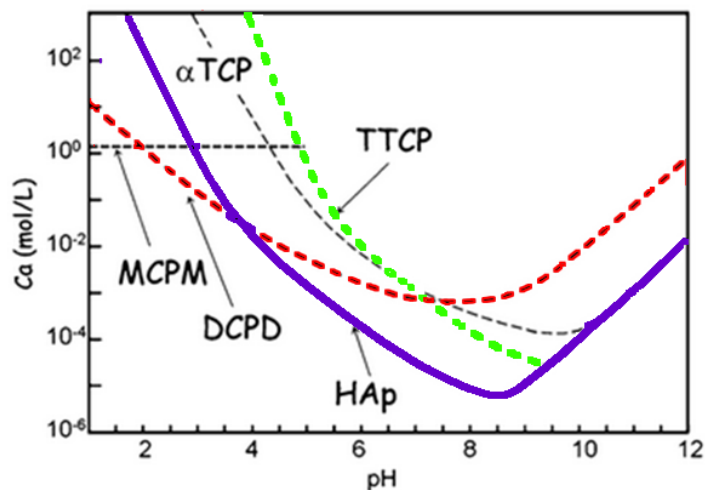


Figure 2: Phase diagram of solubility of calcium phosphates in terms of Ca^{2+} ion concentration as function of pH (Ishikawa, 2014)

Resorption rate of β -TCP ceramics is reported to be 10 times faster than HA ceramics. Resorption rate could be altered by modulating crystallinity, porosity or sintering temperature, and also by substitution of Ca by Mg, Zn, Si and Y. β -TCP ceramics are also used in combination with HA as ‘biphasic ceramics’ (Bansal *et al.*, 2014).

Bioactive glassy compositions (BG) first developed in the 1960's, comprise the basic chemical composition with SiO_2 , CaO , Na_2O and P_2O_5 , the ratio of which decides mechanical properties and bioactivity. The main advantage is the high superficial speed reaction that brings to rapid connections to the tissues and show higher *in vivo* resorption (Montazerian *et al.*, 2016). 'Bioactive glass ceramics' were developed to overcome the low mechanical strength and limited fracture toughness of BG and they contain polycrystalline materials with one or more crystal phases embedded into a residual bioglass structure. The most extensively used glass ceramics are the apatite/ wollastonite glass ceramics with $\text{Ca}_3(\text{PO}_4)_2\text{-CaSiO}_3\text{-MgCa}(\text{SiO}_3)_2\text{-CaF}_2$ (De Aza *et al.*, 2007). Eventhough bioactive glass ceramics did possess mechanical properties comparable to bone structure, they failed in the market due to high cost of production.

1.2.4 Bone fillers

1.2.4.1 The need and significance of bone fillers

Bone originates from osteoblasts derived from mesenchymal osteoprogenitor cells which produce the matrix comprising organic molecules of collagen protein fibres and mineral hydroxylapatite. The release of the the package of this matrix components into extracellular environment finally makes up rigid and flexible bone tissue called osteoid. This natural process called 'remodeling' occurs at the bone graft site. The success of grafting depends on the apposition of the bone substitute to the surrounding host bone. In the case of sintered bioactive blocks and beads type ceramics, it is very difficult to shape them in a way that they fit snugly into the defect site to give good clinical results. Ceramic blocks require machining or carving to fit them in position and the fitting process during surgery can lead to bone loss,

associated trauma and increased surgical time (Zhao et al., 2010). The problem could be managed by introducing cement-like ‘bioactive fillers’.

U.S. Food and Drug Administration released Class II special control guidance document (FDA, 2003), clearly stated the need for bone fillers. According to the document, bone fillers are defined as the resorbable biomaterial device intended to fill bony voids or gaps caused by trauma or surgery that are not intrinsic to the stability of the bony structure. They have potential use in skeletal / bone defect repair in non-load bearing cases.

Inorganic self-setting bone cements were developed for the typical use as bone fillers. Unlike the ceramics, the bone cements can set and harden *in situ* the bone defect site without leaving a gap in the implant-host bone interface. This conformal filling of the irregular bone defect site will lead to better outcome in healing. They also have the potential of a local drug delivery system when drugs are incorporated in to the matrix.

1.2.4.2 Inorganic self-setting bone cement systems

This class of materials could be viewed as third generation bone substitutes. Inorganic self-setting bone cement systems constitute the heterogeneous composition including one or more solid dispersed phase and liquid solvent, which when mixed, develops dough/paste consistency. The physico-chemical reaction in the mix leads to setting and subsequent hardening at definite time period and develops mechanical properties to meet the clinical requirement for bone defect management (Barinov et al, 2011). These compositions have the unique combination of mouldability, osteoconductivity and bioegradability. They are classified in to two groups - Calcium phosphate cements (CPCs) and Calcium Sulfate Cements (CSCs).

(i) *Calcium phosphate cements (CPCs)*

The correlation between the solubility of Ca^{2+} in various calcium phosphate compounds against the pH calculated from their solubility products (Figure 2) provided a scope for the conversion of calcium orthophosphates to apatites (hydroxylapatite, or calcium deficient hydroxyapatite or carbonated apatite). Brushite and octacalcium phosphate based cements are also studied to less extent. In general the binding interaction during the setting process principally embroils acid base reaction and hardly takes in hydrolysis of metastable phosphate in aqueous medium (Barinov et al., 2011).

Among calcium phosphate cements, '*apatitic cements*' which essentially contain the Ca/P ratio 1.67 whose resultant phase is hydroxyapatite are studied in detail. In 1986, Brown and Chow developed poorly crystalline precipitated hydroxyapatite through the exothermic setting reaction of equimolar mixtures of TTCP (Hilgenstockite, a basic component with Ca/P ratio 2.0) and DCPA/DCPD (slightly acidic component with Ca /P ratio 1.0) with water at pH of 7.5-8.0 (Brown *et al.*, 1987, Chow *et al.*, 2001). The rate determining step of the reaction involves the release of PO_4^{3-} ions with respect to the dissolution of DCPA and hence diameter ratio of TTCP/DCPA>1 was opted to get better mechanical properties but setting time remains in the range of 30-60 min (Brown *et al.*, 1987, Chow *et al.*, 2001). The shortening of the setting time to 5 minutes were tried with neutral phosphate salt solution ($\text{Na}_{1.8} \text{H}_{1.2}\text{PO}_4$ or $\text{K}_{1.8}\text{H}_{1.2}\text{PO}_4$) as liquid phase and adding apatite seed crystals to the powder phase (Ishikawa *et al.*, 1995). Dry mixing of MCPM, α -TCP and CaCO_3 with a sodium phosphate solution yielded non-stoichiometric carbonated apatite or dahlite $\text{Ca}_{8.8}(\text{HPO}_4)_{0.7}(\text{PO}_4)_{4.5}(\text{CO}_3)_{0.7}(\text{OH})_{1.3}$ (Constantz *et al.*, 1995).

Brushite based bone cement formulations also was developed in the class of CPCs. Lemaitre et al produced slightly acidic brushite cements by the acid-base interaction between the acidic MCPM or H_3PO_4 and near neutral β -TCP, with a fast setting time of 30s. Up on mixing, the immediate dissolution of MCPM induces acidic condition in the vicinity by producing Ca^{2+} and HPO_4^{3-} which in line promote the dissolution of β -TCP. The consumption of proton during the process increases the pH and precipitates the brushite and bridges the remaining β -TCP (Bohner et al., 1997). Certain studies report replacement β -TCP with α -TCP (Fernandez *et al*, 1998) $\text{Ca}(\text{OH})_2$ (Desai et al., 2007), CDHA (Algel *et al.*, 2009) and that of MCPM with H_3PO_4 (Grovera et al., 2008) and MCPA (Engstrand *et al.*, 2013). An addition (~20wt %) of calcium pyrophosphate ($\text{Ca}_2\text{P}_2\text{O}_7$) and calcium sulfate hemihydrate prolonged the setting time to 5 min and 7 min respectively. The addition increased the diametral tensile strength to ~3 MPa against <1 MPa in bare brushite cement (Mirchi *et al.*, 1989).

The crystallization of HA during the biomineralisation of bone tissue occurs through the formation of intermediate prototype octacalcium phosphate [$\text{Ca}_8(\text{HPO}_4)_2(\text{PO}_4)_4 \cdot 5\text{H}_2\text{O}$] and hence cementing systems based on OCP either as a reagent or reaction product has been explored. The morphology and crystallinity of the OCP are determined by the method of preparation drastically affects the performance of the cement system. Only the combination of α -TCP and DCPD at the Ca/P molar ratio of 1.20-1.47 in aqueous setting medium is explored. (Monma et al., 1988). In a recent study in which 60 wt % α -TCP and 40 wt % OCP (as a reaction product of calcium acetate and sodium acid phosphate) cement powder were mixed with phosphoric acid containing sodium citrate as the hardening liquid and obtained 15wt % OCP in the final reaction products with setting time 10 minutes and compressive strength 30 MPa (Komlev *et al*, 2012).

(ii) Calcium sulfate Cements (CSCs)

Calcium sulfate cements are based on the hydration reaction of calcium sulfate hemihydrate to dihydrate form (gypsum) in a slightly exothermic reaction. Different dehydration pathways are reported for the formation of respective β and α -hemihydrate, like heating gypsum between 45 and 200°C under vacuum/dry air and heating above 45°C in an acidic or salt solution or in water at 97.2°C (Hughes *et al.*, 2015). Calcium sulfate (CaS) based cements are currently in wide use as a rigid-impresion material in dentistry and as a cast material in orthopaedics. Apart from cost-effectiveness and simplicity, its use during the past century as a bone graft material was very sparse. The reasons maybe, limited osteoconductivity and fast resorption (Larsson and Hannink, 2011, Christopher *et al.*, 2006) which creates an acidic micro environment in the surrounding tissues and leaves the implanted site mechanically unstable (Thomas and Puleo, 2005 and 2010). Though a few products are available in the market, there is a lack adequate evidence for clinical use as a bone filler or bone graft (Mirzayan *et al.*, 2001, Buerlein and Mc Kee, 2010).

However, there is a revival of interest in gypsum bone cements in recent years owing to the plausibility of local drug delivery in pathological, metabolic and oncological challenges of the bone. CPC is less useful in this aspect since the acid–base reaction during setting is likely to decompose the drug molecules. The setting mechanism of CSC involves only rehydration and recrystallisation and hence any water soluble drugs can safely be incorporated. The use of CSCs as drug delivery medium for osteoporosis and osteomyelitis has already been demonstrated (Thomas and Puleo, 2008). Currently CaS material suitable for drug loading, in putty form as well as pre-formed beads are commercially available for the treatment of bone

diseases (Buerlein et al., 2010, Hughes et al., 2011). Examples are Osteoset (Wright Medical Technology, Arlington, TN), Calceon 6 (Synthes, Westchester, PA) and JAX (Smith and Nephew, Memphis, TN).

1.2.5 Injectable self-setting bone cements – Towards an ideal bone filler material

The cements described in the previous section are suggested for bone filler applications in open surgeries. For the past 8 years or so, the biomaterial researchers have been trying to develop injectable compositions for minimally invasive bone defect filling. This class of injectable self-setting bone cements (IBCs) is projected as the new generation biomaterials for skeletal repair. These are potentially expedient in inaccessible sites like benign bone lesions, arthroscopic treatment of cartilage in the knee, periapical cysts in mandibular and maxillofacial region, regions in spine, vertebral compression fractures etc. They also find use in extending the bone grafts and stabilizing the implants. Unlike the ceramic granules and pre-shaped scaffold, IBCs ensure the conformal filling of intricate cavities for the bone cell migration and make it easier to transfer in inaccessible sites (Lewis, 2011, Rahman *et al.*, 2012).

Ideally an Injectable Bone Cement (IBC) should be in paste consistency when mixed, which could flow through a narrow cannula under pressure and sets preferably. The setting time and mechanical strength should meet the clinical requirement for the bone defect management (Vorndran, 2013, Larsson, 2011). Bioactivity and osteoconductivity are the essential criterion for IBCs, so that early osseointegration may occur and the material can actively take part in bone remodeling. While exploring the potential candidate materials for IBC, two classes could be identified - calcium phosphates and calcium sulfates (Li, 2000).

1.2.5.1 Calcium phosphate cements as an injectable system

Along with the development of calcium phosphate cements (CPCs), efforts have been put in to develop their injectable formulations also. Conventional CPC formulations do not possess injectability and the cement mix shows phase separation on pressurizing. One method for imparting the injectability of CPC is to use gelling agents like chitosan (Xu et al., 2008), alginate (Zhao et al., 2010) hydroxyl propyl methyl cellulose (Burguera et al., 2006), gelatin (Carey et al., 2005), hyaluronate (Kai et al., 2009), glycerol, poly acrylic acid, chondroitin sulfate, citric acid etc (Gbureck et al., 2004). The introduction of gelling agents escalates the viscosity of the system imparting cohesiveness and anti-washout property to hold the cement in the implantation bed.

Nonetheless the gelling agent possibly impedes the final phase conversion, setting and mechanical properties and the complex interaction between the ions conceivably generate toxic components compromising biocompatibility. CPC design with ACP-DCPD system having 20 wt% sodium alginate in the ACP phase has shown an escalation of setting time to 70.5 minutes compared to 47 minutes without additive but diminished the compressive strength to 10 MPa from the control value of 27.5 MPa. Gelatin also showed analogous effect and 2-5 wt % were found to be the limit for MCPM-CaCO₃ and α -TCP based CPC system respectively to get reasonable cementing properties (Yua *et al.*, 2010). The addition of sodium hyaluronate in liquid phase from 0.4-1.0 % concentration range attributes to the injectability of the TTCP-DCPD system with powders of citric acid, Na₂CO₃ and HAP powders; but showed filter pressing below 0.4% (Kai *et al.*, 2009). Hyaluronic acid with low molecular weight 300 and 750 KDa (at concentration \geq 0.1% in 0.5M citric acid as liquid

phase) was found to increase the setting time of MCPM- α -TCP based brushite cement from 17 to 23 minutes (Perez *et al.*, 2012). Chitosan when introduced in liquid phase with glycerol and gelling accelerator Ca(OH)_2 to the CPC system was found to impart injectability and fast setting (7.9 ± 0.9 min) but impede the precipitation of Hydroxyapatite and showed no improvement in mechanical property (diametral tensile strength) compared to control (Carry *et al.*, 2005). Similar effect was found with citric acid additive as its low pH (1.32) causes the rapid dissolution of calcium phosphate particles while dramatically increasing the calcium and phosphate ion concentration in the binder until the complete consumption of acid; increases the level of super saturation in the citrate containing medium and hence delaying the HA formation (Barinov and Komlev, 2011). Albeit attributed with incongruous results of other cementing parameters, hydroxyl propyl methyl cellulose even at low concentration (0.5 to 1.0%) drastically increased the injectability of TTCP-DCPD to $98\pm 1\%$ from $65\pm 12\%$ and that of TTCP-DCPA system doubled to $99\pm 1\%$ (Burguera *et al.*, 2006). There is negative correlation established with molecular weight of the polyacrylic acid (range <30000 , 30000 and 100000) and initial and final setting time. Higher molecular weight poly acrylic acid and intermediate concentration 20% (range 5, 10, 20%) has given improved compressive diametral tensile and biaxial flexural strength for TTCP-DCPA bone cement (Majekodunmi and Nicholson, 2003). However, in each case cytotoxic limit were critical as the complex interaction between CPC and polymer even at low concentration sacrifices the biocompatibility.

1.2.5.2 Calcium sulfate cements as an injectable system

Injectability is the much sought property of bioactive cements, which enables the delivery of the paste through a narrow needle or cannula before its setting (Liu et al., 2006) and is of great importance in clinical applications, as it will enable the easy delivery into contained defects (like periodontal bony defects, cysts, tumor removal sites and graft substitution gaps). Aqueous-based self-setting inorganic cements generally undergo phase separation during injection through a narrow needle from a syringe or applicator (Bohner and Baroud, 2005) a serious limitation for use in minimally invasive surgery. The choice of gelling agents are limited for CSC as they were found to impede the setting mechanism of rehydration and recrystallisation and the mechanical properties which couldn't be compromised beyond a limit. Complex interaction between the ions may lead to the formation of byproducts which affect the biocompatibility and bioactivity. This is a serious limitation for using it in minimally invasive surgery. The Recently MIIG-115/X3/X3 High Visc (Wright Medical Technology, US), BonePlast (Biomet, US), and CalMatrix (Life core biomedical, US) based on the bassanite have been developed. MIIG X3 and MIIG High Visc contains traces of setting accelerants in liquid part and CalMatrix contains sodium carboxymethyl cellulose in the powder part (Bohner, 2010). No data on the structural and osteoconductive properties of Bone Plast and Calmatrix were found. MIIG used for the treatment of benign bone lesions at humerus, patella, femur, ilium, tibia and calcaneus in patients has showed an average of 8 weeks for graft resorption and bone healing (Kelly *et al.*, 2004). MIIGX3 with high initial compressive strength implanted in the form of pellets in axial medullary defects in proximal humerus of skeletally mature hound type dogs with osteoset as the control, showed substantial

resorption by 6 weeks with very little amount remains in 13 and 26 weeks with bone remodeling and the resorption rate of MIIG slightly slower than osteoset (Urban *et al.*, 2004). MIIG X3 was claimed to be choice for the treatment of weight bearing joints to maintain reduction and filling defects (Yu *et al.*, 2009). Bone Plast was used to treat the aneurysmal bone cysts and found to resorb completely within 8 weeks with good radiological and clinical outcome (Claver *et al.*, 2008).

1.2.5.3 Limitations in the existing cement systems

Based on the described background and the literature survey conducted (as in Chapter 2), limitations of the existing IBC system could be identified. The CPC systems are proved to be bioactive and osteoconductive, but have slow degradation rate 1-2 years or even incomplete during the life time of the patient. The biodegradation could be enhanced with interconnected porosity but the method of inducing porosity may affect the cementing parameters and biocompatibility. Also the acid-base reaction during cementing is likely to hamper the biofunctionality of the drug molecules added. However injectable CSC undergoes very fast degradation within 6-8 weeks which cause local inflammatory reactions and do not favour the early bone regeneration *in vivo*. Conflicting results are reported regarding their successful use which may be attributed to inconsistent crystal structure, purity and quality and also systematic *in vitro* and *in vivo* efficacy studies are missing. However they have the potential to be used as a generic local drug delivery medium for antibiotics, growth factors and osteoclast suppressors for the management of infections and metabolic disorders (like osteoporosis). The encumbering factor in formulating an injectable bone filler cements are the dearth of inherent viscosity of the inorganic cements both CPC and CSC in bare form.

1.3 Hypothesis

On assessing the current status in synthetic bone graft materials, it could be understood that there is a need for an affordable new generation bone cement system which is fully injectable, biocompatible, bioactive and osteotransductive (ie. resorbing at the same pace as that of the new bone formation). It should also has potential to act as a local drug delivery system when the drugs get incorporated in to the system. To accomplish this following hypotheses are conceptualized

- (i) *The physico-chemical properties of the bone cements depend on the morphology and size of the precursor phase and can be tailored for flowability and mechanical property by synthesizing the crystals of low dimension and high purity*
- (ii) *Appropriate choice of the chemical additives, particularly the phosphate group addition, can impart the required bioactivity and osteoconductivity.*
- (iii) *The cement formulation can incorporate higher quantity of drug and enable sustainable controlled delivery greater than minimum inhibitory concentration without the loss of biofunctionality.*

The proof of concept could be validated *in vitro* and *in vivo* including the bone healing efficacy in rabbit femoral defect model and invitro antimicrobial studies to extrapolate the data to clinical applications.

1.4. Objectives of the study

In order to prove the hypothesis the following objectives are defined

- To synthesise calcium based inorganic salt precursor compounds with uniform low dimensional crystal size and high level of purity, through viable chemical methods.

- To develop bone filler cement formulations, to optimise the injectability, setting time and compressive strength parameters corresponding to clinical requirement, and to explore the physico-chemical mechanism leading to injectability.
- To conduct *in vitro* screening tests and *in vivo* biocompatibility evaluation of the optimized cement formulation based on the international standard guidelines.
- To conduct efficacy of the optimized cement formulation in bone defect healing through animal bone implantation study.
- To evaluate the performance of the bone cement as a drug delivery medium for bone infections.
- To explore further scope of modification of the bone filler cement with biocompatible additives.

1.5 Brief overview of the study

The work has been done with the overall aim of developing an injectable and bioactive bone filler cement for clinical applications. The work flow consists of the synthesis and characterization of basic ingredients, their characterization, formulation of the cement compositions, their optimization, biological evaluation of the optimized formulation for establishing *in vivo* safety and bone implantation studies in animals for assessing the efficacy. Also, the usefulness of the optimized cement as a drug delivery medium for bone infection treatment is tested and scope for further modification explored.

The selection of the base material was done on the basis of calcium content, availability, affordability, viability in synthesis, biocompatibility, and ability to form

cement. Calcium sulfate was selected and submicron dimensional gypsum (smCSD) with monomodal particle size distribution, was synthesised by an in-house designed novel ‘drowning out’ wet chemical method. The product obtained (smCSD) was validated for its utility as a medical grade biomaterial through the set of tests and analyses like phase purity, micromorphology, particle size, heavy metal screening, cytocompatibility and hemolysis test. The method was found viable for commercial production. Also the chemical system was analysed by adopting turbidimetry method to identify the parameters deciding particle size. The parameters of formation of the compound were derived through Nucleation Kinetics theory and extended to the process control to obtain particles sizes down to nano level.

The new formulation of bone filler cement was developed by making the compound ‘bassanite’ the hemihydrate form of smCSD, by the heat treatment. The cement design consisted of modification using phosphate ions which get integrated to in the set cement crystal lattices, providing bioactivity for the material. The modified cement was found to have flow properties when mixed, making it smoothly injectable. The physico-chemical mechanism during cementing was explored by analysing the phase, enthalpy of hydration, particle size, micromorphological features and eluted elemental composition. The cement formulation was optimised with respect to the clinically relevant cementing parameters. Quantitative estimation of injectability was done with custom designed capillary rheometer. Setting time analysis was carried out with custom fabricated Vicat needle type apparatus and compressive strength and modulus evaluation with UTM. The optimized cement based on modified low-dimensional calcium sulfate was named as ‘BioCaS’.

The bioactivity of 'BioCaS' was tested *in vitro* by immersion in SBF, with phase and chemical bonding analysis of the coating formed, pH variation, concentration of the Ca^{2+} , P^{5+} and S^{6+} in SBF. It was proved to have bioactivity, *in vitro*. Preliminary biocompatibility screening was done with *in vitro* cell culture cytotoxicity and hemolytic assay. HOS cell viability and its plastic adherence property on the cement matrix was explained. Interaction of the material with biological tissue was explained with *in vivo* tests including acute systemic toxicity test in (mice), an intracutaneous reactivity test (in rabbits), pyrogen test (in rabbits) and a maximization sensitization test (in guinea pigs). The cement BioCaS passed all the tests. Implantation test was carried out in rabbit femoral defect with HA ceramic scaffold as control. Histological and histomorphometric analysis showed that 'BioCaS' is osteoconductive and resorbable leading to the healing of the bone defect.

The capability of the optimised cement 'BioCaS' to act as local drug delivery system for *osteomyelitis* management has been analysed with the drugs gentamicin and vancomycin with *in vitro* drug elution kinetics study. This was repeated for different quantities of the drug loaded and the surface area to volume ratio of the set cement matrix. The 'zone-of-inhibition' studies using pathogenic bacterial species showed that the cement could be used successfully as a drug carrier to control bone infections.

The scope for enhancing the injectability and mechanical property with gelling agent N,O-carboxymethyl chitosan (NOCMC) through calcium cross linking via chelation was studied and explored the mechanism of cementing. Water soluble derivative of chitosan viz. N,O-carboxymethyl chitosan was synthesised and phase

characterised. Calcium cross linking via chelation in the cement matrix with PMR and FTIR respectively was studied. The modification gave a satisfactory formulation with improved properties.

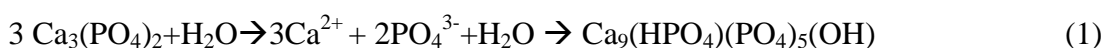
The work, as a whole, demonstrates the design development of an affordable, inorganic self-setting cement suitable for clinical application, and its modification to induce injectability and bioactivity. The optimization and validation studies done authenticate the in vivo use of this cement formulation (BioCaS) for bone defect healing and local delivery of drugs. The objectives of the work are achieved to its full extent.

2. LITERATURE REVIEW

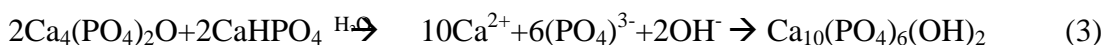
2.1. Early research on calcium phosphate bone cement

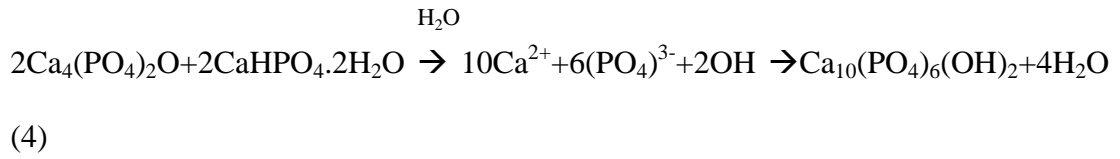
2.1.1 Apatitic bone cements

The bioactive bone cement has been first demonstrated when Monma and Kanazawa developed calcium-deficient HAp (Ca/P molar ratio 1.5) during the setting reaction of metastable α -TCP in aqueous medium (eq. 1) at 60-100°C at pH range 8.1-11.4 with Ca/P ratio unchanged (Monma *et al.*, 1976).

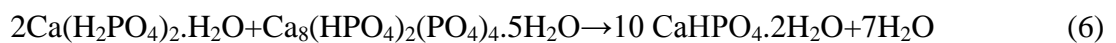
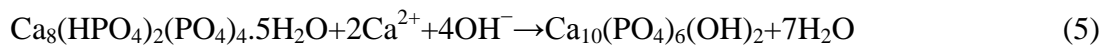


The setting time was of the order of several hours and hence dicarboxylic acid such as citric acid and succinic acid were added to the liquid phase in very slight quantities. Dicarboxylic acids undergo chelate formation with the Ca^{2+} ions on the surface of the calcium phosphate compound and hence shortened the initial setting time of α -TCP powders to 5-10 minutes but delayed the apatite formation (Unezaki *et al.*, 1996, Unezaki *et al.*, 1993). In 1986, Brown and Chow developed poorly crystalline precipitated hydroxyapatite while conducting the remineralisation study of the decalcified enamel which is attributed to the exothermic setting reaction (-134 KJ/mol or 32Kcal/mol) of equimolar mixtures of TTCP (Hilgenstockite, a basic component with Ca/P ratio 2.0) and DCPA/DCPD (slightly acidic component with Ca/P ratio 1.0) with water at pH of 7.5-8.0.





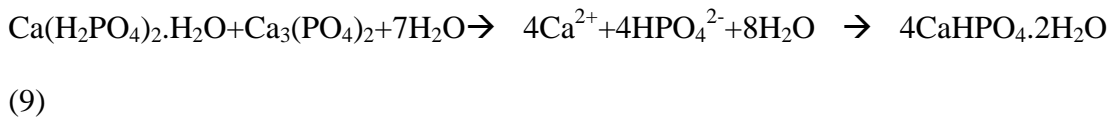
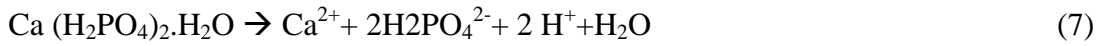
In the apatitic cement with lowest TTCP/DCPA diameter ratio, quick dissolution of the TTCP supplies the more Ca^{2+} and PO_4^{3-} ions which increases pH and the subsequent higher degree of supersaturation with respect to the apatite. This results in the formation of amorphous calcium phosphate or small apatite crystals, which are too small to be interlocked with each other to set (Brown *et al.*, 1987, Chow *et al.*, 2001). The rate determining step of the reaction involves the release of PO_4^{3-} ions with respect to the dissolution of DCPA and hence diameter ratio of TTCP/DCPA > 1 was opted to get better mechanical properties but setting time remained in the range of 30-60 min. The shortening of the setting time to ~ 5 min was tried with neutral phosphate salt solution ($\text{Na}_{1.8}\text{H}_{1.2}\text{PO}_4$ or $\text{K}_{1.8}\text{H}_{1.2}\text{PO}_4$) as liquid phase and adding apatite seed crystals to the powder phase (Ishikawa *et al.*, 1995). Dry mixing of MCPM, α -TCP and CaCO_3 with a sodium phosphate solution yielded non-stoichiometric carbonated apatite $\text{Ca}_{8.8}(\text{HPO}_4)_{0.7}(\text{PO}_4)_{4.5}(\text{CO}_3)_{0.7}(\text{OH})_{1.3}$, or dahlite (Constantz *et al.*, 1995).



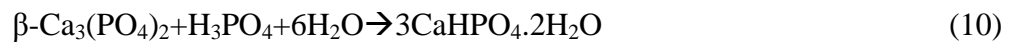
2.1.2 Brushite based bone cement formulations

Lemaitaire et al produced slightly acidic brushite cements by the acid-base interaction between the acidic MCPM or H_3PO_4 and near neutral β -TCP with fast setting time of 30s. Up on mixing, the immediate dissolution of MCPM induces acidic condition in the vicinity by producing Ca^{2+} and HPO_4^{3-} which in turn promote

the dissolution of β -TCP. The consumption of proton during the process increases the pH and precipitates the brushite and bridges the remaining β -TCP (Bohner et al., 1997).



The studies in which the replacement of β -TCP with α -TCP (Fernandez *et al.*, 1998) $\text{Ca}(\text{OH})_2$ (Desai et al., 2007), CDHA (Algel *et al.*, 2009) and that of MCPM with H_3PO_4 (Grovera et al., 2008) and MCPA (Engstrand *et al.*, 2013) were reported.

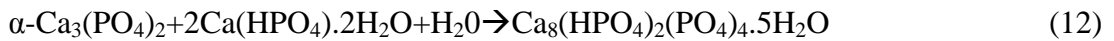


The addition of 20wt % of calcium pyrophosphate ($\text{Ca}_2\text{P}_2\text{O}_7$) and calcium sulfate hemihydrate prolonged the setting time to 5min and 7 min respectively while the 15% CSH with 5wt% pyrophosphate increased the diametral tensile strength to 3 MPa against <1 MPa in additive free brushite cement (Mirchi *et al.*, 1989).. Otherwise 5% Sr containing brushite cement with pyrophosphate additive and H_3PO_4 liquid phase found to have a diametral tensile strength of 5MPa (Alkhraisat *et al.*, 2007).

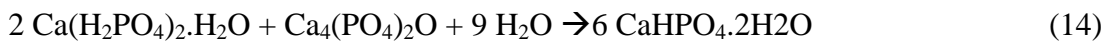
2.1.3 Octa calcium phosphate based bone cement formulations

The crystallization of HA during the biomineralisation of bone tissue occurs through the formation of intermediate prototype octacalcium phosphate ($\text{Ca}_8(\text{HPO}_4)_2(\text{PO}_4)_4 \cdot 5\text{H}_2\text{O}$) and hence is of undoubted interest in developing cementing systems based on OCP either as a cementing reagent or reaction products.

The morphology and crystallinity of the OCP in turn determined by the method of preparation drastically affects the performance of the cement system. There are no well known studies on the latter type except the combination of α -TCP and DCPD at the Ca/P mixing molar ratio of 1.20-1.47 in aqueous setting medium, which is due to the complexity of its preservation as final phase (Monma *et al.*, 1988).



In former type, eventhough the hydrolysis of OCP to HA be thermodynamically favourable, the conversion is possible only with a highly soluble more basic Ca^{2+} and OH^- releasing partner like TTCP (eq. 15). Addition of slight quantity of acidic MCPM simulates the setting through the formation of an intermediate brushite (eq.13 and 14) (Maeyer *et al.*, 2000).



In a recent study, 60 wt % α -TCP and 40 wt % OCP (as a reaction product of calcium acetate and sodium acid phosphate) cement powder were mixed with phosphoric acid containing sodium citrate as the hardening liquid and 15wt % OCP was obtained in the final reaction products with setting time 10 minutes and compressive strength 30 MPa (Komlev *et al.*, 2012).

2.2 Incipient concept of injectable bioactive bone cement

The bone or tissue excision during the treatment of trauma, infection or malignant growth usually leave out defects that affect the integrity and functionality of skeletal structure and hence considered as one of the devastating problems in human health

(Hughes *et al.*, 2015). Traditional therapies used for the bone repairs involves the shaping of the corresponding bone substitutes invitro and their surgical implantation, though provide the satisfactory outcomes, can also cause increased bone loss, trauma for the surrounding tissues, and large surgical wounds. However the extant stratagem of minimally invasive surgical techniques with in-situ setting injectable bone repair material which can be administered through percutaneous or small bone window via precise positioning to provide intimate adaptation to surrounding bone even for irregularly shaped cavities and easily shaped for esthetics in craniofacial repair has become one of the major research focuses (Chen *et al.*, 2015). Bone defect-related infections (i.e.osteomyelitis) are quite common especially in open bone fracture and trauma, which seriously affect bone reunion and are held as contra-indications for bone grafting where surgical debridement and suction–irrigation can control but not treat local infections. Hence synchronizing the treatment for remodelling bone defect and inhibiting related infections are necessary and meritorious in clinical treatment where comes the significance of in-situ setting drug loaded injectable bone cement formulations (Lian *et al.*, 2013). Bone cements with active participation in bone remodeling process with degradation rate at the same pace as that of the new bone formation i.e., *osteotransductivity* is the much sought property.

2.2.1 Calcium phosphate based injectable bone cements

CPCS were developed with acid-base reaction of one or more of the calcium phosphate compounds with water or calcium (eg. $\text{Ca}(\text{OH})_2$) or phosphate containing solution (eg. Phosphate buffer, H_3PO_4 , NaHPO_4 etc) as the liquid phase (as described in section 2.1) with desirable viscosity imparted mostly through chitosan, alginate,

cellulose, hyaluronate, gelatin, chondroitin sulfate, succinate or citric acid etc (Zhang *et al.*, 2014). HA as the major mineral component of the natural bone can well endorse osteoinductive process and hence the injectable CPC transformable into HA during cement precursor setting can lead to revolutionary therapies for bone defects and well explored (Larsson *et al.*, 2011). The gelling agents were imparted through liquid phase or solid phase.

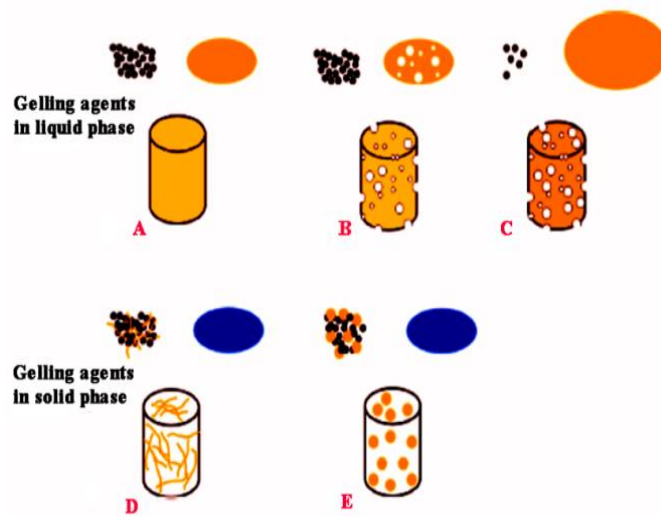


Figure 3: Different approaches towards the incorporation of Gelling agents in CPC system (Perez *et al.*, 2012)

Different strategies could be adopted for incorporating the polymeric additives/gelling agents in CPC system either through liquid phase or powder phase (Figure 3). A) water soluble polymer in CPC liquid phase and present as a continuous phase throughout the CPC after setting B) foaming of the polymer dissolved liquid phase and set with the powder phase to form macroporous CPC C) CPC dispersed in the major phase of the gelling agent liquid phase to form macroporous polymer-CPC scaffold D) polymer fibres in CPC powder phase to form fiber reinforced CPC and E) gelling agent microspheres in powder phase for controlled drug eluting system with simultaneous generation of macropores (Perez *et*

al., 2012). However the additives interact with cementing reaction and hence the optimization by varying the concentration, pH, L/P ratio, shape and size of the precursor particles, molecular weight and polymer chain length etc are of serious concern.

2.2.1.1 Gelling agents in injectable CPC system

Hydroxypropylmethylcellulose, formed by the hydroxylation of cellulose, a linear polysaccharide with 100-1000s of β -D glucose units, in CPC system even at lower concentration (0.5-3 wt% in 0.2 mol/L phosphate buffer) drastically provide homogeneous consistency and prevent filter pressing for TTCP-DCPA/DCPD compositions. Unlike TTCP/DCPA, hardening was fast and in acceptable limit for the TTCP-DCPD system (Burgera *et al.*, 2006). However the higher molecular weight or the higher concentration of the cellulose ether prolongs the setting time of α -TCP-CDHA and TTCP-DCPD cement but not interferes the HA formation after setting. The improved strength of these CPCs is mainly attributed to their smaller porosities and/or reduced crystal sizes. The critical flaws may occur due to the sudden decrease in compressive strength by entrained air bubbles at lower concentration; however, but it tends to stabilize due to the fracture toughness even while porosity increases with concentration (Liu *et al.*, 2013).

Alginate, linear copolymer with homopolymeric blocks of (1-4)-linked β -D-mannuronate and its C-5 epimer α -L-guluronate residues, produce strong viscous gum while its carboxylic group chelates with calcium ions and hence capable of increasing the cohesion and anti-washout property of the cement paste. Dose dependent variation in setting time and compressive strength was observed. For ACP-DCPD cement system, strength was enhanced with not more than 0.4 wt%

alginate in the powder phase (Wang et al., 2007) and in another study the tolerable limit is 20 wt % (Yu et al., 2010). ACP-DCPD, DCPA-TCP, and MCPM-CaCO₃ system caused increase in the setting time with > 2 wt % alginate (Perez et al., 2012).

Chitosan increases the cohesion and antiwashout resistance of the CPC (Carey et al., 2005) but not found to induce injectability (Kai *et al.*, 2009). Its mass fraction in wetting liquid from 0 % to 15 % in TTCP-DCPA cement with rh-BMP increased the compressive strength significantly more than two fold (8 MPa to 19.8 MPa) and fracture toughness 0.18 MPam^{1/2} to 0.23 MPam^{1/2}. Chitosan had no adverse effect on the alkaline phosphatase activity and hence osteoblast cell attachment and cell viability (Weir et al., 2010). However a sharp reduction in setting time from 68 min to 13 min occur only when chitosan mass increased from 15-20 % and the phase conversion to HA was less crystalline and not complete (Sun *et al.*, 2007).

Sodium hyaluronate is a glycosaminoglycan and a long chain polymer of the disaccharide unit of Na-glucuronate and N-acetylglucosamine. The addition of this compound hardly changes the formation of HA in TTCP-DCPD cement. Injectability declines when its concentration increases from 0.1 to 0.4 but escalated up to 1.0 wt %. At all the concentrations up to 1%, the settings times were found to be less than the unmodified form but above the clinically acceptable range (Kai et al., 2009). The bisphosphonate derivatised polymer backbone of hyaluronan improves the affinity of it to the cement matrix and improve the cohesion. Nonetheless doesn't found to improve the compressive and bending strength of the cement (Sanginario *et al.*, 2006, An *et al.*, 2016).

2.2.1.2. CPC system with macroporosity for tunable degradation with foaming agents

CPC generally possess intrinsic micro/submicron porosity allow the transport of nutrients and metabolic wastes throughout the implant site, which is beneficial to *de novo* bone formation. One method to improve the degradation rate of CPC is imparting macroporosity which allows rapid and deep bone cell invasion and angiogenesis for bone regeneration. Conventional method involves the mechanical stirring of the liquid phase to produce foam and mixed with solid phase but difficult to control the volume of air entrapped in it (Perut et al., 2011). Another concept is that the *in vivo* leaching / degradation of the porogen (gelatin, albumin, sucrose, mannitol granules, PLA fibres, frozen sodium phosphate solution and genipin cross linked gelatin microspheres) after cement setting, produce macropores in the shapes of the granules for cell invasion (Chow et al., 2009). The quantity of porogen used is high enough to provide interconnectivity which often compromises the injectability. Hydrogen peroxide, sodium bicarbonate, acetic acid, citric acid and other synthetic surfactant polysorbate were used as foaming agents (Montufur *et al.*, 2010, Chen et al., 2015) to improve the injectability while the liberation of gas after the implantation of the cement paste could have harmful effects on the organism. Syringe foaming with silanised hydroxypropylmethylcellulose (Si-HPMC, cross-linkable hydrogel) hydrophilic polymeric solution in NaH_2PO_4 was used for simultaneous mixing with α -TCP- NaH_2PO_4 precursors to produce foamed cement paste with porosity 100-400 μm . The foamed paste was found to retain the porosity after setting and hardening but resulted in steep decrease in the mechanical strength (1-6 MPa) (Zhang *et al.*, 2016). The incorporation of 20% hyaluronic acid microparticles to

CPC found to impart macroporosity where the median centred around 39 μm (Babo *et al.*, 2016). In conclusion, porogenic/foaming agents in CPC should be biocompatible while in ceramics the porogenic agent is destroyed during sintering and hence its biocompatibility is not a considerable requirement. Concomitantly macro porosity in the cement has always led to a significant decrease in mechanical properties as would be expected (Zhang *et al.*, 2014).

2.2.1.3 Inorganic additives or mineral components in CPC system

Magnesium phosphate, strontium carbonate, hexadecyl trimethyl ammonium bromide in the CPC was found to improve the injectability of the CPC. Magnesium sulfate and strontium carbonate improves the mechanical property and the former reduce the setting time of CPC to 10 minutes and possess higher *in vitro* degradation than the CPC alone (Wang *et al.*, 2007, Wu *et al.*, 2009). Hexadecyl trimethyl ammonium bromide and strontium carbonate also improves the macroporosity of the system and the latter impart radiopacity (Wang *et al.*, 2007).

When properties of the CPC system are regulated by changing mineral components or by adding different organic additives, there is always a compromise to be made between the different properties. For example, increasing the porosity in order to improve cell colonization and bioresorption, leads to a decrease in mechanical strength. Adding inorganic or organic material to improve porosity, injectability or mechanical strength can lead to a much longer setting time and rise concerns over biocompatibility (Bercier *et al.*, 2010).

2.2.2 Brushite based injectable CPC system

Brushite forming formulations are set by the acid–base interaction of the precursors β -TCP + MCPM or H_3PO_4 and TTCP + MCPM + CaO at solution pH < 6 (Tamimi

et al., 2012). They have short setting times and faster *invivo* resorption due to better solubility and metastability of the resultant DCPD phase compared to that of CDHA under physiological conditions, which concomitantly risks the mechanical strength. Sodium citrate, Chondroitin sulfate, glycolic acid as setting retardants is an option to get more workable and less viscous pastes of brushite-forming formulations (Dorokshin *et al.*, 2013). The major drawback is the inflammatory reaction during the early implantation period due to the rapid dissolution of DCPD and its partial transformation to CDHA with release of orthophosphoric acid. Mg could be added to reduce the rate of conversion and to prevent inflammation to certain extent (Bohner, 2000). The rapid dissolution affects the quality of bone formation in the resorbed site. Slowly resorbing β -TCP and bioglass granules added as seed crystals in the DCPD cement pastes acts as bone anchors which encourage the mature bone formation (Flature *et al.*, 2002).

2.3 Research on calcium sulfate cement system

2.3.1 Calcium sulfate as bone void filler

The use of Calcium sulfate as an augmentation material dates back to 1892 when Dreesman used it to obliterate osseous defects caused by tuberculosis osteomyelitis (Thomas *et al.*, 2009). Later CaS columns and tablets were used to fill large metaphyseal, subperiosteal and bone & periosteal defects in canine model, which mostly showed whole resorption within 45-75 days however the complete regeneration was found only if the perisosteum present (Peltier *et al.*, 1957). CaS was tried out in dentistry in extraction or cystic wounds and in surgical and osteomyelitic defects to facilitate the restoration of normal morphological contour and to rebuild

resorbed alveolar ridges (Bahn, 1966). CaS and freeze-dried demineralized bone matrix-calcium sulfate (DBM+CS) composite with a CaS barrier were compared with demineralized bone matrix (DBM) or CaS and gingival flap surgery (GFS) alone in 3-wall intrabony periodontal defects in dogs. After 8 weeks implantation, DBM and CaS, alone or in combination, may result in significantly improved regeneration of alveolar bone and cementum with little difference between them (Kim *et al.*, 1998). The relatively short time frame CaS takes to undergo *in vivo* dissolution could lead to inflammation and transient hypercalcemia which can be a side effect. Surgical grade CaS named OSTEASET[®] reported 20% incidence of sterile inflammatory response with no statistically significant difference with the volume and size of the osteoset used, use of alcohol washes, mixing of OSTEASET[®] with allograft, patient age, sex, drug allergies, or smoking history (Lee *et al.*, 2002). Later this was attributed to the presence of impurities and the pellets (Osteoplast pellets, Interpore-Cross International, Irvine, CA; Osteoset Pellets, Wright Medical Technology, Arlington, TN) and paste (Osteoplast, Interpore-Cross International, Irvine, CA) form of CS was found to support the bone formation in rabbit tibial defect model without any adverse reaction but failed to provide long term three dimensional matrix support for the osteoconductivity since remnants were < 5% after 6 weeks (Stubbs *et al.*, 2004). Conflicting results have been presented regarding the successful use of calcium sulfate graft. Nonetheless early CaS reports should be treated with care due to variance of reported outcomes, possibly from inconsistent crystal structure, purity and CaS quality being assessed at the time.

2.3.2 Calcium sulfate cement in dentistry

The dental fraternity has explored the application of CaS for dentine and bony defects after the report of Alderman in 1969 stating that sterile CSH in infrabony periodontal lesions is beneficial to osseous regeneration. It has also been tried out mainly in guided tissue regeneration, maxillary sinus augmentation and ridge preservation including the repair of furcation perforations, grafting residual defects from root amputations and endodontic lesions (Thomas et al., 2005).

2.3.2.1 Guided tissue regeneration

Guided bone regeneration (GBR) involves creating a space with physical barrier that allows the growth of cells derived from periodontal ligament while preventing the apical migration of the epithelium and gingival connective tissue cells along the root surface. The critical criteria regarding membranes for GBR include: biocompatibility, cell-occlusiveness, integration by the host tissues, clinical manageability, space making function, minimal tissue reactions resulting from the bioresorption of membranes and should not adversely influence the regeneration of the desired tissues. In 1992, Sottosanti introduced CaS as a barrier in combination with demineralized freeze-dried bone allograft, which retards epithelial and connective tissue ingrowth to allow a predictable bone regenerative response. However, he emphasized the need for the histologic evidence of new cementum and connective tissue fiber insertion into a previously diseased root surface (Sottosanti *et al.*, 1992). Randal J Harris demonstrated the successful use of CaS barrier along with composite bone graft (demineralized freeze-dried bone allograft, calcium sulfate, tetracycline, and porous hydroxyapatite) in non-furcation osseous defects in humans (Harris *et al.*, 2004). Nonetheless, later in 2013, CaS vs bovine collagen as a

membrane in GBR procedures in humans reported limited use of calcium sulfate barrier. The membranes may have been too thin and may simply resorb too rapidly for effective GBR regardless of the added stability of mixing with the bone graft. It may be argued that slowly resorbing calcium sulfate-based bone graft material may provide a better outcome (Ghaly *et al.*, 2013).

2.3.2.2 Alveolar Ridge preservation

Alveolar ridge resorption following tooth extraction may lead to esthetic and functional defects due to horizontal and vertical ridge dimensional changes during healing of the extraction sockets which makes the implant placement difficult or impossible. Surgical grade CaS when used in combination with Platelet rich plasma in fresh extraction socket of canine model found to reduce the resorption of alveolar ridge and promoted the bone formation with complete resorption at 8 weeks. The addition of PRP was found to enhance the bone regeneration only in the early phase of healing (Shi *et al.*, 2007). Medical grade CaS alone was proved to increase the lamellar bone from 16.4 to 43.6% from the crestal to the apical region 3 weeks later at implant placement surgery (Aimetti *et al.*, 2009). Later CaS is reported to be as effective as freeze dried bone allograft (FDBA) in preserving the post extraction ridge dimension in non-molar extraction site with greater clearance of CaS (2.5% remnants) with more bone formation after 3 months (Toloue *et al.*, 2012). BondBone™ (MIS Implant Technologies) is composed of two phases of highly pure medical-grade calcium sulfate hemihydrate and dihydrate in a uniquely controlled particle size distribution. This was able to fully resorb and replaced by vital bone in the 4-month time period and hailed as 100% success rate in implant placement and loading (Horowitz *et al.*, 2012).

2.3.2.3 Sinus augmentation

The bone is added between the jaw and the maxillary sinuses when there is not enough bone height in the upper jaw, or the sinuses are too close to the jaw, for dental implants to be placed. Renzo Guarnieri et al formulated the hypothesis that a careful stratification and dry compaction of calcium sulfate may be effective in reducing the resorption rate and the extent of mass contraction during healing and may allow a more complete osteogenesis and lead to proper osteointegration (Guarnieri et al., 2002). Also histological analysis of an immediately loaded provisional implant retrieved six months after simultaneous placement in a human sinus augmented with CaS revealed a native and newly formed bone with small osteocytes lacunae in contact with the implant surfaces (Guarnieri *et al.*, 2006). A good improvement of the amount of the available bone and hence realize correct implant positioning without clinical and radiographic complications are the related outcomes (Laino *et al.*, 2015).

2.3.3 Calcium sulfate cement as local drug delivery system

CSC is most criticized for the fast resorbability while endows it with the ability to be used as implant device loaded with various materials, e.g. antibiotics, pharmacological agents and growth factors and hence revived momentous research interest in nowadays. Simvastatin, a cholesterol synthesis inhibitor capable of enhancing BMP-2 expression in osteoblasts, was combined with the CaS carrier and treated rat calvarial defects. Bone formation started after 5 weeks as intense soft tissue inflammation occurred up to 4 weeks followed remarkable bone formation at 8 weeks. However it was unknown whether previously released simvastatin or that released by a small amount of CaS which possibly remained unresorbed after 4-5

weeks, was responsible for that bone formation (Nyan *et al.*, 2007). Teicoplanin-loaded CSC was evaluated in rabbit model of chronic methicillin-resistant *Staphylococcus aureus* (MRSA) osteomyelitis. In vitro elution studies showed initial rapid release of 49.08% of the loaded drug with mean concentration 1,053.89 µg/ml followed by gradual release (81%) period up to 9 days and plateau phase up to 29 days. Nonetheless it participates in bone generation in the debrided space while did not resolve bone infections in all the treated animals (Jia *et al.*, 2010). The addition of drug moiety was found to alter the morphology of the CS crystals and is explained to be due to the adsorption of the antibiotic molecules along the surfaces of the CSD crystal planes, resulting in slow crystal growth and a smaller aspect ratio, which gets released in to the local environment as it gets dissolved. However, the SEM image of the PMMA beads generally have a similar appearance typical of an insoluble polymeric material and any antibiotic molecules not in direct contact with the surface will not elute (Conoughey *et al.*, 2014). Synthetic CSC beads (Stimulan; Biocomposites Ltd., UK) loaded with tobramycin, vancomycin, or vancomycin-tobramycin dual treatment were assessed for their abilities to eradicate planktonic methicillin-resistant *Staphylococcus aureus* (MRSA) and *Staphylococcus epidermidis* relative to that of PMMA beads. The vancomycin-loaded and vancomycin-tobramycin loaded beads produced strong zone of inhibition against MRSA and *epidermidis* until day 26 and day 34 respectively. However The ZOI of the vancomycin-loaded and vancomycin-tobramycin loaded PMMA beads were completely lost by day 12 for the MRSA and *S. epidermidis* strains. Former group also prevented the biofilm formation of MRSA up to 7 days and the report also

demonstrated the difficulty in clearing the already established biofilms (Howlin *et al.*, 2015).

2.3.4 Development of injectable CSC system

Injectable bioactive CSC with parameters modulated for the clinical requirement if developed could be used for all the applications suggested for the injectable CPC system with drug delivery. However some of the products appeared in the market under this category, research reports on the developmental parts and preclinical safety and evaluation part are seldom found. Accordingly, more efforts have been made to fabricate CSH-based cements by combining with other bioactive materials to improve bioactivity, decrease resorption rate and stabilize pH environment as well as to tailor setting time, compressive strength and most importantly injectability (Qi *et al.*, 2016).

2.3.4.1 Tailoring parameters - Injectability, resorption rate, setting time, mechanical property and bioactivity

Merging CSH with a less-resorbable calcium phosphate was tried out to tailor the resorption rate for instance the injectable composite graft, that incorporated a matrix of CS and DCPD into which β -TCP granules distributed. The concept involves the fast resorption of CaSO_4 -DCPD matrix to promote vascular infiltration deep into the bolus, while the remaining matrix and the TCP granules could provide a scaffold for new bone formation. However less than 10% remained after 13 weeks in canine cancellous defects (Urban *et al.*, 2007). Alpha CSH was mixed with nano calcium-deficient hydroxyapatite/multi(aminoacid) copolymer (n-CDHA/MAC) at 10-40% concentrations has compressive strength in the range of 20-40 MPa. The mechanical strength was endowed in biocomposite with the amide-calcium-amide linkage and

hydrogen bond formed between both. Final setting times were in the range of ≈ 25 - 60 beyond the clinically accepted limit; the higher strength composition with value ≈ 50 min. Unlike the control CSH the composite prevented fibrous tissue in-growth into bone defects and guide bone repair effectively during the 16 weeks degradation period (Qi *et al.*, 2013). Mineralised collagen (nano HA/collagen), tri and dicalcium silicate were imparted to improve the cell adhesion and bioactivity (Liu *et al.*, 2010) (Qi *et al.*, 2017). Recently composite cement based on alpha CSH has been developed by combining with glass-ceramic powder $\text{SiO}_2/\text{CaO}/\text{Na}_2\text{O}/\text{ZrO}_2$ and spray-dried mesoporous bioactive glass particles with composition 70/20/10 wt% and distilled water has been reported. The cement were injectable with vertebroplasty needle (13 gauge) while the initial and final setting times of the samples were too long 46 ± 0.5 and 57 ± 0.5 minutes. The wet compressive strengths after 24 hours were found out to be $(14 \pm 0.7 \text{ MPa})$. The bioactivity was explained to be imparted by spray-dried mesoporous bioactive glass with spherical morphology, large exposed surface area and pore volume. However full degradation was found out within 32 days (Dadkhah *et al.*, 2017).

However, most CaS based bone cements are still inadequate for bone tissue engineering applications due to failure to improve injectability, physicochemical properties and bioactivity simultaneously. So it is still necessary to create better CaS based cement scaffolds for bone regeneration (Qi *et al.*, 2017).

CHAPTER 3

MATERIALS AND METHODS

PHASE 1

3.1 Synthesis and characterization of low dimensional calcium sulfate (gypsum) for the injectable bone cement formulations

3.1.1 Rationale for material selection

The work planned is targeted towards developing an ideal bone filler material, which is injectable and bioactive. Calcium sulfate was chosen as the base material or precursor because as it is a simple cementing material, easily available, economical and has acceptable biocompatibility. In biomedical applications of bone grafting and local drug delivery, material purity and control of particle sizes are of paramount importance for the repeatable, predictable and successful performance. Uniformly distributed low-dimensional crystals are essential, so as to obtain large surface area thereby improved strength and higher bioactivity. Several chemical systems have been suggested for synthesizing calcium sulfate dihydrate (gypsum), like calcium chloride-sodium sulfate (Guan et al., 2010) calcium chloride-sulfuric acid (Yang *et al.*, 2011) and calcium nitrate-sodium sulfate (Rees *et al.*, 1999). However, aqueous-based wet synthesis of calcium sulfate has the limitation of low yield because of its higher solubility in water and limited control over morphology and uniformity (Wang *et al.*, 2008, Eun and Ko, 2003).

The emergence of materials technology made it possible to synthesize calcium sulfate in low-dimensions, viz. sub-microns to nanometers, in the form of

tubes, rods, and wires (Park *et al.*, 2011). Only a very few reports are available for the synthesis of nano CaS, among which the first reported is the water through oil micro emulsion method stabilized by either non-ionic or ionic surfactant (synthesis in both tetraethylene glycol monododecyl ether microemulsions in cyclohexane and aerosol-OT microemulsions in dodecane) (Rees *et al.*, 1999). The cryo-vacuum technique developed by salvadori (Salvadori *et al.*, 2006) was adopted for developing nano dimensional form for osseous regeneration, used quick freezing of a very dilute solution of medical grade calcium sulfate (aqueous solution of 2g/liter) at cryogenic conditions (-196°C) followed by freeze drying under lyophilized vacuum conditions (-55°C at 10⁻²mbar). An indirect and complicated route of hydration of nano anhydrite by flame spray synthesis using precursor containing corresponding calcium and sulfur comprising organic derivatives were also tried (Osterwalde *et al.*, 2007). Recently, the electrochemical oxidation of brownmillerite nano-CaFeO_{2.5} in the acidic medium of 0.1M H₂SO₄ to nano gypsum was also reported (Gupta *et al.*, 2016). Most of the procedures mentioned above are not suitable for biomedical application mainly because of very low production yield and difficulty in purifying out the organic additives and surfactant. Any of these reported gypsum products were passed the biocompatibility and safety requirements to be used *in vivo*. Most importantly some researchers have reported the increase in percentage of the fine crystals during gypsum precipitation by reducing the ‘surface free energy’ which could be ascertained through nucleation kinetics study (Mahmoud *et al.*, 2004, Rashad *et al.*, 2004, Prisciandaro *et al.*, 2012).

The present work has been planned so as to synthesize high purity uniform submicron-dimensional crystals of calcium sulfate dihydrate (gypsum) through a

technique ‘drowning out crystallization’ which involves the quenching of the secondary growth. This section demonstrates the formation of low-dimensional, uniform crystals of gypsum from calcium nitrate-sulfuric acid system assuming that the change in the dielectric constant of the reaction medium affects the ‘surface free energy’ of the chemical system. To confirm this nucleation kinetics study has been carried out and explored the nucleation kinetics parameters.

3.1.2 Materials

The chemicals used for the synthesis were analytical reagent grade ($\text{Ca}(\text{NO}_3)_2 \cdot 4\text{H}_2\text{O}$, 98% assay) purchased from RANKEM/Avantor Ltd. Conc. H_2SO_4 (assay 97–99 %) and 2-propanol [$\text{CH}_3\text{-CH}(\text{OH})\text{-CH}_3$], assay 99.5 %, EMPARTA] were purchased from Merck, Mumbai. Deionised distilled (DD) water from SYNERGY UV Millipore system, Merck was used throughout the study.

For the solubility analysis ethylene diammine tetra acetic acid (EDTA) (assay 96.0%) was purchased from SD Fine Chem Ltd, Mumbai. Solochrome black T obtained from RANKEM/Avantor Ltd, Maharashtra. $\text{NH}_3\text{-NH}_4\text{Cl}$, MgSO_4 , NaOH , phenolphthalein, KNO_3 , CaCO_3 , $\text{CH}_3\text{-OH}$, $\text{CH}_3\text{-CH}_2\text{-OH}$ and $\text{CH}_3\text{-CO-CH}_3$ etc were purchased from Merck, Mumbai. Nonidet P40 (octylphenoxypolyethoxyethanol, 98% assay, SD Fine Chem. Ltd) was used as surfactant during the DLS particle size measurement.

3.1.3 Synthesis of submicron dimensional gypsum (smCSD) by drowning out wet crystallization method

The precursor phase for the production of the cement powder has been synthesized by a novel ‘drowning out’ crystallization by wet chemical method which involves the

quenching of secondary growth. Essentially, this is a wet chemical reaction of sulfuric acid and minimally aqueous solution of calcium nitrate in 2-propanol, by which uniform low-dimensional (3–5 μm) rod shaped crystals of gypsum get precipitated.

The wet reaction has been carried out in a glass vessel of 5L volume mounted on a magnetic stirrer (IKA make). Calcium nitrate tetrahydrate was dissolved in 0.2 L of deionised distilled water and the working solution with 0.5 molar concentration was prepared in 2-propanol to make the total volume 2.2 L in the 5L volume glass reaction vessel mounted on a platform. 2L of equimolar concentration of H_2SO_4 (aq) solution was added drop wise from a separating funnel with constant and vigorous stirring at 1000 rpm at ambient temperature $303\pm 2\text{K}$. The rate of addition was adjusted so that the reaction time is 30 minutes. After the reaction time, the solution was stirred for another 5 min and subjected to centrifugation at 4500 rpm (Thermoscientific Haeraeus Megafuge 40R), to recover the precipitate. It was further washed in the centrifuge with hot water (333K), to remove the remnants of acidic byproducts (as confirmed through pH checking until the value of the supernatant changes from 1.0 to 4.6). The precipitate after centrifugation was kept in the freezer for 12 hrs and freeze dried (Virtis Benchtop SLC lyophilisor) at 220.3 K and 10^{-2} mbar pressure to obtain free-flowing powder. The flow diagram for the synthesis procedures (Figure 4) and chemical equation are given below.

The precursor powder is heat treated to obtain the hemihydrate phase as the cement precursor. The optimum temperature for complete phase conversion was determined through the XRD and TG/DTA analysis as explained in subsequent section.

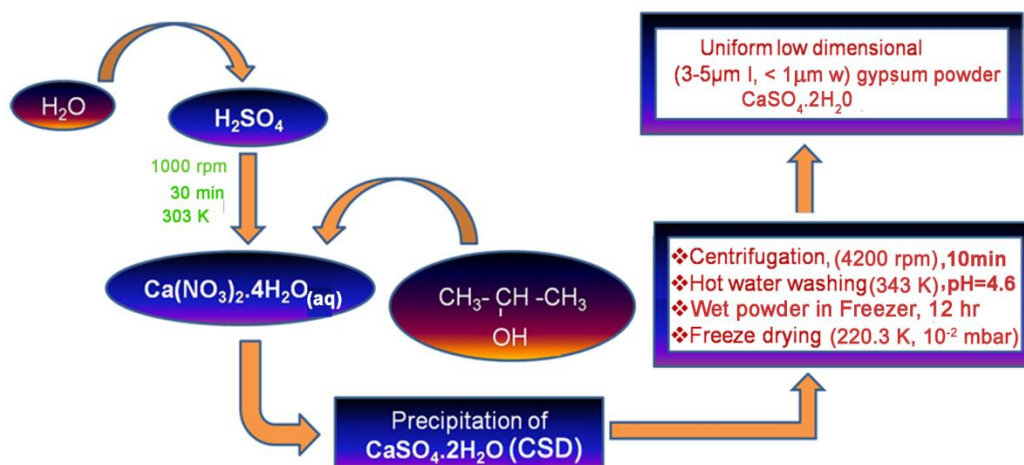
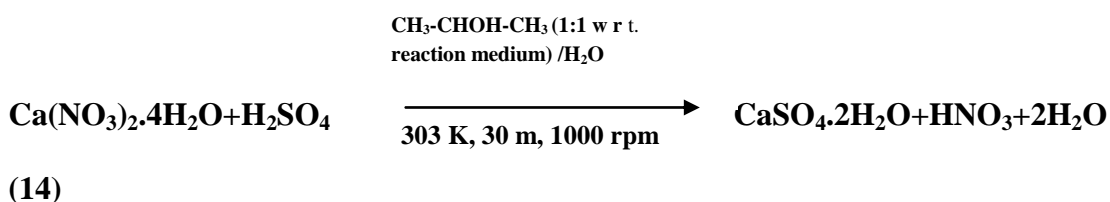


Figure 4: Schema showing the precipitation of submicron dimensional gypsum powder



3.1.4 Characterisation of the precipitated powder

3.1.4.1 Phase and chemical bonding analysis

The precipitate has been characterized for phase and chemical bonding using X-ray powder diffraction (XRD) and infrared spectroscopy (FTIR) respectively. XRD was conducted in Siemens D5005 Diffractometer with Cu K α radiation generated at a voltage of 40 kV and a current of 30 mA. The spectra were recorded in the 2-theta range of 10–60° at a rate of 2°/min with 0.02° step size. The diffraction data was compared with the standard ICDD data cards to identify the phases present. The Fourier Transform Infrared absorption analysis (FTIR) of the precipitate was carried out using Thermo-Nicolet 5700 spectrophotometer by KBr pellet method. Spectrum was recorded as a superimposition of 64 scans in the range from 4000 -400 cm⁻¹ at a

resolution of 4 cm^{-1} . Pellet of spectroscopic grade KBr alone was used to record the background spectra.

3.1.4.2 Micromorphology of the synthesised gypsum

Scanning electron microscopy images were acquired for the synthesised lyophilized gypsum by smearing the powder on conducting carbon tape mounted on copper stubs and loaded in FEI QUANTA 200 Environmental Scanning Electron Microscope, after giving a conductive gold coating for contrast. Precipitate prepared without 2-propanol (only aqueous medium) was used to compare the morphology and size.

3.1.4.3 Transmission electron microscopy and the selected area electron diffraction pattern

Bright-field transmission electron microscopy (TEM) and selected area electron diffraction (SAED) studies were also performed (on FEI Tecnai F30 operating at 300 kV) to observe the morphology and structure and phase purity of the as-formed submicron gypsum. Sample for TEM related studies was prepared by dispersing the gypsum powder in 2-propanol and drying a drop on carbon-coated copper grid.

3.1.5 Optimization route and parameters for selecting the current system

3.1.5.1 ESEM analysis for particle homogeneity

Scanning electron microscopy was conducted for the micromorphological and size analysis of the particles of gypsum by conducting the reaction in organic media of varying polarity i.e. water (H_2O) > methanol ($\text{CH}_3\text{-OH}$) > ethanol ($\text{CH}_3\text{-CH}_2\text{-OH}$) > 2-propanol ($\text{CH}_3\text{-CHOH-CH}_3$) > acetone ($\text{CH}_3\text{-CO-CH}_3$) > diethylether ($\text{CH}_3\text{-CH}_2\text{-O-CH}_2\text{-CH}_3$), following the same reaction conditions. Among this 2-propanol reaction medium was selected and the precipitation was carried out in each case by varying

the concentration ratio of 2-propanol with respect to the reaction medium as 1:9, 1:3, 2:3 and 1:1 (corresponding to 80%, 60%, 40% and 20% aqueous solutions respectively for dissolving $\text{Ca}(\text{NO}_3)_2 \cdot 4\text{H}_2\text{O}$) [The calculation has been done without considering initial DD water used for dissolving]. The lyophilized gypsum powders obtained from all the synthesis route was smeared on conducting carbon tapes pasted on copper stubs after giving conductive gold coating for contrast were scanned in FEI QUANTA 200 environmental scanning electron microscope.

3.1.5.2 Comparative solubility of gypsum in the reaction media

(i) Dependence on the polarity of the reaction medium

The solubility of gypsum with respect to the polarity of the reaction medium were analysed by titration method with ethylene diammine tetra acetic acid (EDTA) with solochrome black-T as indicator. Shortly, an $\text{NH}_3\text{-NH}_4\text{Cl}$ buffer solution (pH=10) has been prepared by adding 142 ml concentrated NH_3 solution (specific gravity 0.88 to 0.90) to 17.5 gram NH_4Cl and diluting to 250 ml with deionized water. Equimolar mixture of Mg complex of EDTA was prepared by mixing equal volumes of 0.2M solution of EDTA and MgSO_4 and neutralised with NaOH solution to a pH between 8 and 9 (until the addition of a drop of which made the phenolphthaleine just turned red). To a portion of the solution, added a few drops of the buffer solution (pH=10) and a few millidrops of the solochrome-black- KNO_3 indicator mixture. Equimolarity was confirmed with the violet colour which turns blue on the addition of a drop of 0.01 M EDTA solution and red on the addition of a single drop of 0.01 M MgSO_4 solution, which gave an approximate 0.1 M solution. If the solution does not pass this test, it may be treated with more EDTA or with more MgSO_4 , until the required condition of equimolarity is attained. Pippetted out 10 ml of the 0.01 M Ca^{2+} ion

solution (CaCO_3) into a 250 ml conical flask, diluted it with about 25 ml of distilled water, added 5 ml of the buffer solution, 1 ml of the Mg-EDTA and 2 drops of the solochrome black- KNO_3 mixture. Titrated it with EDTA solution until the colour changed from wine red to clear blue and standardised the EDTA concentration from the concordant titre value obtained. Filtrate from the three different batches of synthesis were used for triplicate measurement and plotted with standard deviation as error bars.

10 ml each of the filtrate (containing dissolved Ca^{2+} ions) collected, by centrifugation at 12000 rpm (in Thermoscientific Haeraeus Megafuge 40R centrifuge with rotor Thermo Scientific Fiberlite F15-6 \times 100Y, USA with max speed 15000 rpm), after the completion of the reaction in each of the reaction medium (H_2O , $\text{CH}_3\text{-OH}$, $\text{CH}_3\text{-CH}_2\text{-OH}$, $\text{CH}_3\text{-CHOH-CH}_3$, $\text{CH}_3\text{-CO-CH}_3$) were titrated with standardised EDTA solution as per the method described above. The solubility of Ca^{2+} ions in g/ml were calculated for comparison.

(ii) Dependence on the temperature difference of the reaction media

The influence of the temperature difference of the reaction medium on the solubility of gypsum was analysed by synthesising gypsum in reaction medium with 1:1; 2-propanol at the reaction temperatures of 273, 303 and 323 K. For the reaction to be carried out at 273K, $\text{Ca}(\text{NO}_3)_2 \cdot 4\text{H}_2\text{O}$ -2-propanol solution was kept in refrigerator overnight, taken out and monitored the temperature to reach 273K to start the reaction and further carried out the reaction in ice bath. The reactions at 303 and 323K were carried out in IKA Magnetic stirrer. Each of the filtrate collected after the completion of the reaction were analysed for the dissolved Ca^{2+} ion solubility.

(iii)Dependence on the concentration change of organic solvent

The concentration difference were imparted in the reaction medium by varying the 2-propanol concentration ratio 0, 1:3 and 1:1 using i) 0% ii) 50% and iii)100% v/v solution in deionised distilled water for preparing $\text{Ca}(\text{NO}_3)_2 \cdot 4\text{H}_2\text{O}$. The filtrate of the final product collected by centrifugation was estimated for Ca^{2+} as detailed in the previous sections.

3.1.6 Surface area analysis of the low dimensional gypsum with Brunauer Emmette Teller method

The specific surface areas of low dimensional gypsum were determined by the BET method of N_2 gas physical adsorption on the surface of the test material with Micromeritics TriStar 3000 V6.05A, USA. It has been obtained from the three point BET plot of $1/Q ((P_0/P)-1)$ against P/P_0 corresponding to the BET equation correlating the amount of adsorbed gas (Q) as a function of relative pressure (P/P₀) ie.

$$1/ Q ((P_0/P)-1) = (1/Q_m C) + [(C-1/W_m C) (P/P_0)] \quad (15)$$

Where Q_m denotes the quantity of adsorbate monolayer recovering the solid surface and C, the BET constant related to the energetics of the system.

3.1.7 Heavy metal analysis by OES-ICP

As per the ASTM F2224-09, the performance of the surgical implant gets adversely affected by the presence of toxic heavy metals like lead (Pb), arsenic (As), cadmium (Cd) and mercury (Hg) in it and to be limited to minimum. Hence the heavy metal analysis of the low dimensional gypsum has been carried out in inductively coupled plasma–optical emission spectroscopy. 0.1 g of the gypsum powder has been dissolved in 5 ml of conc. HNO_3 by heating and 1ml from the test material solution

was digested with 5 ml of conc. HNO₃. The concentration of Cd_(228.802), Pb_(220.353nm), Hg_(253.652) and As_(188.979) were analysed in optical emission spectrometer (OES–ICP, Perkin Elmer, model: 5300 DV) which has been calibrated for the selected elements using reference standards prepared by diluting commercially PerkinElmer NIST[®] traceable quality control standards.

3.1.8 *In vitro* screening test for the cell compatibility evaluation of synthesised gypsum

3.1.8.1 *In vitro* cell culture cytotoxicity - Test on extract (ISO 10993-5, 2009)

Method of test on extract using mouse fibroblast cells (L929) extract was prepared by incubating 0.2 g of the test material (set cement after crushing) in 1ml of physiological saline at 37±2 °C for 24 h, followed by centrifugation and filtering. It was mixed with Minimum Essential Medium (MEM) 2× with 20% serum, in equal parts to get 50% extract. Further dilution with culture medium supplemented with 10% serum was done to get 25%, 12.5% and 6.25% extracts. Physiological saline, processed in a similar way, was taken as the reagent control. The negative control was prepared by incubating high-density polyethylene (1.25 cm² surface area) with physiological saline at 37±2 °C for 24 h, and the positive control was prepared by diluting the phenol stock solution (91.3 mg ml⁻¹) to 1.3 mg ml⁻¹ with culture medium containing serum. Different dilutions of the positive and negative controls were prepared with serum-containing culture medium, corresponding to the dilutions of the sample. Mouse fibroblast cells (L929 cell line, ATCC, USA) were cultured using 0.25% trypsin EDTA and seeded to 96-well plates (Nunc) and maintained until subconfluency using MEM supplemented with 10% fetal bovine serum (FBS). After removing medium, the cell monolayer was rinsed with phosphate-buffered saline

(PBS). The test extracts of samples at different concentrations, positive control, negative control and reagent control in triplicate were placed on cells. Cells cultured in normal medium were considered as the cell control. After incubating at 37 ± 1 °C for 24 h, the cultures were examined under an inverted phase contrast microscope for the cellular morphological features and scored as follows: 0, no reactivity (discrete intracytoplasmic granules, no cell lysis, no reduction of cell growth); 1, slight reaction (no more than 20% of the cells are round, loosely attached and without intracytoplasmic granules, or show changes in morphology); 2, mild reaction (no more than 50% of the cells are round, devoid of intracytoplasmic granules, no extensive cell lysis, no more than 50% of the growth inhibition observable); 3, moderate reaction (no more than 70% of the cell layers contain rounded cells or are lysed; cell layers not completely destroyed, but more than 50% growth inhibition observable); 4, severe reaction (nearly complete or complete destruction of the cell layers).

3.1.8.2 Metabolic activity via MTT assay using mouse fibroblast cells (L929)

Approximately 1×10^4 cells (L929) were seeded per well in a 96-well plate and cultured in MEM supplemented with 10% FBS as described above. After a monolayer was obtained, the culture medium was removed and the wells were rinsed with PBS. One hundred microliters of the different dilutions of the test material extract (prepared as described in section 3.6.1) were added to the wells, in six replicates. Cells cultured in MEM supplemented with 10% serum alone (i.e. cells unexposed to test material) were considered as the cell control. After incubation at 37 ± 1 °C for 24 h, the test and control extracts were removed from the wells and 50 μ l of MTT solution (1 mgml^{-1} MEM without supplements) was added to each well.

Mitochondrial enzymes in metabolically active viable cells reduce the yellow tetrazolium salt 3-(4,5-dimethyl thiazol-2-yl)-2,5-diphenyl tetrazolium bromide to purple formazan. After incubation for 2 h at 37 ± 1 °C in a 95%/5% CO₂ humidified atmosphere, the MTT solution was removed and 100 µl of isopropanol was added to all wells and the plate was swayed. The colour developed in each well was quantified by measuring the absorbance at 570 nm using a spectrophotometer (ISO 10993-5, 2009).

3.1.9 Analysis of the chemical system and particle size control through nucleation kinetics studies

‘Drowning out wet chemical method’ for the synthesis of medical grade submicron gypsum in the organic compound enriched reaction medium from the Ca(NO₃)₂.4H₂O - H₂SO₄ chemical system hasn’t been reported yet. Theoretical stratagems serve up best as far the repeatability, predictability and eventually the control over the particle sizes in chemical precipitation from precursors in solutions are concerned. Establishing the nucleation kinetics of the new synthesis system is the one critically used for manipulating and controlling crystal sizes in industrial crystallization (Prisciandora *et al.*, 2014). A plethora of studies focused on elucidating the nucleation kinetics of gypsum in aqueous medium and the effect of inorganic additives on the gypsum nucleation. Most of them are for studying the effect of additives on the gypsum nucleation to hinder or delay gypsum scale formation in industrial processes such as sea water desalination, hydrometallurgical operations, industrial water recovery in cooling tower technology etc (Prisciandora *et al.*, 2003, Rabizadeh *et al.*, 2017). It is of paramount importance for quantitative

elucidation of how the gypsum forms to get control over the system to achieve particle size control.

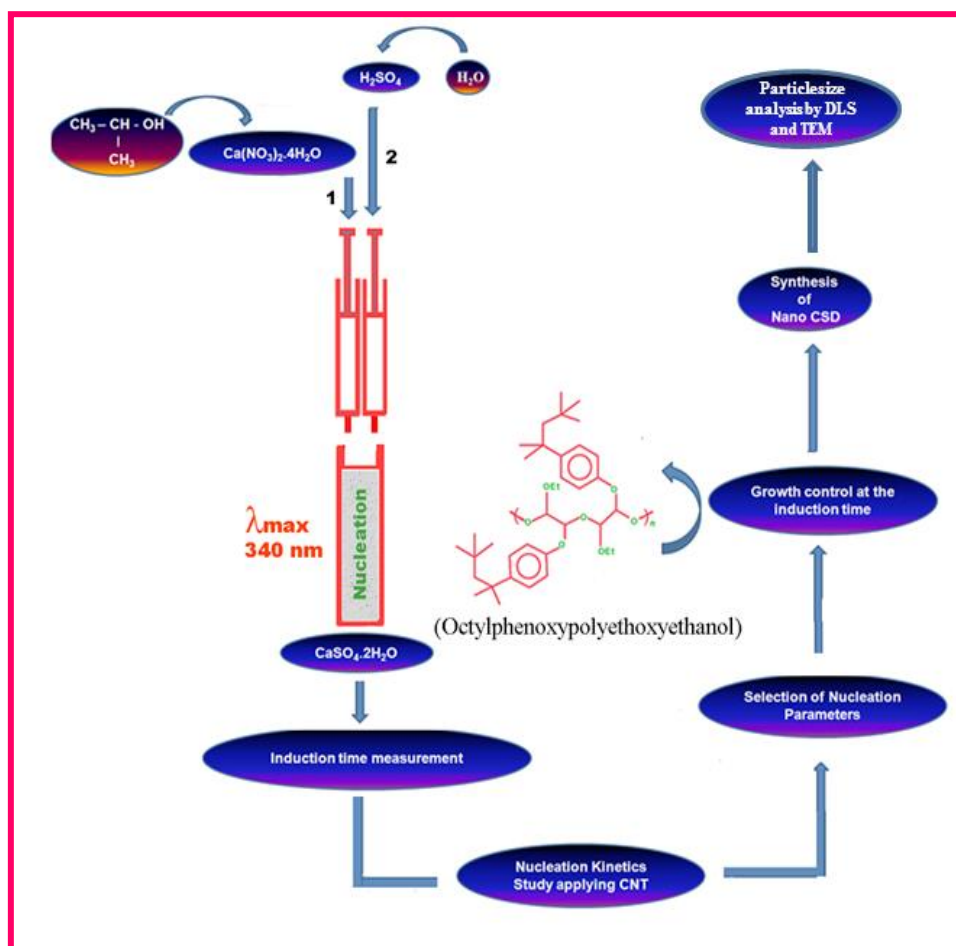


Figure 5: Schema showing the outline of nucleation kinetics study of the low dimensional gypsum formation.

In the present case, it is planned to explore how the variation of the dielectric constant of the medium change the surface energy to contribute to the reduction in particle size. Accordingly nucleation kinetics study has been carried out at ambient temperatures through induction time measurements by turbidimetry. The aim is to identify the controlling parameters of calcium sulfate crystallization so that crystals of predictable size and morphology could be obtained. From the knowledge of the nucleation kinetics parameters, we were able to extend the work to demonstrate the

synthesis of nano dimensional gypsum selecting the required nucleation conditions from the knowledge of nucleation kinetics parameters (Figure 5).

3.1.9.1 Induction time measurements

The induction time for the precipitate formation is an expedient experimental parameter to study the kinetics of nucleation in a wet chemical system thereby articulate the effects of the organic reagent in the crystallization of gypsum (Kulkarni *et al.*, 2013). According to the classical nucleation theory, the precipitation of a product from a solution starts with the formation of small nuclei of the new phase in the large volume of the solvent (Sohnel and Mullin., 1988, Yoreo and Vekilov 2003) which is controlled by the competition between the free-energy gain due to the liquid-to-crystal transformation and the free-energy loss associated with the formation of the interface between the liquid and the crystal. Typically tens to hundreds of molecules of the product phase start organizing as a crystallite and the process progresses by adding more molecules to this nucleus. The nucleation process occurring with equal chances anywhere in the solvent is called *homogeneous nucleation* which gets distinguished from *heterogeneous nucleation* in which the nucleation tend to occur primarily on a substrate surface in contact with the solvent or the nucleus forms in contact with an impurity and the properties of which control the rate of formation of new phase nuclei (Sear *et al.*, 2006). The nucleus formed during *homogeneous nucleation* may tend to decay if the net free energy is higher and hence there is a critical radius above which the probability of growth is more than that of the decay where the growth is irreversible (Wang *et al.*, 2015). The net number of nuclei which grow larger than critical size per unit time per unit volume is termed as the *nucleation rate* (Katz *et al.*, 2010, Vekilov, 2010).

The time elapsed between the achievement of supersaturation and the initiation of the nucleation is generally defined by the term *induction time*. However, it is practically difficult to measure this parameter because the critical nucleus sizes are below the detection limit of even the most sensitive instruments (Brandel *et al.*, 2015). The nuclei should be allowed to grow until they reach a higher size, so that the associated physical changes in the solution are detectable by the instrumentation.

Therefore, in practical sense, the induction time can be considered as the time elapsed between the onset of supersaturation and the first changes in the physical properties of the system due to the formation of solid phase. This is denoted as ' t_{ind} ' and treated differently from the true induction time. The induction time is known to be a function of supersaturation, temperature and the presence of interferences (Sohnel and Mullin, 1988, Mullin, 2001)

The practically observable induction time will be a sum of (i) transient period required for the system to achieve quasi-steady state distribution of molecular clusters, t_r , (ii) time required for the formation of stable nuclei which grows instead of dissolving into the feed solution, t_n , and (iii) time needed for the nucleus to grow to detectable size, t_g . Sohnel and Mullin observed the transient period t_r to be very small (of the order of 10^{-7} s for the nucleation of liquids or solids from vapours) and hence irrelevant in calculations

Therefore, for practical purposes,

$$t_{ind} = t_n + t_g \quad (16)$$

The theoretical relation of t_{ind} with the supersaturation and nucleation rate will vary according to the time fractions of t_n and t_g . However, with certain assumptions and approximations (like moderate supersaturations and negligible

viscosity of the medium), the characteristics of nucleation of the product phase in the system could be studied.

In the present case, the spectroscopic method of turbidimetry is used for the nucleation kinetics study. The induction times (t_{ind}) of formation of gypsum were measured using UV-visible spectrophotometer (Varian Carywin 50 model) by the method suggested by Mahmoud et al (Mahmoud *et al.*, 2004). Solutions of calcium nitrate in IPA and aq.H₂SO₄ were prepared separately so as to obtain the supersaturation of interest up on mixing and subsequently these were mixed in equimolar ratio (2 ml each) directly in standard quartz cuvettes (10 mm path-length and 4.5 ml volume) of the spectrophotometer. Ultrasonically cleaned and dried cuvettes were used to avoid the chances for heterogeneous nucleation on the walls. Absorption was recorded at wavelength of absorption $\lambda = 340$ nm for 20 minutes at a rate of 10 measurements per second at ambient temperature and the measurements were repeated for different concentrations. In the case of precipitation, the UV absorbance with time will show a sudden increase in the absorption. Point of intersection of tangents in the absorbance–time graph will provide the induction time. Though it is known that the induction time is influenced by temperature [Wang *et al.*, 2010], the present study is limited to ambient temperature conditions (300 K).

3.1.9.2 Equilibrium concentration from induction time variation

It is the relative supersaturation which drives the formation of the product phase in a wet reaction. The relative supersaturation with respect to a mineral or crystal is defined as the ratio of the product of ionic concentration of the reactants at the initial time to that at equilibrium.

The basic equilibrium relation in the formation of gypsum could be given as



The kinetics of formation is dependent on relative supersaturation σ , as given by the relation

$$\sigma = \ln \frac{[\text{Ca}^{2+}][\text{SO}_4^{2-}][\text{H}_2\text{O}]^2}{[\text{Ca}^{2+}]_{eq}[\text{SO}_4^{2-}]_{eq}[\text{H}_2\text{O}]_{eq}^2} \quad (18)$$

In the case of low supersaturation in aqueous medium, the activity becomes equal to concentration (where the concentration of the water is considered as constant) and the relative supersaturation σ could be approximated to supersaturation ratio (S).

$$\text{i. e., } \sigma \approx \ln \frac{[\text{Ca}^{2+}][\text{SO}_4^{2-}]}{[\text{Ca}^{2+}]_{eq}[\text{SO}_4^{2-}]_{eq}} \quad (19)$$

i.e., $\sigma \approx [\text{Ca}^{2+}]$ (with respect to calcium nitrate), $[\text{SO}_4^{2-}]$ (with respect to sulfuric acid) and $[\text{H}_2\text{O}]$ represent the corresponding concentrations in the bulk and $[\text{Ca}^{2+}]_{eq}$, $[\text{SO}_4^{2-}]_{eq}$ and $[\text{H}_2\text{O}]_{eq}$ denote those at equilibrium [Guan *et al.*, 2001].

Direct determination of the precise value of equilibrium concentration, however, is difficult. In the present case an attempt is done to find the equilibrium concentration by observing the variation of induction time. It is known that the induction time in a medium is inversely related to the concentration of the reactants (Sohnel and Mullin, 1988, J W Mullin, 2001). The induction time increases drastically at lower concentrations and diverges to infinity at a certain value below which no precipitation occurs. This corresponds to the equilibrium concentration and could be determined from plot of the induction time versus concentration, through extrapolation.

3.1.9.3 The surface energy and nucleation rate

Based on the classical theory of homogeneous nucleation, Sohnel and Mullin derived a relation connecting t_{ind} and supersaturation ratio, assuming t_n is far higher than t_g (i.e., a very short growth time, so that the induction time is practically equal to nucleation time), and a steady state in nucleation is achieved. For aqueous solutions of moderate supersaturation and low viscosity, the induction time for a product phase to form (t_{ind}) is related to the supersaturation ratio S as

$$\log t_{ind} = A + \frac{B}{T^3(\log^2 S)} \quad (20)$$

where T is the temperature (in K), A is a dimensionless empirical constant and B , another constant which is dependent on several factors. In the case of calcium sulfate precipitation, it has been expressed as

$$B = \frac{\beta \gamma^3 v_m^2 N_A f(\theta)}{(2.3R)^3} \quad (21)$$

where β is the geometric shape factor ($16\pi/3$ for spherical nucleus), $f(\theta)$ is a correction factor (1 for homogeneous nucleation and 0.01 for heterogeneous nucleation), v_m is the molar volume ($74.69 \times 10^{-6} \text{ m}^3 \text{ mol}^{-1}$ for gypsum), R is the Universal gas constant (8.314 J/K/mol) and N_A is the Avogadro's constant (6.022×10^{23}). γ denotes the surface energy in J/m^2 (also referred to as interfacial tension), which could be defined as the difference between the free energy per molecule of the bulk and that of the surface. This is always a positive term and acts to destabilize the organizing nucleus of the new phase (Prisciandaro *et al.*, 2006).

Considering equation (22), the plot of $\log t_{ind}$ against $1/(\log^2 S)$ over a range of supersaturation at a fixed temperature gives a straight line with Y-intercept A and

slope B/T^3 . The value of B obtained from the graph can be used to calculate surface energy (Rashad *et al.*, 2004) as follows

$$\gamma = 2.3R \left\{ \frac{B}{\beta v_m^2 N_A f(\theta)} \right\}^{\frac{1}{3}} \quad (22)$$

Number of nuclei of the precipitating phase formed per unit time per unit volume at a particular supersaturation ratio is termed as nucleation rate. The nucleation rate J_s corresponding to the supersaturation ratio S is,

$$J_s = F \exp - \frac{\beta \gamma 3 v_m^2 N_A f(\theta)}{(RT)^3 \ln^2 S} \quad (23)$$

where F is a constant known as pre-exponential factor having a theoretical value 10^{36} nuclei/m³s.

3.1.9.4 Critical radius of the nucleus

The nucleus formation is unstable at very small size due to high interfacial tension. Arrival of more molecules to this ensemble may increase the free energy of the system. Such a nucleus tends to dissolve rather than grow. However, when the formation of the crystalline bulk phase occurs, the arrangement of molecules as lattice reduces the surface free energy. Addition of each molecule to the lattice lowers the free energy of the system and the nucleus starts growing. The phenomenon is known as Gibbs-Thomson effect (Yoreo and Vekilov, 2003).

The transition happens corresponding to a specific size of the nucleus, called the critical size (Yoreo and Vekilov, 2003). The free energy change per molecule (G) when a spherical nucleus of radius r homogeneously nucleates within the solution is given by the sum of the bulk (Gb) and surface terms (Gs),

$$\Delta G = \Delta G_b + \Delta G_s = \left\{ \frac{4\pi r^3}{3\Omega} \right\} \Delta \mu + 4\pi r^2 \gamma \quad (24)$$

where μ is the change in chemical potential of the crystallizing species, v is the volume per molecule and γ is the interfacial free energy.

The critical radius when $\partial(\Delta G)/\partial r = 0$ is given by

$$r_c = \frac{2\Omega\gamma}{K_B T \ln S} \quad (25)$$

where K_B is the Boltzmann constant, T is the temperature in Kelvin, and S is the supersaturation ratio (Alimi, 2000)

3.1.9.5 Synthesis of gypsum nanoparticles

The theoretical knowledge of the nucleation kinetics parameters obtained for the current chemical systems were used to get control over the growth of the crystals and to extend for the synthesis of nanoparticles. Dynamic light scattering (DLS) technique was used for the purpose. The size distribution measurements were conducted in Zetasizer Nano ZS compact scattering spectrometer (Malvern Instruments, Worcestershire, UK) following ISO 22412 standard (“Particle size analysis – Dynamic light scattering”). We have selected the supersaturation 2.12 at homogenous nucleation range with longest t_{ind} (3.75 min). The nucleation process were allowed to occur up to t_{ind} and added 1% nonionic surfactant (Octylphenoxy polyethoxy ethanol, Nonidet P40) to avoid agglomeration of the particles formed. The volume distribution of particles was plotted and cumulant analysis was done to calculate Z-average and polydispersity.

The same sample was subjected to transmission electron microscopy in Hitachi H 7650 model. The mixed solution with the surfactant added, was dispersed on to 200 mesh formvar coated copper grid and dried in vacuum oven. The analysis was done at a voltage of 80 KV.

PHASE 2

3.2 Design development of injectable bioactive bone filler cement

In this work a new injectable bioactive bone filler cement formulation (named 'BioCaS') is developed from the synthesised high purity low dimensional gypsum of 3-5 μm size which provides an enhanced net surface area. The cement paste, before the setting time, is fully injectable from a syringe through a needle (18 gauge), without incorporating any gelling agent. Detailed investigations have been conducted to understand the rheology, setting properties, compressive strength and micro-morphology of the optimised cement and also attempts were done to explore the physico-chemical mechanism leading to injectability.

3.2.1 Optimization of thermal conversion of gypsum to bassanite

The first step in preparing the basic cement material is to convert gypsum (calcium sulfate dihydrate) to bassanite (calcium sulfate hemihydrate), which on wetting with water medium, hydrates and undergo self-setting. The conversion of the high purity low dimensional gypsum obtained by the new process has been optimized systematically.

3.2.1.1 Structural overview of polymorphic analogues of calcium sulfate

Hawthorn and Krivovichev (Hawthorn and Krivovichev, 2000) described the structure of polymorphic forms of Calcium sulfate. Calcium sulfate exists in three polymorphic analogues gypsum (calcium sulfate dihydrate, $\text{CaSO}_4 \cdot 2\text{H}_2\text{O}$), bassanite [calcium sulfate hemihydrate (α or β form), $\text{CaSO}_4 \cdot 1/2\text{H}_2\text{O}$] and anhydrite [calcium sulfate anhydrite (γ or orthorhombic form), CaSO_4].

The chemical structure of anhydrite is centered on the chains of alternating edge-sharing (CaO_8) dodecahedra and (SO_4) tetrahedra and the chains are linked by

corner-sharing between the (SO₄) tetrahedra and (CaO₈) dodecahedra and the edge-sharing between adjacent (CaO₈) dodecahedra (Figure 6 a). The structure contains sheets of edge-sharing chain that are parallel to (-110) (Figure 6 b).

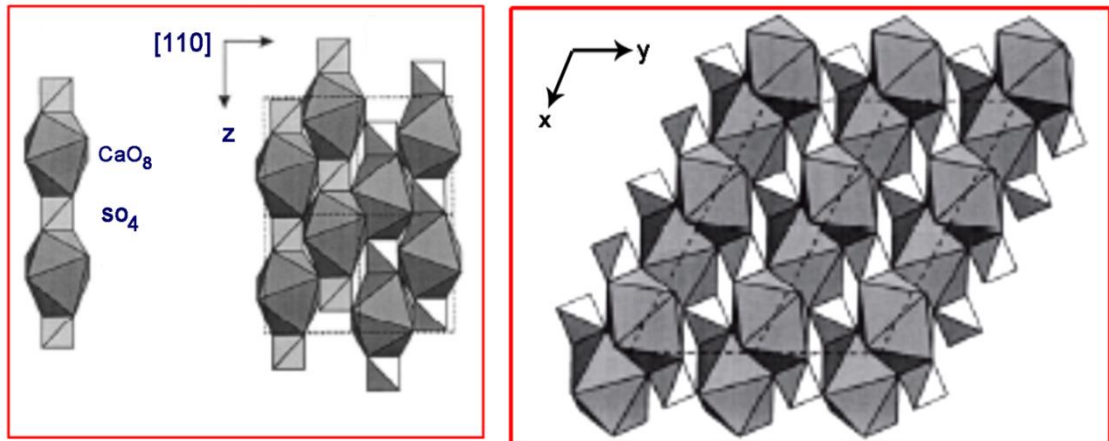


Figure 6: a) The chains of edge-sharing CaO₈ polyhedra and (SO₄) tetrahedra in anhydrite; (b) linking of chains into layers parallel to (-110) in anhydrite c) the layer of chains of edge sharing polyhedra in gypsum (Hawthorn and Krivovichev, 2000)

Gypsum has the edge sharing chains of (SO₄) and (CaO₈) polyhedra are parallel to [101] and all the sheets have same orientation (Figure 6 c). The chain repeats are slightly longer in gypsum ≈ 6.27 Å than in anhydrite ≈ 6.25 Å and the O²⁻ is replaced by H₂O at two of the unshared corners of each 8 coordinated Ca site resulting in sheet structure with hydrogen bonding between water molecules in adjacent chains. (Bishop *et al.*, 2014). Bassanite contains the repeat unit of the chain consists of one CaO₉ and one SO₄ polyhedra, which extends along [001] and are connected to form a frame work (Figure 7). The period of the chain in gypsum, anhydrite and bassanite are 6.27, 6.25 and 6.345Å respectively (Hawthorn and Krivovichev, 2000).

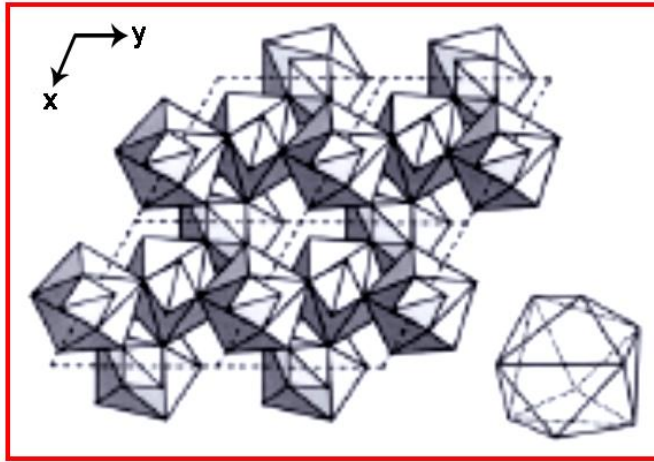


Figure 7: a) The structure of bassanite viewed along [001]; (b) the (CaO_9) coordination polyhedron in bassanite (Hawthorn and Krivovichev, 2000).

Yan et al in 2016 reported the structure of gypsum and bassanite which is followed in the current study (Yan et al., 2016). Figure 8 shows the crystal structure of gypsum and bassanite along the [001] vector.

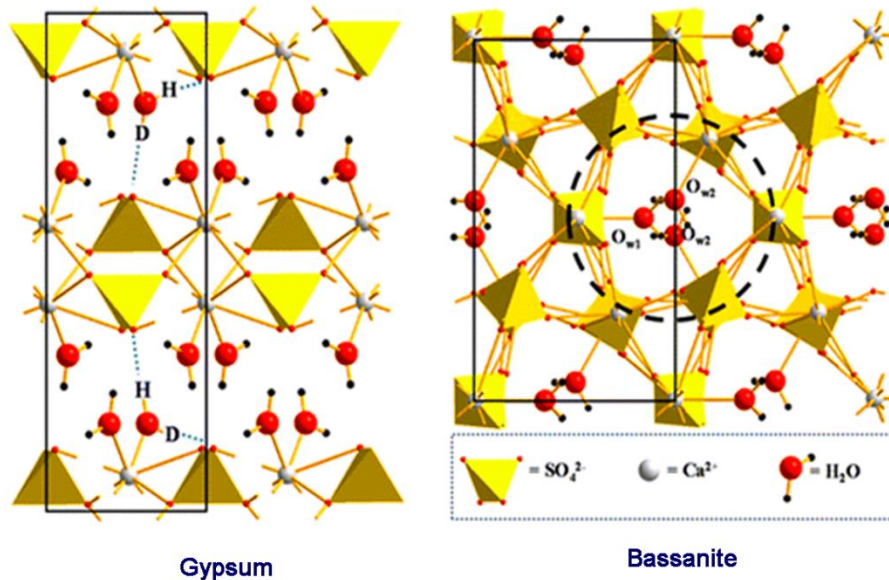


Figure 8: Crystal structure of a) gypsum and b) bassanite viewed along the [001] vector (Yuan et al., 2016).

The [001] face of the unit cell is marked with black solid line. The lattice of gypsum can be viewed as a pattern of alternating water layers and calcium sulfate layers. All water molecules are identical in the lattice, but each water molecule forms two non-identical hydrogen bonds with two different sulfate ions (blue dashed lines

in Figure 8a). Bassanite, the partially dehydrated polymorph of gypsum consists tubular channels in the lattice (dashed black circle in Figure 8 b). Removal of the water produces a change in the lattice structure from the planar structure of gypsum to bassanite. Isolated water molecules reside in these channels of dimension 5.5 Å and form weak hydrogen bonds with sulfate ions with two types of water sites O_{W1} and O_{W2} . One type of water is linked with sulfate ions by hydrogen bonding (O_{W1}), the other one is directly linked to calcium ions (O_{W2}).

3.2.1.2 Simultaneous Thermogravimetry /Differential Thermal Analysis

The dry powder of low dimensional pure gypsum crystals obtained was subjected to simultaneous TG/DTA analysis (mass loss of the material by thermo gravimetry by the method derived from ASTM E-1131-03 and enthalpic changes by ASTM E-537-98) with a thermal analyser (SDT-2960 Universal V4.5A TA Instruments) to find out the thermal processing temperature for the formation of bassanite, which depends mainly on the particle size. 10 mg of the sample and calcined alumina were weighed into the corresponding platinum cup container and were analysed in the temperature range from 273 to 1273K at the heating rate of 5K/min up to 473K and 10K/min from 273-1273K. The samples were heated in an atm of nitrogen of 99.5% purity, 1 ppm moisture and 1 ppm oxygen at the purge rate of 100±5 ml/min.

3.2.1.3 XRD analysis to identify the thermal conversion of gypsum

The synthesised gypsum samples (5g each), heated for 6 hours at different temperatures, from 368K to 1273K in a furnace (Programmable OKAY Raising-Hearth Electric furnace model 45R5Y) at definite intervals were subjected to X-ray diffraction to identify temperature ranges for the existence of phase pure forms and mixtures of different polymorphic analogues and to finally reconfirm the full phase

conversion temperature of gypsum to bassanite. Heating beyond a certain temperature results in further dehydration of CSH leading to the formation of gamma (soluble and reversible) and orthorhombic anhydrite (insoluble and irreversible phase). X-ray diffraction patterns of the samples were recorded in Bruker D8 Advance X-Ray diffractometer, Germany by step scanning mode in the 2-theta range of 10-36° using CuK α radiation (40KV and 30mA) at the rate of 1°/min with 0.01° increment and the diffraction data were analysed using EVA search match software.

3.2.2 Production and characterisation of bassanite

The main chemical moiety of the powder part of the cement comprises Bassanite (β -calcium sulfate hemihydrate). Homogeneity of the particles of the precursor phase gypsum is a critical factor for the repeatable and predictable performance of the bone cement. The literature reports on the calcination temperature varies from 353-423K (Wang and Meldrum, 2012, Tritschler et al., 2015) for the formation of crystalline bassanite attributed to the source, size, shape and morphology of the precursor gypsum particles. From the knowledge of phase conversion temperatures of gypsum from simultaneous TG/DTA and subsequent XRD analysis, dry powder of CSD was prepared in batches (80g), calcined at 393K for 18 h in an oven (Heraeus Thermicon P Vacutherm Vacuum Oven) at the atmospheric pressure and the final product was subjected to X-ray diffraction in Bruker D8 Advance X-Ray diffractometer by scanning the samples in the 2-theta range of 10-56° using CuK α radiation at the rate of 2°/min with 0.01° increment. The diffraction data were analysed using EVA search-match software to confirm the phase and crystalline nature. Fourier transform infrared spectroscopy was carried out on the the ground powder in THERMO NICOLET 5700 FT-IR spectrometer by KBr pelletisation method in transmission

mode for the confirmation of phase purity. The scanning were done in the range of 4000-400 cm^{-1} at the resolution of 4cm^{-1} and the final spectrum was generated with the superimposition of 64 scans. Micro morphological analysis of the bassanite was performed in FEI QUANTA 200 Environmental Scanning Electron Microscope.

3.2.3 Preparation of the cement precursor powder

Modification of the CSC were tried out using different in-house synthesised phosphate compounds like DCPD, DCPA, TCP, precipitated HA and other commercial phosphate salt like NaH_2PO_4 , K_2HPO_4 , KH_2PO_4 , Buffer etc by analysing setting and flow properties. However the disodium hydrogen orthophosphate dihydrate (DHPD) was found to enhance the flow properties and decided to explore the bassanite-DHPD composition which hasn't been reported yet.

The cement precursor powder was the in-house synthesised submicron dimensional β -CSH (bassanite) and different sample compositions were prepared by ball milling with diverse concentrations (w/w percentage) of disodium hydrogen orthophosphate dihydrate (DHPD) [$\text{Na}_2\text{HPO}_4 \cdot 2\text{H}_2\text{O}$ (dorfmanite) (99.5%) SDFCL, Mumbai] in Fritsch pulverisette Planetary Mono Mill PULVERISETTE 6 using zirconia balls. The samples used for experiments were having weight percentages of DHPD-0, 1.5, 2.5, 3.5, 5 and 10 % which are coded in the further text as **smCHD0**, **smCHD1**, **smCHD2**, **smCHD3**, **smCHD4** and **smCHD5**.

The addition of DHPD was limited to 10 % so that it should not cross the threshold of biocompatibility. The cement paste was prepared at ambient temperature ($25 \pm 2^\circ\text{C}$) by adding the wetting medium drop-wise from a syringe and kneading uniformly using a spatula. The liquid to powder ratio (or the wetting ratio) was kept as 0.6 ml/g throughout the sample preparation so as to have a smooth paste

consistency. Appropriate quantities of each composition for the injectability test (3 g), setting time measurements (2.5 g) and compressive strength test (0.6 g), were taken and the pastes were prepared accordingly.

3.2.4 Quantitative determination of injectability of the cement paste-extrusion rheometry

The term ‘injectability’ is related to the ability of a slurry (or paste) to extrude through a narrow cylindrical opening or a capillary, under pressure keeping the homogeneity (Bohner, 2005). It is generally measured by correlating either to the force required for complete extrusion or to the quantity of the cement extruded during a certain period, within the setting time. Researchers adopted different techniques and parameters to measure and quantify injectability of bioactive bone cements, as articulated by Bohner (Bohner, 2010). The samples for quantitative analysis were selected based on the qualitative evaluation of injectability of different compositions manually by trial and error method by extruding cement samples through 18 gauge needle.

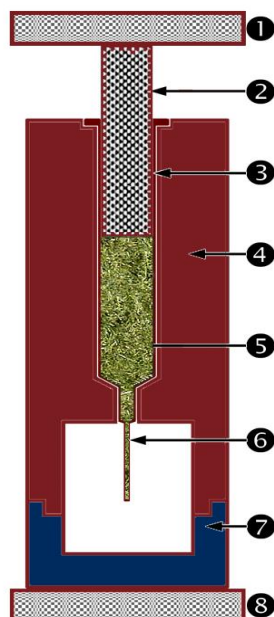


Figure 9: The schematic of the custom designed capillary rheometer (1) UTM crosshead (2) plunger (3) syringe (4) acrylic holder (5) cement paste (6) needle (7) detachable bottom of the holder (8) UTM platen.

In the present study, Extrusion Rheometry technique was opted to determine the viscosity of the cement paste (Lewis, 2011). A capillary rheometer has been custom-made (Figure 9) so as to simulate the actual clinical situation of cement delivery.

It consisted of a plastic syringe of 2.5 ml volume with an internal diameter of 10 mm as the main body and 18 gauge needle (0.838 mm inner diameter and 4.8 cm length) fitted at the nozzle as the extruding capillary. The syringe was snugly inserted into an acrylic holder (Figure 9(4)) which is designed as an adapter to the Universal Testing Machine (UTM, Model: Instron 1193) in which the extrusion process is executed. The holder has a detachable bottom to collect the extruded material. The assembly, having the syringe filled with freshly prepared cement, was loaded in the UTM so that the syringe coincides with the axis of the platen. Compressive force was applied at the pre-programmed crosshead speed and the force-displacement data was recorded digitally (Burgera et al., 2008).

For the test, 3 g powder of each composition was taken on a glass plate, wetted with the liquid in the prescribed ratio, and made into a smooth paste as described in Sect. 3.2.1. The preparation was completed within 2 min and the paste was backfilled in the syringe by removing the plunger, taking care to avoid air bubbles. The plunger was placed back and the holder assembly was arranged quickly in the UTM so that the extrusion process could be started at the third minute after wetting. The quantity of the cement paste was sufficient to fill a length of about 25 mm in the syringe. The plunger was moved at a crosshead speed of 10 mm/min and the force sensed by the load-cell was recorded, setting the cut-off limit at 200 N (Bohner, 2005). Triplicate measurements were done on each sample.

The force data was used to deduce the viscosity of the paste at each instant. Generally, the viscosity of a non-newtonian slurry is a function of shear forces (Bohner, 2010). When extruded from a rheometer; the viscosity μ (in Pa s) at any point of time, is a function of the corresponding pressure (P) as per the *Hagen–Poiseuille* relation (Lewis, 2011, ASTM F451-16).

$$\mu = \frac{\pi P D_n^4}{128 L_n Q_n} \quad (26)$$

where L_n is the length and D_n is the diameter (both in meters) of the capillary. Q_n is the volumetric flow rate in m^3/s , which could be calculated as

$$Q_n = \frac{\text{Total volume extruded}}{\text{Total time taken for extrusion}} = \frac{\pi r^2 H}{T_e} \quad (27)$$

where r and H represents the internal radius of the syringe and the total displacement of the plunger respectively. The pressure at each data point can be calculated from the force-displacement data by knowing the internal diameter of the needle. The pressure drop in the syringe bulk is assumed to be negligible compared to that in the needle. The time value corresponding to each displacement data point was deduced from the cross head speed. The rheometer was calibrated prior to the analysis using fluids of known viscosity (glycerol, paraffin oil and servo-68 lubricant oil). Instantaneous variations could be seen in the force recorded due to the friction between plunger and the walls and slight tolerances of the syringe body, yet these effects get averaged out in triplicate measurements.

3.2.5 Enthalpy of hydration of the modified cement

It is observed in the injectability experiments that the addition of DHPD has significant effect in the viscosity of the CSC paste. Viscous properties must be altered by certain molecular level mechanisms operating in the cement paste. With

the purpose of studying the effect, the enthalpy changes during the wetting process of the cement with and without the presence of DHPD were investigated using isothermal differential scanning calorimetry (TA Instruments Model 2920 DSC V2.4F). 10 mg of the powdered sample of smCHD5 was weighed in the standard aluminium sample pan and kept in the sample holder. Cement from bare submicron bassanite powder [smCHD0] was used as reference. 6 μ L of the wetting liquid (needed to maintain the wetting ratio of 0.6 ml/g) taken in a micropipette was dropped into the pans quickly and the measurements were started within 10s in isothermal mode at 37 °C. The cumulative heat generated against time during the setting was recorded for 1 h. The heat of hydration (ΔH_{hyd} in J/mol) was calculated from the saturation value of the curve. As the heat of hydration is the characteristic of a compound (Newman and Wells, 1938), the difference in value obtained for the sample (smCHD3) with respect to the control (smCHD0) will indicate the effect of ionic interaction during hydration.

3.2.6 Effect of addition of DHPD on the phase conversion

As there was a clear indication in the results regarding the molecular interactions in the cement mixture, it has been decided to explore the phase conversion. The CSC samples with different concentration of DHPD were subjected to X-ray diffraction analysis (Bruker D8 Advance X-Ray diffractometer) using Corundum (Al_2O_3) fine powder [AR Grade, Merck] as the reference standard. Each of the samples was ground to powder after setting and drying for 24 h in a humidity oven at 37°C, which were then mixed with the reference standard in 1:1 weight ratio and scanned with $\text{CuK}\alpha$ radiation at a rate of 0.1°/min and step size 0.01°. The 2-theta range selected was 10°–36°, which covers all the major peak positions of CSH (ICDD: 74-2787) and

CSD (ICDD: 21-0816), along with the (0 1 2) and (1 0 4) peaks of corundum (ICDD: 70-5679). The diffraction data were analysed using search match software to identify the phases.

The phase composition obtained from XRD has been appended by FTIR analysis (Thermo-Nicolet 5700) using KBr pellet technique. The samples powders were thoroughly mixed with spectroscopic grade KBr in the weight ratio of 1:10 and thin transparent pellets were produced in an automatic hydraulic press (X-PRESS model SPEX 3630) using a 10 mm die set at 7 tons/cm² pressure. Bare KBr pellets were used as reference. These were scanned in the range 400–4000 cm⁻¹ at a resolution of 4 cm⁻¹, superimposed 64 scans to get the final spectrum.

3.2.7 Appending phase formation studies with elemental composition analysis

The elution of sulfur (S), calcium (Ca) and phosphorous (P) from the set cement mass has been investigated using Inductively Coupled Plasma Optical Emission Spectrometer (OES–ICP), to see the variation in ionic composition of the CSC. All the cement samples were prepared in cylindrical shapes of 6 mm diameter and 12 mm height using split-moulds. After drying for 24 h, they were washed thrice with deionized water in ultrasonic bath for 5 min duration each. Three pellets of each sample were individually weighed and immersed in 5 ml deionized water taken in a polystyrene vials. These were kept at ambient temperature (25 ± 2 °C) for 48 h and then 1 ml from each vial was taken for analysis. After digesting with 5 ml of concentrated nitric acid, the concentrations of calcium, sulfur and phosphorus were analysed in optical emission spectrometer (OES–ICP, Perkin Elmer, model: 5300 DV) which has been calibrated for the selected elements using appropriate reference

standards. The values for each of the three pellets belonging to each sample were calculated for unit weight and averaged.

3.2.8 Micromorphology of the cement and evidence for the phosphate incorporation in the cement

The micro morphological analysis of the set CSC samples was done using electron microscopy to correlate the changes in the crystal habit of calcium sulfate with the concentration of DHPD incorporated. Freshly fractured surfaces of the washed cement pellets were observed in environmental scanning electron microscope (FEI QUANTA 200) at 20 kV without gold coating.

Energy dispersive spectroscopy (EDS) was done on the surfaces during the imaging using EDAX Genesis XM 4 integrated with the ESEM. Area scans were taken at various regions on the sample to look into the presence of phosphorous (of the additive DHPD) in the calcium sulfate mass. After that, spot analysis was done on specific crystals to check whether the phosphorous is substituted in calcium sulfate crystal lattice or existing as a separate phase (possibly as calcium phosphate). The EDS spot analysis values of P in each sample were determined on 3 typical crystals and were plotted as mean \pm SD against the DHPD concentration.

3.2.9 Particle size analysis via high resolution 3D surface profilometry

Surface image analysis of the smCHD2 and smCHD5 sample was done through non-contact surface profilometry (Talysurf CLI 1000 (Taylor Hobson) 3D profiling System), which could give quantitative particle size distribution data. Chromatic Length Aberration (CLA) gauge in this, works under 'confocal' principle and offer high resolution 3D measurement of the surface. White light is projected on to the sample surface using the spectral aberration lens and the chromatic aberration causes

spectral dispersion and at any point on the surface only a certain wavelength will be in focus. The spectral image reflected from the surface is collected by the same lens and optic cable and passed into the optical analyser with the help of a beam splitter. The pin hole and grating in the analyser permits only the focus wavelength to pass through and the CCD sensor interpolates the spatial position of the data point. The sample is moved in X, Y and Z axes using a high precision motorized stage and data is collected one point at a time. CLA 300 gauge (range 300 μm and resolution 10 nm) was selected and the measurement was carried out at a speed of 200 $\mu\text{m/s}$ with a sampling rate of 200 Hz, in an XY envelope of 100 μm length with 1 μm spacing. The Z axis measurement of the CLA gauge was calibrated using a secondary roughness standard (traceable to United Kingdom Accreditation Service - UKAS) and is capable of providing a measurement uncertainty of ± 25 nm.

3.2.10 Variation of setting time and compressive strength

Most important feature of the bioactive bone cement is the setting parameters, i.e. setting time and compressive strength. Setting time of the CSC should be such that it provides sufficient time for the surgeon to perform the implantation before setting, but not too long to cause delay in closing the surgical site. Being designed as a bone defect filler, the compressive strength of the CSC should be comparable/ greater than that of the cancellous bone. There is a general consensus in the literature that clinically useful bone cements should have a setting time less than 20 min and compressive strength greater than 11 MPa (Dorokshin, 2011). Setting time of the cement compositions mixed at ambient temperatures ($25 \pm 2^\circ\text{C}$), were determined using a custom fabricated Vicat type apparatus (Figure 10) (Komath and Varma, 2004). It consists of a steel needle of 1 mm diameter moving vertically under a

constant load of 100 g force, a stainless steel tray (5 mm depth) kept below to hold the paste and a dial gauge to record the movement of the needle. The apparatus was set in such a way that when we release the holder of the needle, its tip should just touch the bottom of the holder. The stainless steel tray after filling 2.5g of the putty was kept under the needle and the distance penetrated by the tip (mm) to the sample holder at each half minute intervals were measured using an attached dial gauge (with 0.01mm accuracy).

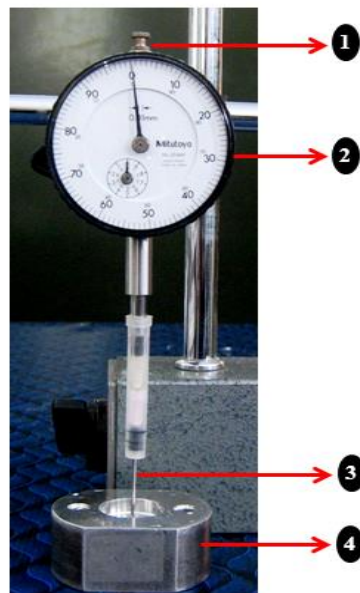


Figure 10: Custom fabricated Vicats needle type apparatus for setting time measurement 1) Knob allowing the vertical movement of the vicat needle 2) dial gauge 3) vicat needle 4) stainless steel holder of 5mm depth.

Setting times were quantified measuring the distance penetrated by the needle against time. The starting of the period at which the needle moves constant depth at each half minute interval (the graph becomes straight line parallel to x-axis) becomes the initial setting time. The time at which the needle do not make an impression at the surface becomes the final setting time. The experiments were conducted at $23\pm 2^{\circ}\text{C}$ at 100% relative humidity. The penetration depth will show a drastic decrease during the setting. The time period elapsed between the complete wetting of the powder to the steep decrease in the measured penetration depth is the initial setting time (t_i) and

the time period at which the cement resists the needle (no penetration) is the final setting time (t_f). The setting time of the various compositions of the cement has been determined. The average values were calculated from triplicate measurements for each composition and plotted as mean \pm SD against the DHPD concentration.

The compressive strength and compressive modulus of the samples were determined as per the ASTM standard specification F451-16. Three different batches of the cement powder for each concentration were prepared and four test samples were taken from each. The test specimens were prepared in split-moulds as cylinders of 6 mm diameter and 12 mm height, and were dried in 100 % relative humidity at 37°C for 24 h. The ends of the specimens are ensured to be flat and smooth and parallel to one another and at right angles to the long axis of the cylinder.

The compressive strength of each of the samples was measured using Universal Testing Machine (INSTRON 1193) by placing the samples between the platens and compressing at a cross head speed of 1 mm/min till the breakpoint. The maximum stress at the point of fracture was used to calculate the compressive strength and the corresponding compressive modulus. Readings without a well defined point of fracture in the stress-strain curves were rejected. The compressive strength values (mean \pm SD) of 12 specimens corresponding to each DHPD concentration were taken to find the effect of the additive.

PHASE 3

3.3 *In vitro* and *in vivo* validation of ‘BioCaS’ as an injectable bioactive bone filler cement

As ‘BioCaS’ is a self-setting injectable material comprising phosphate incorporated low dimensional gypsum crystal lattices for potential bone-filling applications, the new cement has to be authenticated for clinical use in humans. This report presents the methods and outcomes of the safety and efficacy evaluation of BioCaS cement to establish biocompatibility and the ability to heal bone defects. The testing has been planned as per the US Food and Drug Administration guidelines (Class II special controls guidance document, FDA) following ISO 10993 (ISO 10993-1, 2009) and abiding by the ethical and regulatory stipulations.

3.3.1 Materials and cell lines

Commercial reagents for the preparation of SBF include NaCl (99-100.5%), NaHCO₃ (99-100.5%), KCl (99-100.5%), K₂HPO₄ (99%), MgCl₂.6H₂O (99-101%), CaCl₂.2H₂O (99-103%), Na₂SO₄, which were purchased from Riedel-de-Haen, Sigma-Aldrich Laborchemikalie, Germany; tris-hydroxymethylaminomethane [(HOCH₂)₃CNH₂] (99.9%, AR grade) from the SISCO research laboratories pvt. ltd and HCl (98%, GR grade) from Merck, Mumbai.

L929 cell line for the cell culture cytotoxicity experiment were obtained from ATCC, USA and HOS cell lines were procured from NCCS, Pune.

3.3.2. *In vitro* aseptic degradation profile of BioCaS in phosphate buffered saline

Aseptic degradation was performed with 24 h set BioCaS and smCHD0 cement (12 mm length × 6 mm diameter) specimens (2 pellets each) in phosphate buffered

saline (PBS) at 37°C for 10 weeks with a weight-to-volume ratio of 0.2 g/ml (Yu *et al.*, 2013) and the solution was refreshed on alternate days. The samples were removed after incubation for specified time periods, rinsed with deionized water and vacuum dried to obtain constant weight during two subsequent weighing with in half hour interval. In vitro degradation was measured as

$$D=[(W_i-W_f)/W_i]\times 100\% \quad (28)$$

where D is the degradation rate and W_i and W_f are the the initial weight and the final weight of the degraded specimen at time t, respectively. Triplicate measurements were conducted for each set of the sample. Rate of the degradation for each time period were calculated by taking the ratio of mean value of degradation to the time period.

3.3.3 In vitro bioactivity through immersion in simulated body fluid

Immersion in simulated body fluid (SBF) aids as an acceptable method to assess the in vitro bioactivity of a synthetic bone graft material (Kokubo, 2006). BioCaS cement discs prepared in stainless steel moulds of dimension 15 mm diameter and 3.5 mm height were dried for 24 h and immersed in SBF (prepared from NaCl, NaHCO₃, Na₂SO₄, KCl, K₂HPO₄.3H₂O, MgCl₂.6H₂O, CaCl₂.2H₂O buffered with [(OHCH₂)₃CNH₂] as per refined recipe formulated by Kokubo) in 50 ml vials. A SmCHD0 disc prepared in the same way was used as control. Two sets each were prepared to incubate for 2 and 4 days at 310K, in triplicate. After washing gently with deionized water and drying in air, the discs were examined in an environmental scanning electron microscope (FEI QUANTA 200, Netherlands) for surface features after sputter coating with gold. The phase of the deposited material was analysed with XRD (Bruker D8 Advance x-ray diffractometer, Germany), scanning with

CuK α radiation (at tube parameters of 40 kV and 30 mA) in the two theta range 10°–50° at a rate of 2° min⁻¹ in incremental steps of 0.01°. EDS was used to analyse the elemental composition of the surface layer formed. The scratched out powder from the coated surface of 4 day immersed samples of BioCaS and smCHD0 were subjected to FTIR analysis to confirm the formation of apatite layer. pH changes and the change in the concentration of Ca, P, and S at each time point were monitored to get more detailed overview of the apatite layer formation. The pH measurements of the SBF after immersion times before the sample removal help to verify that values remained within the physiological range that allows cells to survive (Dadkhah *et al.*, 2017). The SBF solutions were stored in refrigerator to evaluate the ionic concentrations by using ICP-OES (Inductively Coupled Plasma-Optical Emission Spectrometry) (Oudadesse *et al.*, 2011).

3.3.4 Selection of the tests and regulatory aspects

The safety and efficacy tests on a biomaterial help with its scientific validation for clinical use, as well as for meeting the requirement for regulatory approval for the marketing of the product. The evaluation plan is to be made as per the international standards and guidelines, so as to bring out the ‘safety profile’ of the material pertaining to its end application (Upman, 1999).

The plan for safety and efficacy evaluation of BioCaS cement has been prepared on the basis of ISO 10993 (ISO 10993-1, 2009). The sequence of tests includes biological screening tests of cytotoxicity and haemolysis, cell adhesion and actin staining study with Human osteosarcoma cell lines and toxicological tests such as acute systemic toxicity, sensitization potential via maximization, irritation potential and pyrogenicity. Long-term implantation in animal bone as per ISO 10993

Part 6 ('Tests for local effects after implantation') (ISO 10993-6, 2007) was selected to assess the efficacy of BioCaS cement as a bone filler. The term 'efficacy' refers to the study of local effects upon implantation in bone, including the healing of the defects created in an appropriate animal model. The evaluation plan was discussed in the Biological Evaluation Committee of the Biomedical Technology Wing, Sree Chitra Tirunal Institute for Medical Sciences and Technology, Trivandrum (SCTIMST), India and was duly approved. All experiments involving the use of animal models were reviewed and approved by the Institutional Animal Ethics Committee (IAEC) of SCTIMST. Animals care and management complied with the regulations of the Committee for the Purpose of Control and Supervision of Experiments on Animals (CPCSEA), Government of India. All animals were handled humanely, with due care for their welfare and without inducing any pain or distress. Inbred strains of animals were used in all the experiments and the animal husbandry was maintained in accordance with ISO Standard 10993-2 ('Animal welfare requirements'). In the case of mice, polypropylene cages with a steel top and paddy husk bedding were provided for housing, with five mice per cage. The rabbits and guinea pigs were housed individually in metal (anodized aluminium/stainless steel) cages. Commercially available standard feed and potable water were given ad libitum. All the studies were conducted in accordance with OECD principles of good laboratory practice in an animal surgical facility under aseptic conditions.

3.3.5. In vitro screening tests

3.3.5.1. In vitro cell culture cytotoxicity

(i) Method of test on extract using mouse fibroblast cells (L929): Cylindrical (12mm height × 6mm diameter) specimens of the test material CS with surface area

2.826 cm²/pellet were used for the invitro cell culture cytotoxicity using test on extract method (ISO 10993-5, 2009). Extract was prepared by incubating test materials in physiological saline at surface area to volume ratio 1.25 cm²/ml at 310±2K for 24 h, followed by centrifugation and filtering. The assay was further conducted following the same protocol as described in section 3.1.8.1.

(ii) Metabolic activity via MTT assay using mouse fibroblast cells (L929):

Qualitative assay of in vitro cell culture cytotoxicity by method of test on extract was followed by quantitative evaluation of metabolically active L929 mouse fibroblast cell viability as per ISO 10993-5, 2009. The method was described in section 3.1.8.2.

(iii) Cell viability using human osteosarcoma cells via a live/dead assay:

The in vitro cell viability of human osteosarcoma cell lines (HOS, a cell line of osteosarcoma that demonstrates various osteoblastic characteristics) (Lee and Kim, 2009) with BioCaS was examined through a live/dead assay. HOS cells (procured from NCCS, Pune) were maintained in MEM supplemented with 10% FBS, 3% L-glutamine, 7.5% sodium bicarbonate and 1% penicillin/streptomycin antibiotic (Sigma-Aldrich) incubated at 37°C in 5% CO₂. They were sub-cultured using 0.25% trypsin EDTA, seeded on the test sample discs (1 cm² surface area) and the control (cover glass piece, 1 cm×1 cm) at a density of 1×10⁴ cellscm⁻² and incubated for 48 h. smCHD0 samples were also treated with cells for finding out the change during the crystal modification with the additive. Quadruplicate samples were kept for incubation for both the BioCaS and smCHD0 among them two of each are used for ESEM analysis and the next two are for the florescence microscopic analysis. Cells seeded on control glass coverslips were used for fluorecence microscopic analysis only.

For the fluorescence microscopic analysis, stock solutions of fluorescein diacetate (FDA) and propidium iodide (PI) were prepared for double fluorescent labeling. FDA stock was made in acetone at a concentration of 10 mg ml^{-1} and diluted to 0.1 mg ml^{-1} with serum-free MEM, and PI was mixed in ethanol at a concentration of 1 mg ml^{-1} and further diluted to $0.05 \text{ } \mu\text{g ml}^{-1}$ using culture media. After incubation, the culture medium was replaced with 1ml FDA and incubated for 5 min in the dark, followed by the addition of PI and washing with PBS. Cells were examined under a fluorescence microscope (Leica DMIL 6000 E, with I3/N21 filter cubes). Non-fluorescent FDA passes through the live cell membrane and is hydrolysed by intracellular esterase to a fluorescent material (fluorescein), hence live cells are labelled green. PI cannot permeate the membrane and hence passes through the damaged parts of the dead cell membrane, intercalates with the DNA double helix of the cell and stains the nuclei red (Zaiss *et al.*, 2016).

After incubation, the culture medium was replaced with 1ml FDA and incubated for 5 min in the dark, followed by the addition of PI and washing with PBS. Cells were examined under a fluorescence microscope (Leica DMIL 6000 E, with I3/N21 filter cubes). Non-fluorescent FDA passes through the live cell membrane and is hydrolysed by intracellular esterase to a fluorescent material (fluorescein), hence live cells are labelled green. PI cannot permeate the membrane and hence passes through the damaged parts of the dead cell membrane, intercalates with the DNA double helix of the cell and stains the nuclei red (Zaiss *et al.*, 2016). The sample processed under the same protocol were subjected to the confocal laser scanning electron microscopic analysis with cLSM; Carl Zeiss LSM argon with HFT 488/543 laser (Gantenbein-Ritter *et al.*, 2011).

(iv) Actin staining for evaluating the plastic adherence of HOS cells during the cell adhesion: HOS cells were seeded on the surface of the materials following the protocol described in section 3.4.5.1.3. After incubation for 48 h, the cells were fixed in 4% paraformaldehyde and the test samples were rinsed thrice with 0.1 M phosphate buffered saline followed by permeabilisation with 0.1% Triton X-100 in PBS for 2 minutes. The samples were rinsed with PBS (3 times) and treated with Rhodamine phalloidine (1:100 in PBS) by incubating for 15 minutes in darkness. The samples were again rinsed with PBS and counterstained with 5 µg/ml Hoechst 33258 solution [Invitrogen Corporation, Carlsbad, CA] for 5 minutes. Test samples and controls were rinsed with PBS and examined under fluorescence microscope (Leica DMI6000 with N2.1 (Ex BP 515-560, Em LP 590)/I3 (Ex BP 450-490, Em LP 515) filter cubes. (BP-Band pass filter, LP- Long pass filter).

(v) Scanning electron microscopy for the morphology of HOS cells on the surface of the cement matrix during cell adhesion

The cells treated samples BioCaS and smCHD0 (as per the described protocol in section 3.3.5.1 (iii)) after the incubation period of 48 hours were fixed in 4% paraformaldehyde for 24 h and the morphology of the cells-material interaction surface were analysed by environmental scanning electron microscope (FEI QUANTA 200) at 20 kV under wet conditions without processing involving the fixing in gluteraldehyde and series dehydration in graded ethanol.

3.3.5.2 Haemolytic potential

The haemolysis test was done on the set cement samples using human blood, as per ISO 10993 Part 4 (ISO 10993-4, 2002). Blood from human volunteers was collected into the anticoagulant acid–citrate–dextrose solution, following ethical practice.

Platelet-poor plasma from blood was prepared by centrifuging (4000 rpm, 15 min), followed by aspiration. The cement cylinder of diameter 6 mm and length 12 mm was exposed to 1ml of blood (in triplicate) and incubated for 30 min under agitation at 70 rpm using an Environ shaker thermostated at 35 ± 2 °C. Empty polystyrene culture dishes, exposed to blood, served as the reference. Total haemoglobin (Hb) in the whole-blood samples was measured using automatic haematology analyser (Sysmex K 4500). To measure the free haemoglobin liberated into the plasma, 10 times the volume of 0.01% Na_2CO_3 was added to it in microtubes and mixed well, with 0.01% Na_2CO_3 taken as a blank. The absorbance of oxyhaemoglobin was measured at 415 nm (A_{415} , sorbent band) using a diode array spectrophotometer (HP 8453). In order to eliminate the interference of uroporphyrin absorption, which falls in the same wavelength range as Hb, readings were also taken at 380 nm (A_{380}) and 450 nm (A_{450}). The plasma Hb content in the sample can be given in mgdl^{-1} as

$$\text{FreeHb} = \{ [2 \times A_{415} - (A_{380} + A_{450})] / 1.655 \} \times 1000D/E \quad (29)$$

where 1.655 denotes the correction factor in lieu of the turbidity of plasma sample, D is the dilution factor and E is the molar absorptivity at 415 nm of a 1 g dl^{-1} solution of oxyhaemoglobin (79.46) (Sasidharan *et al.*, 2016). The haemolytic index is calculated as:

$$\text{Haemolytic index} = (\text{Free Hb} / \text{Total Hb}) \times 100 \quad (30)$$

3.3.6 Biocompatibility and evaluation of BioCaS

3.3.6.1 Acute systemic toxicity

This test explores the systemic response in mice caused by leachable or degradation products in aqueous and non-aqueous extracts of the sample as per ISO 10993-11:2006 (ISO 10993-11, 2006); adverse reactions if any generally appears within

first 24 hours (Liu *et al.*, 1997). The extracts were prepared by incubating 4 g of the test material in 20 ml of physiological saline (aqueous) and cotton seed oil (non-aqueous) at 37 ± 1 °C for 72 ± 2 h under 50 rpm agitation. Aliquots from each extract were taken for experimentation after checking the pH. The respective extraction media alone were used as the control in each case.

Healthy and active mice (albino strains) in the body weight range 17–23 g of either sex were randomly selected for the experiment. Ten mice were used for each extract, with five each for the test and the control. Animals were acclimatized for a period of at least 6 days, maintained in a controlled environment (22 ± 3 °C temperature, 30%-70% humidity, 12 h light/dark cycle and 15 air changes per hour). They were fed with mouse chow and filtered fresh water *ad libitum*. The extract in physiological saline and cotton seed oil of the test material and the respective controls was injected into the corresponding groups of animals, following an intravenous route for aqueous extract and an intraperitoneal route for the non-aqueous extract, at a dose of 50 ml kg^{-1} . Each animal was observed at 4, 24, 48 and 72 h for the evidence of any abnormalities, including loss of body weight and death. The observed parameters include respiration, motor control, convulsions, reflexes, ocular signs, cardiovascular signs, salivation, piloerection, analgesia, muscle tone and gastrointestinal abnormalities (Ding *et al.*, 2012). The decision on toxicity is made based on accepted standard criteria.

3.3.6.2. Pyrogenicity

The cement was evaluated for pyrogenic potential which includes (ISO 10993-11, Annex F Document, 2006) includes the pyrogenicity of both microbial endotoxins and non-endotoxins (chemical leachables). Healthy and mature albino rabbits in the

weight range 2.5–2.8 kg were chosen for the test. They were acclimatized for 7 days in a rabbit restrainer at 295 ± 3 K in an area free from disturbances. The body temperature of the animals was recorded (rectal measurement using a calibrated thermometer) at regular intervals and three of the animals were selected whose body temperature was less than 312.8 K and the variation among them less than 1 K. Twenty grams of the test material was taken in a de-pyrogenated beaker containing 100 ml of physiological saline and incubated at 310K for 1 h. The extract was collected by removing the material and then used for the test, at a dose of 10 ml kg^{-1} . The rectal temperature determined 30 min prior to the experiment was taken as the base value. The extract in the required dose was injected through the marginal ear veins of the rabbits, finishing the procedure within 10 min. The rectal temperature was recorded after 1 h, and repeated at 30 min intervals up to 3 h. The rise in temperature with respect to base temperature in each case was determined.

3.3.6.3 Irritation potential

Some kinds of biologically active leachables from an implant can lead to a local tissue response characterized by the usual signs of inflammation, and this could be either immediate or delayed. The irritation potential of the material was assessed in rabbits through an intracutaneous reactivity test (ISO 10993-10, 2010). Three fresh, healthy, thin-skinned adult albino rabbits weighing a minimum of 2 kg were selected. The test area was prepared by closely clipping the fur on both sides of the spine, taking care to avoid mechanical irritation or trauma. The sterility of the area was maintained during the test period. The extracts of the test material in physiological saline and cotton seed oil were prepared as for the acute systemic toxicity test. Physiological saline and cotton seed oil alone were used as controls in each case.

The test extracts were aseptically injected into five sites (0.2 ml/site) each on the upper left and right side, under the prepared skin in the animals. The corresponding controls were injected into five sites on the lower left and right sides. Occlusive dressings were used after the procedure and the local responses at each site were evaluated by grading for erythema, oedema and necrosis at 24, 48 and 72 h, as per the criteria: 0, negligible; 1, very slight; 2, well defined; 3, moderate; 4, severe. The average of the irritation scores of erythema and oedema individually for the test and the control sites for the normal saline and cotton seed oil extracts, were calculated. The difference in the sum of average scores for the control group and test group corresponding to both erythema and oedema indicate the irritation potential of the material.

3.3.6.4 Delayed hypersensitivity

As per ISO 10993 Part 10 (ISO 10993-10, 2010), the hypersensitivity test for finding the immune response to the implants follows the skin irritation test. In the present case, the Magnusson and Kligman method in guinea pigs (Magnusson and Kligman, 1969) was adopted, wherein Freund's complete adjuvant is used to enhance sensitivity. The extract was prepared by immersing 4 g of set cement in 20 ml of physiological saline and shaking for 72 h at 37 ± 1 °C and 50 rpm. The supernatant, filtered with a 0.25 µm syringe-filter was used as the test solution. Fifteen healthy thin-skinned guinea pigs (ten for the test and five controls) of either sex in the weight range 300–500 g were selected for the test. The fur on either side of the intrascapular region was clipped closely, ensuring that the skin was free of mechanical irritation or trauma. Three sites each on the left and right of the clipped area were selected for the

intra-dermal injections (0.1 ml quantity). The test was executed in two phases-the intra-dermal induction phase and the challenge phase.

In the first phase, the extraction medium (physiological saline) mixed with a stable emulsion of Freund's complete adjuvant in 50:50 volume ratio was injected in the top pair of sites in all animals. The undiluted extract was injected in the test animals and the medium alone in the control animals, all in the middle pair of sites. The mixtures of the two solutions (used in the upper and middle sites) in 50:50 volume ratios, were injected in the bottom pair of site in the respective samples.

The challenge phase was initiated with topical application of the test and control extracts to the respective sites using a saturated patch of absorbent gauze (8 cm²). Since the material did not give rise to irritation in the previous test, the sites were treated with 10% sodium lauryl sulfate 24 h prior to this phase. Following the application of the patches, dressings were provided and removed after 48 h.

Fourteen days later, the test and control animals were challenged with test material extract, following similar procedure as above. The patches and dressings were removed after 24 h and the appearance of the challenge skin sites of test and control animals were observed at 24, 48 and 72 h. The skin reactions for both erythema and oedema were scored as per the Magnusson–Kligman scale: 0, no visible change; 1, discrete or patchy; 2, moderate and confluent; 3, intense reaction and swelling.

3.4.6.5 In vivo implantation in rabbit model

(i) Implantation and histology

A bone implantation test as per ISO 10993 Part 6 (ISO 10993-6, 2007) was selected because the suggested application of the material is as a bone filler. The ability of

BioCaS to heal bone defects is to be established in animals as a preclinical trial. The cement powder for the test was packed in sterilization pouches and sterilized by gamma irradiation, and sterile water was used for mixing. The control selected was calcium phosphate (hydroxyapatite) ceramic, instead of CaS material. The responses to bare CSC in animals and humans are already documented (Beuerlein and Kee, 2010), indicating that the material is not stable at an implantation site. The present cement has phosphate ions in it and the test would be meaningful only if compared with a stable calcium phosphate material. Hydroxyapatite porous ceramic prepared in-house was selected as a control, the clinical success of which has already been established (Mohan *et al.*, 2013, Menon and Varma, 2005). The materials were shaped into 2 mm diameter rods and sterilized by autoclaving for the implantation.

A rabbit model was chosen because it reaches skeletal maturity shortly after sexual maturity at around 6 months of age. Convenient size and ease of handling were additional factors. Based on earlier experience, femur bone was selected as the target with three defects per bone, and the evaluation periods were fixed as 12, 26 and 52 weeks. Both femurs were used for implantation, one for the test material and the other for the control. The defect size selected was 2 mm in diameter as prescribed for surgical implants in long bone (Sabareeswaran *et al.*, 2013).

Healthy adult albino rabbits of either sex weighing above 2 kg were used for the experiment with four animals per period, giving a total of 12. All surgical procedures for the implantation were carried out by a toxicologist in an animal procedure room in aseptic conditions. Before surgery the sides of the hind legs were shaved and wiped with antiseptic solution. A premedication with atropine and diazepam (at doses of 0.15 and 2.5 mg kg⁻¹ body weight, respectively) was given

subcutaneously. The animal was anaesthetized with an intramuscular injection of xylazine and ketamine (at doses of 5 and 90 mg kg⁻¹, respectively). After placing the animal in a lateral recumbent position on the procedure table, the skin was lightly swabbed using 70% alcohol followed by betadine solution. Incision was done along the cranio-lateral border of the shaft of the femur to open the subcutaneous fat and superficial fascia. The skin margins were undermined and retracted and the fascia lata was incised along the cranial border of the biceps and vastus lateralis muscle to reveal the femoral shaft. Three defects of diameter 2mm were created 1 cm apart in the mid shaft of the femur using an appropriate burr fitted to a micromotor low-speed drill (SURGIC XT NE111, NSK Nakanishi Inc., Japan) with profuse irrigation of saline and clearing the debris using suction.

The cement samples, mixed as thick putty were transferred into the right limb defects by an applicator and allowed to set. In the left limb defects, the control material (clinically approved hydroxyapatite porous ceramic prepared as rods of 2 mm diameter) was inserted tightly and trimmed to keep it level with the bone surface. After completion of the implantation the retracted muscles were released and replaced. The cut subcutaneous fat and superficial fascia were sutured in the first tier and the skin incision closed in the second tier. Post-operatively, the animals were kept under antibiotic cover for the first 3 days.

After the stipulated period, the corresponding group was euthanized by an overdose of anaesthetic agent. The test and control implanted femurs were collected by autopsy and preserved in 10% buffered formalin. The implant sites were identified grossly after clearing the bone surface. For histopathological analysis, cross-sectional blocks of the bone containing the implanted site were cut using a high-precision low-

speed saw (ISOMET, Buehler) and dehydrated in ethyl alcohol in ascending order of concentration from 80% to 100%, repeating the last step again. The blocks were then embedded in PMMA resin for sectioning using a high-speed precision diamond saw (ISOMET 5000, Buehler). Multiple 100 μm thick serial sections were cut, ground and polished in a variable speed grinder–polisher (ECOMET 3000, Beuhler) and were stained with Stevenels blue followed by counter-staining with Van Gieson's Picro-Fuchsin. The sections were examined in a Nikon Eclipse E 600 microscope and the images were recorded using a Nikon DS-Ri1 digital camera.

(ii) SEM with EDS of histological sections of BioCaS

The bone-implant interface regions in the histological sections of the 12 and 26 weeks BioCaS implanted animal groups were observed in environmental scanning electron microscope (FEI QUANTA 200) at 12.50 kV without conductive gold coating to identify the micromorphology. EDS was conducted with EDAX Genesis XM 4 integrated with the ESEM to confirm the material part observed to be gypsum in the implanted area.

(iii) Histomorphometry

The neobone (woven and lamellar bone) and the residual implant were demarcated from other tissue on the selected region of interest (ROI) (covering the portion of implanted region and the neobone ingrowth region at the host bone–implant dynamic interface) from the stained histology images at the same magnification of control scaffolds and the cement specimens and calculated the analogous area in percentage with respect to total tissue volume with image analysis software (Image J) (n=4 for both the test and control formulation at each time period) (Kasuya *et al.*, 2012). The percentage of the de novo bone ingrowth was otherwise represented by the term

regeneration efficiency (RE). The histomorphometry values were expressed as means \pm SD and the Student's t-test or one-way analysis of variance (ANOVA) with post hoc tests was applied to comparison. Differences were considered statistically significant at $p < 0.05$.

(iv) Micro-CT analysis

Mineralization of newly formed bone, overall morphology of the neobone around the implant and quantification of neobone fraction with respect to host bone were carried out using high-resolution X-ray micro-computed tomography (mCT 40, Scanco Medical, Switzerland). The scanning was carried out with a slice increment $15\mu\text{m}$, X-ray beam energy 70 kV and X-ray intensity 114 mA. In particular, the specific area of the scanned region containing implant was selected and the reconstruction of the selected region was made using the cone beam convergence/back projection algorithm-based software. Based on the density variation of the host bone and the implant, the 3D image of the implant site was extracted. The overall scan time was 300000 μs . From the experimentally measured CT database, a cylindrical region of interest (ROI) was selected for analysis corresponding to the cortical bone during implantation. In order to evaluate bone regeneration within the defect, ROI was further sectioned transversely as top, medium and bottom and radially as outer, inner and core shells. Also, thresholds were suitably applied to images of each sample in order to segment the newly formed bone from the residual implant. After thresholding, the bone volume (BV) was determined by counting the total number of bone voxels and multiplying by their known volume, while the total volume (TV) was determined by counting the bone and non-bone voxels.

PHASE 4

3.4 Injectable ‘BioCaS’ as a local drug delivery medium

The hard tissue structure in the body is protected from the attack of microorganisms through various mechanisms and barriers. Yet infection in bone can happen if the protection structure is breached, i.e. during penetrating injuries, open fractures after trauma and surgical contamination as well as wounds associated with chronic diabetes (Ikpeme et al., 2010). Such bacterial infections called osteomyelitis has become a health burden in global perspective. Considering implant related infection alone, the annual cost of infected revisions to US hospitals is projected to exceed \$1.62 billion by 2020 (Mc Conoughey *et al.*, 2015).

The gram positive pathogen *Staphylococcus aureus* is the dominant pathogen for all classes of osteomyelitis implicated for 45% of infections in the skeletal system while gram-negative bacteria *Escherichia coli* indicates common causes of infection in children after puncture wounds of the feet or open injuries to bone. In most cases symptoms appear after 6 weeks; inadequate therapy may lead to relapsing infection and progression to chronic osteomyelitis where the conventional treatment comprises sequestrectomy, obliteration of dead space, reconstruction of soft tissue defects, stabilisation of bone with fixators and adjunctive systemic antibiotic therapy for 4-6 weeks (Ikpeme *et al.*, 2010, World Health Organization, 2001). Parenteral administration of high dose combination regimens of antibiotics require careful monitoring of the drug serum concentrations to maintain nontoxic systemic levels. As the blood supply to the infected tissue is compromised, the local bioavailability may not be sufficient to prevent the infection and hence osteomyelitis associated with

implant materials are extremely difficult to cure without removal of the device (Ribeiro *et al.*, 2012).

Difficulty in controlling osteomyelitis is primarily due to the formation of 'bacterial biofilms' which instigates with the attachment of free floating microorganisms, subsequently followed by the formation of colonies permanently anchored to the surface. The dense extra cellular matrix and the outer layer of the biofilm protects the interior colonies and bacteria display above 1000-fold tolerance to antibiotics than their planktonic counterparts and significant resistance to innate and adaptive host immunity ultimately result in increased resistance to antibiotic (Teller *et al.*, 2006).

Clinical management of osteomyelitis is done through surgical debridement of the infected area and local antibiotic drug delivery depots with PMMA bone cement and beads. Being a bioinert material, PMMA needs secondary surgery for the removal of beads after treatment. Only heat stable drugs could be used due to highly exothermic setting mechanism and low drug elution profile develops antibiotic resistance (Liu *et al.*, 2010). Once the antibiotics have eluted from nonbiodegradable cement, the surface acts as a potential nidus for bacterial colonization and biofilm formation and hence urged the need for alternative systems (Howlin *et al.*, 2015). HA and β -TCP ceramics, biodegradable polymers such as poly(lactic acid) poly (glycolic acid), and their copolymers, collagen and chitosan have been widely studied and reported limitations such as inadequate degradation rate, poor osteoconductivity, rapid burst antibiotic elution rate, and low mechanical strength (Ding *et al.*, 2014). Research is ongoing to develop injectable bioactive bone filler cements loaded with antibiotics which can be applied through minimally invasive surgery and sets at the

local defect site because it can facilitate the diffusion of antibiotics to avascular areas that are inaccessible by systemic antibiotics while minimizing potential systemic toxicity. Also the infecting organisms that are resistant to drug concentrations achieved by systemic antibiotics are susceptible to the higher drug concentrations provided by local antibiotic delivery (Ding *et al.*, 2014). The ideal delivery device for chronic osteomyelitis should be a material which provides sustained and controlled release greater than minimal inhibitory concentration for at least 14 days for the prevention of biofilm formation or to cope with the host immune system, and eventually resorbs at the site.

This phase of the work explores the potential of ‘BioCaS’ injectable bioactive bone filler cement as a therapeutic local drug delivery system against osteomyelitis. The studies were conducted with drugs gentamicin and vancomycin each against the *Escherichia coli* and *Staphylococcus aureus*. Gentamycin is a broad spectrum aminoglycoside antibiotic active against mostly gram negative bacteria and the gram positive staphylococcus. Vancomycin is a broad spectrum glycopeptide antibiotic active against gram positive bacteria, mainly methicillin-resistant *Staphylococcus aureus* (MRSA) (Chang *et al.*, 2011) (Pishbin *et al.*, 2014).

The antibiotics tested were of low dose (1g/40g), middle dose (4g/40g) and high dose (8g/40g) incorporated through wetting medium in to the powder composition during setting. The optimised sample from the invitro elution profile and characteristics of the bone cement, The biological activity of the released gentamicin and vancomycin antibiotics in the sample aliquots were tested against MSSA strain (ATCC 25923); a gram positive facultative anaerobic non-motile coccus and *E. coli* (ATCC 25922); a gram negative facultative anaerobic motile bacillus.

3.4.1. Chemicals and reagents

Ammonium formate (HCO_2NH_4 , 99%) was purchased from Alfa aesar, USA. Vancomycin hydrochloride (VH) (for intravenous infusion IP, Vansafe-CP 500mg) obtained from VHB Medi sciences Ltd, Uttarakhand, India. Gentamicin sulphate (GS) was purchased from Himedia. Acetonitrile, O-phthalaldehyde, 2-mercapto ethanol, methanol and sodium tetra borate decahydrate were obtained from Merck specialities pvt ltd, Mumbai. Gentamicin injection vial (Genticyn, 80mg/2ml) was obtained from Abbot health care pvt ltd, Mumbai.

3.4.2 Theoretical frame work for drug delivery

The drug release profile from a matrix follows different statistical models mainly zero order (cumulative drug release vs. time), first order (\ln (cumulative drug remaining) vs. time), Higuchi (cumulative drug release vs. $t^{1/2}$), Hixson–Crowell (cube root of drug remaining in the matrix vs. time) and the Korsmeyer-Peppas model (\log [cumulative drug released] vs. $\log t$). The experimental data were compared with each theoretical model and selected the best fitted one with highest value of correlation or regression co-efficient (R^2) for interpretation.

Zero order model refers to the constant drug release from drug delivery systems better represented as

$$Q_t = Q_0 + K_0 t \quad (31)$$

Where Q_t - the amount of drug dissolved in time t , Q_0 - the initial amount of drug in the solution (most times, $Q_0 = 0$) and K_0 is the zero order release constant in units of concentration/time. The data has to be plotted as cumulative amount of drug released vs time.

First order kinetic models can be expressed by the equation

$$\frac{dC}{dt} = -KC \text{ or } \log C = \log C_0 - Kt/2.303 \quad (32)$$

Where C_0 -initial concentration of the drug, K -first order rate constant, C -Cumulative percentage of drug remaining in the matrix at time t (Lokhandwala *et al.*, 2013).. The data are plotted as log cumulative percentage of the drug remaining vs time.

The Higuchi model describes the drug dissolution from a matrix system with drug concentration in the matrix is lower than its solubility and the release occurs through pores in the matrix, given by equation,

$$f_t = Q = \sqrt{D\delta/\tau} (2C - \delta C_s) t = K_H \times t^{1/2} \quad (33)$$

where D -diffusion co-efficient of the drug molecule in the wetting medium, δ - the porosity of the matrix, τ - the tortuosity of the matrix and Q -amount of drug release in time per unit area A , D -diffusion coefficient of drug molecules, C -initial concentration of drug and C_s -solubility of drug in the matrix media, K_H - the higuchi dissolution constant (Ramteke *et al.*, 2014). Tortuosity is the dimensions of radius and branching of the pores and canals in the cement matrix and the Porosity is function of matrix that exist as pores or channels from which liquid penetrate inside for release of drug from granular matrix. The data could be plotted as cumulative percentage drug release vs. square root of time.

Hixon–crowel method is based on the concept that particles regular area is proportional to the cube root of its volume

$$W_0^{1/3} - W_t^{1/3} = \kappa t \quad (34)$$

where W_0 - initial amount of drug in the pharmaceutical dosage form, W_t - the remaining amount of drug in the pharmaceutical dosage form at time t and κ (kappa) - a constant incorporating the surface and volume relation. This model describes the dissolution occurs in planes that are parallel to the drug surface if the tablet

dimensions diminish proportionally in such a manner that the initial geometrical form keeps constant all the time. The plot involves the cube root of drug percentage remaining in the matrix vs square root of time.

To confirm the drug release mechanism, first 60 % of the drug release data was fitted to the Korsmeyer–Peppas model.

$$M_t/M_a = K \times t^n \quad (35)$$

where M_t/M_a represents the fraction of the drug released at time 't'. The "n" (the release exponent) value of the Korsmeyer–Peppas model used to characterize the different mechanisms of drug release from cement system. The values of $n \leq 0.43$ mean Quasi-Fickian diffusion, $0.45 < n < 0.85$ means anomalous (non-Fickian) diffusion due to both diffusion and relaxation, $n = 0.85$ for case II transport (zero order release) and $n > 0.85$ for super-case II transport due to relaxation only (Omidirad *et al.*, 2013). The plot involves the log cumulative percentage drug release vs log time.

3.4.3. Formulation of drug loaded BioCaS samples

The preliminary test for finding the potential of BioCaS as a local drug delivery system was done with low dose antibiotic concentration 1g/40g cement powder. Concentration was selected based on the literature report on the drug loading in commercial PMMA bone cement - surgical simplex from Stryker orthopaedics and Depuy's smartest® Endurance™ (Liu *et al.*, 2010) (Chang *et al.*, 2011) and where the required concentration of the drug was incorporated through the wetting medium. The letter suffixes to the sample names 'G' and 'V' represent the antibiotics incorporated, Gentamicin and Vancomycin respectively. BioCaSG was prepared with BioCaS set with commercial Gentamicin sulfate aqueous solution (Genticyn, 80

mg/2 ml), and moulded as pellets of 6 mm×12 mm dimension. The required low dose vancomycin concentration for loading were prepared with suitable dilution from stock solution of the vancomycin hydrochloride IP 500 mg reconstituted with 10 ml of the deionised water. Vancomycin loaded samples (BioCaSV) were prepared following the same method as mentioned.

Cement cylinders of BioCaSG and BioCaSV (2 numbers with total weight 1g for each formulation) were separately immersed in 5 ml of the sterile phosphate buffered solutions (PBS; pH 7.4) in a Tarsons PS 15 ml sterile spinwin conical bottom centrifuge tube and the medium was collected and interchanged with fresh PBS each day until no drug could be detected (Chang *et al.*, 2011). The collected medium was stored at 2°C protecting from light before analysis.

3.4.4 Detection of gentamicin eluted from the BioCaSG cement formulation

The eluted Gentamicin was derivatised with the O-phthalaldehyde (OPA) to convert to chromophoric product and analysed by a UV-visible spectrophotometry (Neut *et al.*, 2010). OPA reagent for the derivatisation was prepared by dissolving 0.5 g of OPA in 12.50 ml methanol and added with 0.6 ml of β -mercaptoethanol. 112 ml of 0.04 M borax or sodium tetra borate decahydrate ($\text{Na}_2\text{B}_4\text{O}_7 \cdot 10\text{H}_2\text{O}$) in deionised distilled water was added to the OPA solution and stored in the amber bottle in the dark at room temperature for at least 24 hours prior use. The shelf-life for the prepared reagent was one week. Standard solutions of gentamicin sulfate in the range of 10 -140 $\mu\text{g}/\text{ml}$ were prepared for the calibration. 1 ml from the eluted test samples were added with 5 ml of 4:1, 2-propanol solution and 1 ml of the OPA reagent. 2-propanol solution was added to avoid the precipitation of isoindole derivative. After vortexing for 20 seconds, the solutions were kept for the derivatisation up to 1 hour

before subjecting to spectrophotometric analysis at wavelength of absorption (λ_{\max}) 333 nm. 1ml of deionised distilled water mixed with 5 ml of 2-propanol solution (4:1) and 1ml of OPA processed similar were used as blank.

3.4.5 Detection of Vancomycin eluted from the BioCaSV cement formulation

Vancomycin loaded BioCaS pellets were immersed in 5 ml of phosphate buffered saline into a Tarsons PS 15 ml Sterile Spinwin conical bottom centrifuge tube. The medium was replaced every day and the aliquot collected at pre-determined time periods was quantified using UV-visible spectrophotometer at wavelength 280 nm (Kim *et al.*, 2005). A calibration curve was obtained with vancomycin concentration within the range of 0.015 - 5 mg/ml, in which the curve was linear with a relationship of absorbance = $4.34303 \times \text{concentration}$ ($\mu\text{g/ml}$) following beers law. Special care was taken that the concentration of released drug lay within the calibrated range (absorbance <2) by diluting the solution with additional PBS if required. Using the relationship, the absorbance measured in the test was directly converted to an apparent drug release after dividing the quantity of drug released by the initial cement weight (mg/ml/mg cement). The in vitro drug release tests were performed in triplicate, and data were represented as mean \pm SD.

3.4.6 The validation of UV-Visible spectroscopic detection with HPLC analysis

High pressure liquid chromatographic assay as per the USP standard specification methods (USP 34 NF 29, 2011) was also conducted for the detection of vancomycin hydrochloride from the same samples, using a model LC 210A HT liquid chromatograph, Shimadzu corporation, Japan with a Purospher Star® RP 18 encapped column, 250 \times 4.6 mm and 5 μm particle size. This is for the validation of drug release profile obtained by UV-Visible spectroscopy. The mobile phase

consisted of water-acetonitrile-100 mM ammonium formate in the composite ratio 78/12/10 with the flow rate of 1mm/minute. The column temperature was set at 40°C with the auto sampler temperature 5°C. Injection volume of the samples were 10µL and detection was done with UV detector at wave length of absorption 280 nm. The concentrations of the antibiotics in the cement cylinders were obtained from the HPLC analysis through comparison made with the prepared standard curves where the peak areas were correlated with the antibiotic concentration.

3.4.7 Kinetics of GS release with concentration and surface area/volume ratio change

BioCaSG1, BioCaSG2 and BioCaSG3 cement consisting respectively of 1g (low dose), 4g (middle dose) and 8g (high dose) of antibiotics per 40 gram of the precursor cement powder were formulated by dissolving the corresponding quantity of GS powder in the wetting medium DI by considering the l/p ratio of 0.6 ml / gm (41.66 mg/ml, 166.66 mg/ml and 333.33 mg/ml GS stock solution of GS concentrations respectively for BioCaSG1, BioCaSG2 and BioCaSG3). The drug elution study conducted as per the method suggested in section 3.4.2 and 3.4.3. The dimensions of the pellets were 8.8 mm diameter and 13.3 mm height.

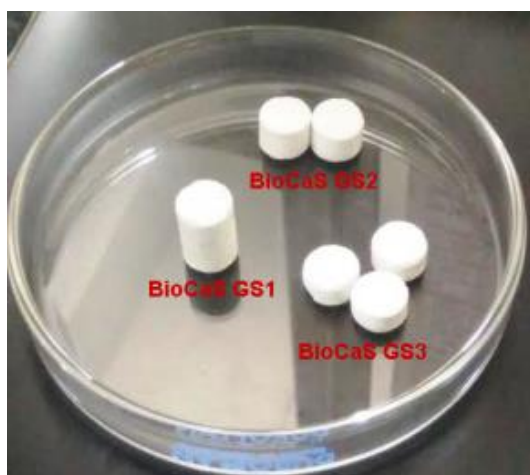


Figure 11: Three set of low dose drug loaded BioCaS cement samples with varying surface area to volume ratio

Similarly BioCaSGS1, BioCaSGS2 and BioCaSGS3 cement loaded with low dose concentration of antibiotics differing only in the surface area to volume ratio (keeping volume and weight of the specimen constant) were prepared as per the Figure 11. The BioCaSGS1 cylinder has dimension 8.95 mm diameter and 13.20 mm height with $S/V = 0.37 \text{ mm}^{-1}$. BioCaSGS2 was prepared with half the height and used 2 pellets for elution with total $S/V = 0.53 \text{ mm}^{-1}$ and BioCaSGS3 was prepared with $1/3^{\text{rd}}$ of the height and 3 pellets were used with 0.68 mm^{-1} S/V ratio in total.

3.4.8 Kinetics of VH release with concentration and surface area change

Like GS loaded cement, low dose, middle dose and high dose VH loaded BioCaS cement specimens viz. BioCaSV1, BioCaSV2 and BioCaSV3 respectively are formulated. The VH 500 mg (Vansafe) were reconstituted with 10 ml of the DI and diluted to get 41.66 mg/ml for the stock solution of low dose formulation. 500 mg reconstituted with 2 ml were used for the stock solution preparation of 166.66 mg/ml and 500 mg reconstituted per ml of the DD water were used for the preparation of the 333.33 mg/ml of the stock solution for BioCaSV3. Similarly BioCaSVS1, BioCaSVS2 and BioCaSVS3 with escalating ratio of S/V with low dose VH was prepared as described in section 3.4.9.

3.4.9 Cementing Characteristics of the GS and VH loaded BioCaS

The injectability of the BioCaSG1, BioCaSG2, BioCaSG3 and BioCaSV1, BioCaSV2 and BioCaSV3 was tested with extrusion rheometry as described previously (section 3.2.3). 3 g of the cement powder was mixed with wetting medium of the corresponding drug concentrations dissolved and extruded from the syringe by applying force at a cross head speed of 10 mm/min using Universal testing machine. The setting times of the compositions were analysed with custom fabricated Vicat's

needle type apparatus (following ISO 9917) ISO and compressive strength with ASTM standard specification F451-16 (section 3.2.9)

3.4.10 In vitro Antibacterial activity of the drug loaded BioCaS

From the results of the elution study and cementing parameters the BioCaSG3 and BioCaSV3 was optimised and opted for *in vitro* antibacterial study by Kirby-bauer disc diffusion method. The cement precursor powders and mixing and filling spatulas were sterilised by autoclaving and the Teflon moulds and glass plate for mixing were sterilised by ETO method. BioCaSG3 and BioCaSV3 cement cylinders of 8.8 mm diameter and 13.3 mm height were prepared with high dose antibiotic concentrations as described in section 3.4.9 and 3.4.10. Drug elution in PBS was conducted as per the method described in section 3.4.2 and interchanged medium was collected every day and kept at 6°C and but not for more than one week. Inhibitory effect of Gentamicin and Vancomycin in the PBS sample was examined with bacterial strains *Escherichia coli* (ATCC 25922); a gram negative facultative anaerobic motile bacillus and *Staphylococcus aureus* (ATCC 25923); a gram positive facultative anaerobic non-motile coccus, using a modified Kirby-bauer disc diffusion test, which is one of the agar diffusion methods. The test was performed on the surface of a solid nutrient medium Mueller-Hinton agar medium. The medium was prepared from a quality control tested lot according to the manufacturer's recommendation (pH - 7.2 to 7.4) and approximately 25 to 30 ml was poured on to 9 cm plate and stored at 2 to 8°C. The bacterial inoculum was prepared from a pure culture. For standardization, Mc Farland 0.5 turbidity standard (barium sulphate) prepared from barium chloride dihydrate and sulphuric acid was used. The density of the test suspension was adjusted to that of the standard by adding more bacteria or more sterile saline or clear

broth, so as to have a uniform growth during the experiment. A sterile cotton swab moistened with the inoculum is used to inoculate the plates. The surface of the medium is streaked evenly with the swab in three directions. The inoculum was left to dry, with the lid closed for a few minutes at room temperature. All the samples should be brought to room temperature prior to the test.

Paper discs with 1 cm diameter, cut out from the Whatman no.1 filter papers were used for loading 40µl of the PBS containing eluted drugs and left to dry. Standard 10µg discs (6mm diameter) of gentamycin and vancomycin were used as the positive control and the Whatman no.1 filter paper disc without drug was used as the negative control. Using a sterile forceps the test and control sample discs were placed on the inoculated plates at least 24 mm apart. After incubating at 35°C the diameter of each zone of inhibition (including the diameter of the disc) was measured to the nearest millimeter. The zones of inhibition produced by these materials are compared with a standard which is used as a positive control for this organisms. The degree of the antibacterial activity is assessed based on the diameter of this zone. Triplicate elution was conducted for each sample and Sextuplicate measurements from randomly selected specimens were done for the first day samples followed by the quadruplicate in the subsequent days for each drug against each bacteria and all the values are expressed as mean \pm S.D.

PHASE 5

3.5 Injectable bioactive bone filler cements incorporating N,O-Carboxymethyl chitosan as gelling agent

The purpose of the study is to develop biocompatible and fully injectable gypsum based cement system with improved rheology and higher mechanical strength, by incorporating gelling agent, possibly without compromising the bioactivity. Different gelling agents like sodium alginate, chitosan, citric acid and hydroxyl propyl methyl cellulose were tried out but found unacceptable due to retarding of setting time (greater than 60 minutes) and poor mechanical properties (crumbling under finger pressure) at higher concentrations. However, promising results were found with the gypsum modified with the derivative of chitosan viz. N, O-Carboxymethyl chitosan (NOCMC). CMC has a long clinical history as a biocompatible material for medical application especially for drug delivery and its durable water holding capacity which would impart a distant aim for the incorporation of more amount of drug for applications in orthopaedics and in dentistry (Liu *et al.*, 2007). The *in vivo* excretion pathway is through the degradation by lysosome to natural byproducts of the glucosamine and N-acetyl D-glucosamine which gets incorporated into glycoproteins or extruded as carbondioxide (Brown *et al.*, 2006).

This part of the work involves the development and optimization of the injectable bone cement composition using CMC. Cement was designed constituting the powder part with bassanite and the additive *di*-sodium hydrogen orthophosphate dihydrate (DHPD) at different weight percentage. Water soluble derivative of chitosan viz. N, O-Carboxymethyl chitosan (NOCMC) at different concentrations in

DI served as the wetting medium. BioCaS is proved to be having higher bioactivity than gypsum based cement. Having carboxylate ions (COO⁻) on polymer chains, CMC is considered as a good candidate for Ca²⁺ cross linking via chelation (Liu *et al.*, 2007) and hence can induce viscous nature with uniform consistency to the cement and enhance the mechanical property by acting as a cement clinker. Optimization of the cement formulation was done with respect to injectability, setting, morphological and mechanical property, exploring the mechanism of cementing and assessing the *in vitro* biocompatibility, bioactivity and osteoblast cell adhesion.

3.5.1. Materials

For the synthesis of N, O- carboxymethyl chitosan, the precursor low molecular weight chitosan [M.W. 100-150 kDa] with degree of deacetylation 85-95% was obtained from Sigma-aldrich, USA. Other reactant monochloroacetic acid (> 99%) and reagents sodium hydroxide (98%), methanol (99.8%) and glacial acetic acid (99-100%) were purchased from Merck, Mumbai. Deuterium oxide (99.9%) for the ¹H NMR analysis were collected from Sigma Aldrich, USA. Deionized distilled water collected from SYNERGY UV Millipore water purification system, Merck was used for all the experiment wherever required. All the reagents and chemicals used for cell culture analysis unless otherwise were purchased from Sigma-aldrich, USA.

3.5.2 Synthesis and characterizations of the N,O-Carboxymethyl chitosan (NOCMC)

N,O-Carboxymethyl chitosan is one of the water soluble amphiprotic ether derivative of chitosan which is a cationic co-polymer of β-(1-4)-linked N-acetyl-D-glucosamine; 2-Acetamido-2-deoxy-β-D-glucopyranose (acetylated unit) and D-

glucosamine; 2-Amino-2-Deoxy-D-Glucopyranose (deacetylated unit). NOCMC could be prepared with the carboxymethylation of chitosan as some of the –OH groups and –NH₂ groups were substituted by –CH₂COOH groups. NOCMC was synthesized by the scaled down and slightly modified procedure reported earlier using monochloroacetic acid as the carboxymethylating agent in alkaline medium (Chen *et al.*, 2004, Anitha *et al.*, 2009). Shortly, 4 g of the chitosan powder was mixed with 40 ml of isopropyl alcohol and the resulting slurry was stirred in 250 ml two necked flask after fitting with water condenser maintained at 25°C for half an hour. To the stirred slurry 10.2 ml of 10 N aqueous NaOH solution was added in 6 equal portions at 4 minute intervals. The alkaline slurry was stirred for 45 minutes. Then 4.8g of solid monochloroacetic acid was added in five equal portions for a period of 25 minutes. Stirring was continued at 60° C for another 3 hours.

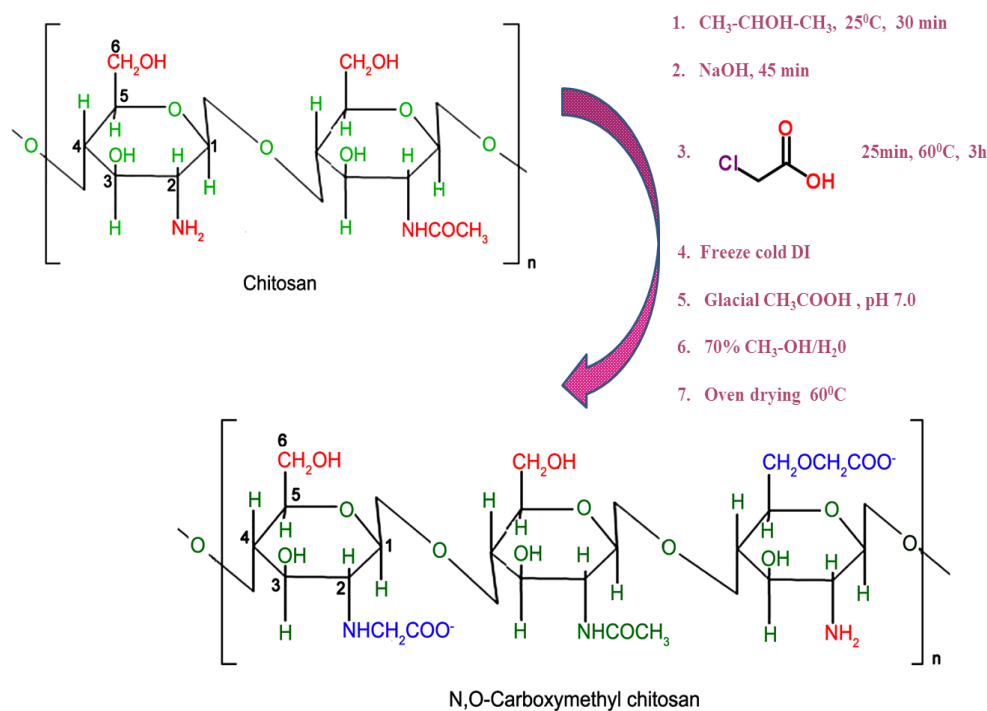


Figure 12: The schematic representation for the formation of N,O-carboxymethyl chitosan

3.4 ml of freeze cold distilled water was added to the mixture and adjusted its pH to 7.0 with glacial acetic acid. The reaction mixture was filtered and the solid product was added to 60 ml of 70% V/V methanol-water mixture in which it was stirred to wash the product. The mechanism involves; chitosan swelled with isopropanol while treating with NaOH leads to the formation of a Na-Chitosan complex; which on derivatisation with monochloroacetic acid yields NOCMC by adjusting the pH to neutral with glacial acetic acid (Ujang *et al.*, 2011). The washed product with light yellowish shade was filtered, collected and dried overnight in an oven at 60°C. The chemical reaction during the NOCMC synthesis is shown in Figure 12.

3.5.3 Characterisation of the synthesised NOCMC

The synthesised powder was casted in to a thin film and subjected to FTIR in transmission mode. IR Spectrum recorded as per the procedure described in section 3.1.4.1 was used to confirm the formation of phase pure NOCMC. Substitution of Carboxymethyl groups ($-\text{CH}_2\text{COO}^-$) on the amino ($-\text{NH}_2$) and primary hydroxyl ($-\text{OH}$) sites of the chitosan results to form the derivative N,O-carboxymethyl chitosan. NOCMC has been chosen as the wetting medium for the cement preparation as the $-\text{COOH}$ groups in them are amenable to metal chelation (Farang *et al.*, 2013), in the current context the potential for cross linking with the calcium ions in bassanite during the cement setting stage.

^1H NMR studies of the samples were carried out on an NMR spectrometer (Bruker Avance 500MHz NMR SPECTROMETER) using deuterium oxide (D_2O) as solvent at a concentration of 20 mg/ml.

3.5.4 Preparation of the cement

Different weight percentages of DHPD (1.5%, 2.5% and 3.5%) were added to the bassanite, which served as the powder part for the cement preparation. These formulations were selected as they showed considerable injectability (described in phase 2) and hence to find out how the cement properties change with gelling agent. The wetting medium has been prepared by dissolving NOCMC in three concentrations (0.60%, 0.30% and 0.15% (w/v)] in DD water. Different compositions (with sample code) as comprehended in the table 1 were prepared. The powder part and wetting medium were mixed, at the liquid to powder ratio (wetting ratio) of 0.6 ml/g, on a smooth glass plate. The wet mixture was kneaded well with a spatula to attain smooth paste like consistency. The following compositions were chosen based on the regularity of the paste up on mixing.

Sample code	Concn. of DHPD W/W w.r.t β -CSH	Concn. of N,O-CMC W/V% w.r.t DI
CS151	1.5	0.15
CS153	1.5	0.30
CS156	1.5	0.60
CS251	2.5	0.15
CS253	2.5	0.30
CS256	2.5	0.60
CS351	3.5	0.15
CS353	3.5	0.30
CS356	3.5	0.60

Table 1: Sample code of the set cement with preset additive compositions

3.5.5 Quantitative assay of the Injectability of the bone cement composition

The prime interest of the present study is to find out whether the gelling agent has enhanced the injectability of the bone cements. For the test, 3 g powder of each composition comprising bassanite and DHPD was taken on a glass plate, wetted with the corresponding NOCMC solution in the prescribed ratio, and made into a smooth paste within 2 minutes of wetting. After filling it in syringe and assembling the capillary rheometer, measurement and analysis were done with UTM as per the described procedure (section 3.2.4) with triplicate measurements for each sample.

3.5.6 Self setting times and compressive strength of the cement compositions

Setting times have to be well-defined for an injectable bone cement composition as the clinician must be aware of the time up to which he can deploy the cement mix without any detrimental effect on its properties. Self-setting time was measured following ISO 9917 and using a custom fabricated Vicat type apparatus (described in section 3.2.10).

ASTM standard specification F451-16 (ASTM F451-16, 2016) for acrylic bone cement has been adopted for the measurement of compressive strength as explained in section 3.2.10.

3.5.7 Characterizing the set cement composition

It is presumed that during cement formation, Ca^{2+} -NOCMC cross linking via chelation induce flow properties. To investigate this, FTIR spectrum of DHPD and NOCMC with β -CSH during the cement formation and to confirm the predicted Ca^{2+} -NOCMC cross linking via chelation, FTIR spectrum of DHPD, NOCMC, smCHDO and the modified compositions were taken and compared. CMC has been analysed as thin polymer sheet in transmission mode and all other compositions by

KBr pelletisation method in transmission mode. The sample was scanned in the range of 4000-400 cm^{-1} at a resolution of 2 cm^{-1} with the superimposition of 64 scans. The micro morphological analysis of the set cement specimens were done to get information which could be correlated to the mechanical property and injectability of the cement specimen. The fractured surfaces of cement specimens were pasted on copper stubs, sputter coated with gold and scanned in FEI QUANTA 200 Environmental Scanning Electron Microscope.

3.5.8 Invitro degradation study in phosphate buffered saline

The degradation study was conducted by incubating the cement specimens CS251 and CS253 in PBS (w/v ratio 0.2mg/ml) at 37°C for 10 weeks by refreshing the medium at alternate days. The tests were conducted as per the method suggested in section 3.3.2.

3.5.9 In vitro bioactivity of the material

The sample CS253 was selected for the study as it contains higher concentration of gelling agent among the optimised cements. Cement disc of dimension 15 mm diameter and 3.5 mm height after setting for 24 hours was soaked in SBF in 50 ml vials at 37°C with surface area to volume ratio 10 and further experiments were conducted as per protocol in section 3.3.3. BioCaS samples were used as control for comparison of the rate of biomineralisation. The top surface after immersion period was phase characterized by XRD and the surface morphologies were analysed by ESEM. EDS was used to analyse the elemental composition of the surface layer formed. FTIR analysis was done to confirm the possibility of formation of apatite layer. The pH changes and the change in the concentration of Ca, P, and Ca/P ratio

at each time point were monitored to get more detailed overview of the apatite layer formation (Oudadesse *et al.*, 2011).

3.5.10 In vitro biocompatibility evaluation of the optimised composition

Cylindrical specimens (6 mm diameter × 12 mm height) of the test materials CS 153, CS 251 and CS 253, 6 each with surface area 2.826 cm² were used for the *in vitro* cell culture cytotoxicity using test on extract method based on ISO 10993-5, 2009 (ISO 10993-5, 2009). The test was further conducted by the same protocol described in section 3.3.5.1. MTT assay was conducted for the quantitative analysis of the metabolic activity of cells. The protocol followed was described elsewhere (see section 3.3.5.1 ii).

In vitro hemocompatibility assay [ISO 10993-4:2012 (E)] was conducted to analyse the hemolytic potential of the material. Among the two optimised compositions CS253 contains the highest concentration of the additive DHPD and the gelling agent NOCMC and hence selected. Human blood was collected (following ethical practices) into the anticoagulant acid-citrate-dextrose solution. The testing protocols and the principles followed were explained in section 3.3.5.2.

3.5.11 Cell adhesion study using human osteosarcoma cells by ESEM

HOS, a cell line of osteosarcoma that exhibits various osteoblastic characteristics were purchased from NCCS, Pune. Cell adhesion study was performed for test samples CSC and CS253 to realize the potential of the test material to act as a scaffold for the cells to adhere and spread. HOS cells were retained in minimum essential medium supplemented with 10% fetal bovine serum, 7.5% sodium bicarbonate, 3% L-glutamine, and 1% penicillin/streptomycin antibiotic (Sigma-Aldrich) incubated at 37°C in 5% CO₂ atm. After sub-culturing using 0.25 % trypsin

EDTA, control glass cover slip and test sample disc of unit surface area (cm^2) were seeded with HOS cells ($\approx 1 \times 10^4$ cells/ cm^2) and incubated at $37 \pm 1^\circ\text{C}$ under humidified atmosphere comprising 5% CO_2 for 48 h. Samples incubated in medium were considered as sample control. After the incubation period cell seeded coverslip and test materials were washed with PBS, fixed in 1% glutaraldehyde in Sorensen phosphate buffer for 24 hours and dehydrated in a graded ethanol series. The morphology of adhered and attached HOS cells on the device was visualized by Scanning Electron Microscopy.

3.5.12 Cell viability study by live/dead assay

Furthermore viability of human osteosarcoma (HOS, a cell line of osteosarcoma that demonstrates various osteoblastic characteristics) cells on the surface of the material was confirmed via live/dead assay. Cells were examined under a fluorescence microscope (Leica DMIL 6000 E, with I3/N21 filter cubes) as per protocol described in section 3.3.5.1 (iii).

CHAPTER 4

RESULTS

PHASE I

4.1 Synthesis and characterization of low dimensional calcium sulfate (gypsum) for the injectable bone cement formulations

4.1.1 Phase and chemical bonding analysis of the synthesised powder

It was observed during the synthesis procedure that instantaneous precipitation occurs when sulfuric acid is added drop-wise into calcium nitrate solution with 2-propanol, in the reactor. The XRD of the dried precipitate is shown in Figure 13 in which all the major peaks match with the reported standard peaks of gypsum (ICDD 21-0816).

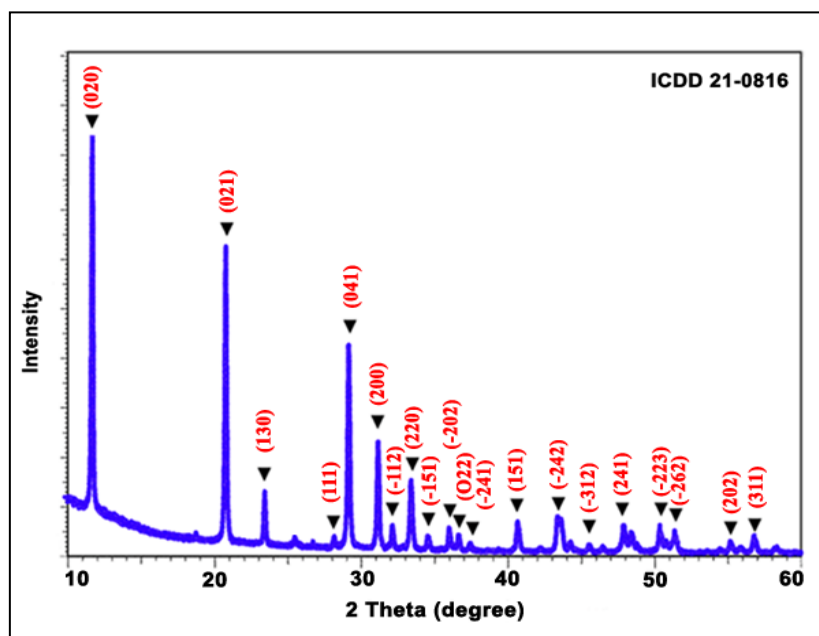


Figure 13: X-Ray diffraction pattern of the precipitate obtained in 2-propanol. Peak positions of standard gypsum (ICDD 21-0816) are given.

The FTIR spectrum of the precipitate obtained in transmission mode by KBr pelletisation method is given in Figure 14. The spectrum contains all the typical absorptions corresponding to gypsum. The band in between 1100–1300 cm^{-1} (with peak at 1120 cm^{-1}) corresponds to S-O asymmetric stretch (ν_3) and the peaks at 463, 601 and 669 cm^{-1} correspond to SO_4 antisymmetric bending vibrations (ν_4) of the sulfate tetrahedron. First overtones of asymmetric stretching vibration ($2\nu_3$) of SO_4 and binary combination band of two internal fundamentals ($\nu_1+\nu_3$) of SO_4 are present as shallow absorptions around 2238 and 2116 cm^{-1} . The ν_1 bending mode of H_2O gives a peak at 3406 cm^{-1} and the ν_3 mode could be seen at 3492 and 3550 cm^{-1} . An additional ν_2 bend of H_2O could be observed at 3243 cm^{-1} . The in-plane deformation vibrations of OH..O groups manifest as doublet at 1621 [$\nu_2(\text{Bu})$] and 1686 cm^{-1} [$\nu_2(\text{Au})$], attributes to two crystallographically distinct species of water.

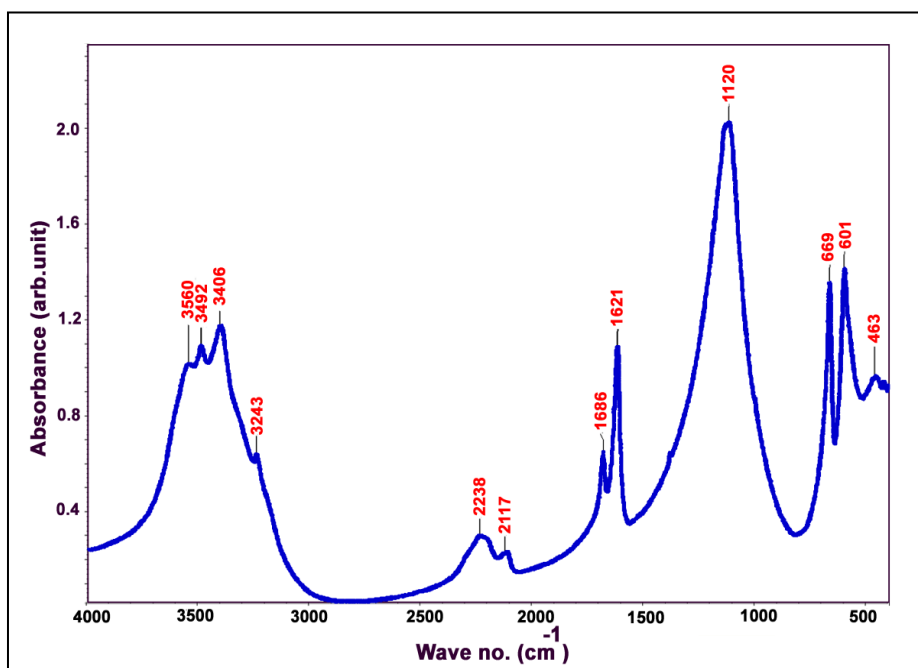


Figure 14: FTIR spectrum of the precipitated powder. All the major absorption band corresponds to that of gypsum

The lower frequency and high intense peak at 1621cm^{-1} is due to the H_2O linked with SO_4^{2-} by hydrogen bonding and the other indicates water linked to Ca^{2+} ions. The above results confirm the precipitate to be phase pure form of calcium sulfate dihydrate (gypsum) (Gupta *et al.*, 2016). Co-existence of hemihydrate and anhydrite phases often reported during the synthesis of gypsum involving sulfuric acid reactants (Song et al., 2011). The present system is capable of producing the phase pure material.

4.1.2. Micromorphology of the synthesised gypsum (smCSD)-ESEM analysis

The micromorphology of the smCSD could be seen in Figure 15. There is no significant morphological variation and monomodal distribution of particles with rods of dimension $< 10\ \mu\text{m}$ length and $< 1\ \mu\text{m}$ width were obtained.

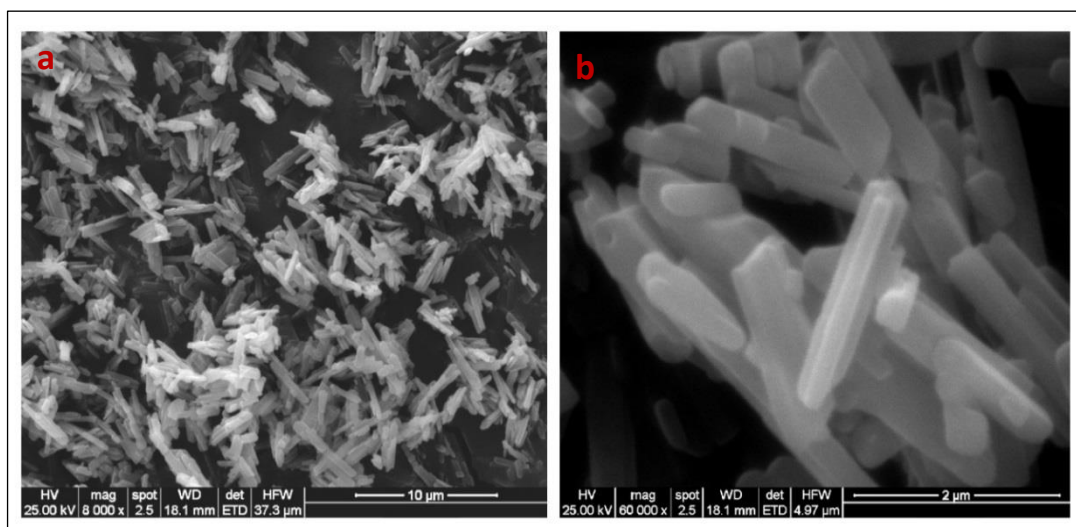


Figure 15: SEM image showing the micromorphology of the synthesised submicron dimensional particles of a) gypsum revealing monomodal low dimensional particle size distribution b) magnified view

The image of the precipitate synthesised adopting the conventional precipitation method in chemical systems $\text{CaCl}_2\text{-H}_2\text{SO}_4$ (Song et al., 2011), $\text{Ca}(\text{NO}_3)_2\text{-Na}_2\text{SO}_4$ (Rees et al., 1999), $\text{Ca}(\text{NO}_3)_2\text{-H}_2\text{SO}_4$ is given in Figure 16(a-c) for

comparison, wherein the sizes and shapes vary drastically. Needles in the range of 20 to 30 μm length were observed along with large sheet structures measuring 50 μm \times 50 μm or above with flower-like aggregates of dimension greater than 100 μm diameter. Also solvent exchange method for the retraction of precipitate with organic solvent from very dilute aqueous solution (1g/l dissolved by heating) of commercial gypsum at varied temperature concentration were tried and precipitated uniform submicron dimensional whiskers or wires but exempted the method due to unfeasibility and very low production yield and the micromorphology of which has been shown in Figure 16d.

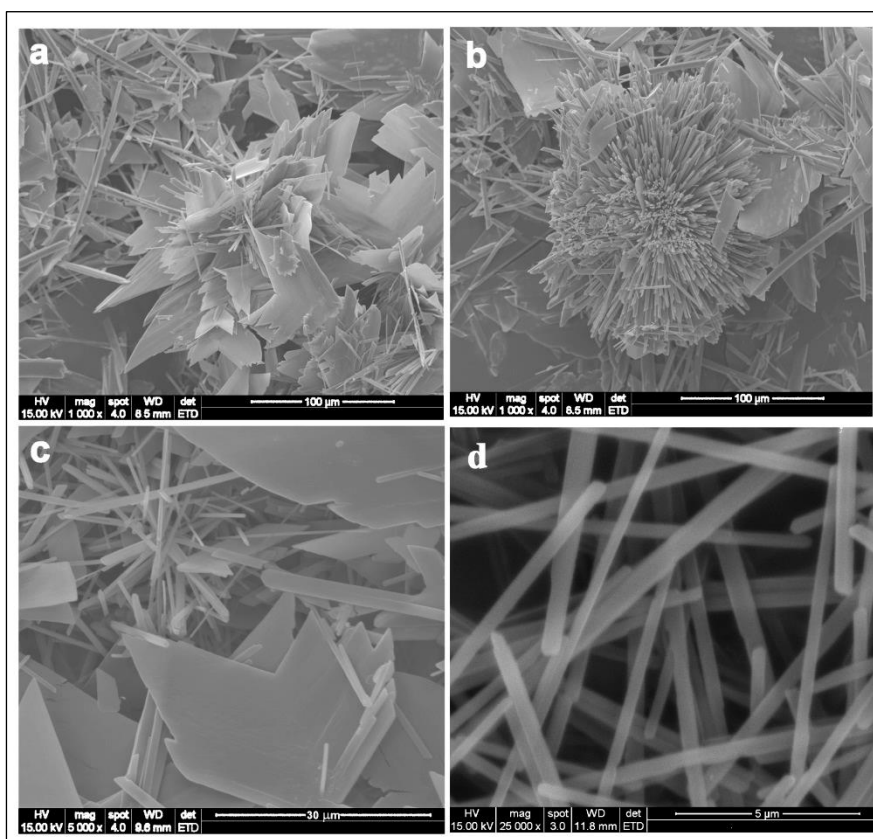


Figure 16: SEM image a) - c) of gypsum particles formed adopting the same reaction parameters in a) $\text{CaCl}_2\text{-H}_2\text{SO}_4$ b) $\text{Ca}(\text{NO}_3)_2\text{-Na}_2\text{SO}_4$ c) $\text{Ca}(\text{NO}_3)_2\text{-H}_2\text{SO}_4$ chemical systems in aqueous medium respectively d) Particles obtained in solvent exchange technique.

However the morphological analysis indicates that the presence of medium with low dielectric constant compared to water has influenced the crystal sizes and uniformity. The significance is discussed in the later section in nucleation kinetics.

4.1.3 Particle size of the synthesised gypsum through transmission electron microscopy (TEM)

As per the bright-field TEM micrograph and the magnified view of the synthesised particles shown in Figure 17 (a) & (b), the length and width of the individual rods were confirmed to be in the range of 3-5 μm and < 500 nm respectively.

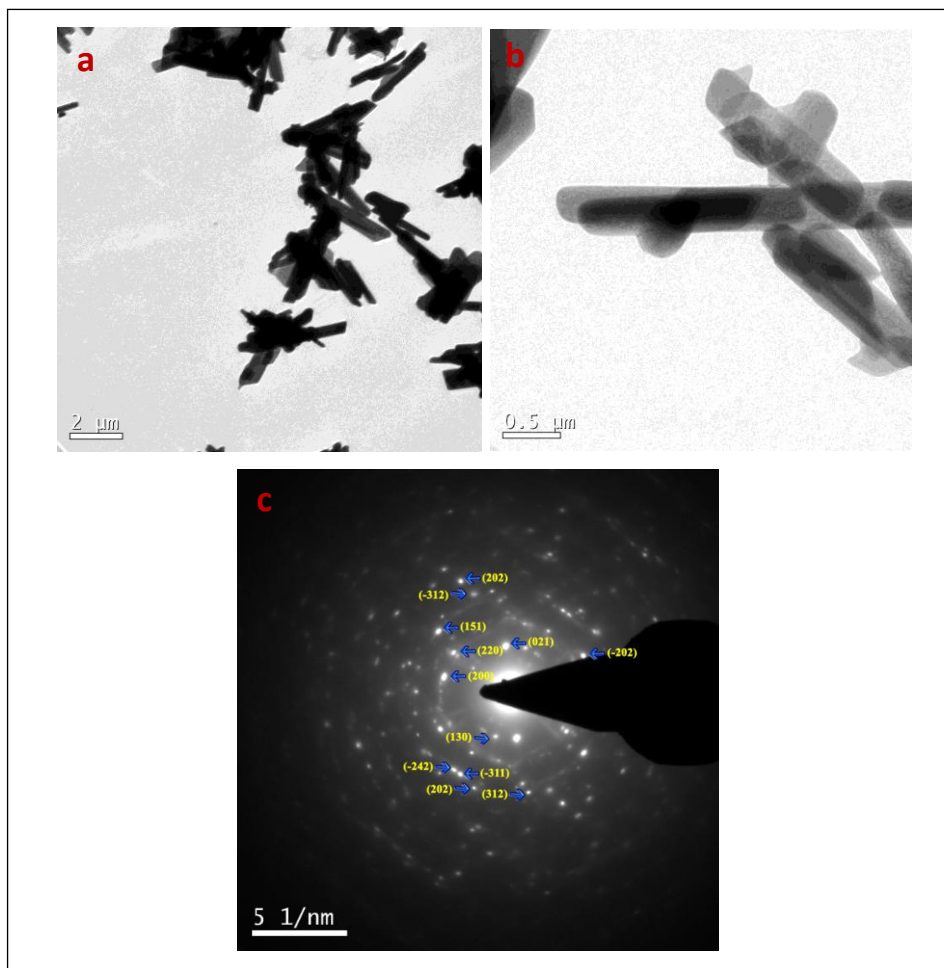


Figure 17: a) Bright field TEM image and b) the magnified view of the precipitate revealing uniform rod-like submicron particles (c) Corresponding electron diffraction pattern confirming all the major reflection attributed to phase pure gypsum.

Selected area electron diffraction pattern (SAED) of the single crystal displays diffraction spots (Figure 5c) and the calculated d values that all can be indexed to that obtained in the XRD pattern. TEM and SEM images together show uniform population of rod-like submicron particles which were further confirmed to be phase pure gypsum by means of both XRD and SAED.

4.1.4. Regulation of parameters for the new chemical system

Relative polarity values of the organic reaction medium selected for the synthesis with respect to water increases in the order H_2O (1.000) > CH_3OH (0.762) > $\text{CH}_3\text{-CH}_2\text{-OH}$ (0.654) > $\text{CH}_3\text{-CHOH-CH}_3$ (0.546) > $\text{CH}_3\text{-CO-CH}_3$ (0.355) > ether (0.117) (Reichardt *et al.*, 2003). The shape of the particle changed from nonuniform flaky to uniform needle with reduction in particle size while decreasing the polarity or dielectric constant of the reaction medium Figure 18(a-e).

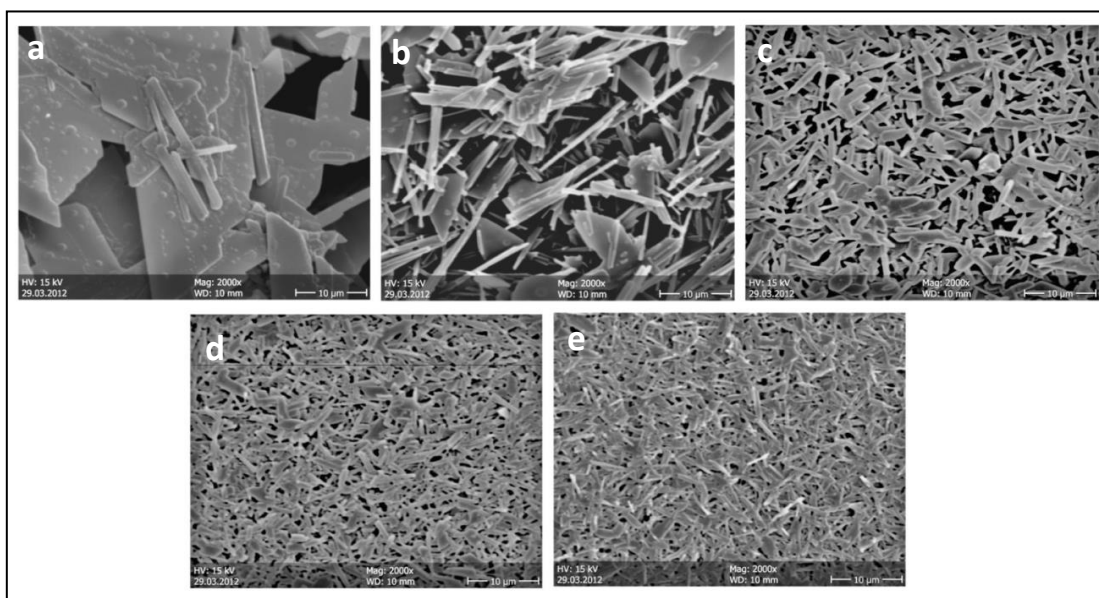


Figure 18: Micromorphology of the low dimensional gypsum synthesised in different reaction medium a) water b) Methanol c) Ethanol d) 2-propanol and e) Acetone showing the successive gradation in particle size

Highly uniform thin rod shaped particle sizes were obtained in acetone. The synthesis was not possible when the relative polarity of the medium becomes very low as in ether in which $\text{Ca}(\text{NO}_3)_2 \cdot 4\text{H}_2\text{O}$ gets precipitated and excluded.

The evaporation rate of the solvent affects the particle size distribution and hitherto preferred solvents with low vapour pressure which also provide a wider window for optimization of other parameters (Rietveld et al., 2006). The boiling point of the solvents decreases in the order H_2O (373K) > CH_3OH (337.6 K) > $\text{CH}_3\text{-CH}_2\text{-OH}$ (351.5 K) > $\text{CH}_3\text{-CHOH-CH}_3$ (355.4 K) > $\text{CH}_3\text{-CO-CH}_3$ (329.2 K). Considering the low evaporation rate of 2-propanol medium with respect to acetone due to intermolecular hydrogen bonding, former has been selected for further optimisation.

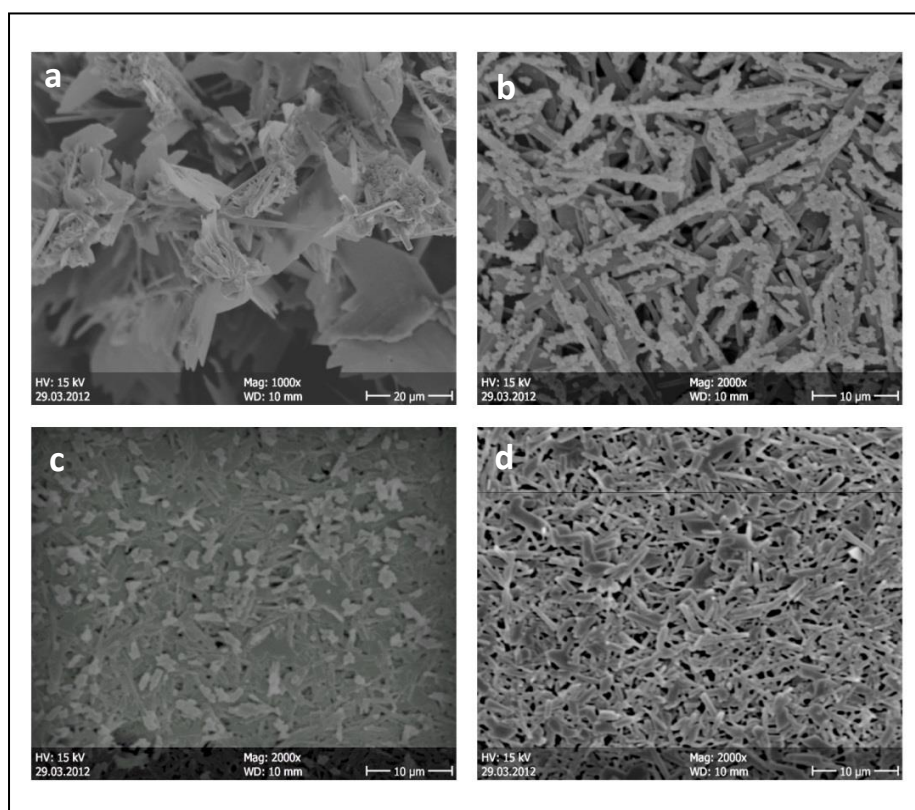


Figure 19: SEM images of the synthesised gypsum with concentration of 2-propanol in reaction medium a) 1:9 b) 1:3 c) 2:3 and d) 1:1 (v/v) [20%, 50%, 80% and 100% respectively as solvent of $\text{Ca}(\text{NO}_3)_2 \cdot 4\text{H}_2\text{O}$] showing the controlled morphology towards the higher concentration and low polar ends.

Towards low dielectric constant end, polymodal particle size distribution including flakes, rods, sheets, needles and granules with irregular growth features could be observed as shown in Figure 19. Hence the maximum concentration possible to get narrow size distribution with thin rod like morphology was found to be 1:1 above which the reverse trend was found. It is also observed that, towards high dielectric constant end, the longer will be the onset of precipitation. It is clear that the presence of 2-propanol brings down the equilibrium concentration of the calcium sulfate with respect to Ca^{2+} ions in $\text{Ca}(\text{NO}_3)_2$ -2-propanol and SO_4^{2-} ions in H_2SO_4 such that the ionic product exceeds the solubility product even at low concentrations, making it supersaturated.

4.1.5 Validating the chemical system with the solubility parameter

The solubility of the synthesised gypsum, based on the weight of the dissolved Ca^{2+} in centrifuged supernatant with respect to change in reaction media after the completion of the reaction, were quantified in Figure 20(a). The considerable reduction in solubility (2.9 times) was found when medium with high dielectric constant, H_2O changed to that containing organic media with low dielectric constant, CH_3OH which contributes to the final yield. Eventhough gradation in solubility is small with decreasing polarity in organic solvents, the difference in values were found to be statistically significant as per anova single factor and student's t test ($p < 0.05$). In short the reaction medium with low solvent polarity or dielectric constant controlled the particle size of precipitating gypsum to get monomodal distribution and reduced the solubility.

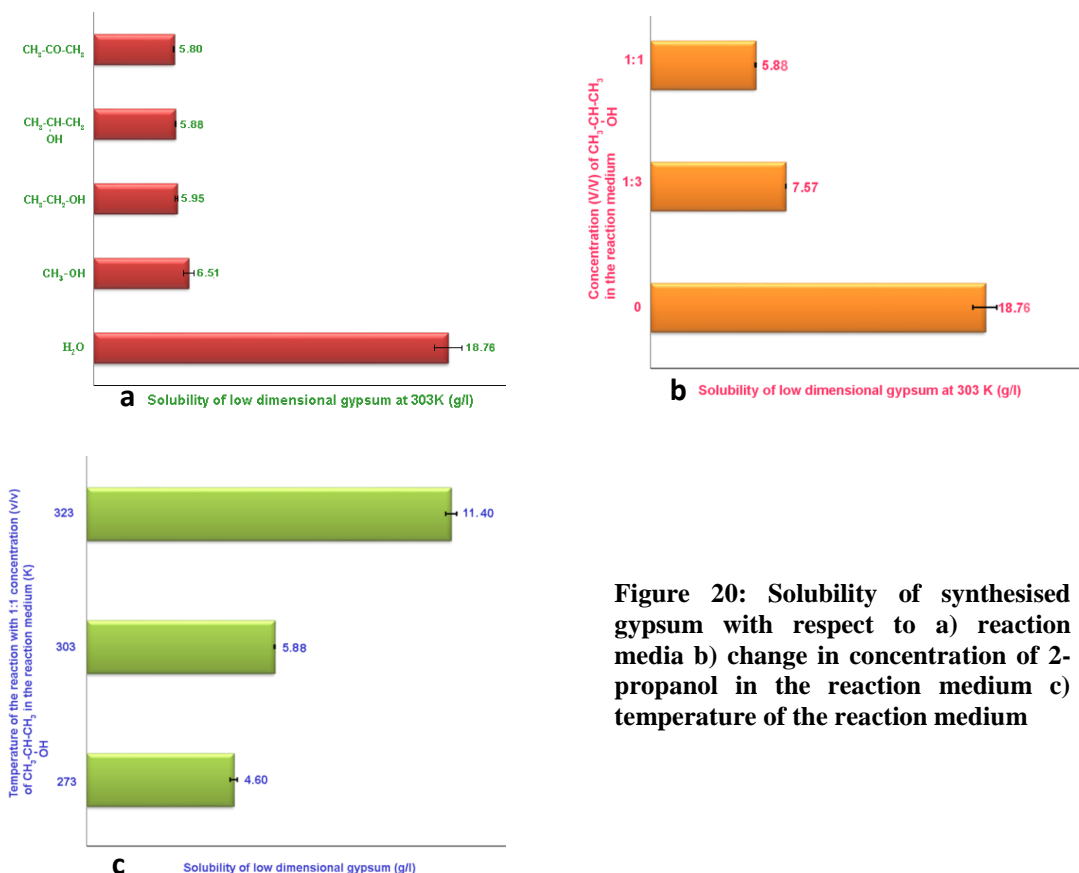


Figure 20: Solubility of synthesised gypsum with respect to a) reaction media b) change in concentration of 2-propanol in the reaction medium c) temperature of the reaction medium

However minimising the rate of evaporation withholding the possibility to create polarity gradient in the reaction medium ensures homogeneity of the precipitating particle during the large scale synthesis and hence opted 2-propanol.

Solubility of the gypsum is found out to be 2.5 times lower when imparted 2-propanol in the reaction medium in 1:3 ratio. This could further be reduced to 1.3 times by changing the concentration to 1:1, which is the maximum concentration possible to apply in the system (Figure 20(b)).

Estimated solubility of the gypsum in the filtrate when temperature of the reacting system increased (Figure 20(c)) by 20K from 303K was found to be approximately twice and reduced 1.2 times when declined the temperature by 20K. The high temperature reaction was found out to give polymodal particle size

distribution, may be owing to the creation of polarity gradient on the surface of reaction interface due to the high evaporation rate. Yet there were no significant micromorphological variation observed at the lower two temperatures. Hence considering the feasibility of the reaction the temperature of the reaction was selected as 303K.

4.1.6 BET specific surface area analysis of the synthesised gypsum

Slope (s) and Y-intercept (i) obtained from the BET plot of $1/Q((P_0/P)-1)$ against P/P_0 as shown in Figure 21 were $0.33 \pm 0.04 \text{ g/cm}^3$ and $0.0058 \pm 0.0002 \text{ g/cm}^3$ at STP. The quantity of gas absorbed (W_m) equal to $(1/s+i)$ was found to be $2.95 \text{ cm}^3/\text{g}$. Total surface area (ST) calculated from W_m by equation $S = [W_m N_A / M]$, where N - Avogadro no., A - molecular cross sectional area of N_2 [0.1620 nm^2] was 3.52 m^2 . Hence BET specific surface area, the ratio of the total surface area to sample weight, was obtained as $12.85 \text{ m}^2/\text{g}$.

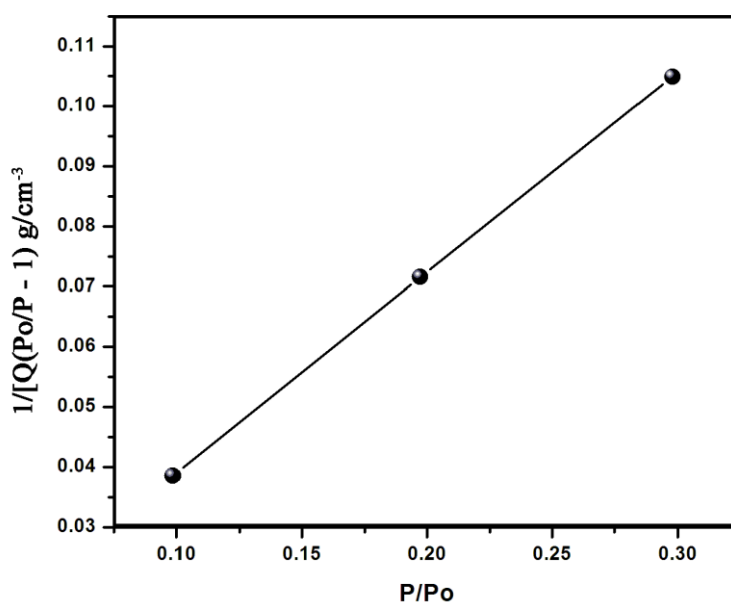


Figure 21: BET plot for the surface area analysis of the synthesised gypsum powder

4.1.7 Heavy metal screening for the synthesised gypsum

Any biomaterial for implantation in the human body should not contain toxic heavy metals above a stipulated quantity. The levels of arsenic, cadmium, mercury and lead are regulated by international standards. From the OES-ICP analysis (Figure 22), the quantity of arsenic and mercury were found out to be 6.44 ppm and 0.60 ppm respectively while cadmium and lead were below the detectable limit or absent.

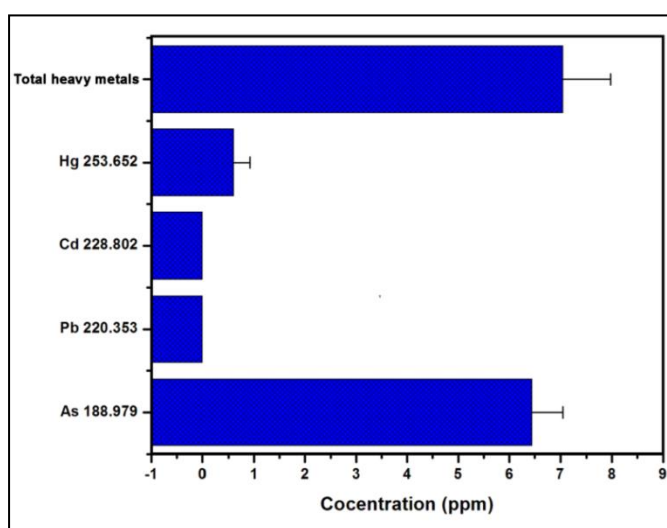


Figure 22: Trace elemental analysis data of the synthesised low dimensional gypsum by OES-ICP method

The total heavy metal content in the gypsum were found out to be 7.0491 ± 0.921 ppm only and when phase converted to bassanite at 393K total mass will be reduced by 16.21% but the quantities of the trace elements present in the dihydrate are not affected. So the concentration of trace elements in bassanite gets increased to 16.21% ie. 8.19 ppm due to the loss of 16.21 weight percentage which is also well within the limit (<10 ppm) and hence conform to the ASTM standard specification F2224-09 for medical grade quality

4.1.8 *In vitro* tests for cytotoxicity

Images of the L929 mouse fibroblast cells after the cell culture cytotoxicity test are shown in Figure 23. The negative control (extract of high-density polyethylene in

saline) and reagent control did not affect the cell morphology (grade 0) and the positive control (phenol and culture medium) caused severe damage to the cells (grade 4). Gypsum sample extract in physiological saline at 50% dilution did not cause lysis of cells or reduction in cell growth. Discrete intracytoplasmatic granules were seen, at a grade value less than 2. The material, therefore, could be considered to be non-cytotoxic.

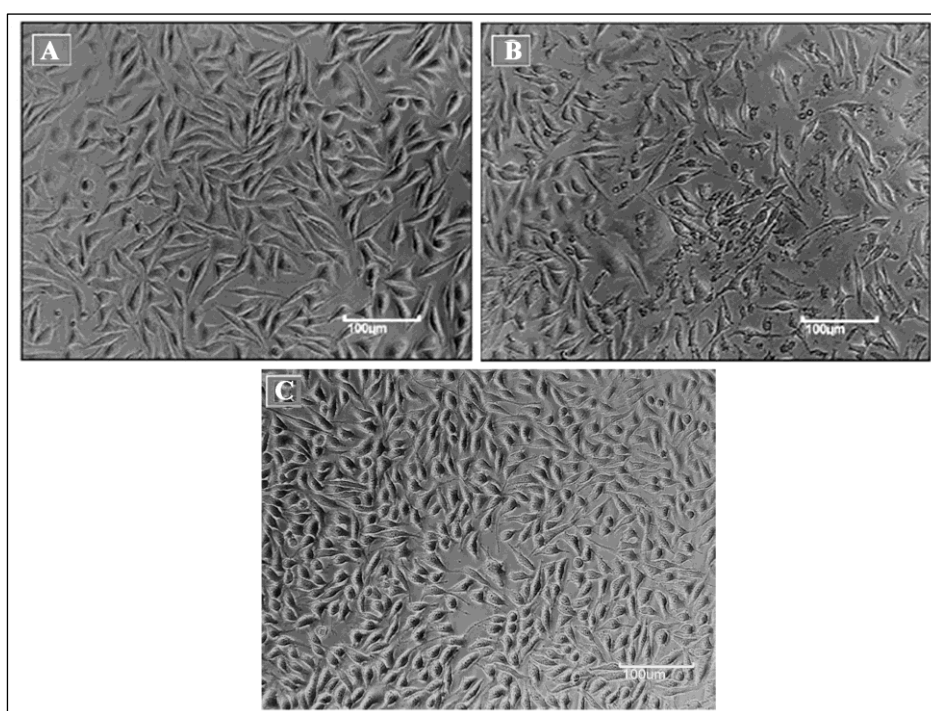


Figure 23: L929 cells after incubating with A) negative control B) positive control and C) 50% extract of submicron dimensional gypsum

The outcomes of the MTT assay are shown in Figure 24, wherein the metabolic activity values are expressed as mean \pm SD, with n=6. All the gypsum extracts showed greater than 82% metabolic activity directly related to metabolically active cell viability. The cytotoxic limit is 70% metabolic activity, hence the synthesised powder could be considered as cell compatible. According to ANOVA

single factor analysis there is no statistically significant difference in values as $p > 0.05$ for different dilutions of the physiological saline extract in MEM2X medium.

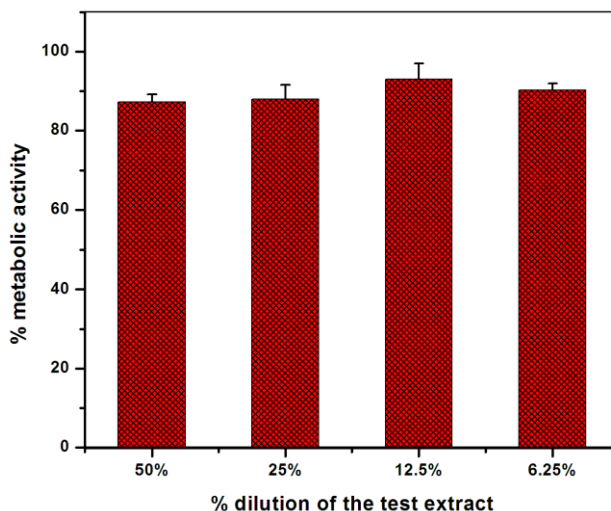


Figure 24: MTT assay for the metabolic activity of viable cells. Percentage metabolic activities at different dilutions of the test extract are expressed as mean \pm SD (n=6) and are normalized against the activity of the control.

4.1.9 Nucleation kinetics parameters and synthesis of gypsum nanoparticles in the chemical system

4.1.9.1 Induction time measurement by turbidimetry

The method of determining the induction time and the variation of induction time with concentrations are given in the graphs in Figure 25 (a, b and c). The progressive values of UV absorbance (at 340nm wavelength) of the reacting solutions starting from the time of mixing, could be found in Figure 25 (a). Initially, the graph will have a low slope region till the onset of precipitation of particles, and then it progresses to a region with high slope corresponding to opacity due to thick precipitate. The point of time at which the two slopes meet is taken as the induction time (as described in section 3.1.9.1). The induction time measurement at various concentrations of the reactants in the range 1.19 mM to 2.70 mM at constant

temperature 303 K are shown in Figure 25 (b). The graph Figure 25 (b) shows that the induction time decreases with the increase in concentration of the reactants. There is a minimum value of concentration at which the particle formation ceases to occur. This value corresponds to the *equilibrium concentration*, which could be determined through the extrapolation of the graph.

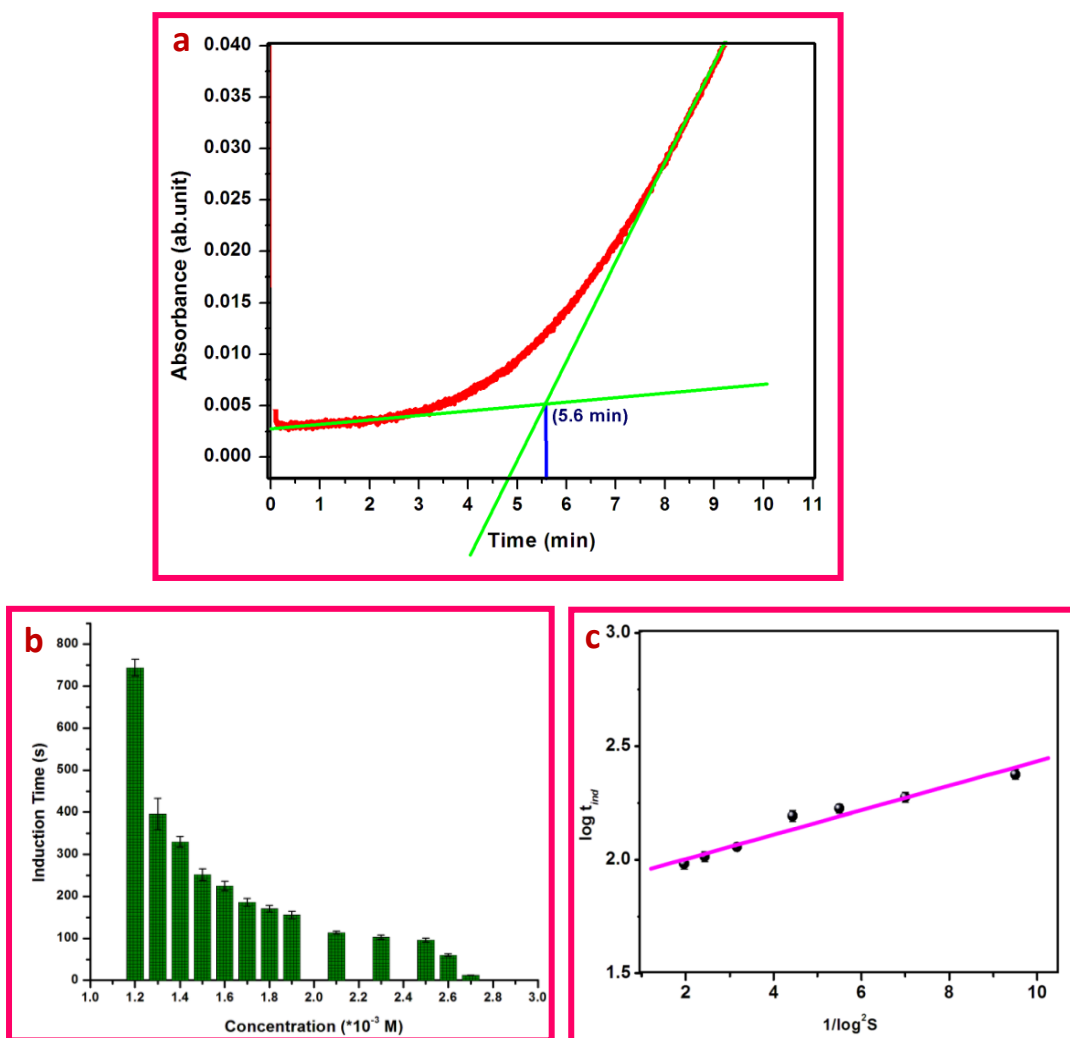


Figure 25: a) Representative graph demonstrating the finding of induction time induction time for the crystallization of the gypsum from the absorption kinetics b) Variation of t_{ind} with molar concentration of each of the independent reactant in the corresponding solvent (c) Relation between $\log t_{ind}$ and inverse square of \log supersaturation ratio.

The equilibrium concentration of the calcium and sulfate ions in the bulk medium at which the induction time becomes infinity is determined to be 0.55×10^{-3} M. This value is used to calculate the supersaturation ratio at each concentration in the reaction medium, as per equation (19). At the high concentration end, the induction time was observed to decrease very fast after the concentration 2.50 mM. Beyond 2.70 mM, it was not possible to determine the induction time owing to the instantaneous formation of the precipitate.

4.1.9.2. Determining the interfacial tension or surface free energy

The $\log t_{\text{ind}}$ against $1/\log^2 S$ graph, as represented in Figure 25(c), follows a linear trend (with correlation coefficient 0.9525), but only in the range of supersaturation 2.12 to 5.16. A straight line was fitted using spreadsheet software which gave the slope of 0.0507 and a Y-intercept of 1.9118. According to equation (20) the Y-intercept corresponds to the dimensionless constant A and the slope corresponds to B/T^3 . The value of the constant B was calculated to be 1.4104×10^6 , with the help of eq. (21).

The interfacial tension γ (or the surface energy between the growing gypsum crystals and solvent) is the crucial parameter for understanding the rate of nucleation and critical radius size at each supersaturation. On substituting the value of B obtained from figure 26 in equation 22, the value of γ for the system is obtained as 5.6 mJ/m^2 . This value is comparatively lower than those reported for the formation of gypsum from aqueous based systems (described in discussion, part 5.1.2).

4.1.9.3 Determining the nucleation rates and critical size

The nucleation rates were calculated for different supersaturation ratios from 1.39 to 6.02, by substituting the surface free energy value in eq. (23). The graphical

representation of the variation of nucleation rate with supersaturation ratio is given in Figure 26 (a). The nucleation rate increases exponentially with the supersaturation ratio. When the supersaturation ratio varies from 1.39 to 6.02, the nucleation rate changes from 3.98×10^{27} to 8.6×10^{29} nuclei/cm³s.

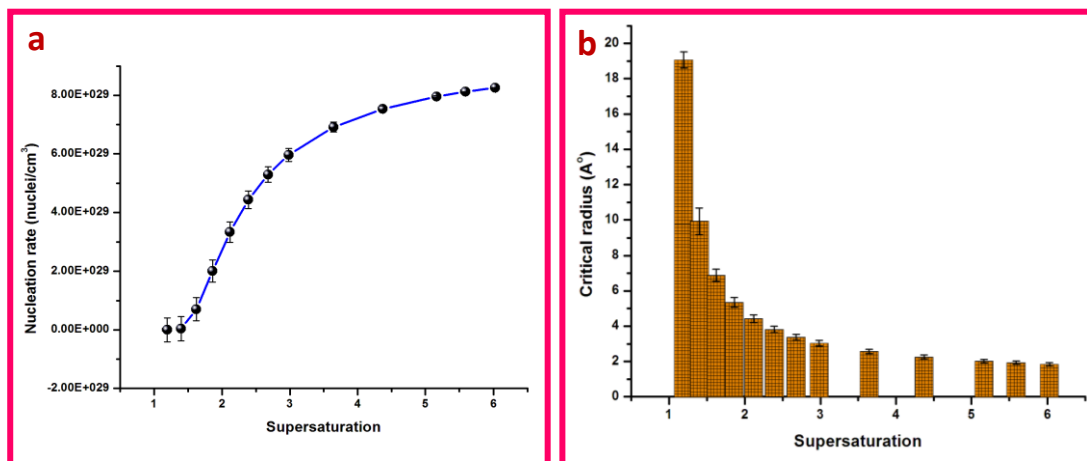


Figure 26: Variation of a) nucleation rate and b) critical radius size with supersaturation ratio

A low nucleation rate implies comparatively higher size of the nuclei, as they get chance to grow utilizing the available concentration of the reactants with the available surface free energy and viceversa (El-shall *et al.*, 2002). Calculations using equation (25) supported this assumption. The variation of the critical radius of the nuclei at various supersaturation values is given in Figure 26(b). The critical radius decreases with the increase in supersaturation ratio. In the supersaturation range 1.19 to 6.02, the radius decreased from 19.1 Å to 1.8 Å. It is notable that the lowest value is one order lower than the unit cell dimensions of gypsum. This ambiguity may be due to the limitations of the classical nucleation theory (CNT). It has been demonstrated that CNT under-predicts the critical nucleus size by at least a factor of two at moderate supersaturations (Horsch *et al.*, 2008)

4.1.9.4 Particle size analysis of the nano gypsum

The particle size analysis was done for the supersaturation ratio 2.12, for which the observed induction time is 3.75 min. The non-ionic surfactant nonidot-P40 was added in the mixed solutions before this period to arrest further growth. The result of the DLS analysis of the solution is given in Figure 27. The particle size distribution by volume showed monomodal dispersity. The curve has a peak at 8.2 nm (Z-average = 11.74 nm) and a width of 2 nm, which is attributed to 100% volume of particles. The cumulants analysis gave an z-average value of 11.74 nm with a poly dispersive index of 0.290.

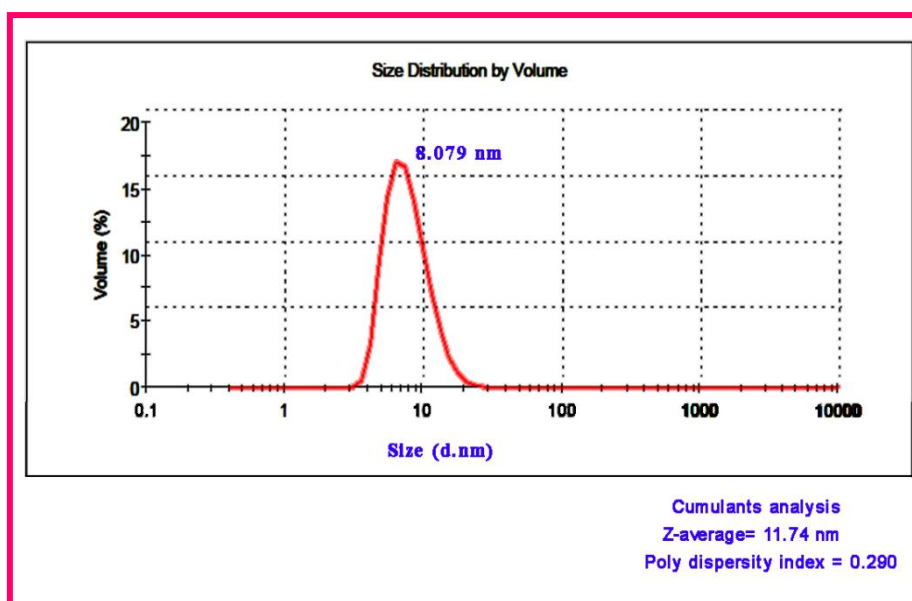


Figure 27: Particle size distribution obtained in dynamic light scattering for the supersaturation ratio 2.12

The particles formed in the same solution were subjected to TEM analysis. The general appearance was as agglomerated material. Most of the parts are hazy as obtained for other workers (Osterwalder et al., 2007). Individual particles were seen in the size range around 10 nm (Figure 28). This corresponds well with the DLS particle size measurement.

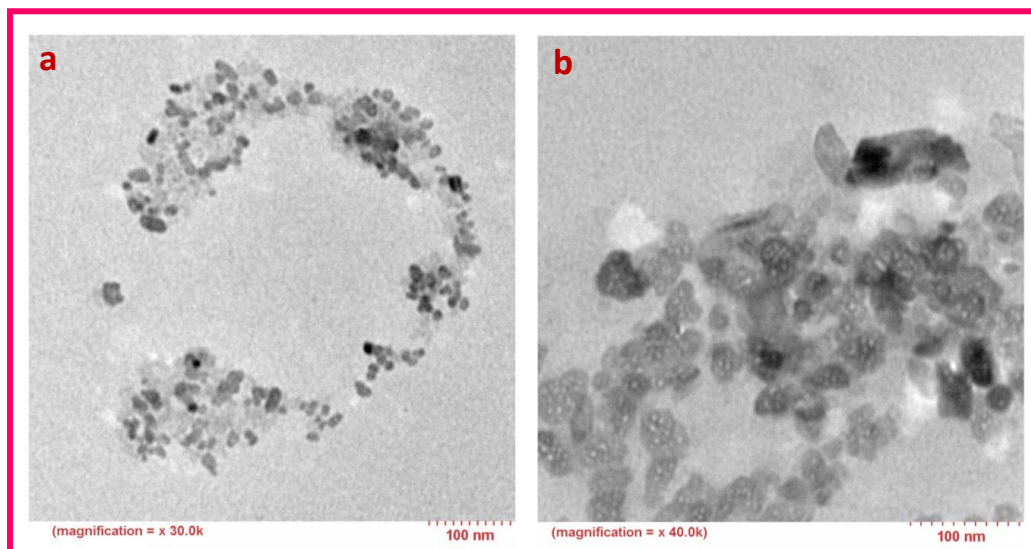


Figure 28: TEM images of the particles formed at the supersaturation ratio 2.15 in presence of surfactant, taken at 80 kV. Regions of agglomeration could be seen in Picture A (X30,000). Magnified view of the particles are shown in Picture B (X40,000)

PHASE II

4.2. Design development of injectable bioactive bone filler cement

4.2.1 Thermal conversion of phase of the synthesised gypsum (smCSD)

Simultaneous TG-DTA analysis gave the weight and enthalpy changes occurring as a function of temperature during the calcination of gypsum as shown in Figure 29. From the thermogram, major loss in weight % ($\approx 11\text{g}$) of gypsum occurs in between 375 and 408 K as shown in Figure 29(a) which corresponds to the substantial loss of water of crystallization from gypsum. Differential thermogram (Figure 29 (b)) showed two successive endothermic peaks; a strong and sharp peak at 393.5 K and a feeble broad peak at 467.95 K (corresponding to the weight loss 16.12 and 21.96 wt% respectively from gypsum), followed by a less distinguished exothermic peak 613 K (analogous to 23.44 wt% loss). The results could be better explained in combination with XRD analysis (Figure 30).

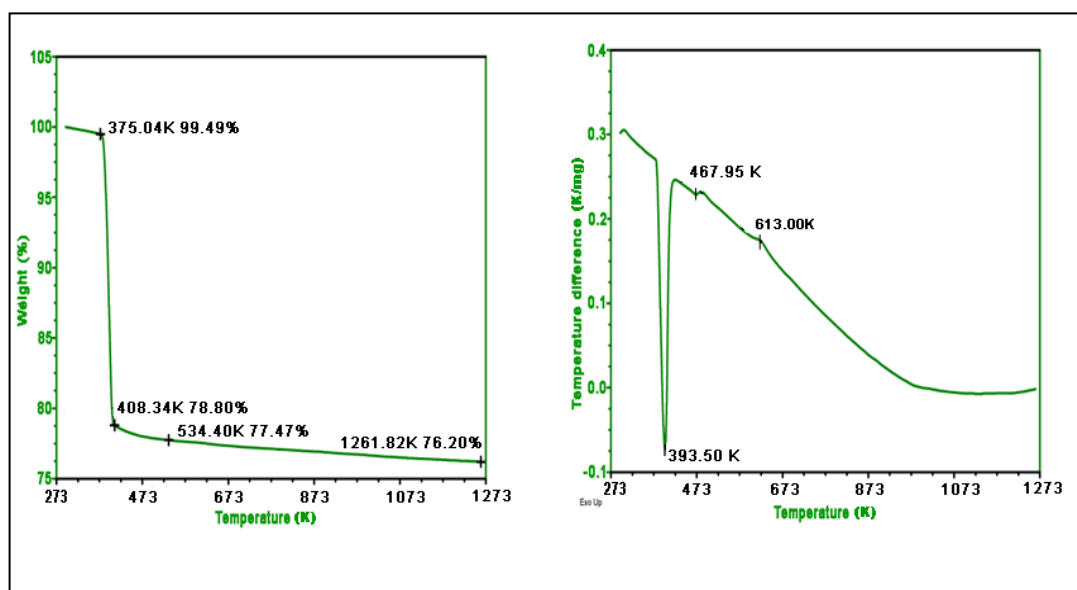


Figure 29 : Simultaneous TG/DTA thermograms of smCSD showing the weight loss and transition temperature for the phase conversion.

The peak positions of XRD patterns of the samples were corrected with respect to the peak positions of reference standard corundum (Al_2O_3). All the major peak positions in XRD pattern up to 368 K best matches with monoclinic gypsum as per the ICDD data card no. 21-0816. The co-existence of the peaks of XRD pattern ICDD 74-2787 with 21-0816, could be observed from 373K onwards attributed to the formation of bassanite (Monoclinic, space group I2) indicating the loss of water of crystallization. At 383 K, the peak due to (0 2 0) plane in gypsum got diminished. The complete phase conversion to bassanite was found at 393K since all the major peak positions matched best with ICDD74-2787.

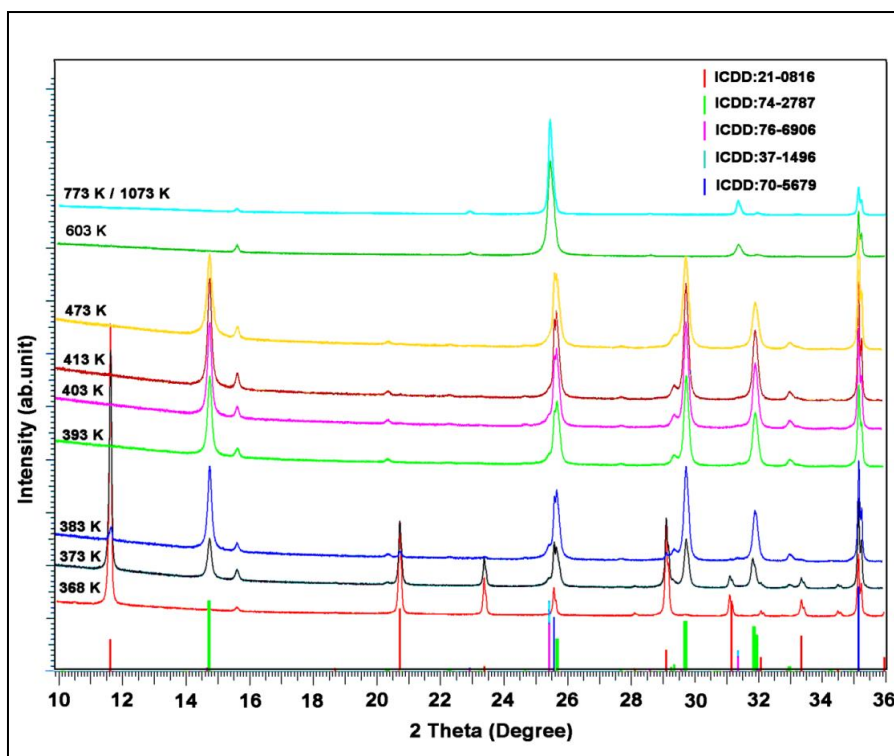


Figure 30: Stacked XRD patterns of the smCSD at different calcination temperatures. The standard patterns with respect to ICDD data card numbers for gypsum (21-0816), Bassanite (74-2787), hexagonal anhydrite (76-6906) and orthorhombic anhydrite (37-1496) are marked along with the internal reference standard corundum (70-5679).

XRD data of 613 K sample shows the formation of insoluble anhydrite (CaSO_4 , AIII) which is the thermodynamically stable orthorhombic form [ICDD:37-1496]. This

conclusion is further ensued by the exothermic peak in DTA. No distinct phase of γ or soluble anhydrite, (CaSO_4 , AII) was found. The exothermicity arises due to the rearrangement of hexagonal anhydrite crystals to orthorhombic anhydrite. However the exact temperature range for the existence of γ -anhydrite couldn't be refined from XRD as the peak positions [ICDD:76-6906, Space group P6222] overlap with orthorhombic anhydrite. However the formation temperature could be from 467.95K in accordance with second endothermic peak in DTA. On the other hand the reported transition temperature of gypsum-bassanite and gypsum- γ anhydrite and gypsum-orthorhombic anhydrite are in the range of 318-473K, 403-473K and 473-1273K respectively (Anusavice, 2004, Bishop *et al.*, 2014). The differences are attributed to the variation in particle size, crystallinity, surface area and degree of lattice perfection.

4.2.2. Characterisation of the bassanite or β -CSH

The XRD pattern (Figure 31) of the gypsum powder after optimization of the calcination process at 393K best matched with the ICDD data card no.74-2787 corresponding to monoclinic bassanite.

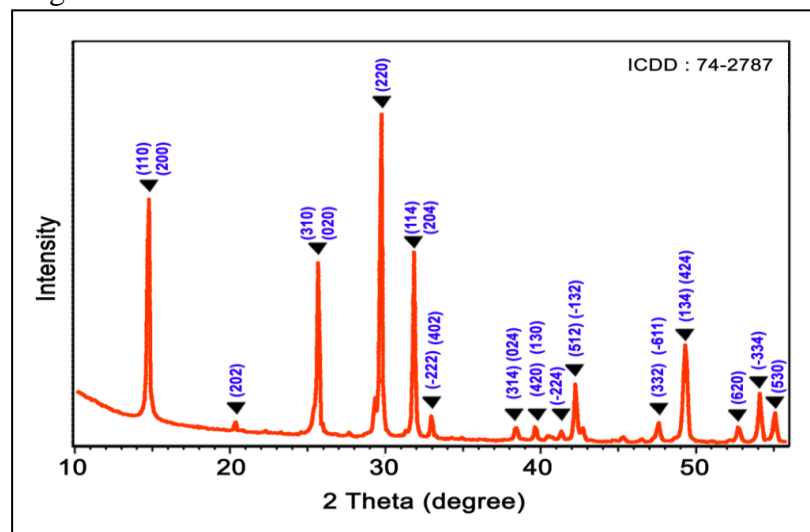


Figure 31: XRD pattern of the phase converted smCSD (the standard peaks of bassanite are marked, ICDD data base no. 74-2787)

All the FTIR peaks could be attributed to this particular phase (Figure 32). In FTIR spectrum, the strong absorption band around 1150 cm^{-1} and a shoulder peak at 1093 cm^{-1} , correspond to the ν_3 antisymmetric stretching modes of SO_4^{2-} tetrahedra and doublet at 658 and 600 cm^{-1} correspond to ν_4 anti-symmetric bending of S-O. The band due to ν_2 symmetric bending of SO_4 tetrahedra could be observed at 429 cm^{-1} . The ν_1 symmetric stretching mode of SO_4^{2-} tetrahedra appears as a weak shoulder peak at 1006 cm^{-1} . The peaks at 3546 and 3606 cm^{-1} are the ν_1 symmetric stretching and ν_3 antisymmetric stretching modes of water and the one at 1620 cm^{-1} represents the OH bending mode (Liu et al., 2009, Lane., 2007). The result ensures the complete phase conversion from the Gypsum to Bassanite at 393 K .

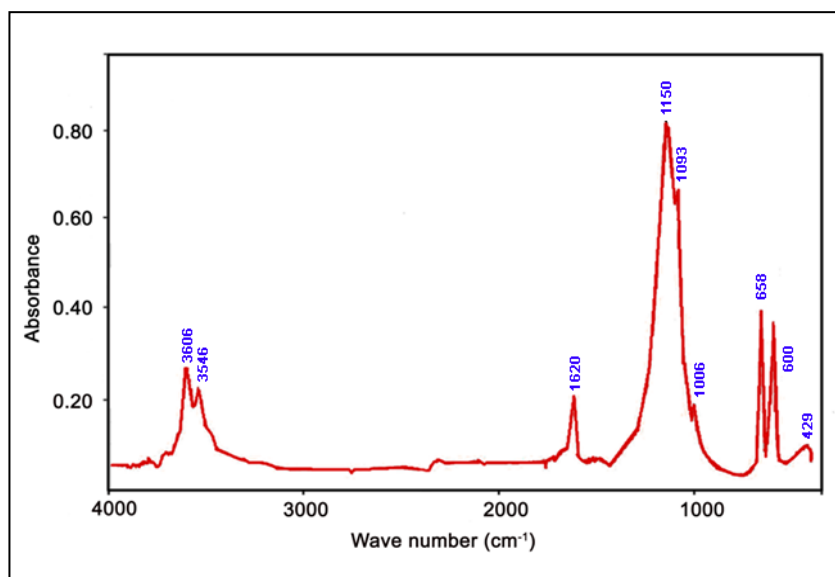


Figure 32: FTIR spectrum of smCSD after calcination at 393 K . All the major absorption band corresponds to that of bassanite

The micromorphology of the bassanite as shown in Figure 33 reveals the submicron dimensional particle even lower than precursor. The lumps are found to be made up of the fine particular aggregates. The phase transition doesn't affect the

particle dimension considerably which is attributed to the morphology and size of the precursor smCSD.

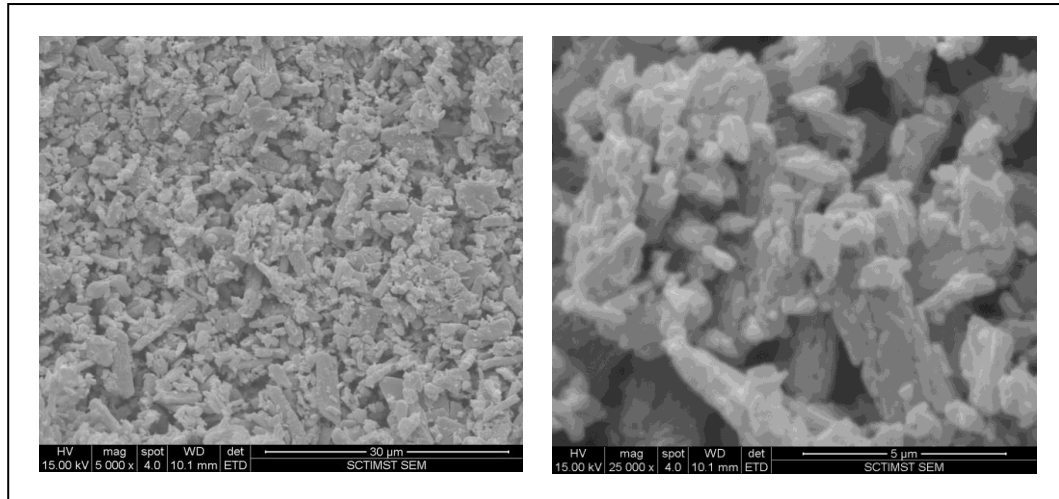


Figure 33: SEM image of the bassanite showing fine particles and lumps. At high magnification the lumps are found to be formed from the very fine particulate aggregates

4.2.3 Effect of DHPD addition in the injectability of the cement

The variations of viscosity with the time of extrusion of different CSC compositions containing varying quantities of DHPD (averaged over triplicate measurements) are plotted in Figure 34. The curves have a common trend, with a ‘build-up’ region at the beginning and a fast increasing region at the tail end. The build-up region corresponds to the initial packing of the cement in the syringe under pressurization. The tail end is determined by the ‘shear thickening’ effect on the paste (due to poor convergence of flow) when the plunger approaches the end of the syringe. In addition, the values at the tail end generated by the Hagen-Poiseuille relation will get amplified, as the pressure drop becomes comparable to that in the needle (Lewis, 2011). There is a ‘plateau region’ in between where the viscosity tends to remain nearly constant. The assumptions of the Hagen-Poiseuille equation will hold good in this region.

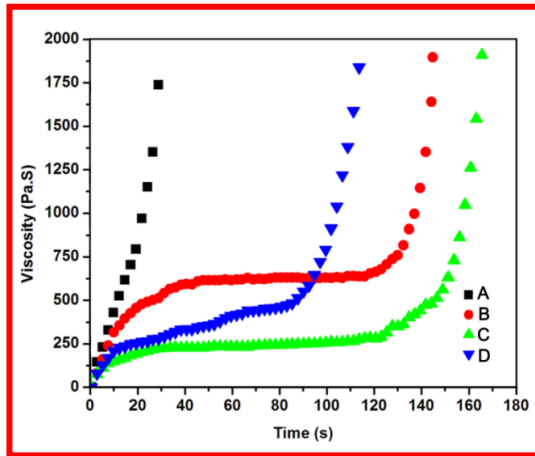


Figure 34: The variations of viscosity with time, of the cement compositions obtained from injectability study. A - smCHD0, B - smCHD1, C - smCHD2 and D - smCHD 5.

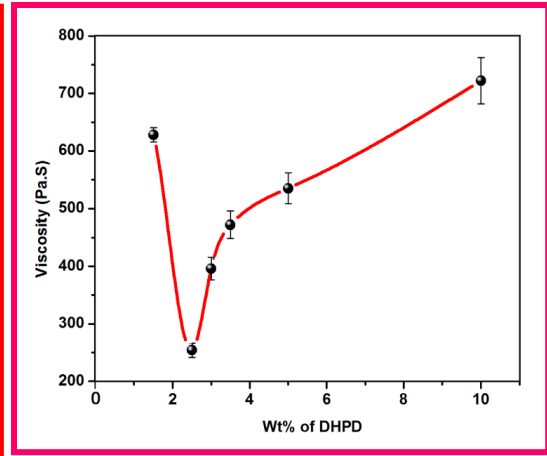


Figure 35: Mean viscosity value of the cement pastes with varying concentrations of DHPD (from 1.5 to 10 % added in smCHD), corresponding to 98 s extrusion period.

Paste made with phase pure CSH powder (smCHD0) showed a strong non-Newtonian behaviour, evidenced by the steep rise in the force within a few millimetres of plunger travel. Filter pressing was observed right from the beginning, wherein the liquid part oozed out through the needle leaving the solid particles behind. Corresponding viscosity plot crossed 1000 Pa.s within 20s, indicating the non-injectable nature of bare CSC. It has been reported that extrusion of a paste from a syringe through a cannula, either manually or mechanically, is not possible beyond 1000 Pa.s (Dorozhkin, 2010).

The filter pressing effect got drastically reduced when DHPD is added in small quantities (<1 %) and significant changes were observable from 1.5 % DHPD onwards. At this concentration, the cement paste extruded smoothly and fully to the maximum possible extent of plunger travel. The average viscosity of the paste was calculated to be 600 Pa.s. On increasing the DHPD content, up to 2.5 %, the viscosity value declined considerably. Beyond 3 % DHPD content, up to 10 %, the average

viscosity was observed to increase, but well within the limit of injectability. The plots of smCHD0, smCHD1, smCHD2 and smCHD5 are shown in Figure 34.

The viscosity values for the analysed compositions (0–10 % DHPD in the cement) at a time period of 98 s, plotted as mean \pm SD (n = 3) against the DHPD concentration, could be seen in Figure 35. There was considerable variation in viscosity among the compositions. Smooth flow of the smCHD2 is shown in Figure 36. The compositions having higher DHPD content (smCHD4 and smCHD5) showed anomalous behaviour with continuous increase in the force during the extrusion. This means that the DHPD concentration in the cement pastes beyond a certain value causes deviation from near-newtonian behavior and shows shear thickening.

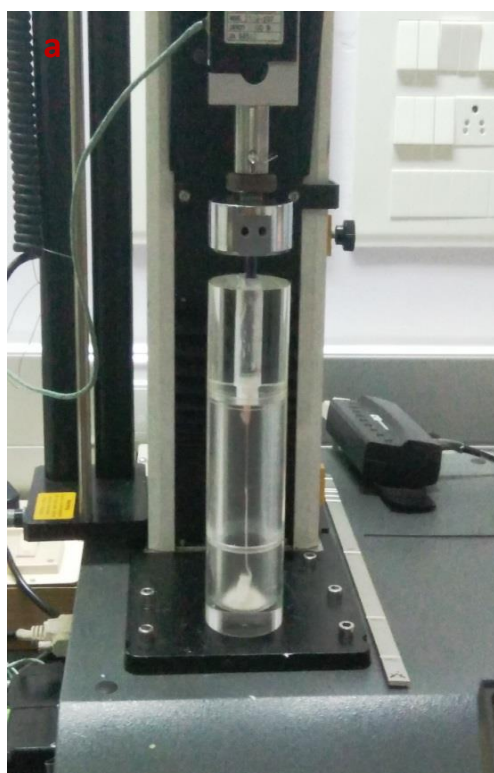


Figure 36: a) Smooth flow of smCHD2 cement paste through the needle during the extrusion rheometry b) Set cement paste after extrusion collected from the detachable bottom



4.2.4. Enthalpy change of hydration in presence of the additive

The DSC analysis in isothermal mode at 310K gave the plot of cumulative heat evolved against time Figure 37. Unmodified cement smCHD0 and the test sample

smCHD3 reached the saturation value at 7.4 and 7 min respectively. The corresponding enthalpies of hydration were found to be 30.27 cal/g (126.63 J/g) and 62.3392 cal/g (260.82 J/g) respectively. The ΔH_{hyd} of smCHD0 falls within the range of reported values for β -CSH (111–134 J/g) (Fischer *et al.*, 2012). The incorporation of 3.5 % DHPD resulted in an increase of ΔH_{hyd} to twice the value.

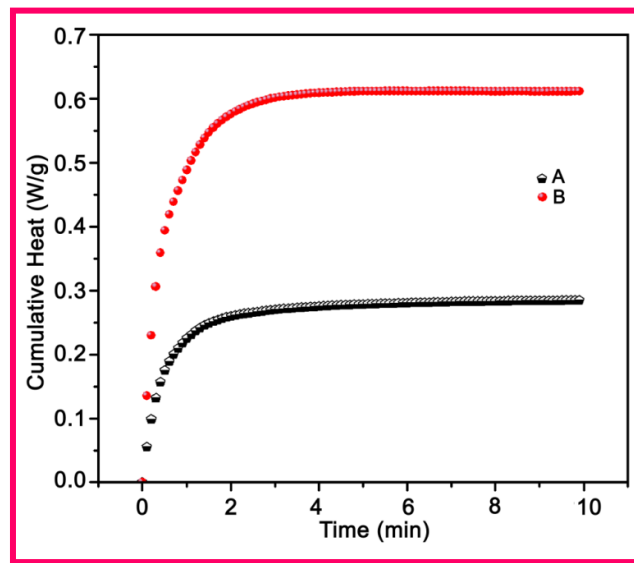


Figure 37: Isothermal DSC plot of cumulative heat of hydration against time – A) smCHD0 and B) smCHD3

4.2.5 Influence of the additive in the phase conversion of bassanite during cementing

X-Ray Diffraction spectra of the set mass of all the compositions best matched with the standard spectra of gypsum (ICDD data card 21-0816). No other significant peaks corresponding to any other likely phases (sodium phosphates, calcium phosphates and sodium sulfate) were found. Figure 38 A & B corresponds to the XRD pattern of the preset cement compositions ie. bassanite and DHPD whereas C is that of set cement smCHD5. A notable difference is that the smCHD5 sample carries a small hump at 11.630° (d value = 7.6031 \AA), by the side of the peak at 11.634° (d value =

7.6005 Å) corresponding to (0 2 0) plane, which has been shown magnified in the inset (red trace). The inference is that certain domains in crystals had undergone lattice expansion in the (0 2 0) plane to a spacing of 0.0026 Å, possibly due to substitution of a larger ion. As per the unit cell structure of CSD, the (0 2 0) plane is inhabited by SO_4^{2-} tetrahedra (Yan et al., 2016, Weiss and Brau, 2009, Pinto et al., 2012).

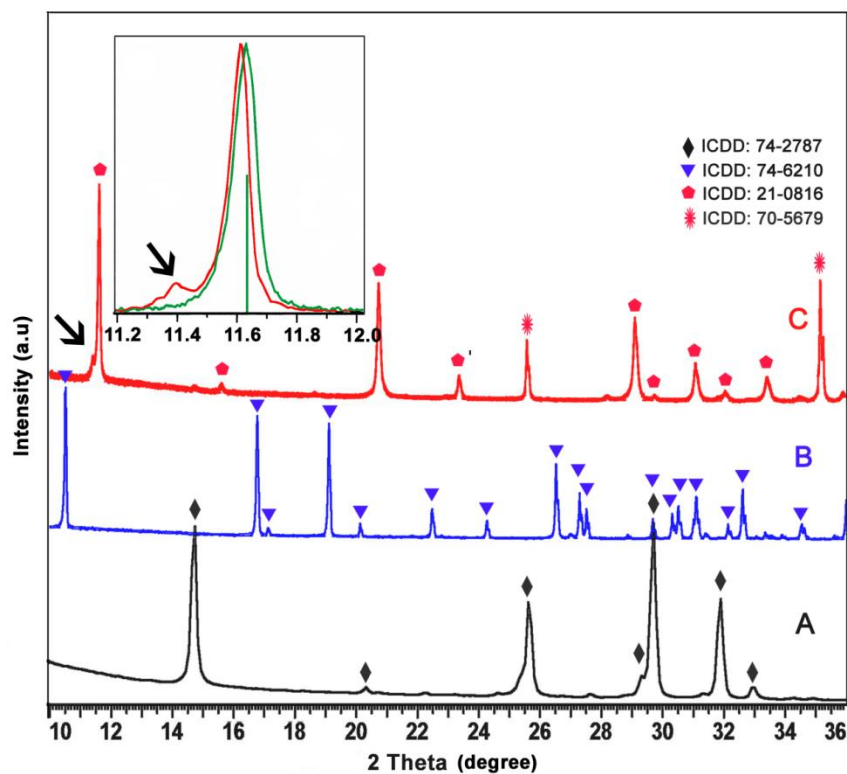


Figure 38: XRD patterns of - preset cement compositions A) Bassanite & B) DHPD and C) set cement smCHD5. Peaks of CSD (ICDD data card no. 21-0816), bassanite (74-2787), DHPD (74-6210) and corundum (ICDD: 70-5679) are marked. The 0 2 0 peaks of smCHD5 are shown magnified and superimposed with that of the smCHD2 in the inset. The red trace corresponding to smCHD5 carry a hump at 11.630° 2-theta (arrow marked). The green trace in the inset is that of smCHD2 sample

The hydration reaction and crystal formation in presence of DHPD might have led to the substitution of phosphate in their positions, leading to a slight expansion of the corresponding plane spacing. In short the variation is due to the compositional heterogeneities due to the presence of P enriched microdomains in

crystal lattices. The spectrum of smCHD2 sample (shown as green trace in the inset) did not possess this hump, may be because the extent of the substitution is below the detection limit of the XRD. However, the EDS analysis (Section 4.2.8) showed the smCHD2 sample to contain phosphorous (possibly in the form of HPO_4^{2-} ions) in a concentration about 0.1 % w/w (extrapolated from Fig. 46).

FTIR spectra of the above samples along with those of smCHD0 and DHPD are given in Figure 39. The infrared absorption of smCHD0 sample showed all the typical absorption peaks of gypsum (section 4.1.1). On adding DHPD, the cement exhibited considerable variation in the FTIR spectrum, which is evident in the traces C and D corresponding to smCHD2 and smCHD5 respectively.

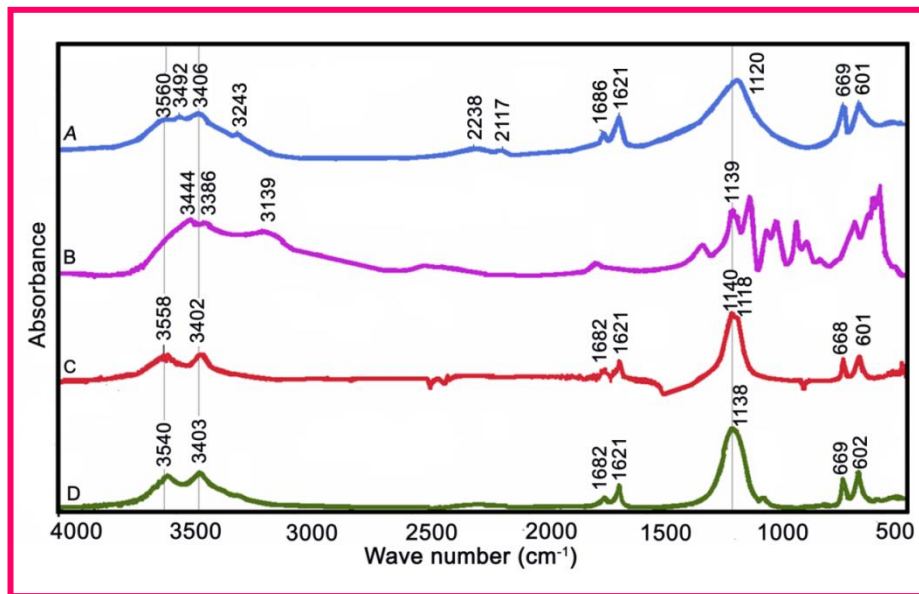


Figure 39: FTIR spectra of A) unmodified cement smCHD0, B) DHPD alone C) smCHD2 and D) smCHD5

In the sample smCHD2, the band with the peak at 1120 cm^{-1} got narrowed to a region in between 1100 and 1250 cm^{-1} and a shift in the peak is observed (to the position $1,140\text{ cm}^{-1}$). It is notable that one of the characteristic absorption of HPO_4^{2-} coincides with this position (Eichert et al., 2005, Khashaba et al., 2010). The ν_1

symmetric stretch and ν_1 bending of H_2O seemed to be prominent and intense at 3558 and 3402 cm^{-1} respectively. The ν_3 anti-symmetric stretch at 3492 cm^{-1} was diminished and the additional ν_2 bend of H_2O at 3243 cm^{-1} is missing. The spectrum of sample smCHD5 shared similar features, except for the slight broadening of the band at 1138 cm^{-1} (corresponding to HPO_4^{2-}). The bands around 3540 and 3403 cm^{-1} were more prominent.

On comparing with the characteristic absorption of DHPD in Figure 43, only the peak around 1140 cm^{-1} corresponding to HPO_4^{2-} was present in the spectra of smCHD2 and smCHD5 samples. The relative broadening in the samples may be due to the ν_3 antisymmetric stretch of S–O coinciding in the same region. This substantiates the observation of phosphate at the sites of SO_4^{2-} in the crystal domains. The shifts in the ν_1 symmetric stretch (3560 cm^{-1}), the diminished frequency of ν_3 anti-symmetric stretch (3492 cm^{-1}) and ν_1 bending mode vibrations of H_2O might have appeared due to the interference of vibrations of phosphate included in the lattice.

Compiling the results, the all-inclusive mechanism for the formation of bassanite based bone cement system could be defined.

4.2.6. Chemical mechanism for the formation of cement

The comprehensive procedure for the formation of bassanite based cement could be better represented as in Figure 40.

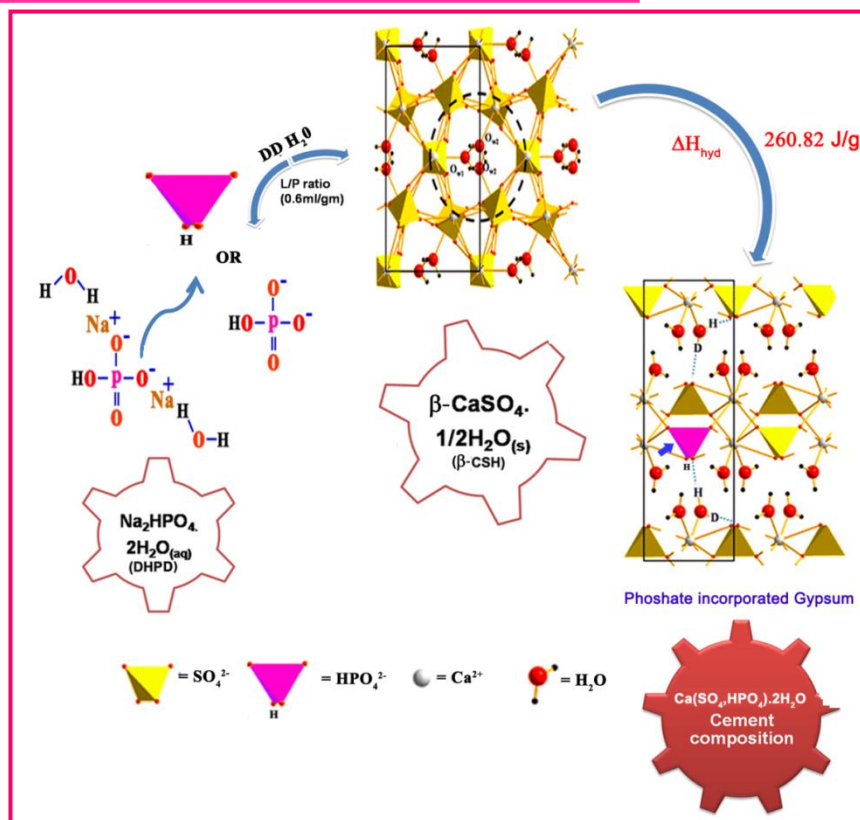
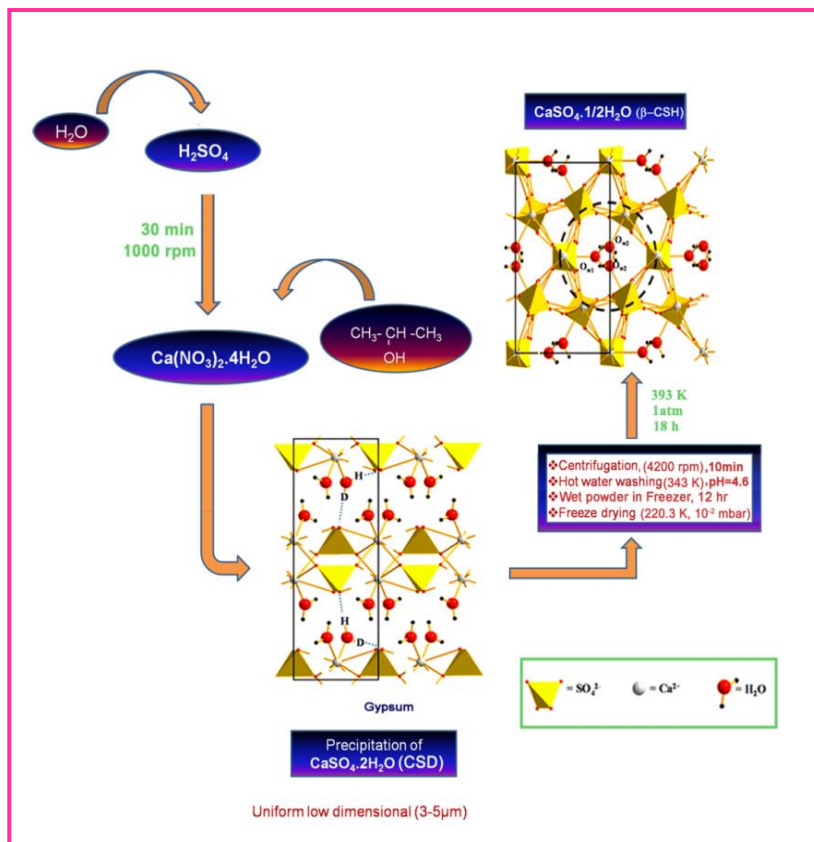


Figure 40: Overall schema showing the mechanism of formulation of injectable bone cement

4.2.7 Micromorphological variation of the set cements due to the additive

The electron microscopy images of the samples (10,000×) are compiled in Figure 41. Certain interesting features observed (highlighted by arrow heads) are further magnified (40,000×) and compiled in Figure 42.

The bare cement smCHD0, Figure 41(a) showed non-uniformly distributed rods and oblong sheet-like particles of size 1–10 μm . They appear discrete, without any interconnection. The significant change in crystal habit was observed in smCHD1. Predominantly needle shaped crystals (length 5 μm and width 1 μm) were found, interconnected with flower like features with diameter $<2 \mu\text{m}$, which were evenly distributed throughout (given magnified in Figure 42(a)). It may be contributing to better cohesiveness of the particles. In smCHD2 (Figure 45c), the average length of needle shaped crystals got reduced and interconnecting features changed to flattened form (Figure 42 (b)).

SmCHD3 (Figure 42(d)) showed further reduction in crystal sizes and the interconnecting features took the form of reticulated network having entangled particles of very low particle sizes (Figure 42(c)). Crystal sizes were considerably reduced ($<2 \mu\text{m}$) in smCHD4 sample (Figure 41(e)) and they appeared engulfed in the interconnecting particle-aggregate structure (Figure 42(d)). While in smCHD5 (Figure 41(f)), the particle aggregate structure dominated and the whole mass appeared in sheet like morphology composed of very small, sub-micron particulates (Figure 42(e)).

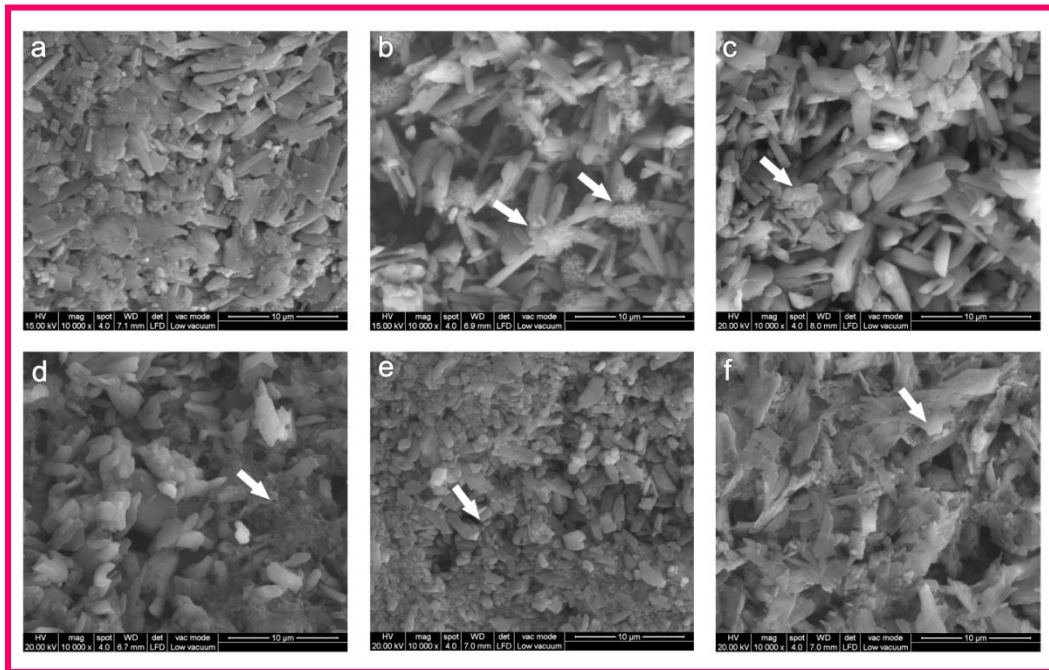


Figure 41: ESEM images of the set cement corresponding to-a smCHD0, b smCHD1, c smCHD2, d smCHD3, e smCHD4 and f smCHD5. Special features of formation are marked with arrow heads. These are given magnified in Figure 42

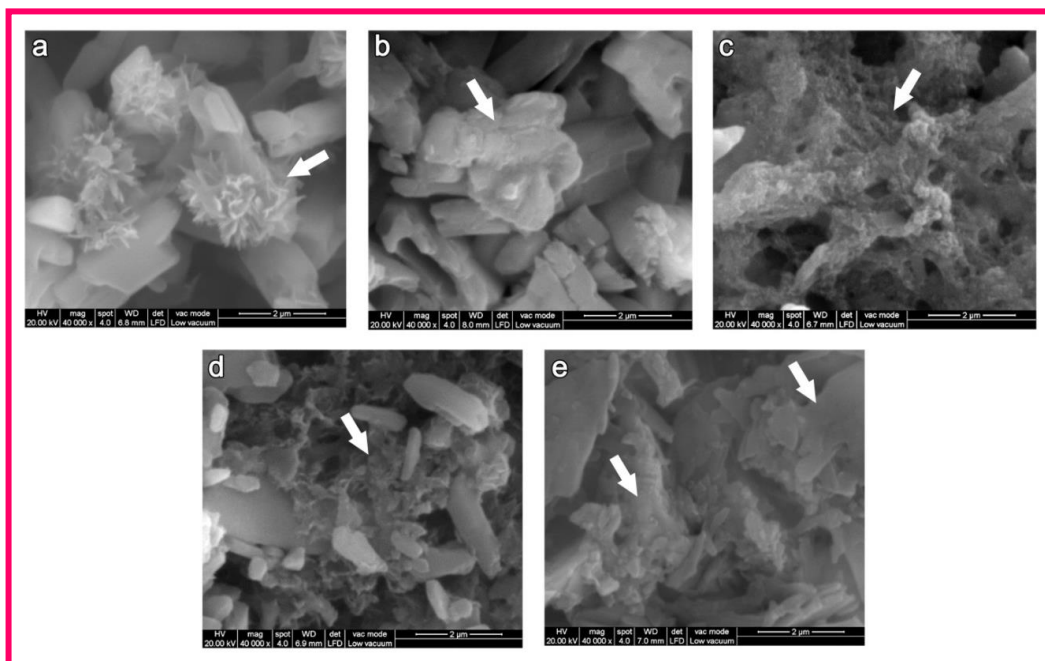


Figure 42: The growth features and aggregates observed in the set cement corresponding to – a) smCHD1, b) smCHD2, c) smCHD3, d) smCHD4 and e) smCHD5. Locations of interest are marked with arrow-heads.

4.2.8 Particle size distribution of the cement from high resolution 3D surface profilometry

The 3D surface profile and the particle size distribution profile of the smCHD2 obtained in the Talysurf CLI 1000 is as shown in figure 43. An estimate of the particle sizes could be obtained from the peak count histogram. The size distribution ranges from 2.1 to 5.9 μm , centered around 3.65 μm .

While the corresponding diagrams for smCHD5 could be found out in figure 44, which gives the particle size range of 1-2.4 μm centered around 1.5 μm . Very narrow range of particle size with monomodal distribution could be observed. Estimated values confirms the reduction in particle size with the higher integration of phosphate in the crystal lattice as observed in the SEM analysis.

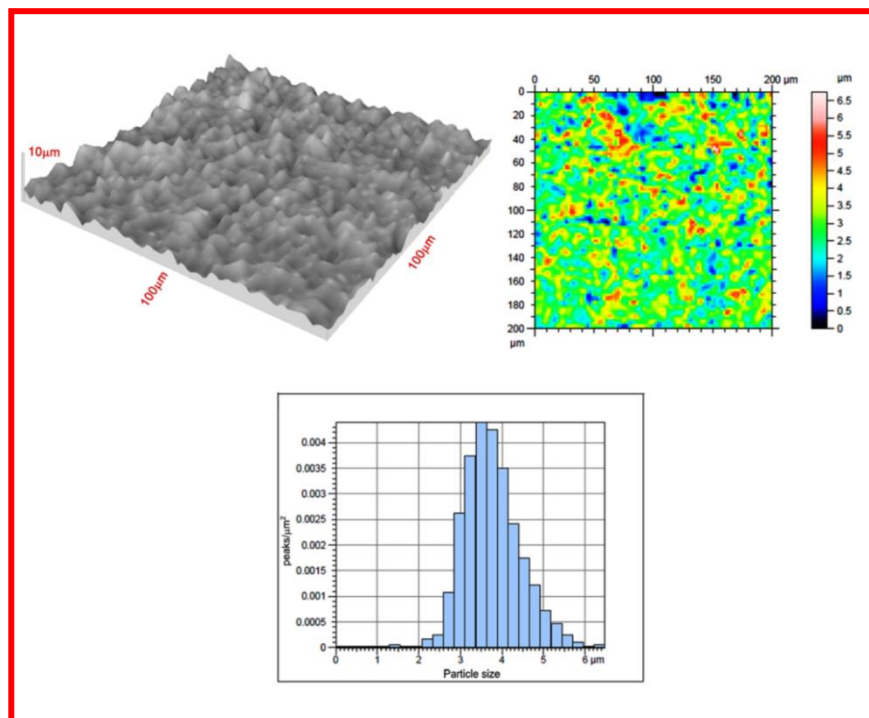


Figure 43: a) 3D surface profile b) particle size distribution profile of the surface and c) the corresponding peak count histogram of the smCHD2 obtained through Talysurf CLI1000

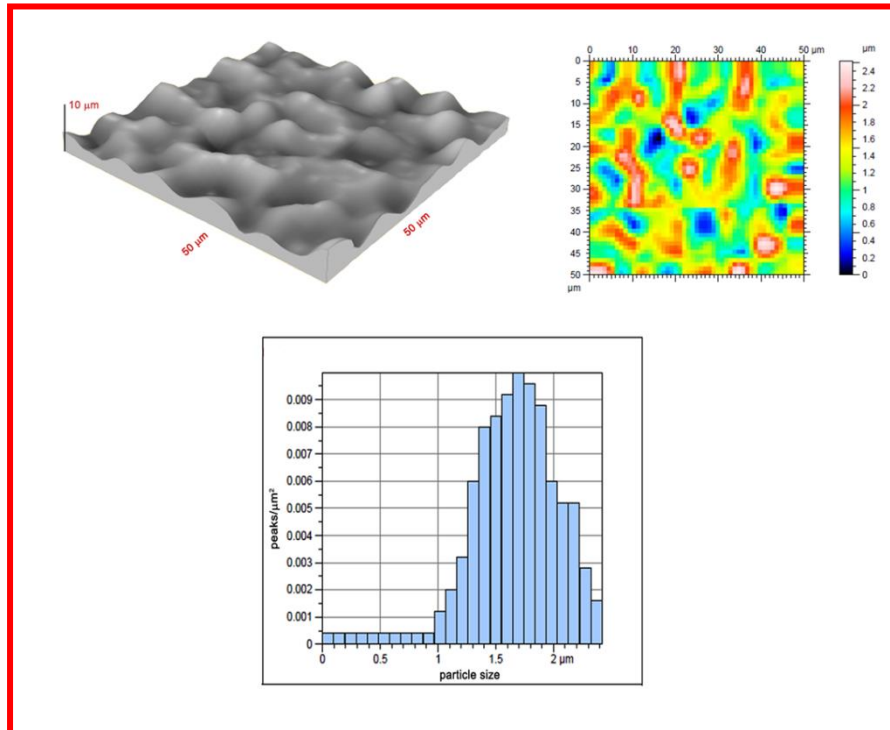


Figure 44: a) 3D surface profile b) particle size distribution profile of the surface and c) the corresponding peak count histogram of the smCHD5 obtained through Talysurf CLI100.

4.2.9 Appending phase formation studies with elemental analyses

Energy dispersive analysis has been done during the electron microscopy observations because it can give indications about the elemental substitution/inclusion in crystals. The area scan corresponding to the image for each sample (Figure 41 a–f) was taken. Peaks of Ca, S and O could be seen in all samples. Peaks of phosphorous (P) started appearing in samples mixed with DHPD. The EDS for smCHD0 and smCHD5 are given in Figure 45 for comparison. Considering the facts that the samples were washed prior to the analysis and XRD showed no remnant phases of phosphates, the phosphorous content appeared in EDS must be that got incorporated inside the cement crystals.

The area of the phosphorous peak was observed to increase according to the DHPD content in the samples.

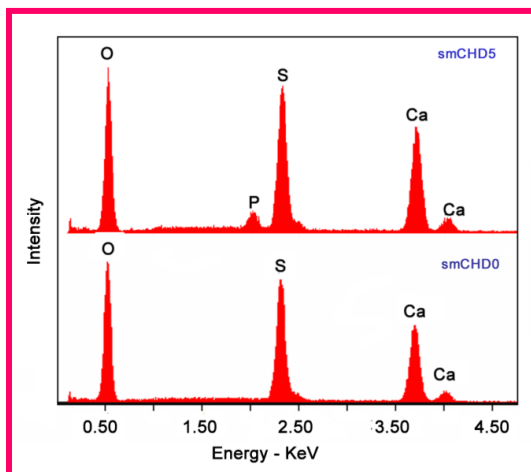


Figure 45: EDS spectra corresponding to smCHD0 and smCHD5, obtained from area scan. Presence of P is seen in smCHD5.

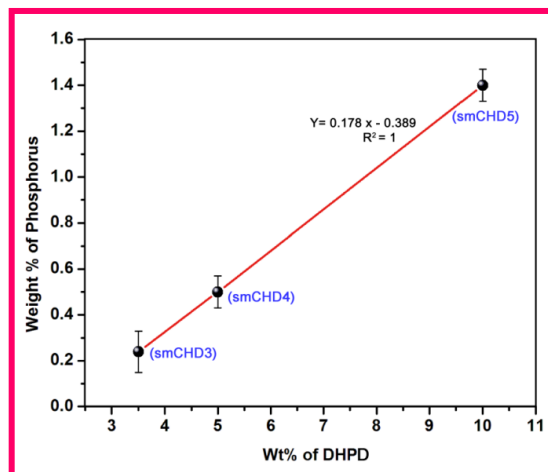


Figure 46: Percentage content of P in different cement samples obtained from the spot EDS analysis

The results support the conclusion of the phase analysis (Sect. 4.2.5) that the substitution of phosphate has occurred in the crystal lattice of CSD. To re-confirm the inference, spot EDS was taken by focusing the beam on a particular crystal (marked with arrowheads in the images from a to f, in Figure 41). A count build up time of 60 s was given and the weight percentage of phosphorus was calculated. The values of phosphorus content ranged from 0.1 to 1.3 % (w/w). Its plot against the percentage of DHPD content in the sample is given in figure 46, which shows a linear relation.

The OES–ICP results of the elution of sulfur, calcium and phosphorous from the samples supported the finding that phosphorous gets substituted in the crystals (as HPO_4^{2-}). On increasing the percentage of DHPD from 0 to 10 % the elution of Sulfur increased from 3.894×10^{-3} to 5.661×10^{-3} mg/ml. Calcium and phosphorus elution decreased from 0.953×10^{-3} to 0.673×10^{-3} mg/ml and 1.651×10^{-3} to 1.461×10^{-3} mg/ml

respectively. The graphical representation of the data is given in figure 47. It shows more sulfur atoms get expelled when the DHPD concentration increases in the sample, whereas the calcium and phosphorous elution are linearly decreasing. This can happen only when the sulfate ions in the crystals get replaced by hydrogen orthophosphate ions.

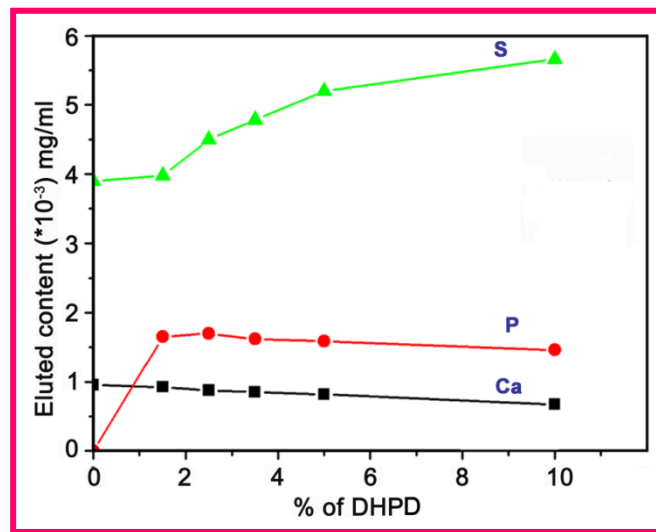


Figure 47: Eluted quantity of calcium (Ca), phosphorous (P) and sulfur (S) estimated through OES–ICP analysis

4.2.10 Effect on the setting time and compressive strength

The setting time data of the calcium sulfate cement samples, as a function of wt% of DHPD, is represented in figure 48. Generally, two setting times (the initial setting time and the final setting time) are observed in the case of calcium phosphate cements (CPC). The initial setting time (t_i) is the end of the workability of the paste after mixing and the final setting time (t_f) indicates the full hardening of the set mass (Khashaba *et al.*, 2010). Unlike CPC, a single setting time has been reported for calcium sulfate cements (CSC) in the literature (Komatha and Varma., 2004). In the present case, this was true for the smCHD0 sample, which had a quicker setting time

of 5 min. Interestingly, with the addition of DHPD, the two setting times (t_i and t_f) could be identified, and they got prolonged with the increase of DHPD. The t_i values increased from 9.5 to 15 min when the DHPD content varied from 1.5 to 5 %. However, smCHD5 showed a slightly lower t_i (13 min) compared with smCHD3 (13.5 min) and smCHD4 (15 min). The t_f showed a steeper but non-linear rise with the increase in the DHPD content.

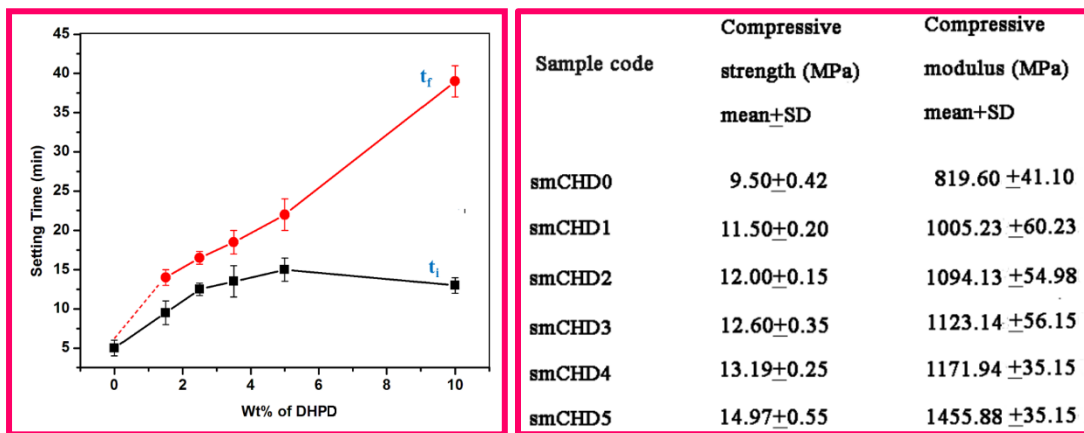


Figure 48: The variation of the initial (t_i) and final (t_f) setting times of the cement with DHPD concentration

Table 2: Compressive strength and compressive modulus variation of the set cement as a function of weight percentage of DHPD

SmCHD4 and smCHD5 had the final setting time of 22 and 39 min respectively, which are too high for practical applications. Therefore, the optimum concentration of DHPD was selected to be 2.5 %, which has $t_i = 12.5$ min and $t_f = 16.5$ min.

The compressive strength and the corresponding compressive modulus variations of the set cement (mean \pm SD for $n = 12$) as a function of the DHPD content are shown in Table 2. From ANOVA and student's t test analysis, all the values were found to be statistically significant ($P < 0.05$). The bare cement (smCHD0 sample) showed a compressive strength of 9.5 MPa. The addition of DHPD resulted in an increase of the compressive strength. These values are in clinically acceptable

range in comparison with that of the cancellous bone, which is in the range of 5–10 MPa (Rahman, 2011).

The improvement of compressive strength with the DHPD content could be attributed to the decrease in particle size during the precipitation and the consequent tight packing (as seen in the SEM images). It is clear that the interconnecting aggregate structures (containing very small particles) have also a significant role in increasing the compressive strength.

The compressive modulus of human cancellous bone found in literature varied within the range of 1.1–9,800 MPa (Purvi, 2008). However the compressive modulus required for low load bearing applications such as sinus augmentation or filling extraction sites are reported to be 0.05-1GPa (Harrison et al., 2016). All the cement samples showed compressive modulus within the range and the value was found to increase with the DHPD content. The compressive strength and compressive modulus of the optimised cements smCHD2 are 12 ± 0.15 MPa and 1094.13 ± 54.98 MPa respectively.

PHASE III

4.3 *In vitro* and *in vivo* validation of ‘BioCas’ as a bone filler cement

4.3.1 *In vitro* screening tests

4.3.1.1 Immersion in simulated body fluid

When immersed in SBF the BioCaS cement pellet showed globular deposits over its surface at 24 h (not shown here), indicating growth of hydroxyapatite as illustrated by Kokubo (Kokubo., 2006). This was seen to grow as a thick layer by 4 days of immersion, as represented in figure 49(b).

The underlying cement surface can be seen through a crack in the left upper corner in the picture. The cross section of this layer, shown in (c), gives an estimate of the average thickness of 10 μm (marked). The region marked in (b) is shown at higher magnification in (d), which reveals the ‘cauliflower-like’ micromorphology. Such growth features are typical of hydroxyapatite layer growth (Kokubo, 2006). The surface of the unmodified CSC immersed under the same conditions in SBF for 4 days can be seen (e), with a magnified view (f). Apatitic growth features are present, mainly larger globular growth, but at a very slow rate, and the layer is irregular and discontinuous. The underlying cement particles are visible in most areas (marked by an arrow in (f)). Comparing the results, it can be understood that BioCaS is substantially more bioactive than unmodified cement smCHD0 *in vitro*, which qualitatively correlates with the *in vivo* bone bioactivity of the material.

XRD pattern of the BioCaS and smCHD0 (unmodified cement) disc surfaces on immersion in SBF after the second and fourth days are shown in Figure 50.

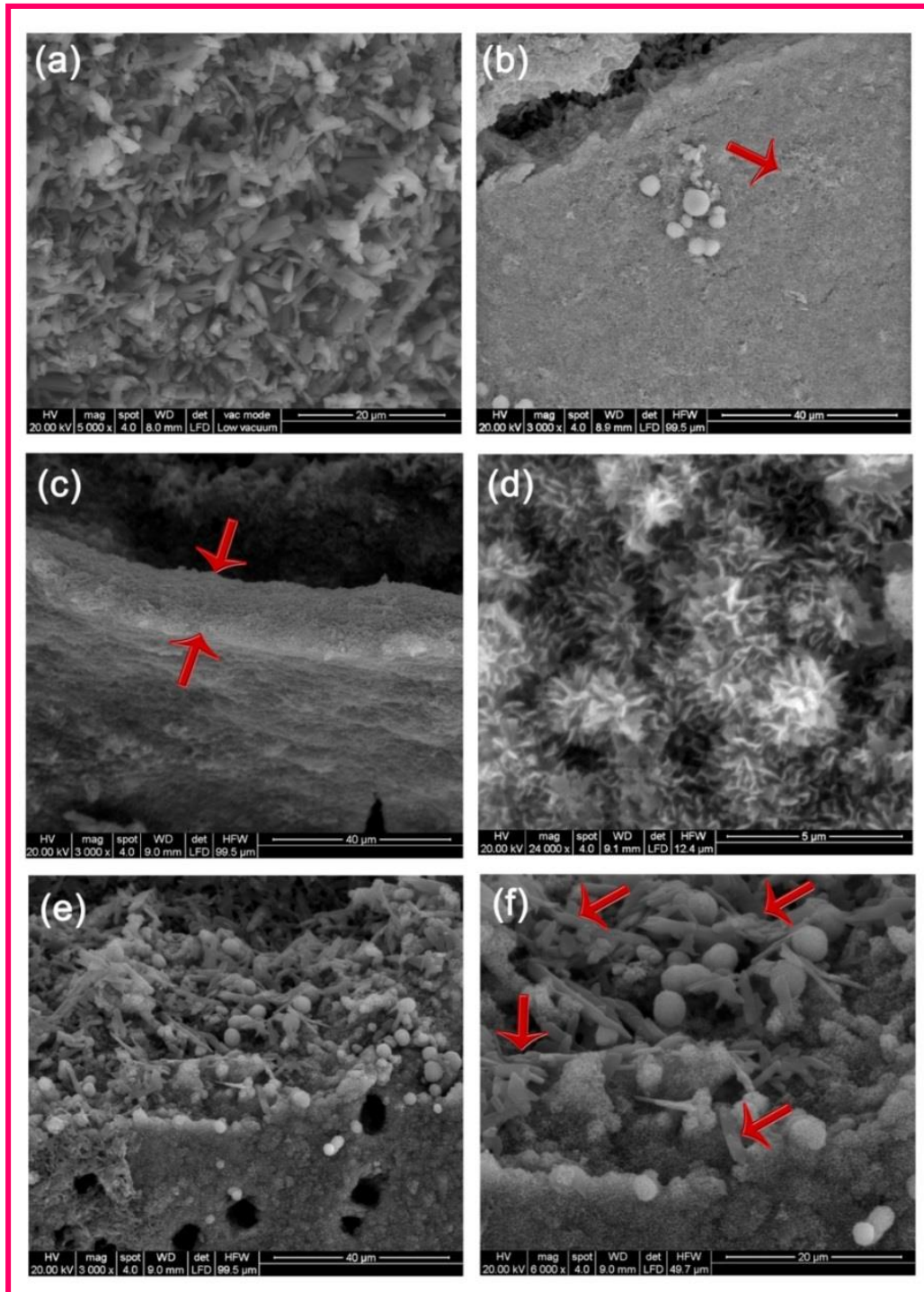


Figure 49(b): SEM images of cement samples in the *in vitro* bioactivity test. (a) surface of the BioCaS disc (b) after 4 days of immersion in SBF (c) cross section showing the interface of the thickly coated apatite layer and the bulk BioCaS cement. (d) magnified view of the area marked with an arrow in (b) showing the typical micromorphological features of the HA layer (e) surface of unmodified CSC i.e. smCHD0 after 4 days of immersion wherein the HA layer is non-uniform and discontinuous (f) magnified view of the region in figure (e) revealing the underlying cement particles in most places (marked with arrows).

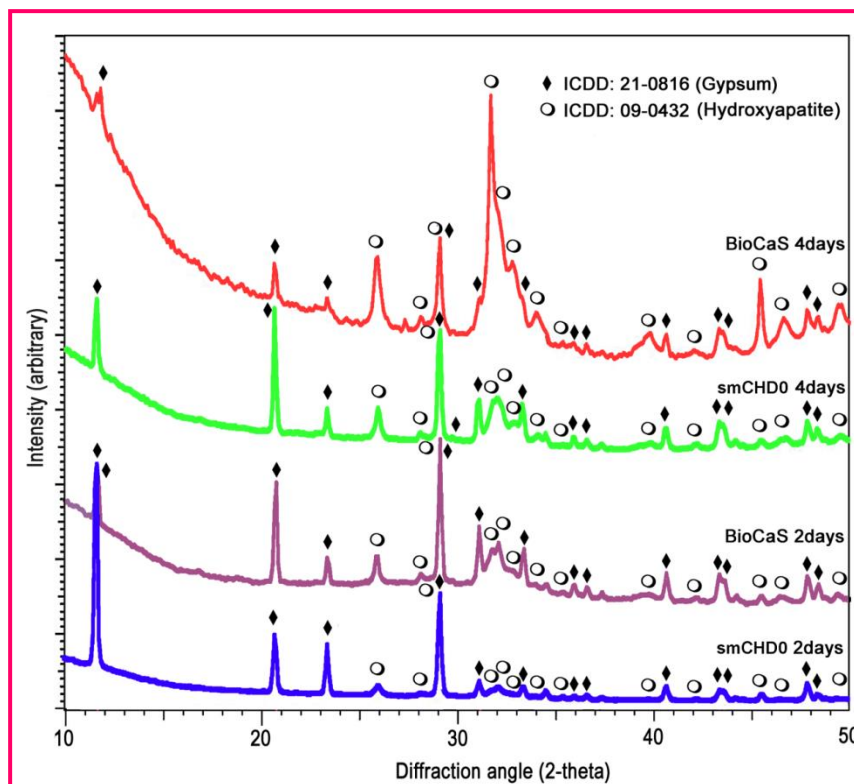


Figure 50: XRD patterns of the BioCaS and smCHD0 disc surfaces on the 2nd & 4th days of immersion in SBF. A progressive increase in the intensity of HA peaks in BioCaS compared with smCHD0 is evident

In BioCaS the characteristic peak of HA (ICDD 09-0432) are seen in both cases, along with peaks of the underlying gypsum (ICDD 21-0816). The intensity of the major HA peaks is found to increase with immersion time, and in the fourth-day sample it over shadowed that of the gypsum peaks. The broadness of the hydroxyapatite peaks indicates low crystallinity and the high background at low angles indicate the amorphous content, typical of apatite layers formed in SBF immersion (Lin *et al.*, 2014).

The intensities of HA peaks on smCHD0 were very low, and appreciable peaks were found only by the fourth day. In order to have a quantitative comparison, the ratio of the intensities (raw area under the curve) of the highest peak of hydroxyapatite (at two theta = 31.779°) to that of gypsum (at two theta= 11.634°)

was calculated in each case. The values for CSC and BioCaS for 2 days' deposition are 0.1358 and 0.6472, respectively. The corresponding values for 4 days' deposition are 0.8181 and 2.1969. This proves the higher bioactivity of BioCaS with respect to bare calcium sulfate (gypsum alone).

In the FTIR spectrum of BioCaS (Figure 51), The 960 cm^{-1} bound in the spectra assigned to ν_1 (PO) symmetric stretching. The broad band observed at 3451 cm^{-1} and the peak at 1630 cm^{-1} indicates the stretching and bending mode of OH^- vibration of the absorbed lattice water in HA during the formation. The broadness of the peak at 1035.5 cm^{-1} (assigned to ν_3 (PO_4) antisymmetric stretching mode characteristic to the molecular structures of the polyhedron of PO_4^{3-} in the crystalline apatite lattice) indicates less crystalline HA while the presence of the characteristic PO_4^{3-} doublet at 601 and 568 cm^{-1} (corresponds to ν_4 (OPO) bending mode) excludes the possibility of fully amorphous phase (ACP) (Paz *et al.*, 2012).

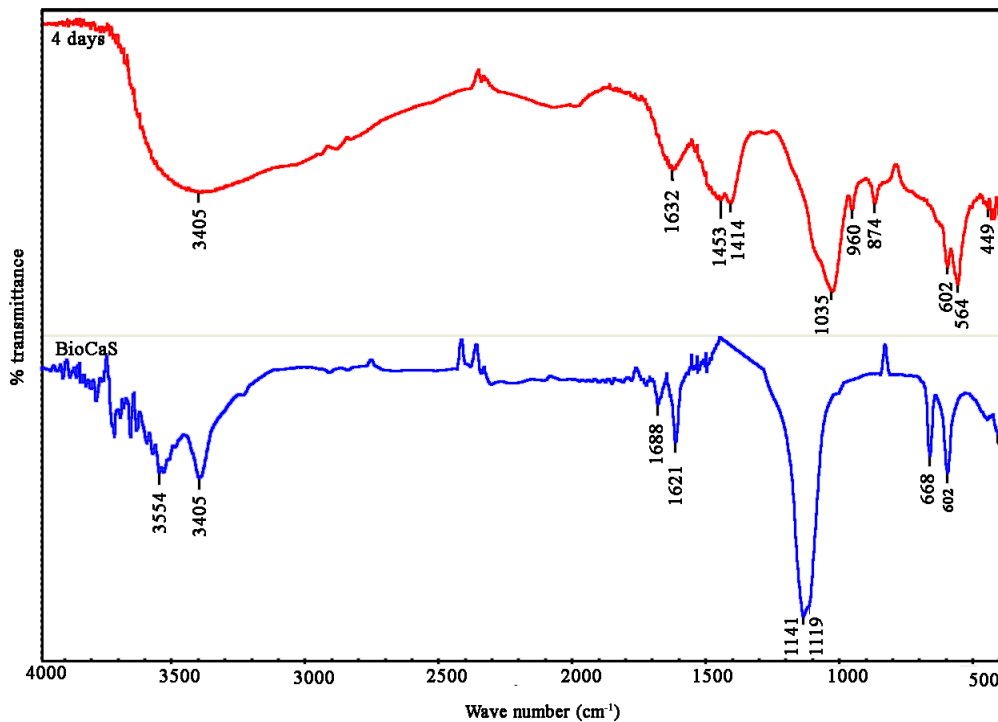


Figure 51: FTIR spectrum of the BioCaS disc before and after 4 days of immersion in SBF has shown the formation of carbonated hydroxyl apatite on the surface.

The spectrum also shows the carbonate peaks in the range of 1500-1400 and 873.9 cm^{-1} corresponding to the asymmetric stretching (ν_3) mode and out of plane bending (ν_2) mode vibrations of C-O liaisons in carbonate groups respectively (Paz *et al.*, 2012). It indicates the formation of a layer of hydroxyl carbonated apatite on the surface of the material. The obtained results highlight the rapid formation of apatite layer on the surface of BioCaS.

In the curve for smCHD0 sample (Figure 52), peaks of gypsum were prominent however the characteristic bands of hydroxycarbonated apatite (PO_4^{3-} : 603 and 1039 cm^{-1} and CO_3^{2-} : 874, 1457 and 1416.4 cm^{-1}) could be well distinguished. Unlike BioCaS, the peak at 1630 cm^{-1} and the broad band at 3451 cm^{-1} attributed to bending and stretching mode of OH vibration due to the absorbed lattice water (Oudadasse *et al.*, 2011) were absent among which the former is indistinguishable due to the overlap of strong in plane deformation vibration of OH--O group at 1621 and 1686 cm^{-1} due to two crystallographic distinct type of water in gypsum and the latter is suppressed due to the ν_2 and ν_3 bending mode of water at 3406, 3492 and 3550 cm^{-1} in gypsum.

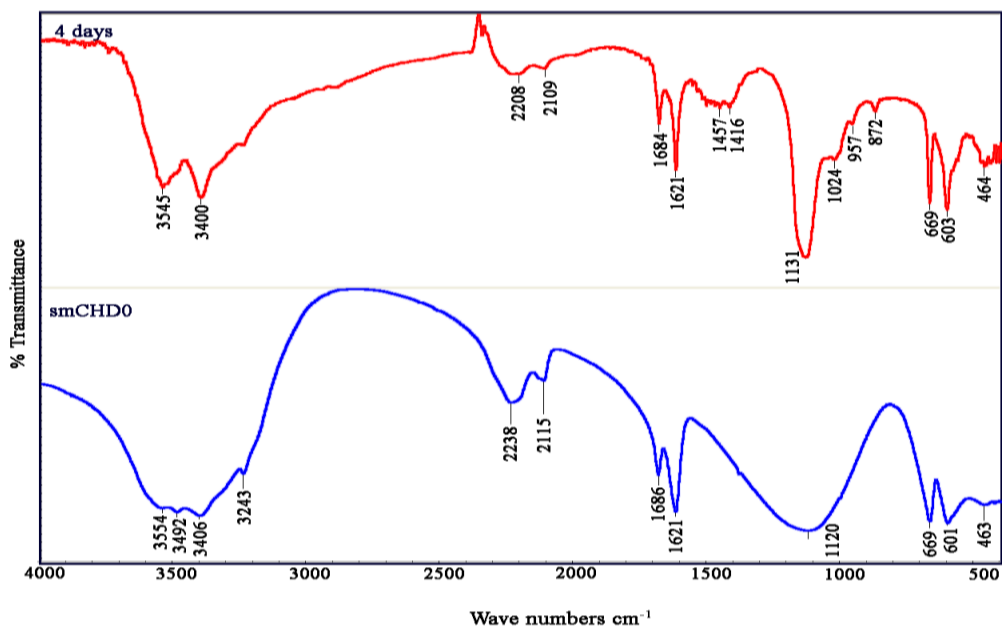


Figure 52: FTIR spectrum of the smCHD0 disc before and after 4 days of immersion in SBF has shown the appearance of the carbonated HA on the surface along with the prominent peak of gypsum

This concludes the irregular and thin layer formation of carbonated hydroxyapatite on the surface of the smCHD0 sample. The peak remains the same even after 7 days of soaking and hence BioCaS was proved to be highly bioactive than smCHD0.

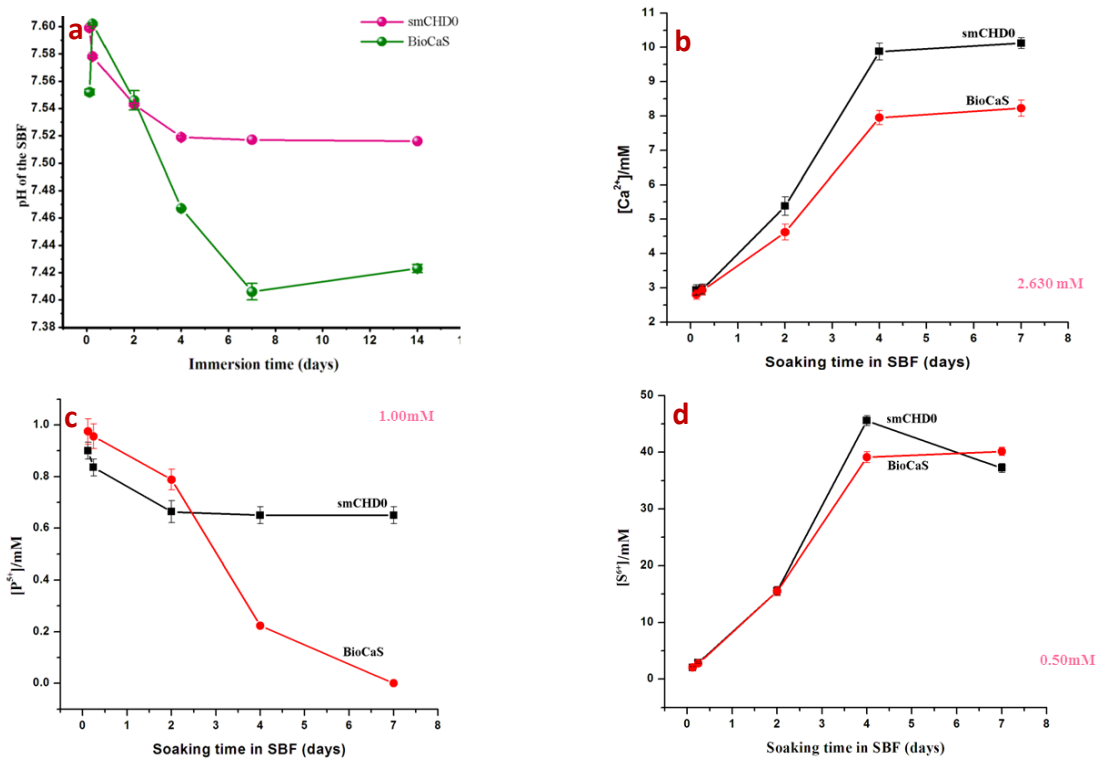
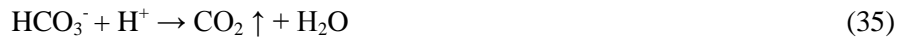


Figure 53: a) pH variation of SBF with immersion time (3 and 6 hours and 2, 4, 7 and 14 days) of BioCaS compared to unmodified CSC b)-d) Elemental concentration profile of b) Ca²⁺ c) P⁵⁺ and d) S⁶⁺ estimated by OES-ICP with the soaking time of cements in in SBF

The pH values of the SBF solution collected throughout the 14 days of immersion are analysed (Figure 53(a)). The immersion of smCHD0 leads to a sharp augmentation of pH value from 7.4 to 7.59 within 3 hours after immersion and a gradual decrease in value to 7.52 up to 4 days and after that the value remains constant up to 14 days. The pH of the BioCaS immersed solution showed an increase in value to 7.60 up to 6 hours and showed decrease up to 7 days with decreasing trend comparatively higher than smCHD0 after 2 days of immersion. After 7 days the value reached 7.41 and remains almost same during 14 days (value 7.42). Initially during the soaking, the rate of release of calcium is greater than the

consumption and showed an increase from value 7.4, which is due to the exchange with H⁺ ions in SBF.

The rapid increase in pH value was also contributed to the reaction of HCO₃⁻ with the replaced H⁺ ions from the solution to form CO₂ and H₂O (Paz *et al.*, 2012).



During the second stage, the formation of HA crystals seeds in the solution which causes the rapid consumption of OH⁻ groups and incorporation of CO₃²⁻ and subsequent biomimetic precipitation of HCA [Ca_{8.3}(PO₄)_{4.3}(HPO₄,CO₃)_{1.7}(OH,CO₃)_{0.3}] by the reaction. The incorporated HPO₄²⁻ in the BioCaS also play significant role in increasing the bioactivity by the formation hydroxycarbonate apatite (Stanciu *et al.*, 2007). Hence the rate of consumption gradually increases and thereby reducing the pH. This declining trend more predominating in BioCaS than smCHD0 after 2 days of soaking explains its higher bioactivity which corresponds to the thick layer of formation of HA on the surface which may be due to the surface integrity of the BioCaS which adheres the precipitating HA layer. While in smCHD0, the faster dissolution from the precipitated HA layer over the surface reduces the biomineralisation capability which is confirmed by the irregular and nonuniform formation of the HA coating on the surface. However the elution of SO₄²⁻ ion also causes slight reduction in pH and also affect the graphical trend and hence conclusion could be made by compiling with other results. pH measurements also ensured that the material in SBF is within the limit of the osteoblast viability threshold pH of 8.0.

The concentration of Ca²⁺, P⁵⁺ and S⁶⁺ ions in SBF solution as a function of soaking times are shown in Figure 53 (b)-(d). The calculated concentrations of Ca²⁺, P⁵⁺ and S⁶⁺ in reference SBF solutions are 2.63 mM, 1.0 mM and 0.5 mM respectively. Concentration of Ca²⁺ was found an increase from 2.9±0.15 to 9.8±0.25 mM in smCHD0 and from 2.8±0.14 to 7.95±0.21 mM in BioCaS from 3 h to 4 days and not showed much variation thereafter.

However the elution of calcium were found to be higher in smCHD0 samples. P^{5+} concentration was found to be decreasing from 0.9 ± 0.03 to 0.66 ± 0.04 mM in smCHD0 samples and from 0.98 ± 0.05 to 0.79 ± 0.04 in BioCaS from 3 h to 2 days. The decreasing concentration of P^{5+} shows the deposition of calcium phosphate layerst of the P^{5+} was consumed with in 4 days in BioCaS and the value reduced to zero during 7 days which indicates the higher deposition rate of HA layer by consuming all the P^{5+} available. This effect along with the presence of SO_4^{2-} in medium causes the considerable reduction in pH. $[P^{5+}]$ concentration and $[Ca^{2+}]$ remains more or less constant in smCHD0 during this period, probably due to the dissolution of the formed HA layer and reprecipitation which could be confirmed by the irregular layer thickness and discontinuity of the coating on the surface of the material. $[S^{6+}]$ was found to increase from ≈ 2 mM to ≈ 15 mM in both samples during the first 2 days followed by higher rate of release in smCHD0 samples compared to BioCaS which indicates the higher solubility of smCHD0. After 4 days the decrease in concentration in smCHD0 shows the redeposition of gypsum on the surface of the samples but in BioCaS the trend shows the thick hydroxyapatite layer coated prevent the further redeposition. It was conjuctured that osteoblsts might preferentially proliferate and differentiate to produce apatite and collagen on the surface of biomimetic apatite formed on the material; thus bound to the surface apatite and the surrounding bone. This ensures tight chemical bonding between the material and the living bone through mediated apatite layer.

4.3.1.2 *In vitro* degradation profile of the bone cement

The percentage of aseptic degradation of the BioCaS during the first 10 weeks was found out to be $55.04 \pm 4.11\%$ lower than smCHD0 $61.74 \pm 2.42\%$ (Figure 54). The difference in values were fond out to be statistically significant as per anova single factor and students t'test. The difference in values were found to be statistically significant as $P < 0.05$ during anova single factor and students t'test. After the initial 2 days period, the rate of degradation was found to be almost constant for each cement. The data is based on the weighing of the

pellet after definite intervals while discarding the cement remnants in the solution and hence the actual degradation rate will be lower than the displayed profile.

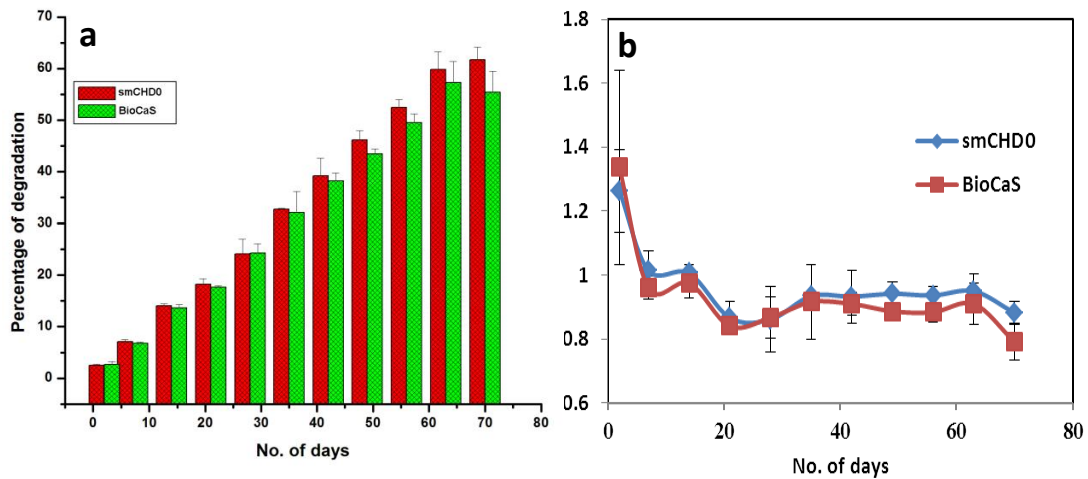


Figure 54: Degradation profile in terms of a) percentage of degradation and b) rate of degradation of BioCaS and smCHD0

4.3.1.3 In vitro tests for cytotoxicity

(i) Test on extract method : Images of the L929 mouse fibroblast cells after the cell culture cytotoxicity test (using the extracts at 50% dilution) are shown in figure 55. Cell control, SmCHD0, BioCaS and smCHD4 samples did not cause lysis of cells or reduction in cell growth. Discrete intracytoplasmic granules were seen, at a grade value less than 2. The material, therefore, could be considered to be non-cytotoxic. While considerable cell lysis occurred in smCHD5 samples in 50 and 25% physiological saline extract and hence not cytocompatible. Higher phosphate integration in the bone cement was found to affect the biocompatibility.

(ii) Metabolically active cell viability – MTT assay

The outcomes of the MTT assay are shown in Figure 56, wherein the metabolic activity values are expressed as mean±SD, with n=6. All the smCHD0, BioCaS and smCHD4 extracts showed greater than 80% metabolic activity directly related to metabolically active cell viability. The cytotoxic limit is 70% metabolic activity (ISO 10993-5, 2009), hence three of them could be considered as cell compatible.

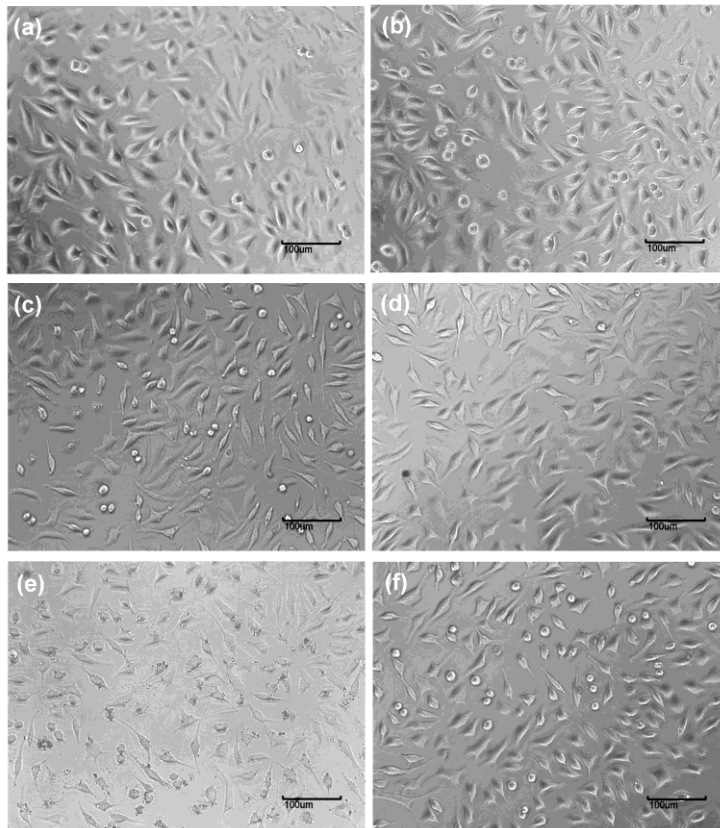


Figure 55: L929 cells incubated with (a) cell control and 50% extracts of (b) smCHD0 (c) 'BioCaS' (d) smCHD4 (e) smCHD5 and (f) 6.25% extract of the smCHD5.

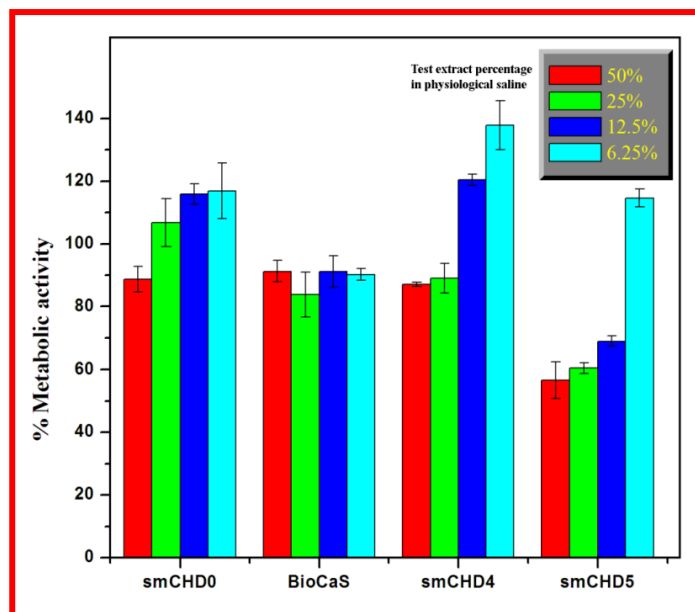


Figure 56: MTT assay results of smCHD0, 'BioCaS', smCHD4 and smCHD5, normalized against the control.

According to ANOVA single factor analysis there is no statistically significant difference in values as $p > 0.05$ for different dilutions of the same sample in BioCaS and as per students t-test the variation between the two samples at particular concentrations are negligible. However, smCHD4 and smCHD5 samples show concentration dependent variation in cell viability but smCHD5 was found to be cytotoxic except 6.25% extract.

(iii) Human osteoblast like HOS cell compatibility- Live-dead assay

In the live–dead assay, fluorescence microscopic images (Figure 57) showed well-distributed viable cells on the surface of BioCaS. Only a very few necrotic cells were present, and hence negligible. HOS cells adhered well and spread on the surface, and attained a typical flat morphology occupying greater surface area (Lee and Kim, 2009). Whereas in smCHD0, very few cells were observed to be attached on the surface along with the dead cells distribution throughout. Unlike BioCaS, live cells display slightly flattened shape.

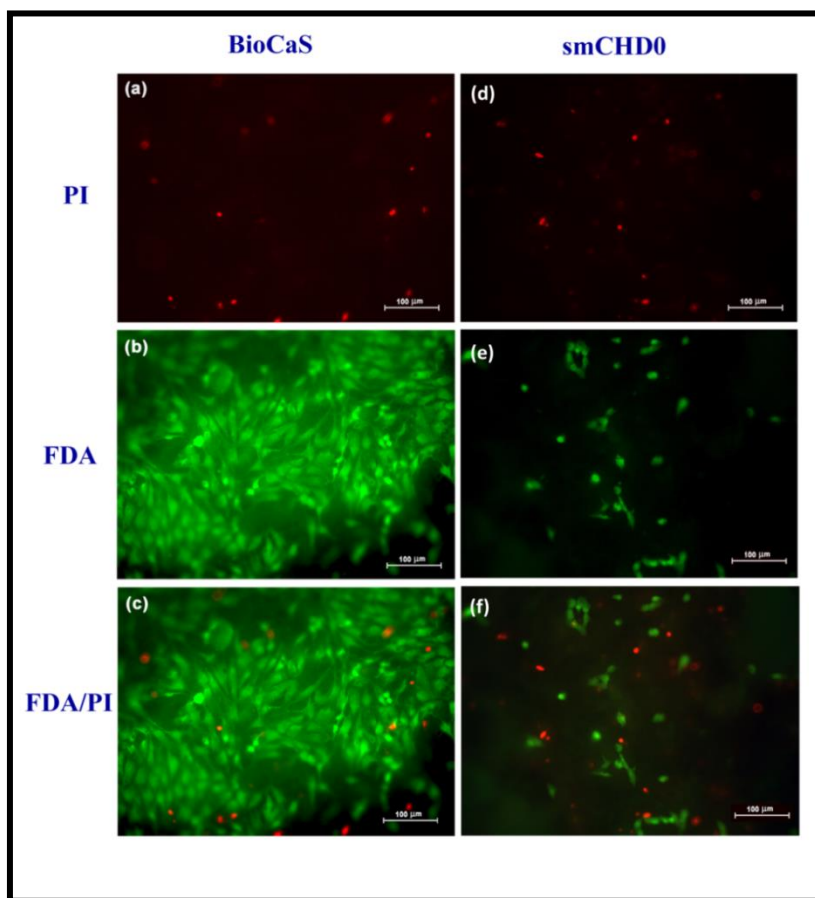


Figure 57: Live/dead double staining of HOS cells adhered on the surface of the BioCaS and smCHD0 a) PI signal b) FDA signal and C) overlay of FDA and PI signal (scale bar 100 µm)

Z-stack confocal microscopic images of the HOS cells at consecutive depth intervals of 11.2 μm from the surface of the BioCaS and depth code profile as shown in figure 58&59 depicted that the viable HOS cells were significantly attached on the surface and pores of the BioCaS material. Necrotic cells were absent and noted that viable cells were found up to 101.1 μm inside the cement. However in smCHDO the necrotic cells were found to be distributed along with viable cells (Figure 60). Depth code profile (Figure 61) has shown that most of the viable cells are found to be on the surface of the cells with very little population towards depth which extends to a maximum of 45 μm . Hence BioCaS is ensured to be suitable scaffold for attaching and adhering the bone cells.

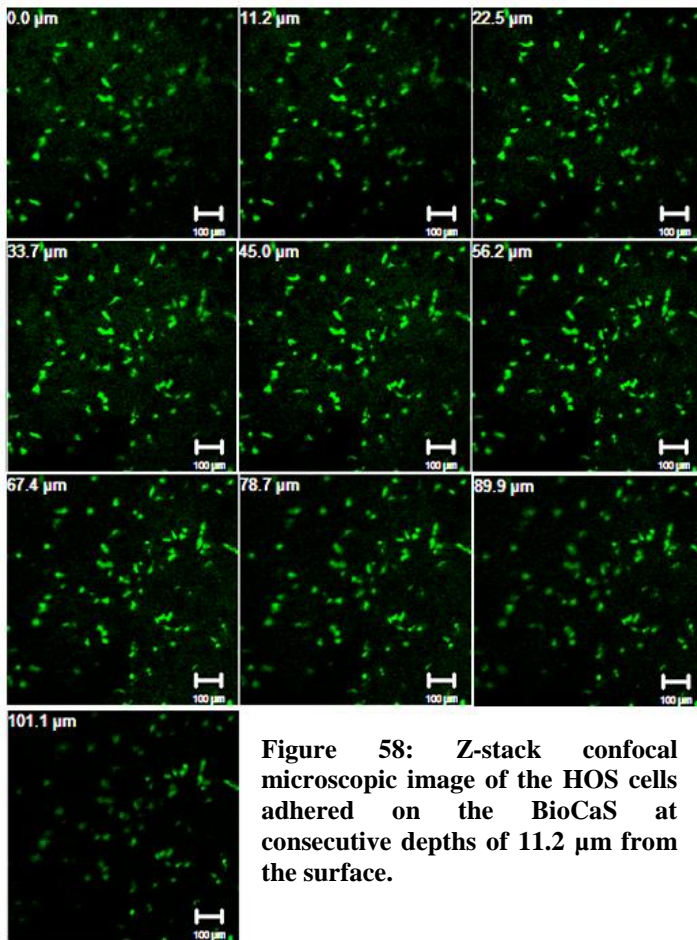


Figure 58: Z-stack confocal microscopic image of the HOS cells adhered on the BioCaS at consecutive depths of 11.2 μm from the surface.

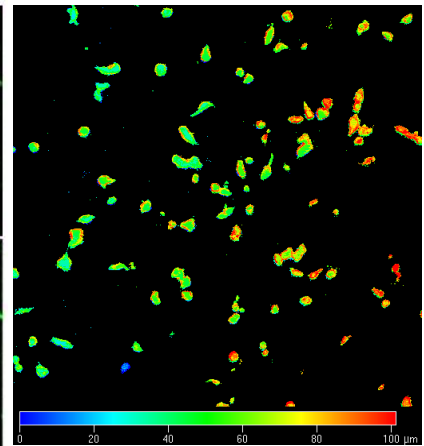


Figure 59: Depth code analysis showing the cell viability on the BioCaS bone cement.

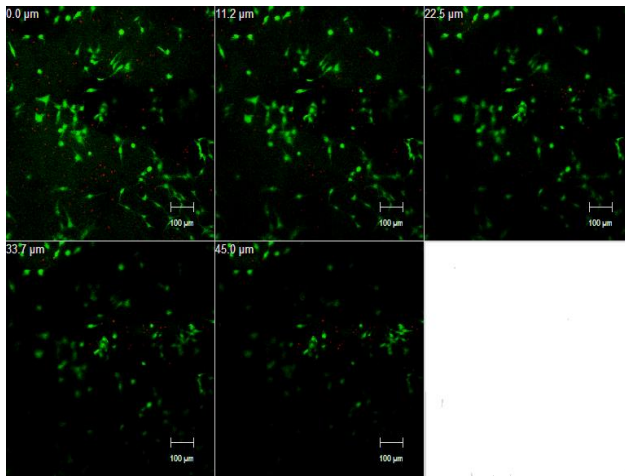


Figure 60: Z-stack confocal microscopic image of the HOS cells adhered on the smCHD0 at consecutive depths of 11.2µm

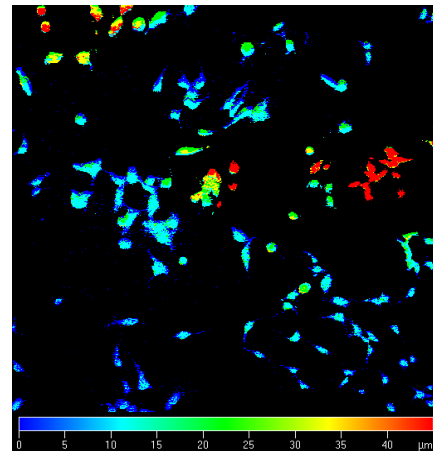


Figure 61: Depth code analysis showing the cell viability on the smCHD0 bone cement

(iv)Plastic adherence of HOS cells during cell adhesion – F-actin staining

Further we examined the effect of the BioCaS and smCHD0 on the fundamental component of cytoskeleton structure ie. F-actin of osteoblasts, which evaluate the plastic adherence property of HOS cells on cement matrix.

Polystyrene/plastic adherent HOS cells are shown to spread quickly upon adhesion with an increase of cytoskeleton associated F-actin. Fluorescent microscopic images of actin staining are shown in Figure 62. However in BioCaS, the no.density of F-actin were observed to be more and diffusely distributed throughout the cells compared to smCHD0. Cells in the smCHD0 contained a few F-actin fibers distributing around the nuclei of the cell and disorganised structure could also be seen. Cells in smCHD0 are found to be attached but spreading and proliferation were found to be less compared to BioCaS (Cenni *et al.*, 2011). However the very low cell number density in smCHD0 may due the property of the material, i.e. uneven surface and leaching of the ions and hence removal of the cells during the washing process. On the otherhand the surface of the BioCaS enhances better cell adhesion.

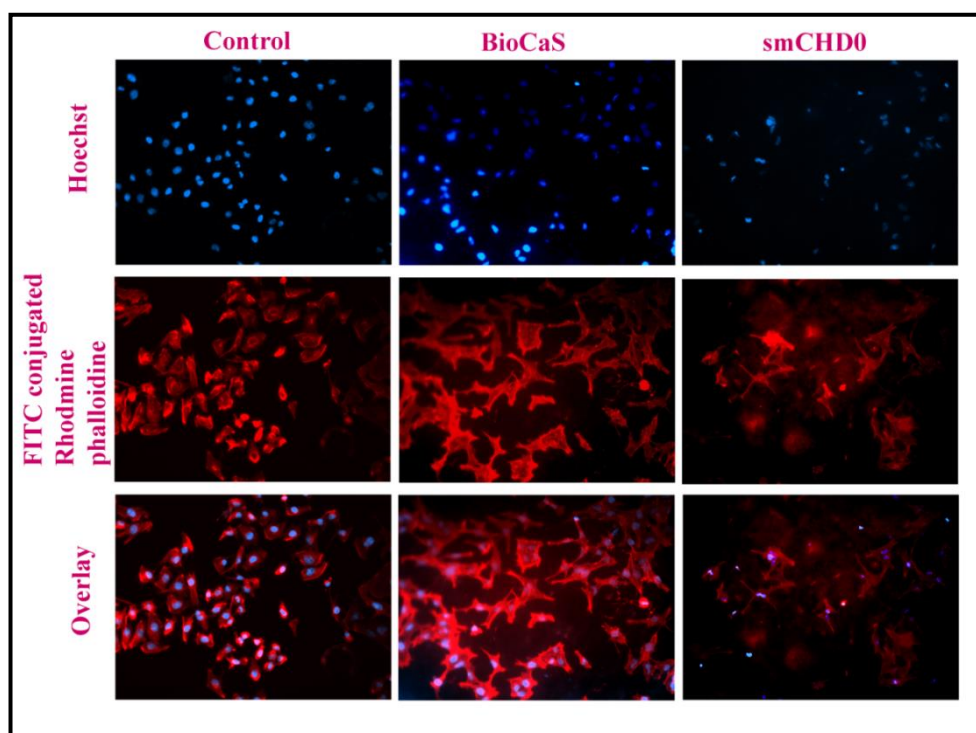


Figure 62: F-actin of HOS cells, adhered on the surface of glass coverslip, BioCaS and smCHD0 stained using rhodamine-phalloidin and nuclei stained with Hoechst 33258 (magnification $\times 20$).

(v) Cell Morphology and adherence of HOS cells seeded on the bone cement Using Scanning Electron Microscopy

As evident from the ESEM micrograph, HOS cells were well attached and evenly spread on the surface with cell to cell contact and attained typical flat morphology within 24 hours after treatment (Figure 63a). Some of the cells were found to develop filopodia and the magnified view of one such region is as shown in Figure 63(b) indicating the focal adhesion with the matrix linking it to the cell surface (Lodish *et al.*, 2004). However in smCHD0 the cells were noted to be attached but with low population Figure 63(c). Magnified view showed typical morphology but no filopodia formation Figure 68d. It is evident that the surface of the BioCaS injectable bone cement with phosphate incorporated calcium sulfate dihydrate crystal lattices perform well as a suitable scaffold for bone tissue regeneration

which excluded from the normal limitation of limited biocompatibility of the Gypsum based bone substitute material.

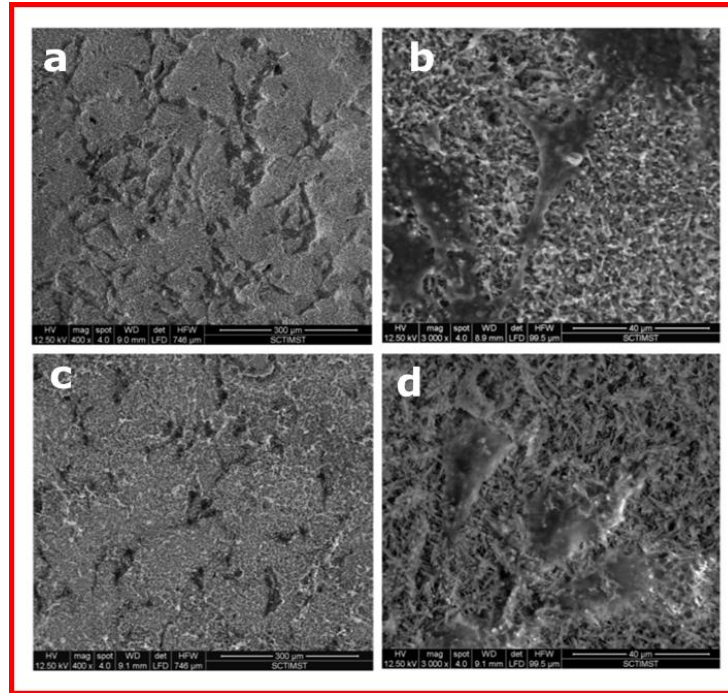


Figure 63: SEM image of HOS cells a) on the surface of BioCaS b) the corresponding magnified view c) on the surface of smCHD0 d) the magnified view.

4.3.1.4 Haemolytic potential

In the test for haemolytic potential, the smCHD0 and BioCaS cement gave an average percentage haemolysis of 0.16 ± 0.3768 and 0.14 ± 0.03 respectively whereas that for the reference material (empty polystyrene dishes) was 0.07 ± 0.01 (where $n=3$). As per ANOVA single factor and subsequent students' t-test, there is no significant difference between the smCHD0 and BioCaS towards hemolysis (Figure 64).

However both of them show considerable hemolysis compared to reference material. The free plasma hemoglobin concentration is normally 0 mg/dl to 10mg/dl *invivo*, where as the normal range of total blood haemoglobin concentration is 11000mg/dl to 18000mg/dl'. Considering the range it could be clear that the normal hemolysis value highest limit is $\approx 0.1\%$. Nevertheless for a biomaterial for implant applications, the tolerable limit of

haemolytic potential is specified as 5% (Kapusetti *et al.*, 2013, Montanaro., 2001). The haemolytic potential of smCHD0 and BioCaS sample is well below this limit and hence considered to be haemocompatible.

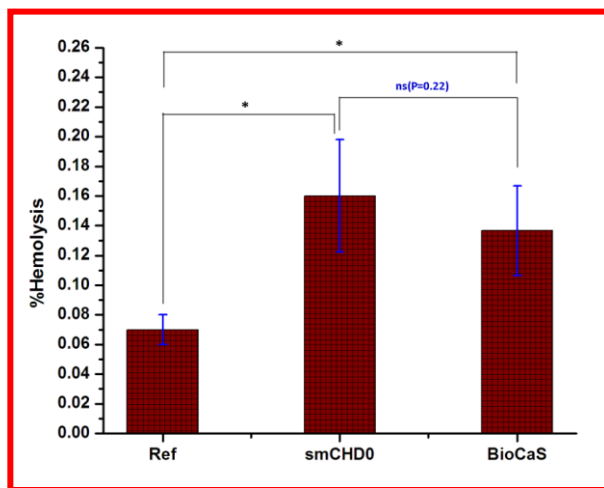


Figure 64: Potential of the BioCaS cement compared to unmodified cement and the reference material expressed as mean \pm SD (n=3) ns: non-significant.

4.3.1.5 Biocompatibility evaluation *in vivo*

(i) Acute systemic toxicity

The result of acute systemic toxicity testing was evaluated on the basis of toxic signs, symptoms (such as lethargy, hyperactivity and convulsions), body weight reduction or death of animals. The sample will be disqualified if: (1) two or more mice die, or (2) abnormal behaviour (such as convulsions or prostrations) occur in two or more mice, or (3) a body weight loss greater than 2 g occurs in three or more mice, during the procedure.

All the animals were healthy after the test and showed an increase in body weight (the change being <26%) after 72 h. No adverse clinical signs were observed for the cotton seed oil extract and the controls (cotton seed oil and physiological saline alone). The animals injected with physiological saline extract of the test material showed a transient reduction in motor activity immediately after the injection. They recovered to normalcy in a very short period of time (within in 30 seconds). Clinical observation data sheet for the test material is shown in Table 3.

Clinical observation	RE	MO	CO	RE	OC	CA	SA	PI	AN	MT	GI	SK
Intravenous route of administration Observation time interval - Imm./4h,24h,48h and 72h												
Control Group response (PS)	N	N	N	N	N	N	N	N	N	N	N	N
Test Group response (PS extract)	N	A	A	N	N	N	N	N	N	N	N	N
Intraperitoneal route of administration Observation time interval – Imm.4h,24h,48h and 72h												
Control Group response (CS)	N	N	N	N	N	N	N	N	N	N	N	N
Test Group (CS)	N	N	N	N	N	N	N	N	N	N	N	N



N-normal, A-abnormal,  -Throughout the time period of observation,  -Immediate

Table 3: Clinical observation data sheet for acute systemic toxicity RE-respiratory, MO-Motor, CO-convulsions, RE-Reflexes, OC-Ocular signs, CA-Cardiovascular signs, SA-Salivation, PI-Piloerection, AN-Analgesis, MT-Muscle tone, GI-Gastrointestinal, SK-Skin.

So we have analysed the PS extract of the test material for the estimation of eluted $[Ca^{2+}]$, $[P^{5+}]$ and $[S^{6+}]$ (Figure 65) . Blood serum calcium and phosphorus concentration in albino mice were in the range of 0.087 to 0.101 mg/ml and 0.054-0.093mg/ml respectively which is comparable to the human and were found out to be 0.105 mg/ml calcium, 0.031 mg/ml phosphorus and 0.016 mg/ml sulfur (Stringham et al., 1967, Quesenberry et al.). However the elutant contains 0.48 ± 0.03 mg/ml of calcium, 0.1662 ± 0.01 mg/ml of phosphorus and 0.44 ± 0.05 mg/ml of sulphur. .However the calcium concentration in the extract is found out to be higher compared to blood serum concentration and hence the slight prostrations and convulsions during the intravenous injection of the test extract may be due to the influx of calcium (situation similar to hypercalcemic condition) causing twitches and weakness and control the motor activity. Once it passes through the systemic circulation the

effect get reduced due to the dilution effect (Aguilera and Vaughan, 2000). This phenomenon might have occurred due to the presence of eluted calcium ions from the cement. Despite this observation, no adverse event (mortality or morbidity) was observed. As there were no deaths or abnormal behaviour or weight loss in the test animals, the material is declared to pass the test.

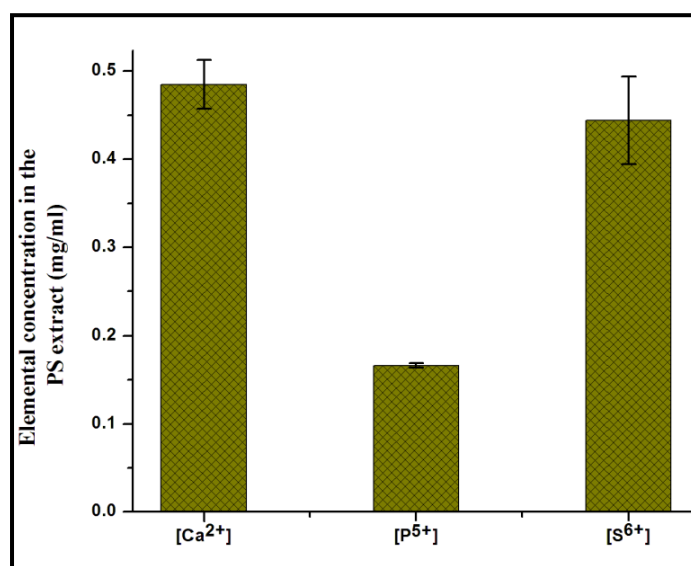


Figure 65: Eluted elemental concentration in the intravenously administered PS extract through OES –ICP

(ii) Pyrogenic potential of BioCaS

The criterion for pyrogenicity is a rise of 0.5 °C in any of the three rabbits above their control basal body temperature. During the experiment the three test animals showed temperature rises of 0.26, 0.31 and 0.13 °C. The sum of the three individual maximum temperatures is 0.7 , whereas the stipulated limit for the same is 1.4. Hence the test material could be considered non-pyrogenic.

(iii) Intracutaneous reaction and skin sensitisation

The intracutaneous reactivity test was uneventful-the animals did not show any abnormalities after intradermal injection. The average of the irritation scores for erythema and oedema for each of the animals were calculated. The sums were taken for the control group and test group. The requirements of the material to pass the test could be met if the difference

between test sample mean score and the control mean score is less than or equal to one. The physiological saline and cotton seed oil extracts of the BioCaS cement gave a total mean score difference of 0, thus making the material acceptable.

In the skin sensitization study with the extract of the material in guinea pigs, the test and control animals were observed at 24, 48 and 72 h after the challenge phase and the reactions for erythema and oedema were scored (Magnusson et al., 1975). An escalation of one grade or higher in the test group compared with the control group indicates sensitization. The physiological saline extract of BioCaS did not show any adverse reactions during the induction or challenge phase. The scores for erythema and oedema after the challenge phase were equal to the grading corresponding to the controls. It could be concluded that the material does not elicit hypersensitivity under the laboratory conditions simulated.

(iv) Efficacy evaluation of BioCaS through bone implantation

(a) Histology evaluation

Figure 66 shows the image of a rabbit femur during surgery after delivering the cement material from syringe, which conformally filled and set in the defect site.

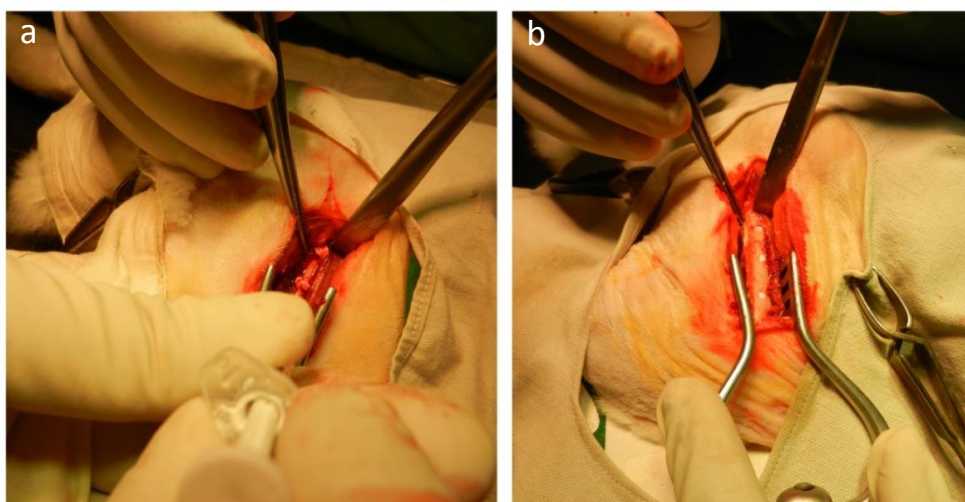


Figure 66: Placement of samples in bone implantation study in rabbit femur : a) Injecting the BioCaS cement in the defect site using syringe b) BioCaS cement after setting. Details of the surgical procedure are given in the text.

The post-implantation period was uneventful, without any mortality or morbidity. Macroscopic evaluation of the explanted sites did not reveal any discoloration, haemorrhage, encapsulation, evidence of infection, degeneration or necrotic changes in any of the time periods. At least 10 test sites and 10 control sites were evaluated for each time period, as suggested in ISO 10993 (Larsson and Hannink., 2011). On an overall estimation, the histological sections did not show any non-calcified fibrosis, inflammation or necrosis at the implant site.

At 12 weeks, the test sites showed implanted material to be well integrated with the host bone at the defect boundaries. In some samples, resorption was seen in the central part (Figure 67(a)). New woven bone formation was observed from periosteal and endosteal surfaces and along the sides of the cavity. The material part, seen as a dark region in low magnification, revealed very fine particles at high magnification (Figures 67(c) and (e)). A certain amount of the implanted part at the boundaries was seen replaced by new bone.

There was very good apposition between the implant material and the newly formed bone. New woven bone formation was observed at the implant–bone interface. In the resorbed portions, voids were present with foci of new woven bone with osteoid matrix. Osteoblasts were appreciable in number (stained in blue) with good osteoblastic activity. The rosettes of osteocytes indicated the maturation of woven bone. Early formation of the Haversian system was seen in the host bone–implant interface and in the resorbed portions indicating maturation (Figure 67(c)).

The control sites at 12 weeks showed very slight material resorption (Figure 67(b)). Mature woven bone was seen formed from the periosteum, endosteum and along the sides of the cortex. Good integration was observed between the implant material and new bone. Higher magnification revealed the porous ceramic structure. Ingrowth of mature woven bone into the implant pores and on either side of the implant was noted (Figures 67(d)&(f)).

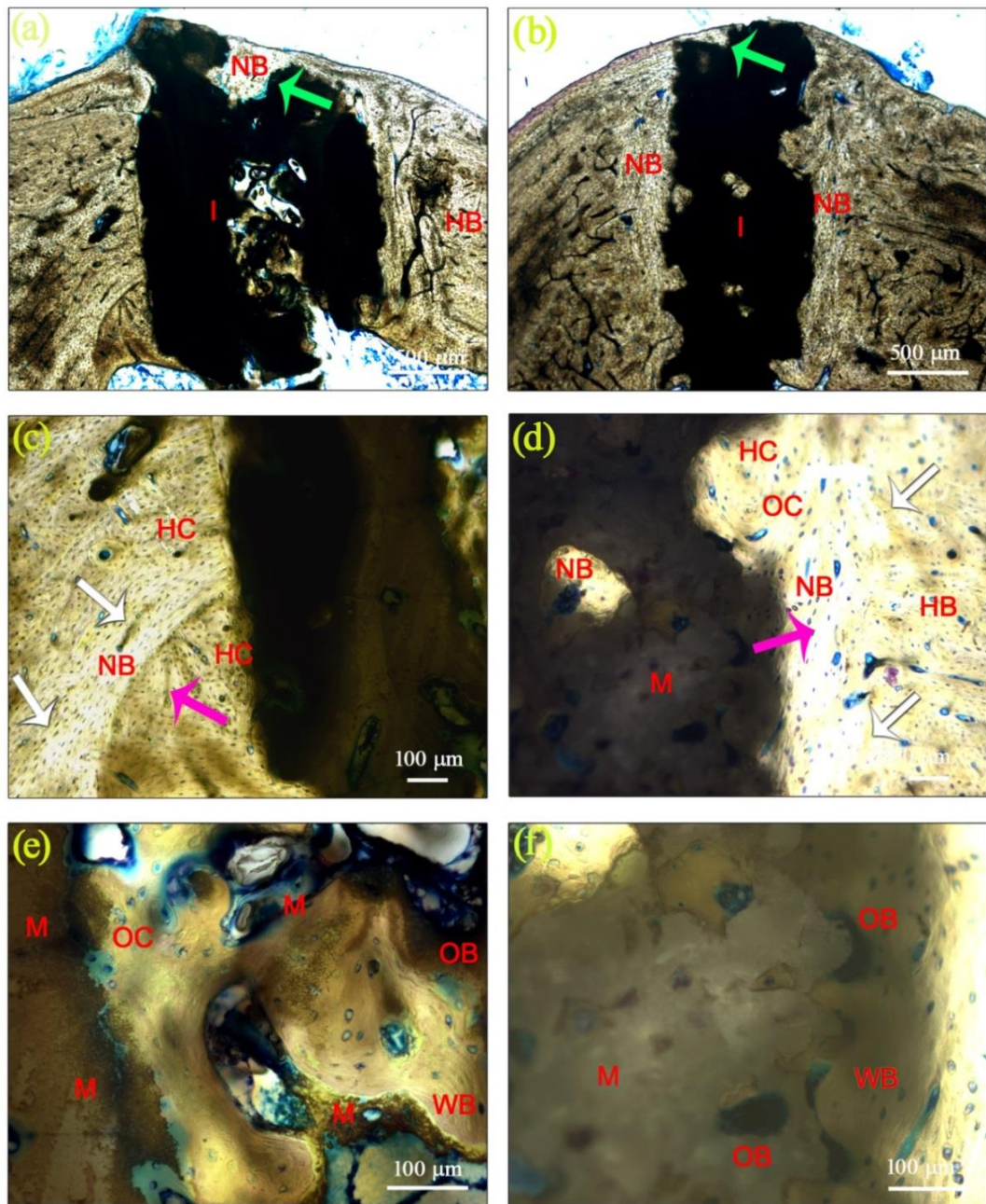


Figure 67: Photomicrographs of stained histological sections (Stevenels' blue staining followed by counter-staining with Van Gieson's Picro-Fuchsin) of the test sample (BioCaS, (a), (c) and (e)) and the control sample (hydroxyapatite ceramic, (b), (d) and (f)) at 12 weeks. Parts (a) and (b) show the implanted region at 4×magnification. Parts (c) and (d) show the implant to host bone boundary at 10×magnification. Portions of these regions are further magnified in (e) and (f) at 20×magnification. Abbreviations and symbols used: implanted site (I); newly formed bone (NB); host bone (HB); implanted material (M); new woven bone (WB); lamellar bone (LB); osteoblast (OB); osteocyte (OC); Haversian canals (HC). Arrow heads: interface of the host and new bone trabecula (white); bone formation from periosteal aspects of the cavity (green); bone formation from endosteal aspect of the cavity (pink).

In some locations, Haversian system formation was found. Osteoblasts were also found in good number with osteoid formation inside the pores of the implant material.

The test sites at 26 weeks showed drastic changes compared with the earlier period. Healing of the defect region and remodelling of new bone was noted in both groups. Most of the test material was replaced by newly formed bone (Figure 68(a)). New woven bone and lamellar bone with a Haversian system was observed in the implant site with active resorption of the implant material. These new bone trabeculae with osteoid and cells were fully integrated with the material (Figures 68(c)&(e)). Even in the dark regions lamellar structure was present, with very little material remaining (seen as islands of fine particles). Some voids due to resorption could be seen which were inhabited by osteoblasts and osteocytes. In the corresponding control sites (26 weeks) material resorption was evident, but not to a great extent (Figure 68(b)). New mature woven bone was observed which almost completely filled the grooves and pores in the hydroxyapatite ceramic. Very good apposition was seen between the new bone and implant and also between the implant material and newly formed woven bone (Figures 68(d) and (f)). The Haversian system was also detected in the area of new bone formation, indicating osteogenesis.

At 52 weeks, healing of bone defects and remodelling of new bone was more prominent in both groups. In the test implantation site the cement particles were still present, but scarcely at the implant site, engulfed with new bone (Figure 69(a)). New bone from host side was in indistinguishably close apposition with the implant in multiple areas (figure 69(c)). New mature woven bone with a well-formed Haversian system filled the implanted area, with good osteoblastic activity (Figures 69(c) and (e)).

The hydroxyapatite ceramic control material was still present in the 52 week sample, more than half the portion remaining (Figure 69(b)). Woven bone was observed in the pores and mature woven bone formation with a Haversian system was observed in the cortical bone–implant interface (Figures 69(d) and (f)).

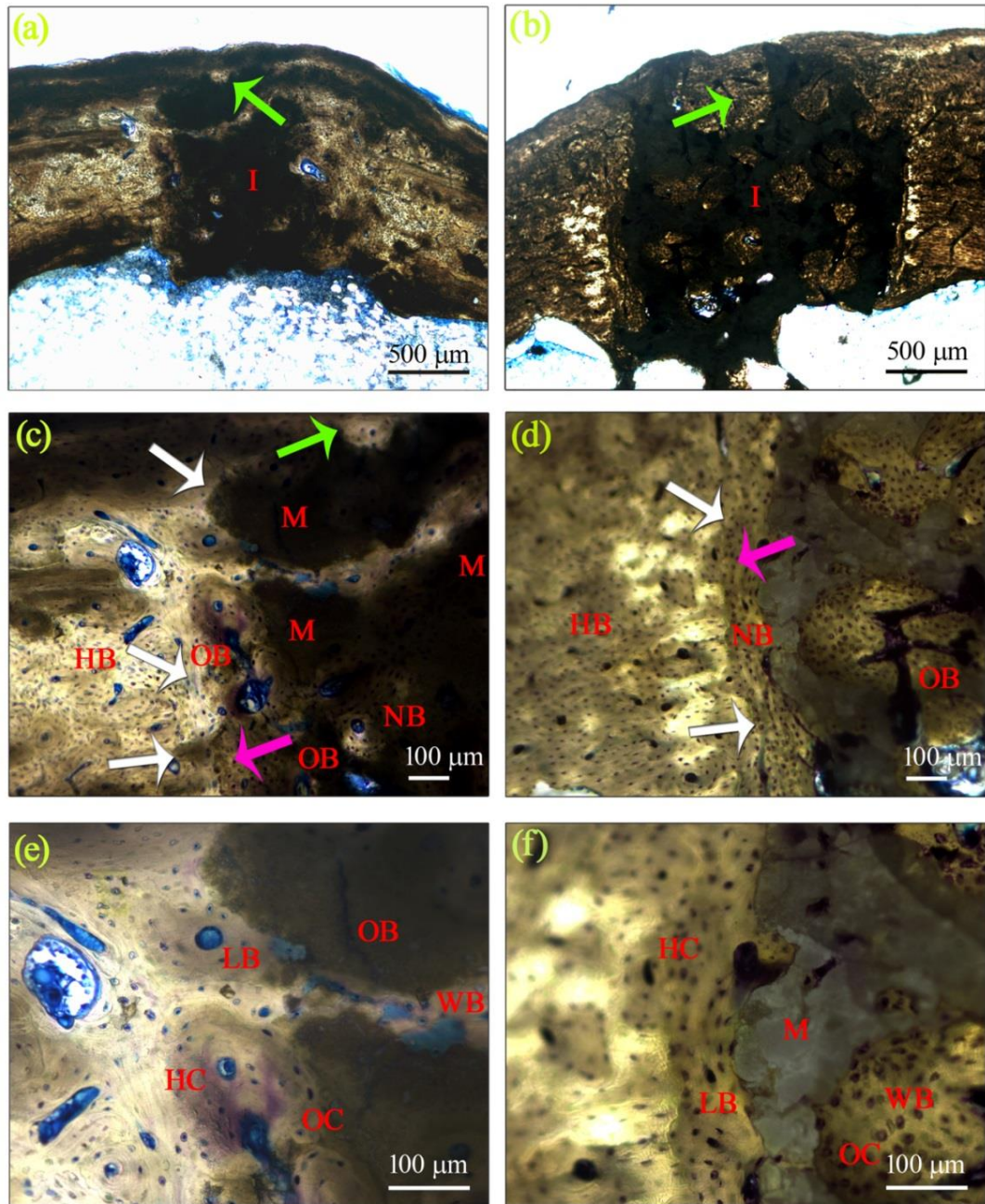


Figure 68: Photomicrographs of stained histological sections (Stevenels' blue staining followed by counter-staining with Van Gieson's Picro-Fuchsin) of the test sample (BioCaS, (a), (c) and (e)) and the control sample (hydroxyapatite ceramic, (b), (d) and (f)) at 26 weeks. Parts (a) and (b) show the implanted region at 4×magnification. Parts (c) and (d) show the implant to host bone boundary at 10×magnification. Portions of these regions are further magnified in parts (e) and (f) at 20×magnification

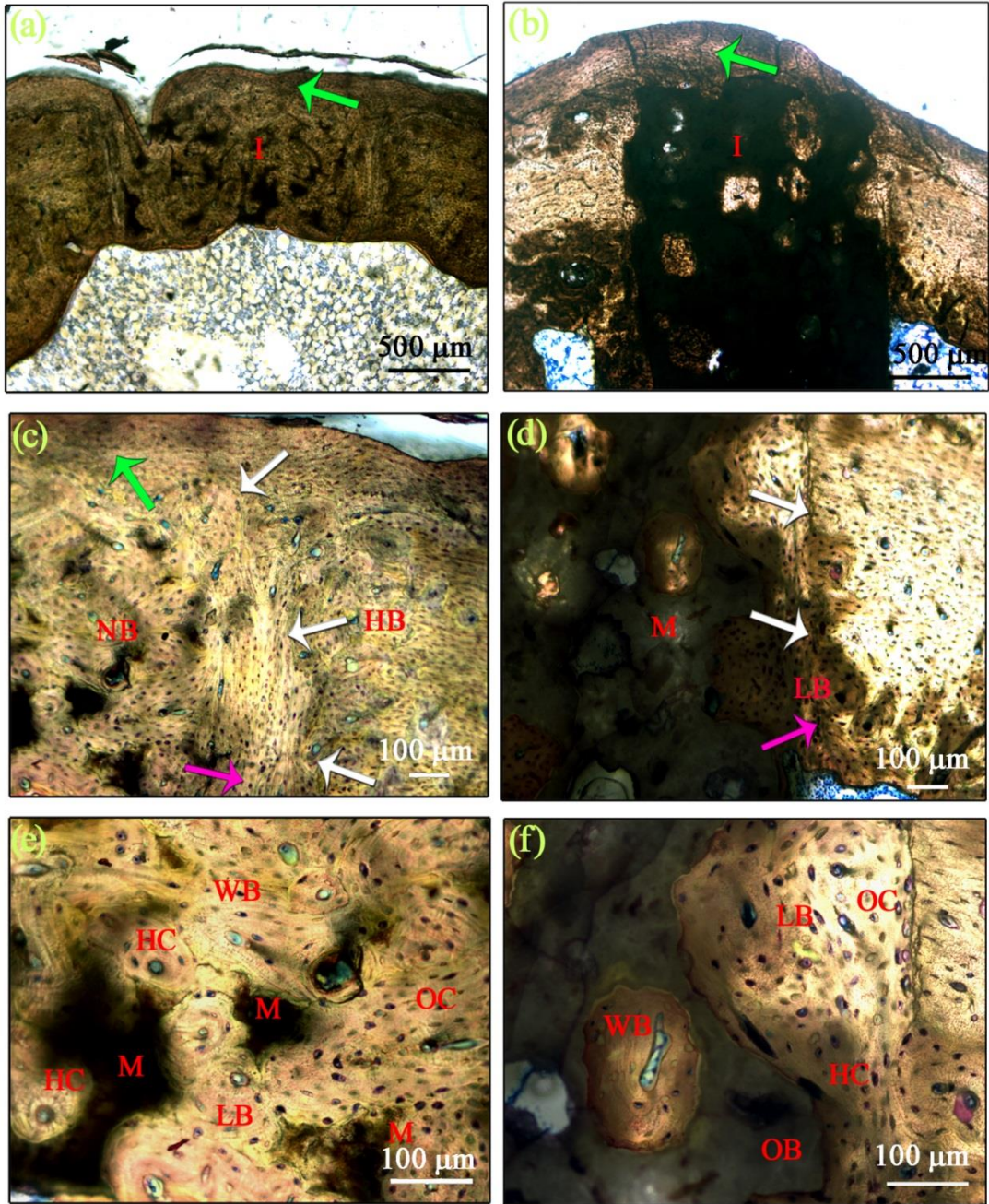


Figure 69: Photomicrographs of stained histological sections (Stevenels' blue staining followed by counter-staining with Van Gieson's Picro-Fuchsin) of the test sample (BioCaS, (a), (c) and (e)) and the control sample (hydroxyapatite ceramic, (b), (d) and (f)) at 52 weeks. Parts (a) and (b) show the implanted region at 4×magnification. Parts (c) and (d) show the implant–host bone boundary at 10×magnification. Portions of these regions are further magnified in (e) and (f) at 20×magnification

(b) Elemental composition analysis in the defect site of BioCaS implant

The dried histological samples (BioCaS) were analysed in SEM and EDS to check the micromorphology at the interface and identify the elemental composition. In the 12 weeks section (Figure 70(a)), the interface could be identified with new bone infiltration towards material and the area scan showed the peaks of Ca, S and considerably high intense peak of P. The analysis confirmed the presence of BioCaS in the section along with the bone mineralisation (formation of hydroxyapatite). At 26 weeks, considerable resorption of the BioCaS with the replacement of new bone is evident. The EDS pattern confirms the presence of traces of BioCaS (Figure 70(a)).

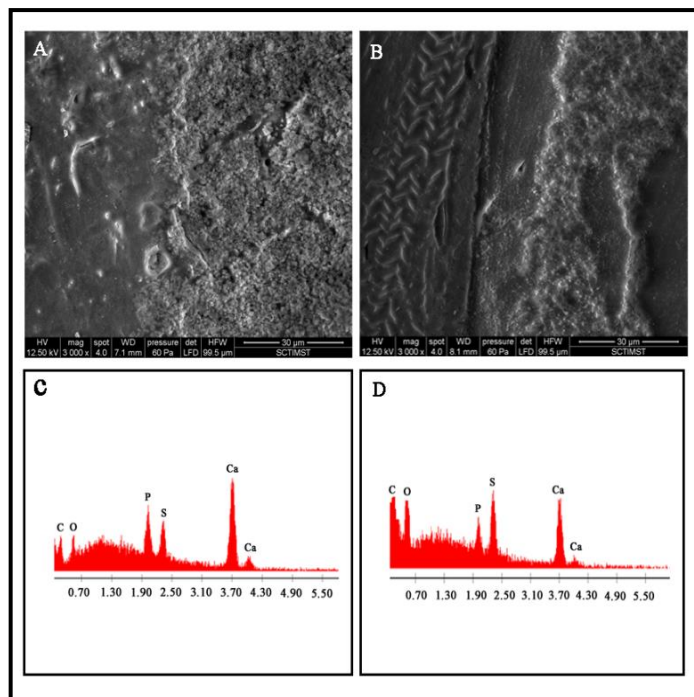


Figure 70: The interface regions of implanted BioCaS A) 12 weeks after implantation B) 26 weeks after implantation and C) and D) their corresponding EDS pattern (scale bar=30μm)

(c) Histomorphometric evaluation of the implanted sections

At all the time points test groups have shown higher biodegradation rate compared to control HA (Figure 71 b). At 12 weeks the the residual material of the BioCaS was found out to be 59.65% against the 73.69% of the control scaffold. At 26 weeks, only 32.7% bone cement

remains in the implanted site while in HA it is 57.2%. Even after one year >40% of HA still remains in the site, but only a very little quantity of BioCaS remained in the defect site ie. 10.37% after one year. The degradation rate of BioCaS hence promoted the new bone formation.

At 12 weeks, $40.34 \pm 1.17\%$ regeneration efficiency observed which increased to 64.85 ± 3.70 and 88.72 ± 1.60 during 26 and 52 weeks respectively (Figure 71a). However even with very high osteoinductivity the low degradation rate prevent the bone regeneration at residual material containing region in HA implanted group, for which the RE ratio is only 24.76 ± 3.02 , 34.05 ± 3.56 and 57.81 ± 2.03 after 12 , 26 and 52 weeks. The osteoconductive nature of BioCaS compared with HA scaffold is evident through the quantitative assay. The material however has shown slow degradation compared to the reported degradation rate of calcium sulfate ie. 6-12 weeks.

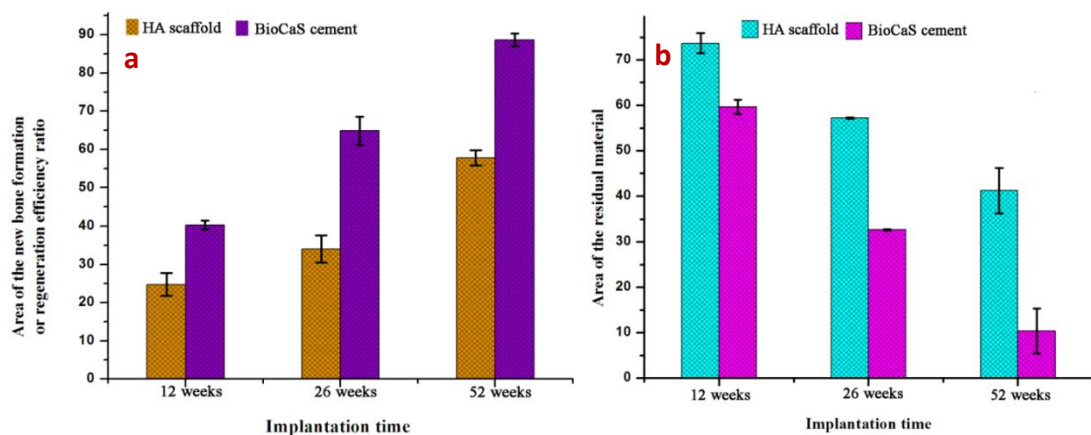


Figure 71: Histomorphometrical evaluation. a) The new bone formation area b) The residual materials corresponding to HA and BioCaS after 12, 26 and 52 weeks of implantation

(d) Micro-CT analysis

Density histograms across the host bone implant interface of the defect site of the implanted group at three time periods are shown in Figure 72-74 respectively. The approximate average values in the new bone and host bone region are marked in each density histogram. The reference line BMD value of host bone of the implanted animals in the experimental groups

were found to be in the range of 1237-1340 mg/cm³. Bone mineralisation density (BMD) of the newly formed bone in the density histogram of the control scaffold implanted group has shown considerably higher values above 2100 mg HA/cm³ irrespective of the implantation period.

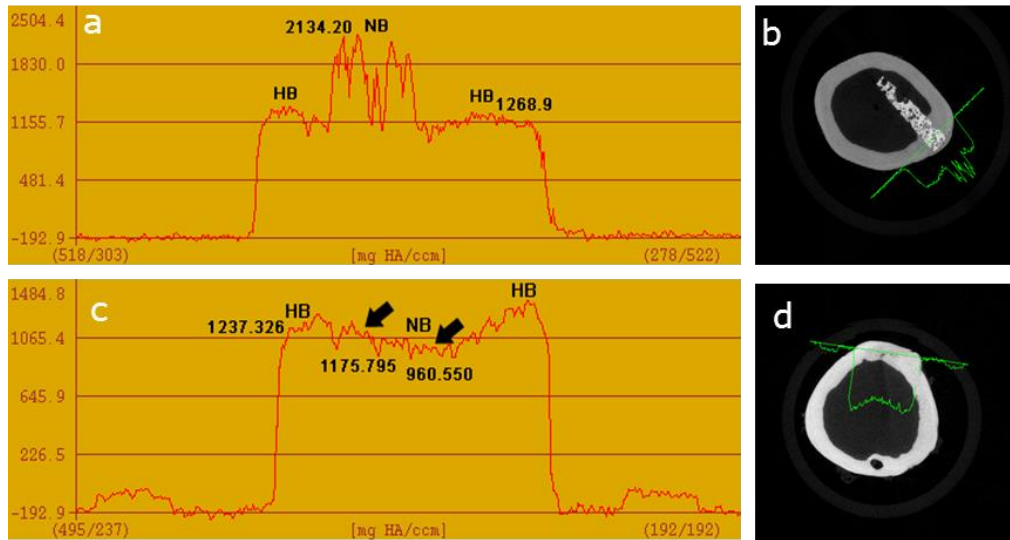


Figure 72: a) and c) Density histogram evaluation of 12 weeks implanted site depicting the bone mineralization density (in mg HA/ccm indicating milligram of HA per cubic centimeter) across the defect site including the newly formed bone (NB) and the host Bone (HB) in BioCaS and HA scaffold implanted group, respectively, derived from the corresponding 2D micro-CT slices shown in (b) and (d).

A sharp increase in the BMD was observed when crosses from host tissue to control scaffold implant region and the higher value was recorded irregularly over the entire new bone region at all the time period which is attributed to the higher density of the sintered ceramic (prior to implantation). However in the BioCaS group at 12 weeks implantation, the BMD was found to be in the range of 960.550 to 1175.795 (attributed to low density of the cement compared to ceramic) compared to the host tissue density of 1237.326 mg/cm³.

At 26 weeks the value increased to 1226.95 against the HB of 1240.917 mg/cm³ and perfect matching continuity with host bone with BMD value around 1257.297 was observed at 52 weeks which indicates the bone remodelling and the quality of the new bone formation.

The higher mineral density of the control scaffold compared to HB indicates the low degradation rate.

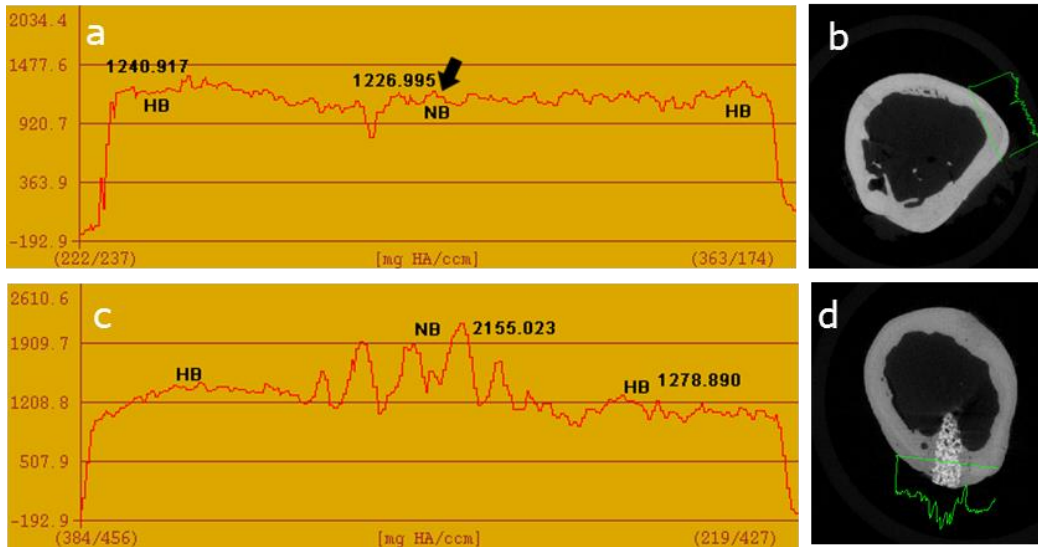


Figure 73: a) and c) Bone mineralization density distribution plot [mg HA/ccm indicating milligram of hydroxyapatite, HA per cubic centimeter] across the defect site in BioCaS and HA scaffold implanted group acquired from the corresponding 2D slices (b) and (d) respectively 26 weeks post implantation

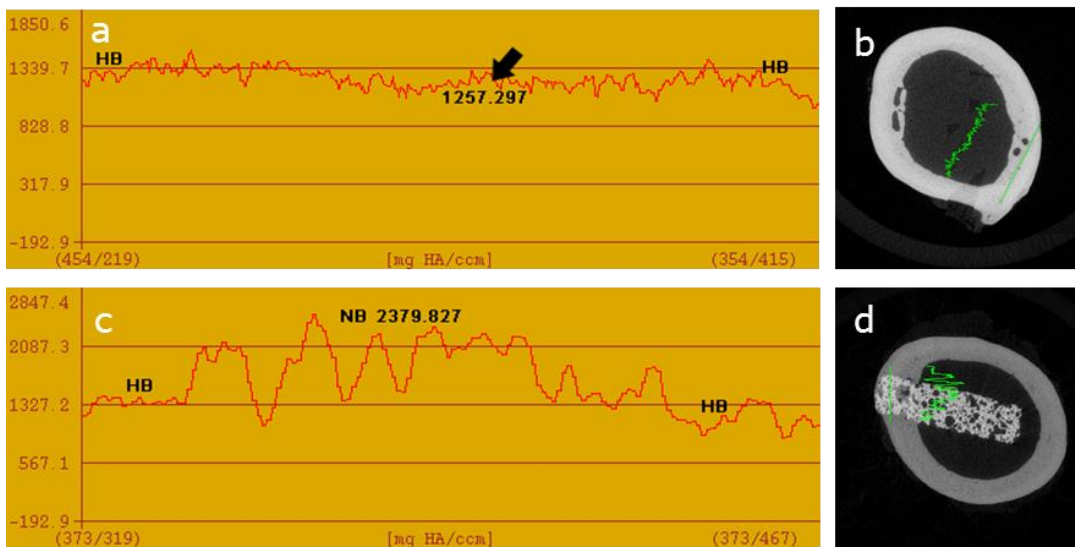


Figure 74: a) and c) Bone mineralization density distribution plot [mg HA/ccm indicating milligram of hydroxyapatite, HA per cubic centimeter] across the defect site in BioCaS and HA scaffold implanted group acquired from the corresponding 2D slices (b) and (d) respectively 52 weeks post implantation

The BMD value close to the HB in alternate regions of the histogram of NB site in control HA at all time points indicates the new bone formation at the resorption site. However in both the case the continuity across the HB/NB interface with out any gap or considerable drop indicates the integration of the host tissue with the implant. Nonetheless the density (BMD) of the newly formed bone on both test and control implants was uniform throughout the tissue construct.

PHASE 4

4.4 Therapeutic efficacy of injectable BioCaS

4.4.1 Injectable BioCaS for Gentamicin (GS) loading in the BioCaS cement and in vitro elution profile

The required concentration of the drug (corresponds to 1g of the drug per 40 g of the cement powder) of BioCaS cement were incorporated with 0.6 ml of the wetting medium. The chemical reaction for the OPA-gentamicin derivatisation is based on the formation of isoindole derivative. OPA reacts with the free amino groups in Gentamicin sulphate in the presence of a reducing reagent like β -mercaptoethanol to form their isoindole-derivative which is chromophoric, making them suitable for UV detection at 333nm which was confirmed by the scanning of standard concentrations (Figure 75). Isopropyl alcohol were added to prevent the precipitation of derivative formed (Virto *et al.*, 2003).

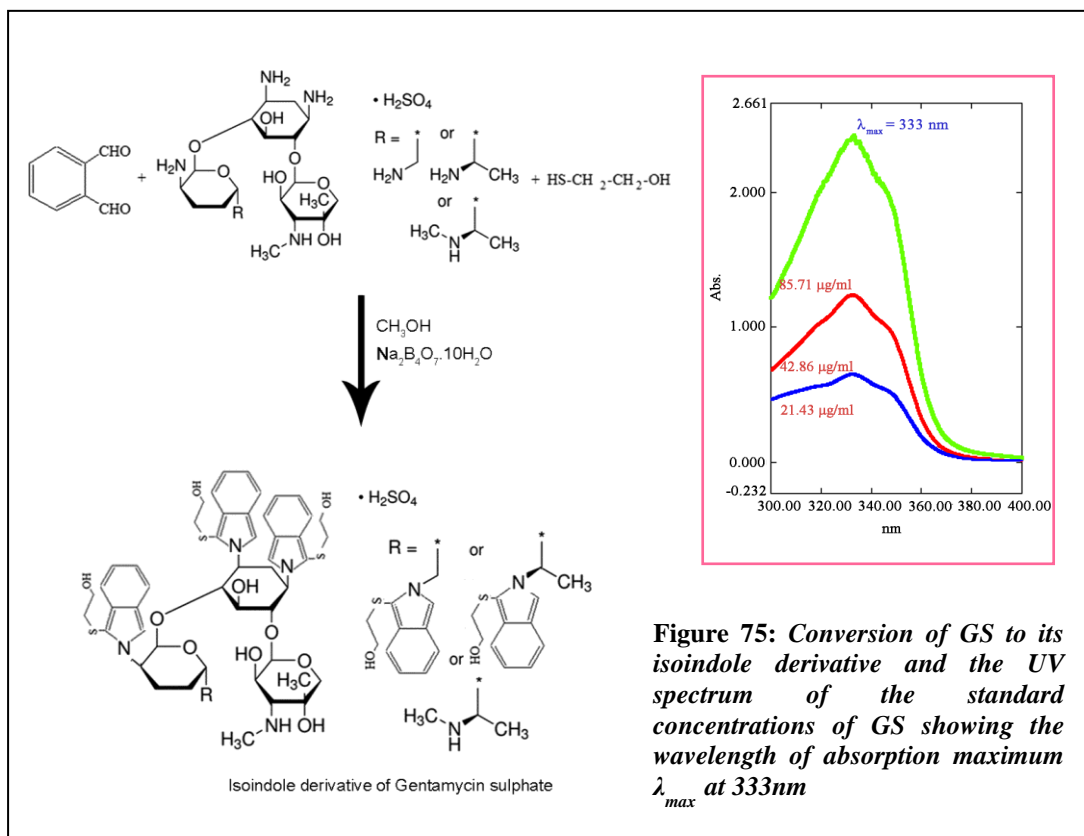


Figure 75: Conversion of GS to its isoindole derivative and the UV spectrum of the standard concentrations of GS showing the wavelength of absorption maximum λ_{max} at 333nm

Elution profile of the Gentamicin were plotted with the amount of the GS eluted in mg/ml/g against the number of days. The cumulative amount of the drug released and the percentage cumulative amount of the GS were plotted in Figure 76. After the initial burst release the sustained release greater than minimum inhibitory concentration (MIC- 2-4 μ g/ml) was found out to be up to 17 days.

Almost $40.51 \pm 6.33\%$ of the loaded drug was released within the time period with the release of 11.34 ± 1.77 mg/ml/g (n=3). The drug elution was better fitted with Kosmeyer-peppas model ($R^2 = 0.95$) (Figure 76d); release exponent was derived from the slop of the log (M_t/M_∞) vs. log t (where M_t/M_∞ is the fraction of the drug released at time t)

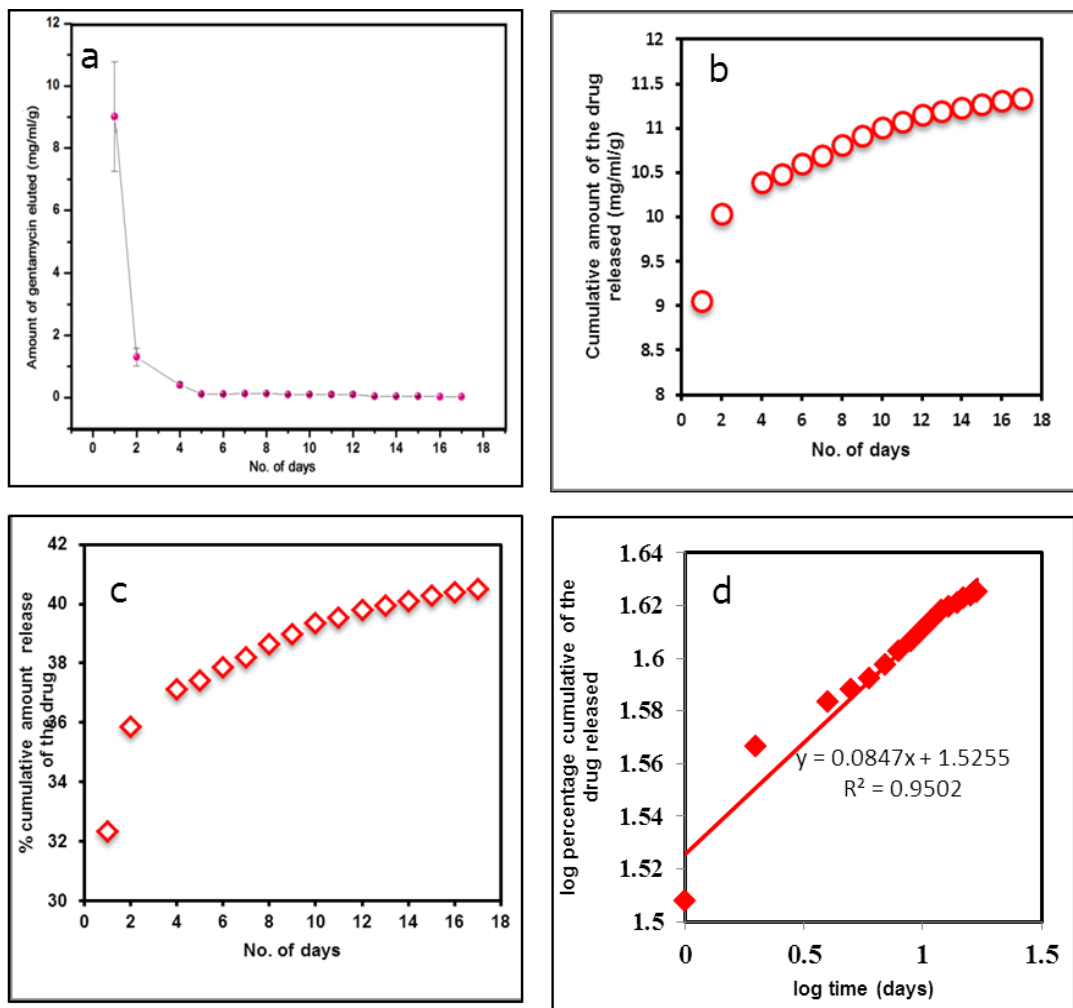


Figure 76: Drug elution of GS from BioCaS bone cement a) Elution profile, b) Cumulative amount of the drug released and the c) The percentage cumulative drug release against time. d) shows the fitting in Korsmeyer- peppas model

which is equal to 0.0847 with quasi-fickian diffusion mechanism ($n < 0.45$) i.e. controlled predominantly by diffusion (Khan *et al.*, 2010). The diffusion flux goes from region of higher concentration to region of lower concentration, which is proportional to the concentration gradient, where drug molecules are supposed to pass through a preferential way inside interconnected pores, guided by wicking, which involves the penetration of buffer medium by the action of capillary pressure and the mass transport of the dissolved drug from the interface to the exterior liquid. However the very low value of n indicates apart from diffusion the release may get affected by some physico-chemical phenomena for instance chemical interaction of the drug with matrix, surface elution etc.

4.4.2 Invitro elution profile of Vancomycin loaded BioCaS

Required concentration of Vancomycin hydrochloride (VH) (corresponds to 1g of the drug per 40 g of the cement powder) was loaded among the particles of the BioCaS through the wetting medium during cementing reaction. The structure of the VH and λ_{\max} of UV absorption are shown in figure 77.

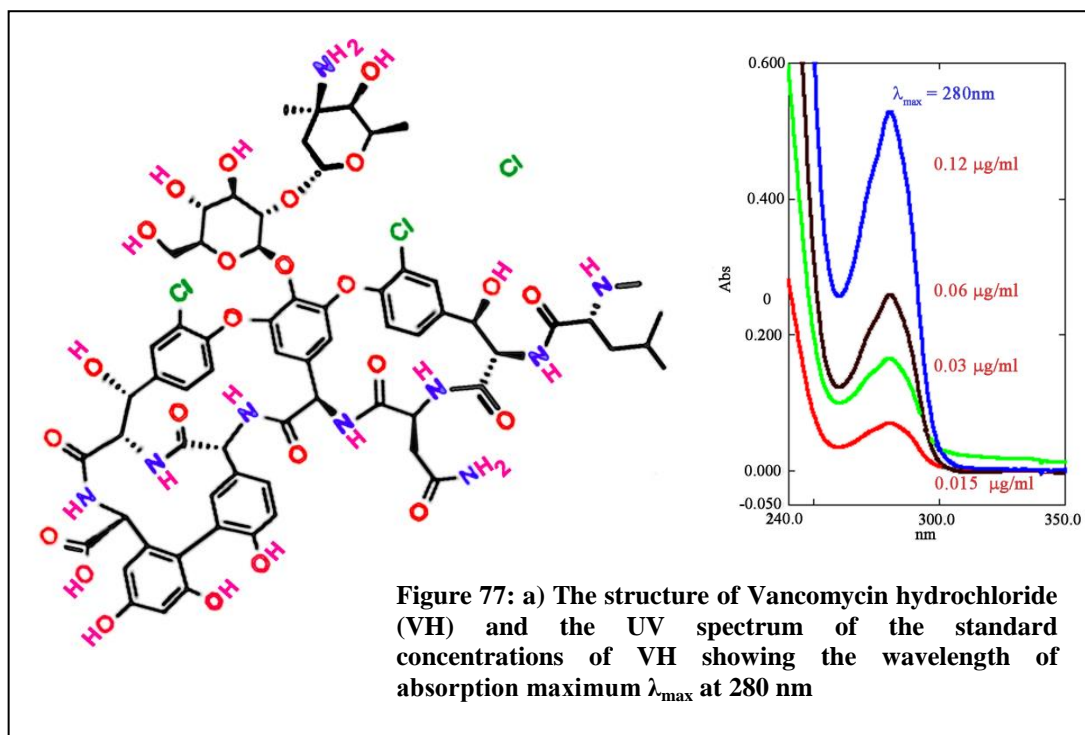


Figure 77: a) The structure of Vancomycin hydrochloride (VH) and the UV spectrum of the standard concentrations of VH showing the wavelength of absorption maximum λ_{\max} at 280 nm

The drug release profile data are shown in figure 78. After the initial burst release, sustained release greater than MIC-4 μ g/ml was found up to 47 days. The cumulative amount of the drug released was found out to be 2.71 ± 0.16 mg/ml/g (n=3) and the cumulative percentage of the drug released were found out to be only $10.85 \pm 0.62\%$ of the initial loaded drug. In BioCaSV also, the curve fitting was best done with K-P model with n value close to 0.43 ie. the released amount of the drug were controlled purely with diffusion mechanism. Low drug release percentage may be due to the drug entrapped inside the matrix which could come out only during the degradation or due to the interaction of the drug with matrix. In comparison with GS, the entrapment could be higher in the VH.

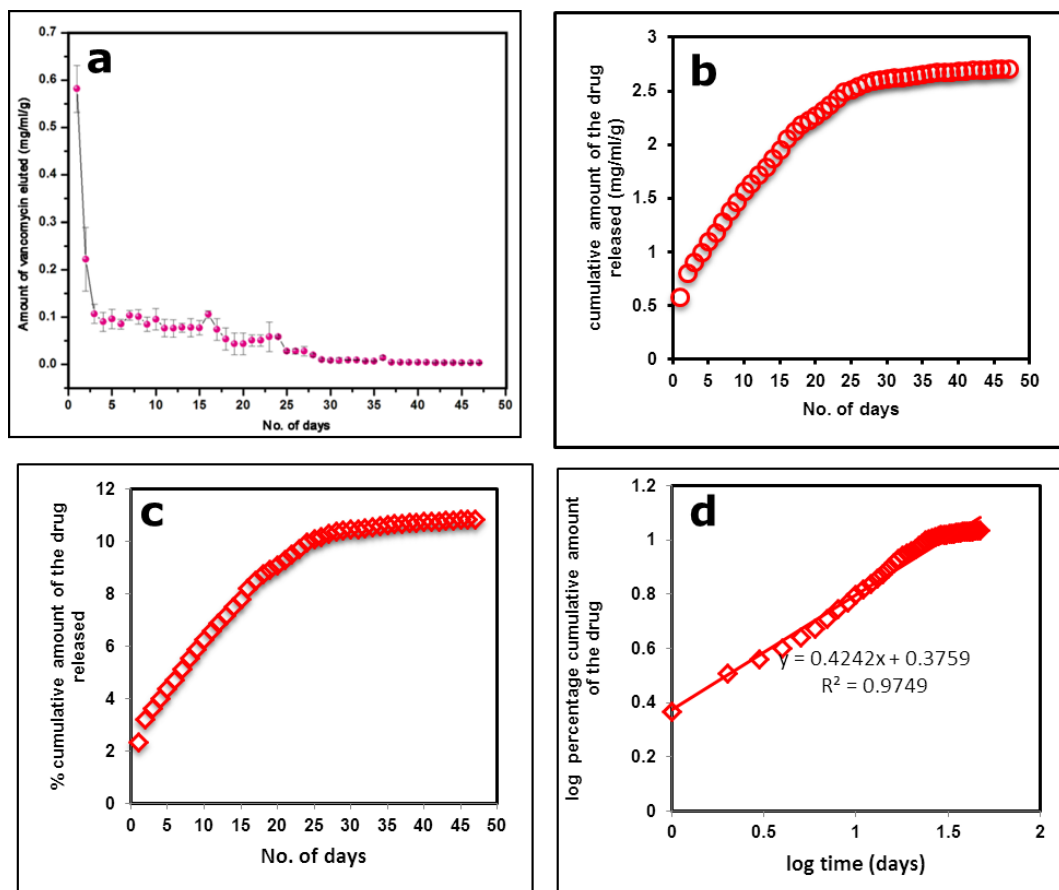


Figure 78: Drug elution of VC from BioCaS bone cement a) Elution profile, b) Cumulative amount of the drug released and the c) The percentage cumulative amount of the drug released against time. d) shows the fitting in Korsmeyer- peppas model

4.4.3 Validation of drug release pattern with HPLC

As the USP suggested standard method for the detection of GS (USP 38 NF 33: 2015 and USP 34 NF 29: 2011) and VH are HPLC, the elution profile of the VH was cross checked with HPLC. HPLC chromatograms of the eluted drug samples at two different time period with that of PBS buffer has shown the distinguishable peak of VH at the retention time (R_t) 4.5 minutes (Figure 79).

The linearity of VH standard curve was observed within 0.015-0.24 mg/ml with peak area = $(2 \times 10^6) \times \text{concentration} - 1578.6$ with correlation coefficient $R^2 = 0.9968$ (Chang *et al.*, 2011). The elution profile of the drug from the chromatographic and spectrophotometric methods were shown compiled in Figure 80.

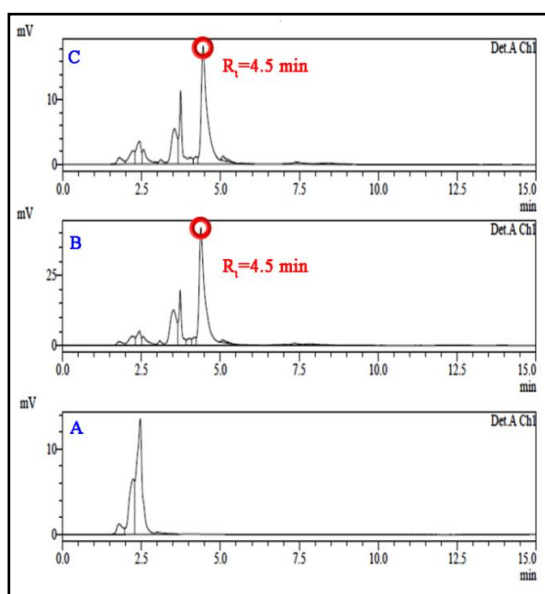


Figure 79: HPLC chromatogram of A) PBS B) and C) eluted samples at day 2 and 10 with the corresponding peak of vancomycin hydrochloride marked with retention time 4.5 minutes

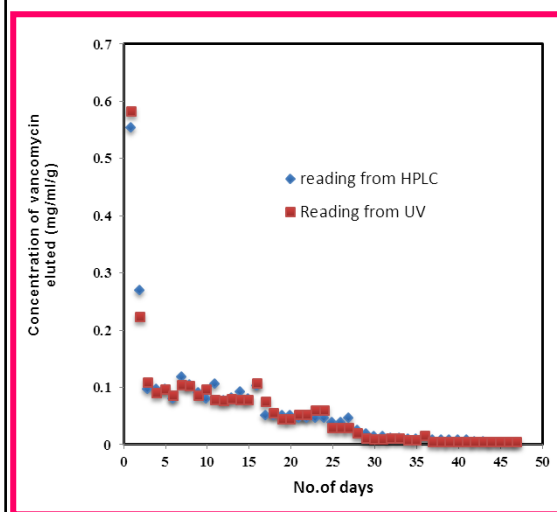


Figure 80: Compiled elution plot VH obtained through HPLC and UV-Visible spectrophotometry.

Cumulative amount of the drug released was found out to be 2.79 mg/ml with percentage cumulative release of 11.17% (HPLC) against the 2.71 ± 0.16 mg/ml/g and $10.85 \pm 0.62\%$ (UV). As per anova single factor the difference in values were not significant

as $P > 0.05$ (where $P = 0.67$). Hence further comparative release kinetics analysis by varying the concentration of the GS and VH in BioCaS and surface area to volume ratio were carried out with UV-Visible spectrophotometry.

4.4.4 Elution profile and kinetics of VH loaded in BioCaS with concentration change

The drug elution profile of the BioCaSV3 (high dose) was found out to be highly irregular; however more sustained release was found out for the BioCaS V1 and BioCaS V2 (Figure 81). Escalation of the cumulative amount of the drug released was found out to be increased with the concentration from low to high correspondingly 2.59, 4.23 and 9.83 mg/ml/g for BioCaS V1, BioCaS V2 and BioCaS V3 but the percentage of drug release with respect to the initial loading was found out to be 10.4, 4.2 and 4.9% respectively and hence the release efficacy was higher for low dose drug loaded cement.

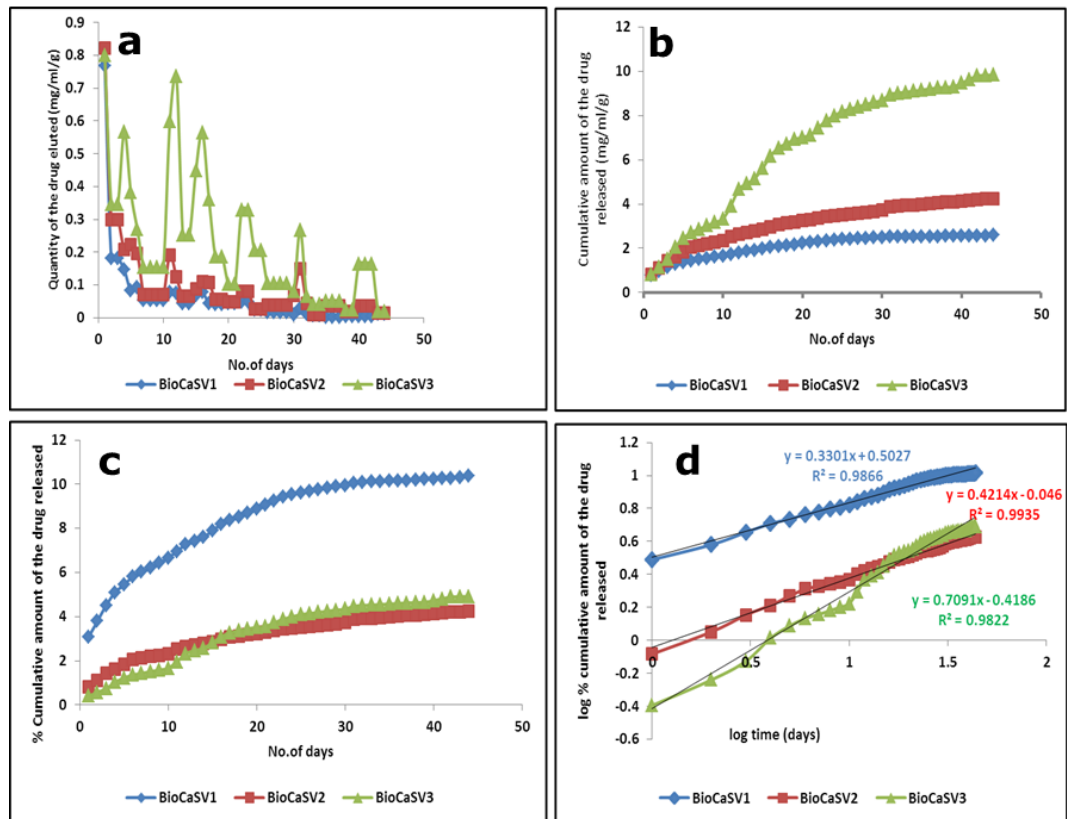


Figure 81: a) Elution profile b) cumulative amount of the drug release c) percentage cumulative amount of the drug release and d) Curve fitting in Korsmeyer–peppas model for the BioCaSV1, BioCaSV2 and BioCaSV3

The drug release kinetics best matches with K-P model where R^2 for all compositions were >0.98 . In K-P model fitting graph of log percentage cumulative drug release against log time, the slope was found to decrease from high to low dose group and hence the release exponent, n values were 0.33, 0.42 and 0.71 respectively. From the n value, the low dose follows quasi-fickian diffusion mechanism and becomes fickian diffusion controlled at middle dose group. However the higher dose group follows non-fickian diffusion mechanism where the drug release is due to both diffusion and relaxation due to degradation of the gypsum matrix (Khan *et al.*, 2014). Appending this, BioCaS V1 and BioCaS V2 pellet regained after study was found to be intact compared to BioCaS V3 where the features of irregular surface erosion could be found.

4.4.5 Elution profile and kinetics of VH loaded in BioCaS with S/V ratio

For the low dose VH loaded group, with respect to the surface area to volume ratio cumulative amount of the drug released and hence the releasing efficacy was found to be

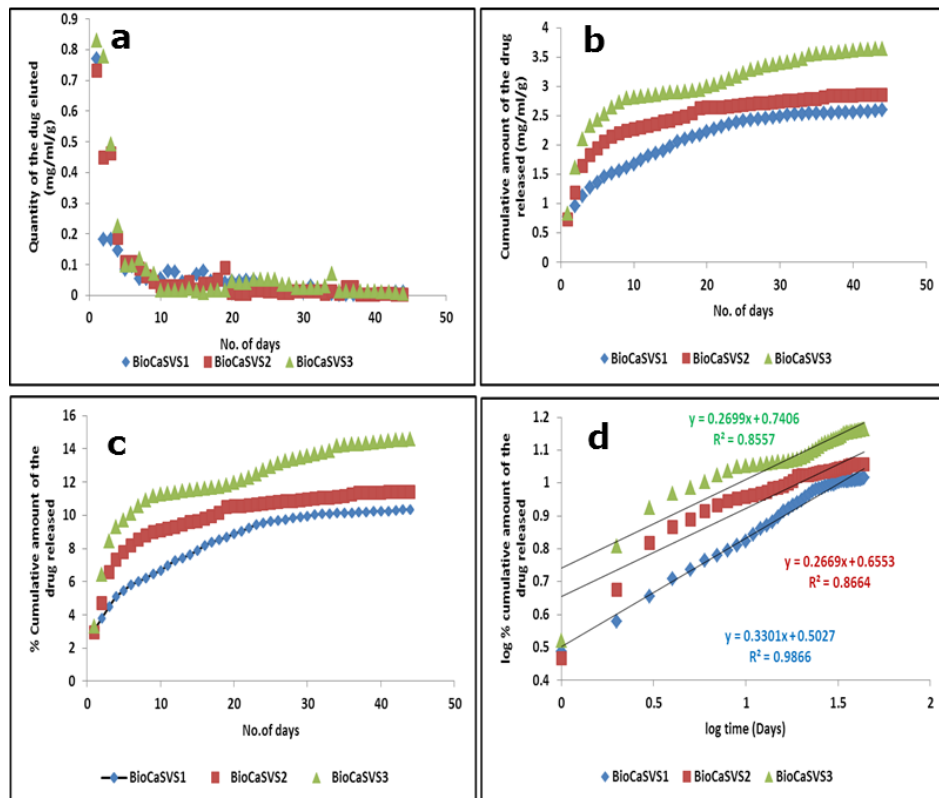


Figure 82: a) Elution profile b) cumulative amount of the drug release c) percentage cumulative amount of the drug release and d) Curve fitting in Korsmeyer–peppas model for the BioCaSVS1, BioCaSVS2 and BioCaSVS3.

improved from 10.37 to 14.57% (Figure 82) . At the lower surface area the curve fit well in K-P model ($R^2=0.9866$).At higher surface area to volume ratio of the pellets, the curve fit well in none of the statistical model but comparatively higher correlation co-efficient was again found for the K-P model only ($R^2=0.8664$ and 0.8557 for BioCaSVS2 and BioCaSVS3 respectively), while both are having the n value= 0.2669 . The very low value of n indicates the physico-chemical phenomenon of drug interaction with matrix operating and hence the percentage cumulative drug release was found to be not in direct proportion with surface area to volume ratio of the cylindrical matrix.

4.4.6 Elution profile and kinetics of GS loaded in BioCaS with concentration change

As the drug elution pattern of the BioCaSG1 has stopped after 20 days, comparison of release kinetics was also done up to that time. Even though the cumulative amount of the drug released was found out to be slightly higher for the BioCaSG2 and BioCaSG3

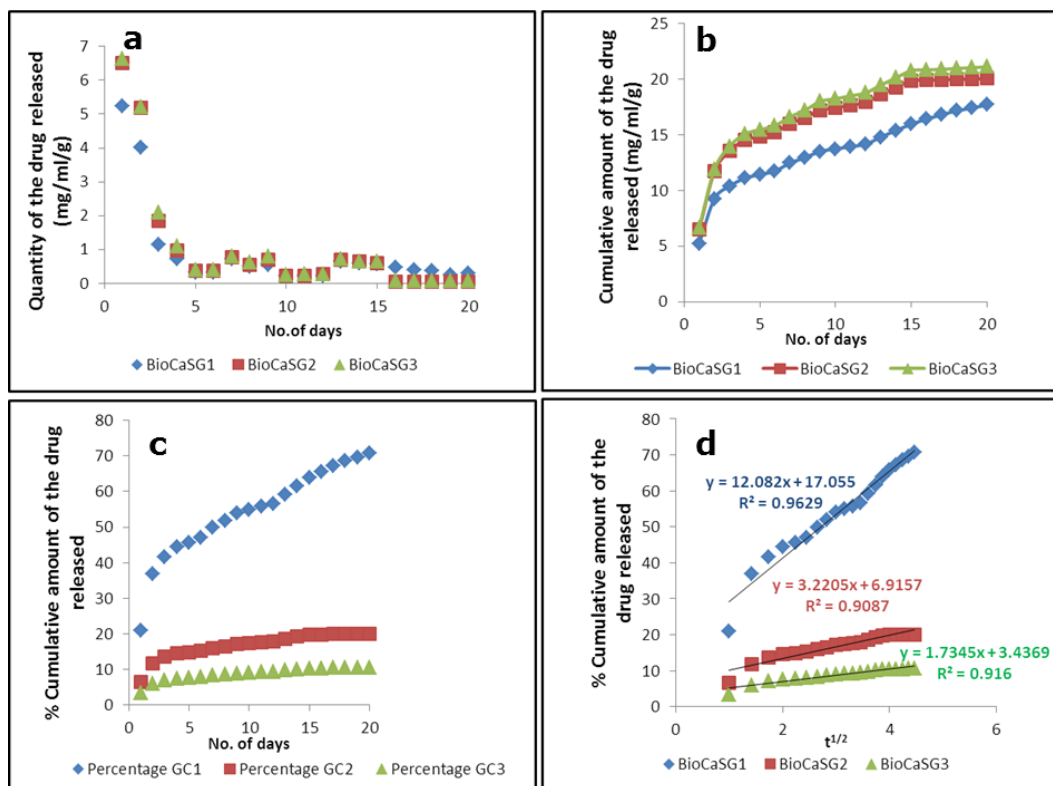


Figure 83: a) Elution profile b) cumulative amount of the drug release c) percentage cumulative amount of the drug release and d) curve fitting in Higuchi model for the BioCaSG1, BioCaSG2 and BioCaSG3

, the percentage cumulative amount of the drug release was found out to be 70.78, 20.06 and 10.55 respectively (Figure 83). It indicates the higher release percentage at lower concentration and the release kinetics was best fitted in Higuchi model ie. percentage cumulative amount of the drug release is square root of time dependent more related to the the porosity and tortuosity of the channels in the matrix. Low percentage of release at higher concentration and deviation from higuchi pattern indicates the entrapment of the drug due to ionic interaction and may due to the absence of interconnected porosity.

4.4.7 Elution profile and kinetics of GS loaded in BioCaS with surface area to volume ratio change

The drug release for the BioCaSGS3 stopped after 15 days and hence 15 days of drug elution profile was used for comparison with BioCaSGS1 and BioCaSGS2 (Figure 84).

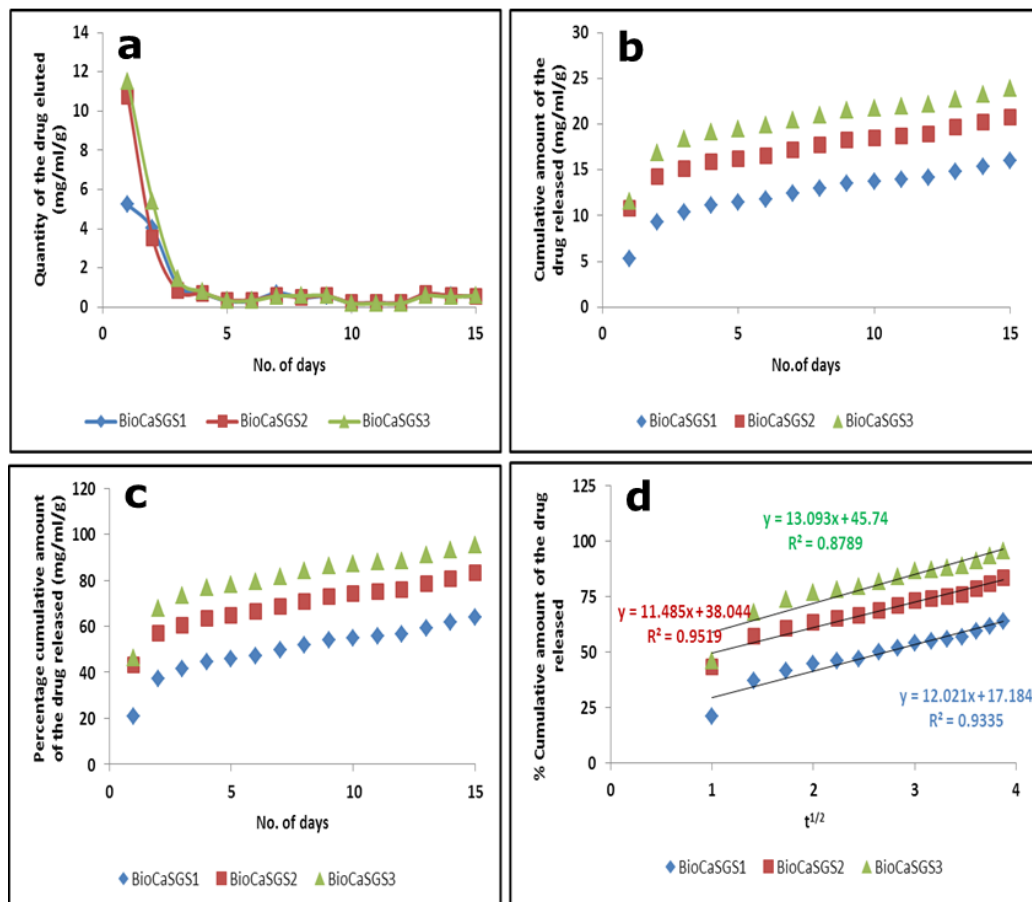


Figure 84: a) Elution profile b) cumulative amount of the drug release c) percentage cumulative amount of the drug release and d) curve fitting in Higuchi model for the BioCaSGS1, BioCaSGS2 and BioCaSGS3

Percentage cumulative amount of the drug release was found to be escalated to 83.16 and 95.38 % respectively for the next higher S/V ratio with respect to 63.81% in low S/V ratio cement. The highest S/V ratio cement deviated from the kinetic models of interest while the other two obeys Higuchi model to a greater extent ie. square root of time dependent diffusion controlled release governed by tortuosity and porosity of the matrix. However due to the significantly higher burst release, 10.76 and 11.52 mg/ml of the BioCaSGS2 and BioCaSGS3, surface area of exposure should be minimized as far as possible. However conclusion couldn't be made without in vivo experimentation since the serum concentration of the drug will be low compared to the local administered dose as blood supply to the affected hard tissue is compromised.

4.4.8 Injectability with concentration of the drug loaded

Viscosity-time profile of the GS loaded cement specimens with varying loading percentages were as shown in figure 85 (a) and that of the VH loaded specimens in (b). Viscosity was found to continuously escalated in low dose and middle group in GS group while better fluidity with low slope was found for higher dose group. In VH group, low dose drug loaded cement was found to be non-injectable due to filter pressing and viscosity crossed 1000 Pa.S within 30s while two other concentrations have acceptable flow properties with complete extrusion of the cement paste. However better injectability was found for the BioCaSV3.

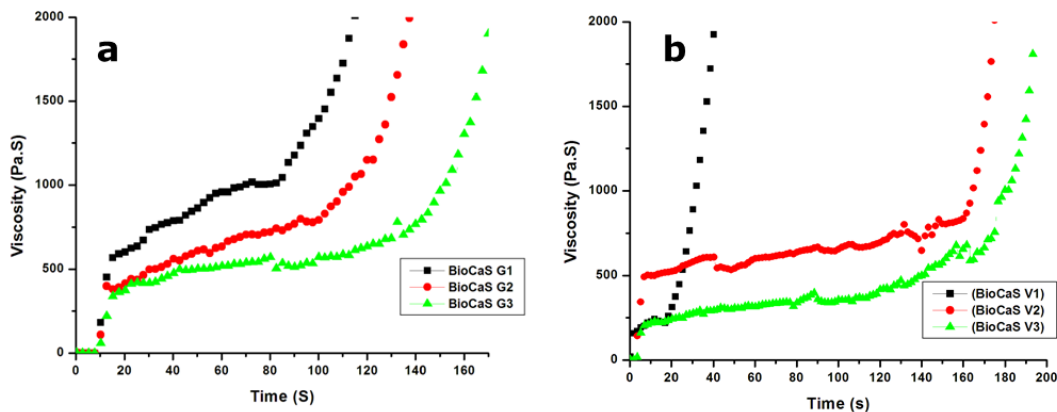


Figure 85: Viscosity-time profile of the a) GS & b) VH loaded BioCaS with change in concentration of the drug loaded

Hence for the invitro antimicrobial study we have selected the high dose drug loaded cement from the two groups ie. BioCaSG3 and BioCaSV3.

4.4.9 Setting times and mechanical property of the BioCaSG and BioCaSV group

GS loaded cement showed two setting times (t_i and t_f) as that of BioCaS (Figure 86). BioCaS has initial setting time 12.5 and final setting time 16.5 min. However in BioCaSG1 the final setting time was found to be 26.5 ± 0.5 min which is out of the acceptable range of < 20 min and not useful. In BioCaSG3 final setting time was in the boarderline ie. 19.66 ± 0.28 . As per the anova single factor, F-Test two sample for variance and t'test, the differences were significant except the t_i of BioCaSG1 and BioCaSG3 compared to BioCaS and t_i of BioCaSG1 and BioCaS G3 ($P > 0.05$). Comparatively lower t_i and t_f were obtained for BioCaSG2.

Unlike GS loaded BioCaS, BioCaSV group has shown single setting time (Figure 87) due to fast setting in which the difference in t_i and t_f becomes indistinguishable. A descending succession could be found from low dose to higher dose where latter one set very fast within 6.16 ± 0.28 min.

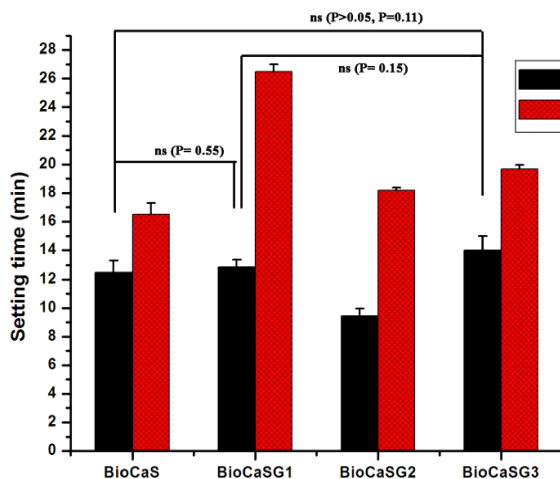


Figure 86: a) Initial and final setting times of the BioCaS loaded with low, middle and high dose GS (ns-not significant)

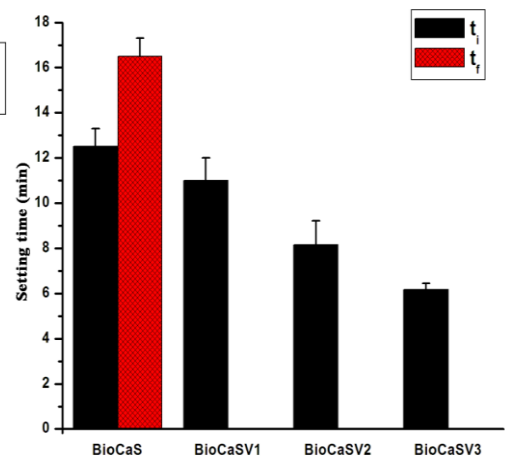


Figure 87: a) Initial and final setting times of the BioCaS loaded with low, middle and high dose VH (ns-not significant)

The compressive strength of drug loaded compositions were found out to be between 8.0 to 14 MPa (Figure 88). Difference in values between low and middle dose group of each drug in BioCaS were not statistically significant. Comparatively higher values were obtained for the higher dose drug loaded cement. The compressive strength of BioCaSG3 improved to 13.15 ± 0.52 with respect to BioCaS ($P=0.001$). BioCaSV3 has slightly lower value 11.05 ± 0.79 than BioCaS but the difference was not significant ($P>0.05$).

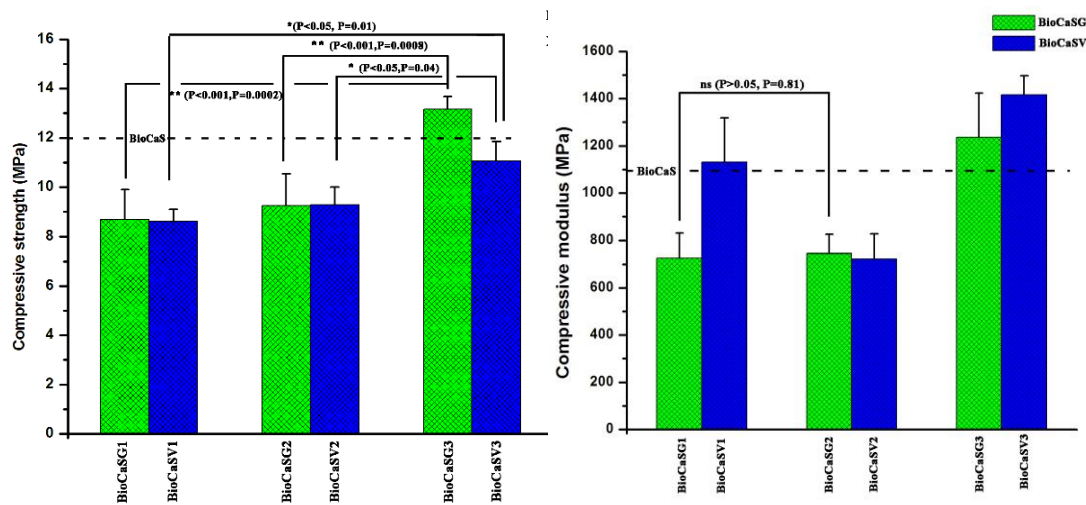


Figure 88: Compressive strength and corresponding compressive modulus of the BioCaS loaded with low, middle and high dose antibiotic group

The compressive modulus values of BioCaSG3 & BioCaSV3 were found to be higher than BioCaS (1094.137 ± 54.98 MPa) (Figure 88). The difference in value of BioCaS with BioCaSG3 are not significant as $P > 0.05, P = 0.17$ while that with BioCaSV3 is significant ($p > 0.001, P = 3.71 \times 10^{-7}$). However comparatively higher compressive strength and compressive modulus values were obtained for BioCaSG3 and BioCaSV3 respectively. Considering the injectability, setting time, compressive strength and the corresponding compressive modulus values of the BioCaSG and BioCaSV group with varying concentration, BioCaSG3 and BioCaSV3 were selected for the *in vitro* antimicrobial testing for the biological activity of the drug in cement.

4.4.10 *In vitro* antibacterial activity of the drug loaded BioCaS

The bacterial inhibition assay revealed that the gentamicin and vancomycin released from the BioCaSG3 and BioCaSV3 has retained its biological activity. Figure 89 and 90 describes the inhibition zones around the eluted drug loaded disc along with positive control (standard disc of drug) and negative control (disc without drug) [Only representative images for the first 3 days during the 20 days study period are included].

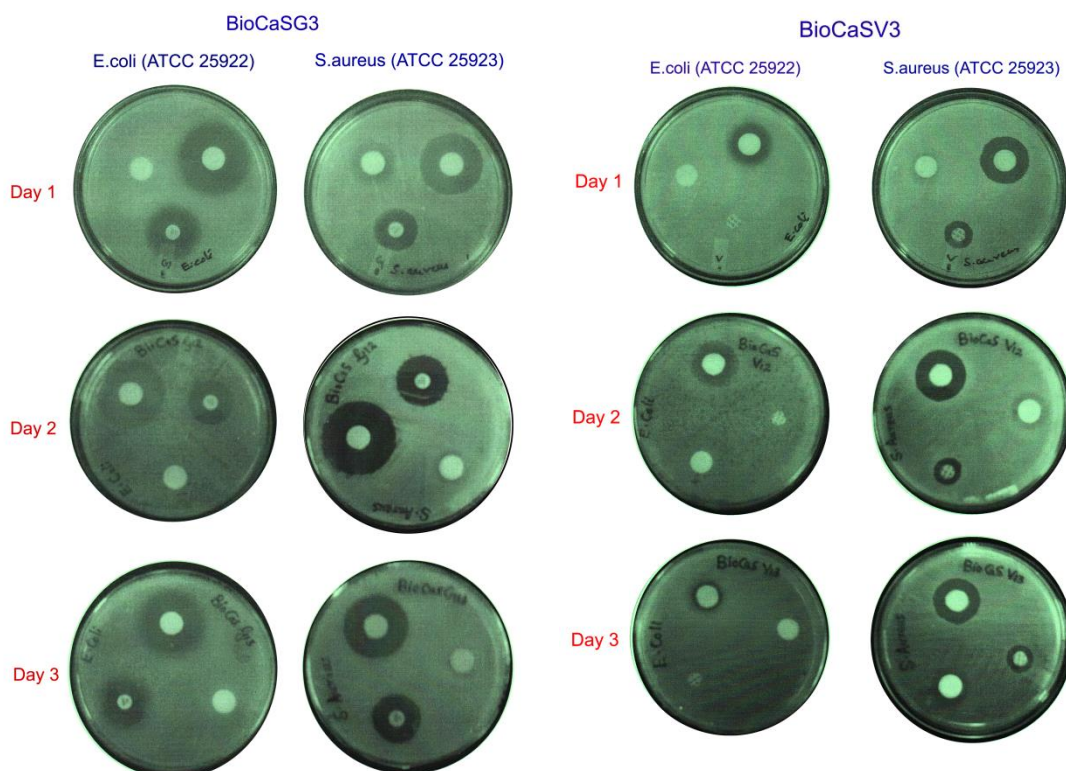


Figure 89: Growth inhibition of E.Coli and S.aureus by Gentamicin eluted from the BioCaSG3 (Positive control and negative control are included in each of the culture plate)

Figure 90: Growth inhibition of E.Coli and S.aureus by Vancomycin eluted from the BioCaSV3 (Positive control and negative control are included in each of the culture plate).

The plot showing the average diameter of the inhibition zone as a function of the release time are shown in figure 91 and 92. The standard zone size of 10 μ g disc of 6 mm diameter gentamicin disc against E. coli ATCC 25922 was found out to be 20.06 ± 0.07 and against S.aureus was 23.52 ± 3.78 mm which falls in the reported standard range 19-26 and

19-27 mm respectively. The Gentamicin and vancomycin susceptibility could be confirmed with ZOI of 15 mm or above and intermediate susceptibility in the range 13-14 mm and resistant when 12 mm. (Performance standards for antimicrobial disk susceptibility test CLSI, 2008). For Vancomycin the standard zone size against S.aureus was estimated to be 11.88 ± 0.60 mm. In all the cases we could not detect any zone of inhibition around the negative control discs and hence the antimicrobial property is due to the drug eluted from the BioCaS injectable bone cement construct. BioCaSG3 has shown antimicrobial susceptibility up to 15 days against E.coli while intermediate susceptibility thereafter. ZOI was found to be significantly higher for the first two days irrespective of the bacterial strain. However S. aureus was found to be fully susceptible during the entire period of study.

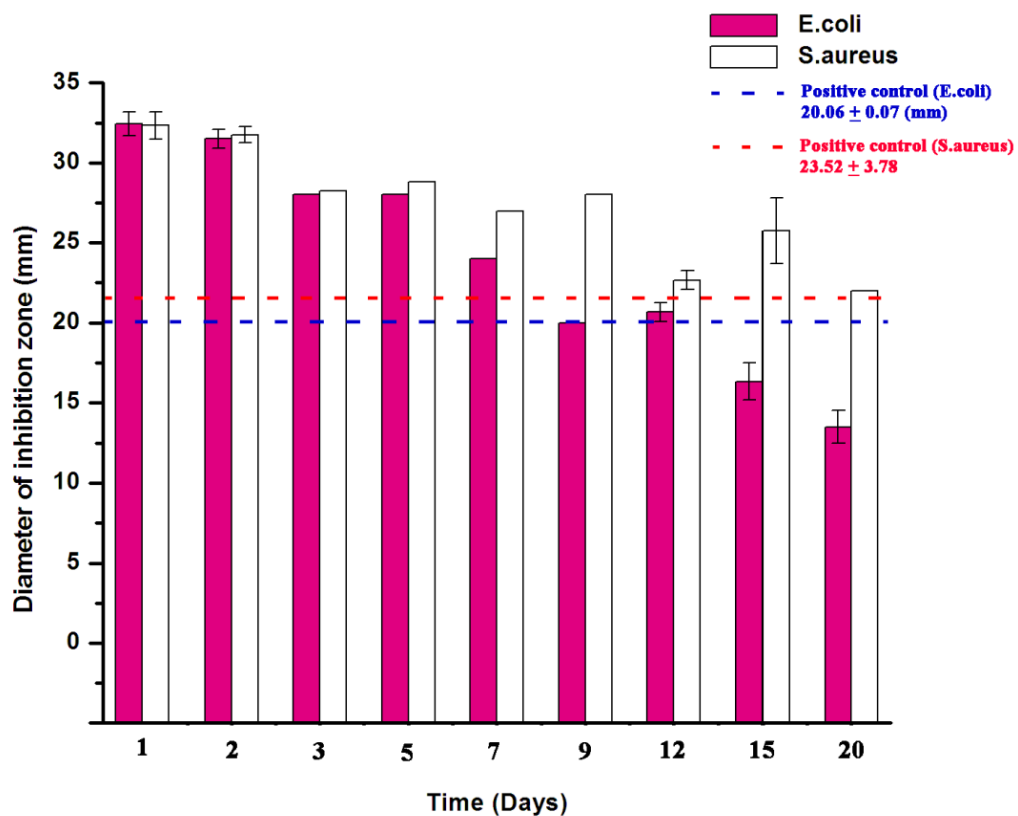


Figure 91: Diameter of inhibition zone of E.Coli and S.aureus by Gentamicin eluted from the BioCaSG3 injectable bone cement at days 1, 2, 3, 5,7,9,12,15 and 20 along with positive and negative control

Vancomycin inhibits the growth of gram positive bacteria and the ZOI for the positive control was found out to be 11.88 ± 0.60 mm. The susceptibility range reported for S.aureus was found to be 17-21 mm and hence the BioCaSV3 was found to be well effective up to 20 days. Also the eluted drug quantity was detected to prevent the growth of gram negative E. coli for the initial week while the positive control couldn't produce any inhibitory effect.

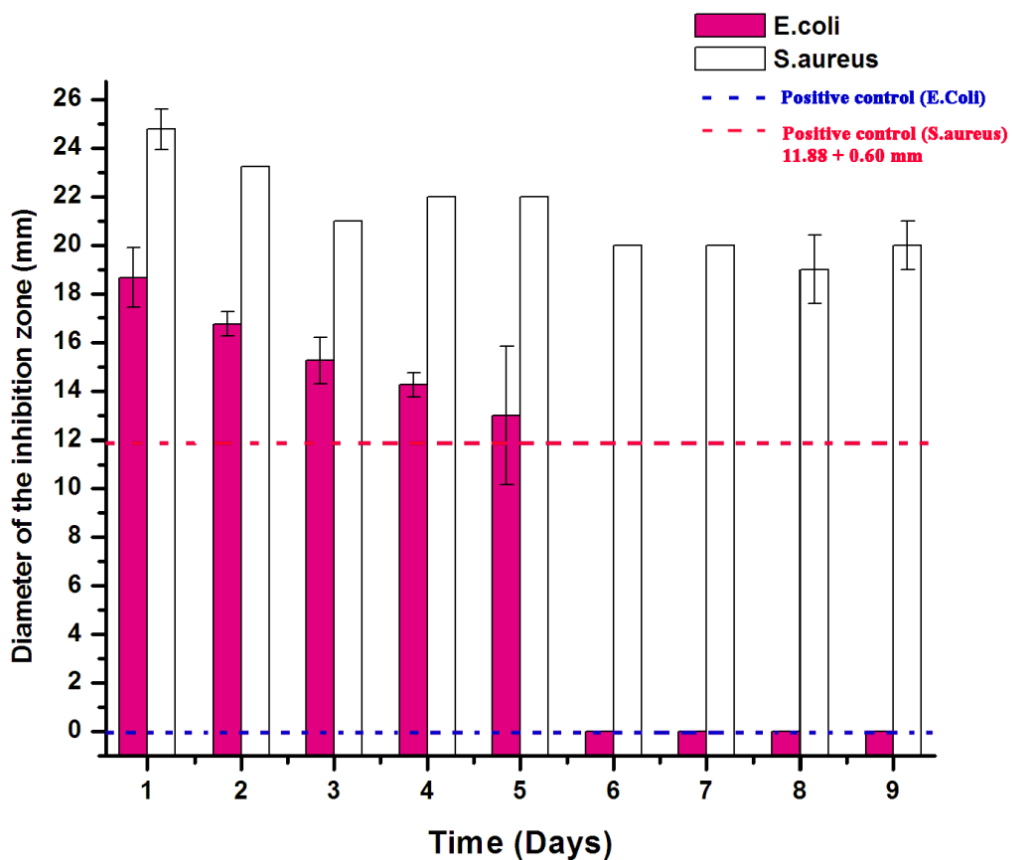


Figure 92: Diameter of inhibition zone E.Coli and S.aureus by Vancomycin eluted from the BioCaSV3 injectable bone cement at days 1, 2, 3, 5,7,9,12,15 and 20 along with positive and negative control

Phase V

4.5 Injectable bioactive bone filler cements incorporating N,O-carboxymethyl chitosan as gelling agent

4.5.1 Phase and chemical bonding analysis of the synthesised NOCMC

The FTIR spectrum analysis gave the confirmation of carboxymethylation of chitosan to form NOCMC. Stacked FTIR spectrum of chitosan and the synthesised product are shown in Figure 93. The peak of -NH_2 deformation vibration at 1654 cm^{-1} was shifted to 1597 cm^{-1} in NOCMC which is due to the -COO^- antisymmetric stretch induced by the associated carboxylic acid salt. It indicates the substitution of carboxymethyl group ($\text{-CH}_2\text{COO}^-$) in NOCMC. The peaks observed at 1070 and 1029 cm^{-1} in both the spectrum were that of the secondary hydroxyl group (characteristic peaks of -CH-OH in cyclic alcohols, -C-O stretch) and the 1° hydroxyl group (characteristic peak of $\text{-CH}_2\text{-OH}$ in 1° alcohol, -C-O stretch).

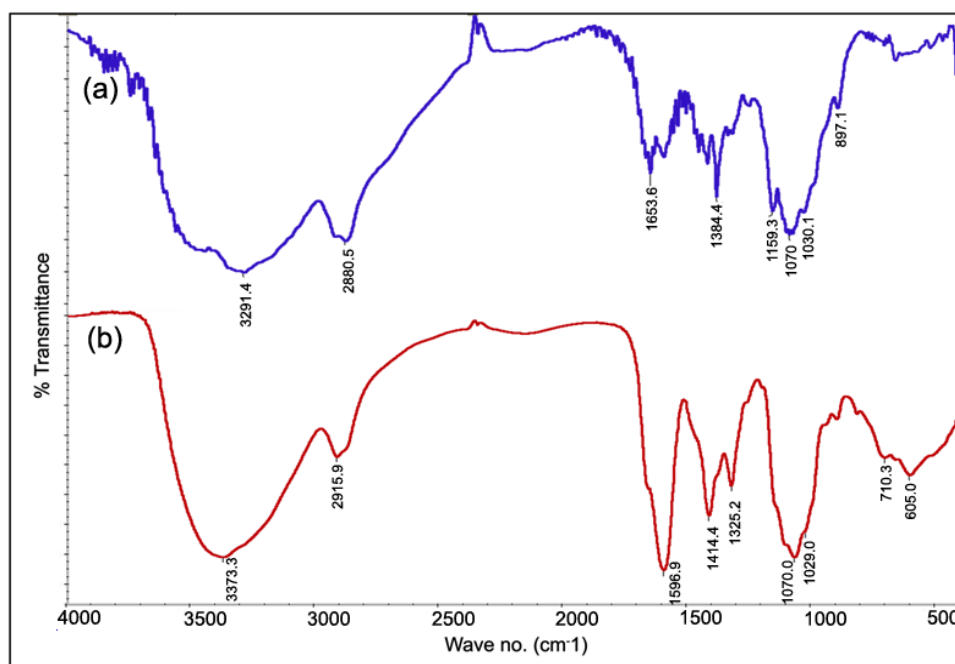


Figure 93: FTIR spectrum of a) chitosan and b) chitosan after carboxymethylation. All the major transmission peak of spectrum b) matches with N,O-Carboxymethyl chitosan

The peak intensity of 1070 cm^{-1} was not affected by the substitution. The decrease in intensity ratio of 1030 to 1070 peak from 1.0353 in chitosan to 0.7211 in the derivative product indicates the substitution of carboxymethyl group to $-\text{CH}_2\text{-OH}$ at C_6 position of the chitosan (Anitha *et al.*, 2009). FTIR spectrum of NOCMC has also characteristic bands of chitosan around 3373 cm^{-1} and 2916 cm^{-1} assigned for $-\text{NH}$, $-\text{OH}$ and $-\text{CH}$ stretching modes. Carboxymethylation on both the amino and hydroxyl group is confirmed by the co-existence of intrinsic peak at 1597 cm^{-1} and a moderate band at 1414 cm^{-1} . The peak at 1414 cm^{-1} is attributed to the asymmetric axial deformation vibration of $-\text{CH}_2\text{COOH}$ group attached to the $-\text{OH}$ group. The peak in the range 1062-1027 (1068.9 cm^{-1}) represents C-O and C-O-C stretch of the polysaccharide skeleton including the vibration of glycoside bond confirms the intact backbone (Ujang *et al.*, Mourya *et al.*, 2010). The peak at 1325 cm^{-1} also represents the $-\text{C-O}$ stretching vibration mode of NOCMC (Chen *et al.*, 2004).

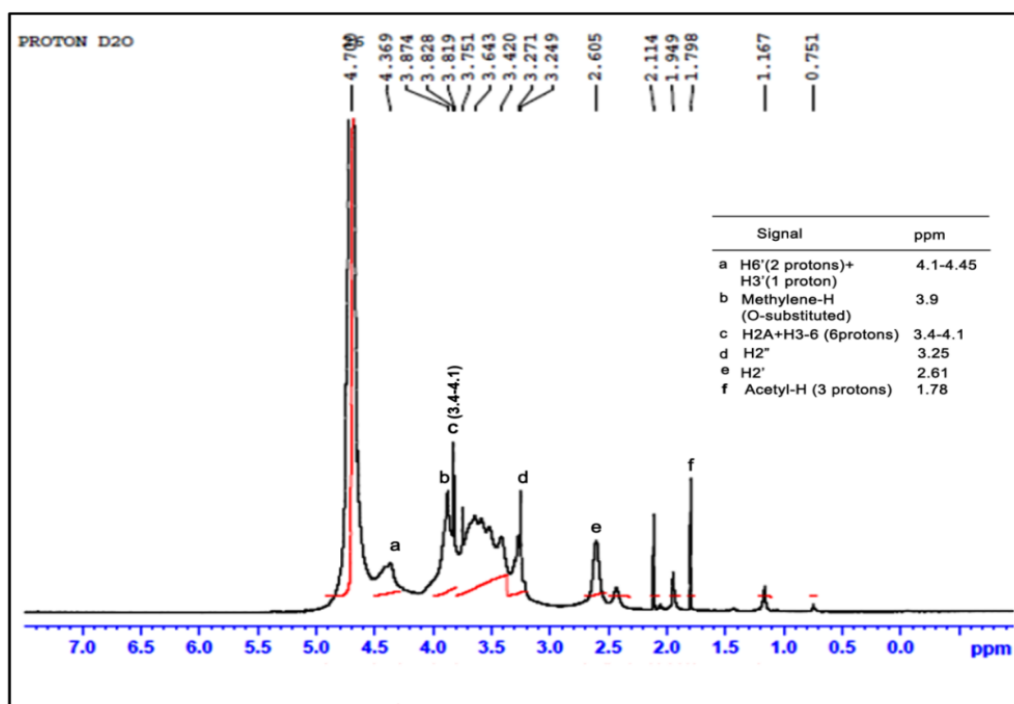


Figure 94: ^1H NMR spectrum of NOCMC in D_2O at $22.3\text{ }^\circ\text{C}$ and the corresponding spectral data.

The ^1H NMR spectrum of NOCMC in D_2O is shown in Figure 94. In the region between 4.05 and 4.55 ppm, the resonances are the protons of 3- and 6-substituted carboxymethyl ($-\text{O}-\text{CH}_2\text{COOD}$) of CMC i.e., 3 protons from H-6' (2 protons) and H-3' (1 proton).

The resonances of 3.4-4.1 are due to H3-6 protons (total no. of proton 6) and due to H bonded to C2 of the acetylated unit. The methylene protons of N-substituted ($-\text{N}-\text{CH}_2\text{COOD}$) and O-substituted ($-\text{O}-\text{CH}_2\text{COOD}$) carboxymethyl chitosan gave signal at 3.25 ppm and 3.9 ppm respectively. The methine protons at C_2 of the NOCMC has shown signal at 2.61 ppm. The signal at 1.78 ppm is the acetyl protons of the acetylated glucan unit. The result shows that the amino groups were partly carboxymethylated along with the hydroxyl groups. A and D refers to acetylated and deacetylated units, H' refers to protons of a carboxymethylated unit and H'' that in the carboxymethyl group itself.

4.5.2 Comparison of the flow properties of the bone cement compositions

The viscosity-time plot of (Figure 95 (a)-(c)) of all the nine modified compositions are shown in the figure as three sets. Except CS151 and CS156, all the bone cements are acceptable as injectables considering the magnitude along with the ability to keep almost constant viscosity throughout the extrusion period. CS153, CS253 and CS353 compositions among the three set possess better flow properties while considering the lowest magnitude and homogenous viscosity throughout the extrusion period.

For comparison, the average viscosity at 120 sec at the three concentration of DHPD against the weight % of NOCMC has been plotted (Figure 95 d). At a particular concentration of DHPD, with the increase in concentration of NOCMC from 0.15 to 0.3%, viscosity first dropped followed by an increase at 0.6 % NOCMC.

Up to an optimum composition the binding of the NOCMC with calcium ions generate very smooth consistency and after that the binding effect causes sudden increase in the viscosity and hence the reverse trend in the injectability. It could also be found out that the increase in concentration of DHPD with constant composition of NOCMC contributes to the injectability. Both the Dorfmanite and NOCMC have compiled effect in enhancing the rheology of the compositions.

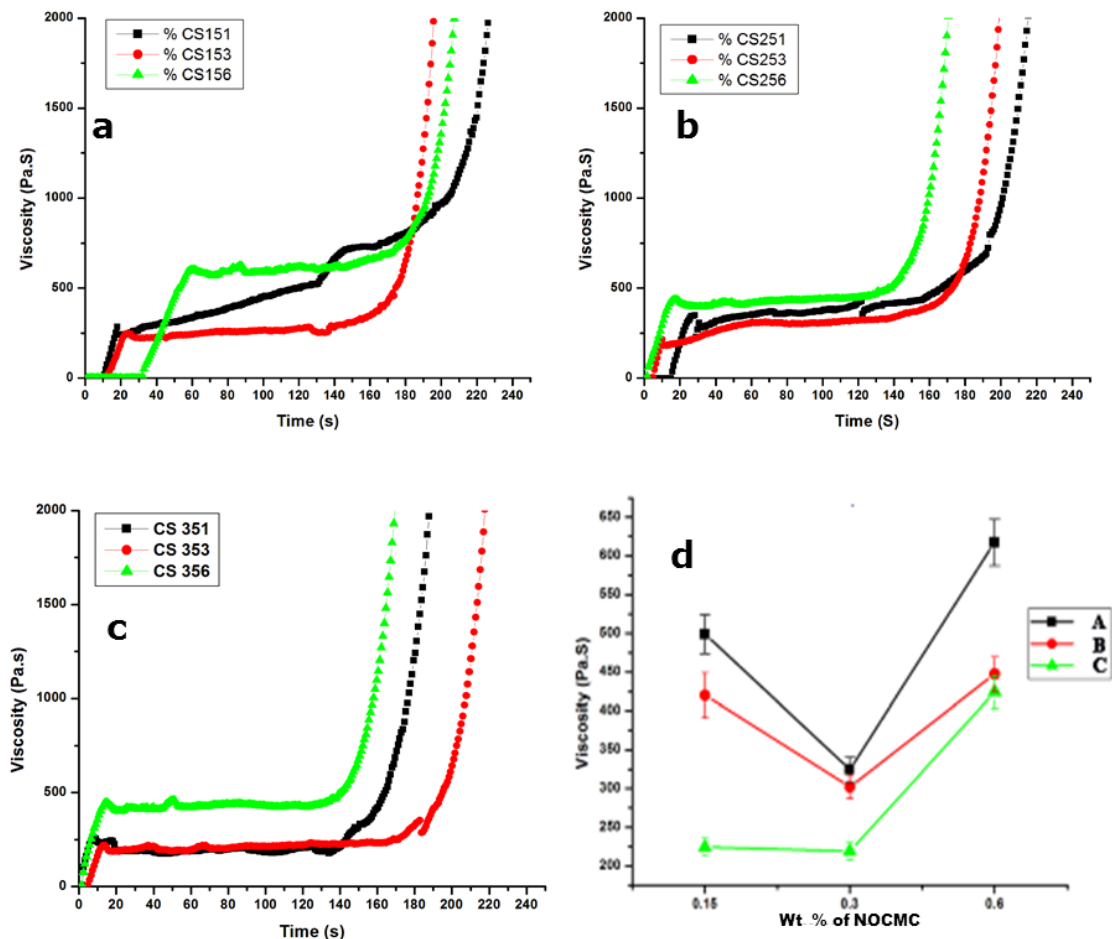


Figure 95: Viscosity-time plot describing the flow property of the bone cement pastes with varying concentration of NOCMC a) 1.5% DHPD incorporated cement b) 2.5% DHPD incorporated cement c) 3.5% DHPD incorporated cement each with varying concentration of NOCMC d) The average viscosity at 120 sec at the three concentration of DHPD against the wt.% of NOCMC (A-1.5%DHPD, B-2.5%DHPD, C-3.5% DHPD).

The viscosity of the BioCaS at 120 s was found out to be 254 ± 12.7 Pa.s. The viscosity below the value of BioCaS and hence the improved rheology was found only for CS351 and CS353.

4.5.3 Setting times of the bone cement compositions

Analysis of the setting times of the compositions modified with DHPD and NOCMC has shown significant results (Figure 96). Escalation trend was shown while increasing the concentration of NOCMC by keeping the concentration of DHPD constant. The trend may obviously be due to the increased water holding capacity of NOCMC as stated in literature (Mourya *et al.*, 2010). Hence the rate of evaporation of the excess water content other than the water of crystallization may be low. Setting times of a CSC with a particular concentration of CMC has also increased with the increase in the additive concentration of DHPD.

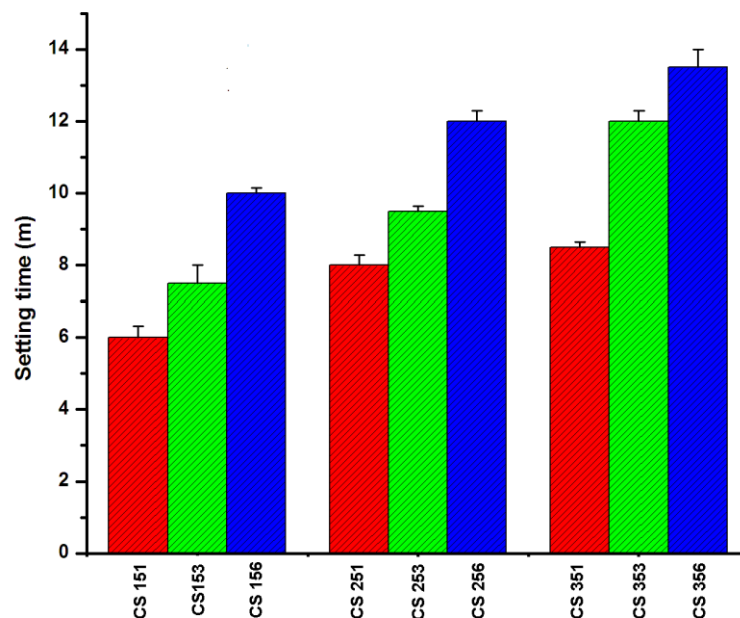


Figure 96: Setting times of the bone cements with varying compositions of DHPD and NOCMC

However the injectable bone cement should have a setting time greater within the range of 8-20 minutes, such that it provides sufficient time for the surgeon to perform

the implantation before the setting, but not too long to cause delay in closing the surgical site. The setting times of the modified compositions are found out to be in the range of 8-14 minutes. Hence considering the requirement, all the compositions are found to be convenient and acceptable except CS151 and CS153.

4.5.4 Comparison of the compressive strength of the compositions

The compressive strength and the corresponding young's modulus values of the CSCs as a function of the DHPD and CMC composition are shown in figure 97. All the cement compositions have compressive strength value greater than 5 MPa. Unmodified CSC showed a compressive strength of 9.5 MPa. A value greater than 10 MPa is considered to be effective to act as a bone filler. For a constant value of DHPD with the increasing concentration of CMC, the compressive strength showed declining trend. The declining strength from CS153 to CS156 was found out to be statistically significant which may be due to the increased setting time as NOCMC has higher water holding capacity and delaying the crystal entanglement.

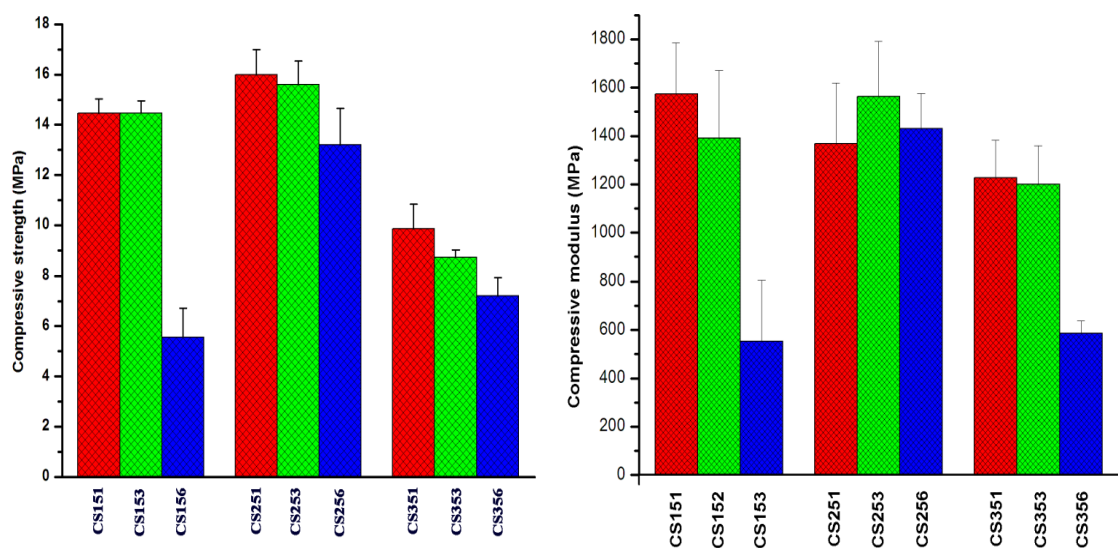


Figure 97: a) Compressive strength and b) compressive modulus values of the bone cement with varying compositions of DHPD and NOCMC

Compressive strength first increased and then declined while keeping the concentration of NOCMC constant and varying DHPD. By taking the compositions with values equal to or greater than 10 MPa, CS 156, CS 353 and CS 356 should be excluded. The highest compressive strength was observed for the CS251 ($=15.9 \pm 1.0$ MPa) followed by CS 253 ($=15.6 \pm 0.95$ MPa). The differences in values were not significant as $P > 0.5$. CS151 and CS153 showed almost equal compressive strength (~ 14 MPa). Most of the compositions except CS156 and CS356 have values greater than 1.1 GPa. The higher modulus values obtained were also for the henceforth selected compositions based on the compressive strength values. Considering the compressive strength (12 ± 0.15 MPa) and modulus ($1,094.137 \pm 54.98$ MPa) for the BioCaS, the CS251 and CS253 gave significantly higher values as $P < 0.05$.

4.5.5 Characterising the bone cement composition

First 3 trace of the figure 98 shows the stacked FTIR spectrum of smCHD0 cement, DHPD and NOCMC, (explained in section 4.2.5 and 4.5.1). While examining the CS253 and CS356, the broad band with peak at 1120 in the smCHD0 has been shifted to a narrow region in between 1100 and 1250 cm^{-1} with peak at 1140 cm^{-1} where the characteristic absorption band of HPO_4^{2-} coincides. It indicates the incorporation of hydrogen orthophosphate ions. The chelating effect of NOCMC on cement has been confirmed by the presence of an additional peak around 1347 cm^{-1} in CS253 and CS356. The diminished intensity of the peak at 1414 cm^{-1} due to the asymmetrical axial deformation vibration of $-\text{CO}$ in $-\text{CH}_2\text{COOH}$ and a well-defined peak at 1348 cm^{-1} in CS 253 and CS356 indicates the chelating effect of Carboxyl group of NOCMC with Ca^{2+} ions in cement pastes (bathochromic shift). Hence the mechanism of cementing could be represented as in figure 99.

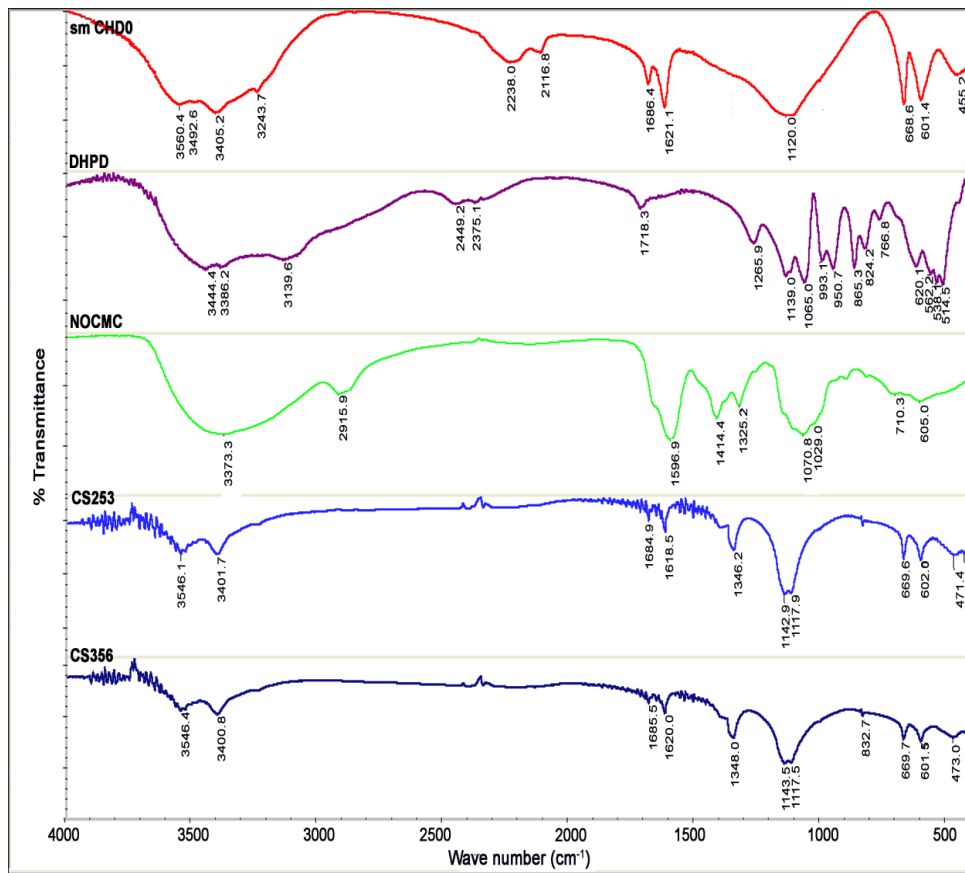


Figure 98: Stacked FTIR spectrum of smCHD0, DHPD, NOCMC, CS253 and CS356

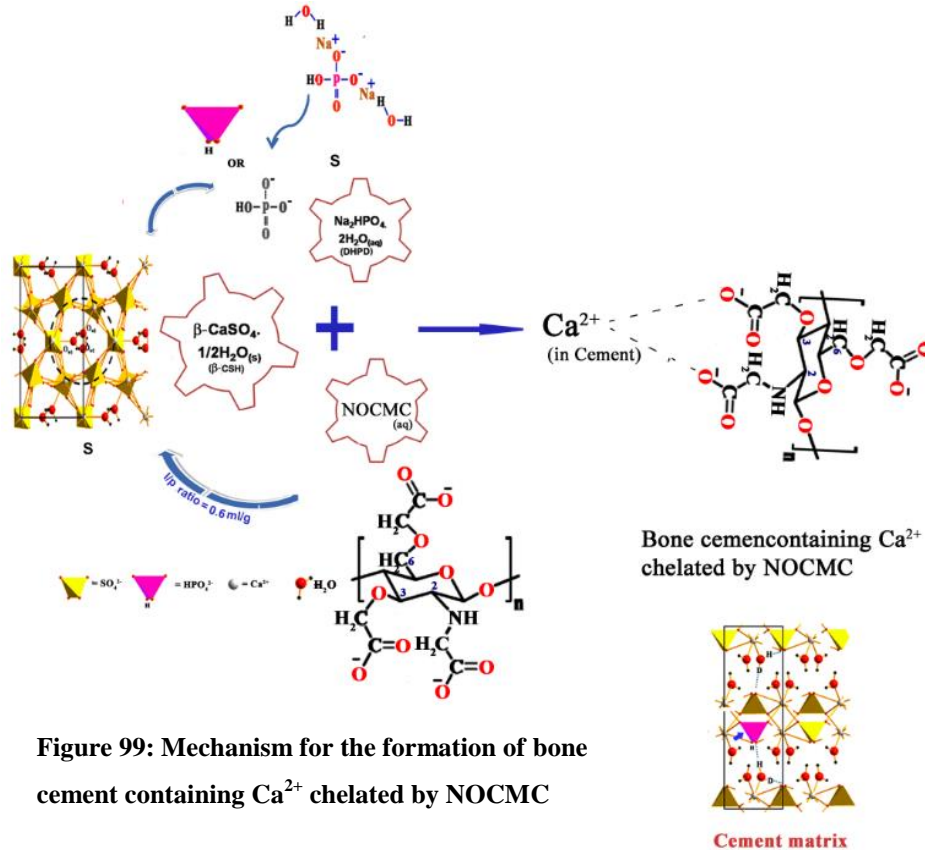


Figure 99: Mechanism for the formation of bone cement containing Ca^{2+} chelated by NOCMC

4.5.6 Micro morphological variation of the set bone cement composition

SEM image of the crushed cement pellets are as shown in figure 100. CS251, CS253 followed by CS151 and CS153 show comparatively better tight packing and hence contribute to mechanical property. Non-homogeneous particle size and less tight packing were observed for CS156, CS351, CS353 and CS356 and leads to reduction in compressive strength. CS351 contains very small particle agglomerates to mostly larger than 10 μm sized rods. Irregular pores could be seen in between the particles and such inhomogeneity prevents tight packing at certain regions and makes the material easily brittle. Unlike CS156 and CS356, CS256 has very fine submicron sized particles which aggregates and intercalates themselves to get better close packing comparable to that of the chosen compositions.

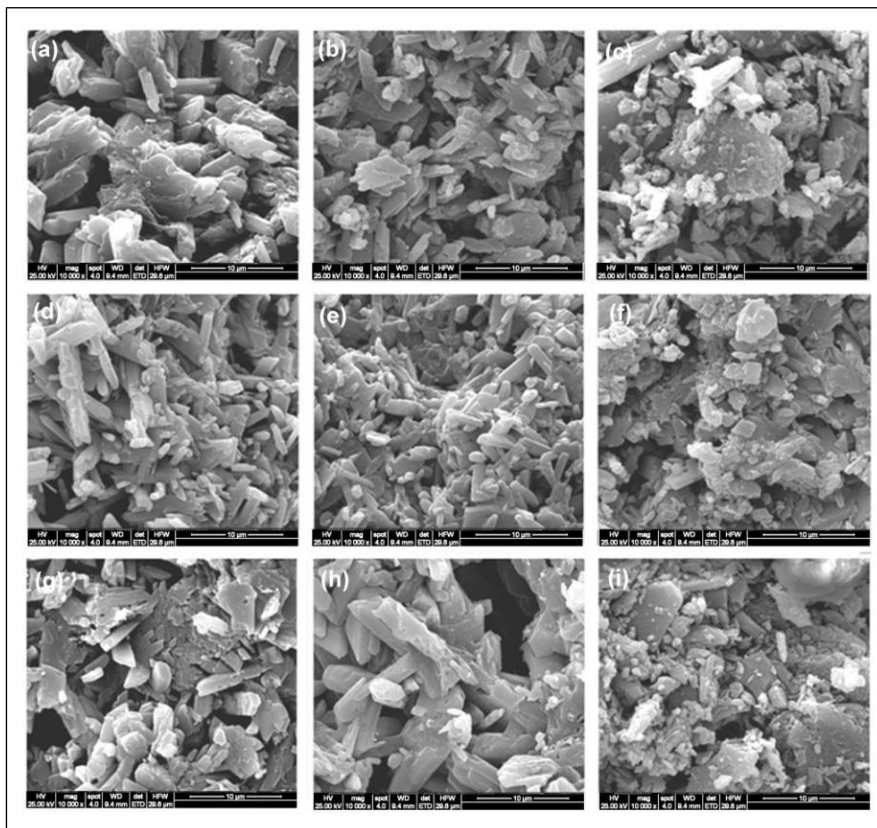


Figure 100: The scanning electron microscopic images of a) CS151 b) CS153 c) CS156 d) CS251 e) CS253 f) CS256 g) CS351 h) CS353 i) CS356

It is evident that the 2.5 wt % DHPD containing compositions have homogeneity in particle size compared to lower and higher composition counterpart.

4.5.7 In vitro degradation studies of the cement composition

The *in vitro* degradation percentage of the BioCaS was found out to be $55.04 \pm 4.11\%$ (section 4.3.1.2) during the 10th week. However the histomorphometric analysis has given the lower value 40.35%. The figure 101 shows the percentage of degradation and rate of the percentage of degradation of the two samples against time. As per anova single factor, no significant difference in degree of degradation was observed for CS251 and CS253. Even after 11 weeks, the degradation percentage was only 36.66 ± 0.77 and $37.76 \pm 0.25\%$. However the incorporation of NOCMC found to reduce the degradation rate. Even though the initial rate of degradation of CS253 was comparatively higher, no differences in values were obtained after 2 weeks.

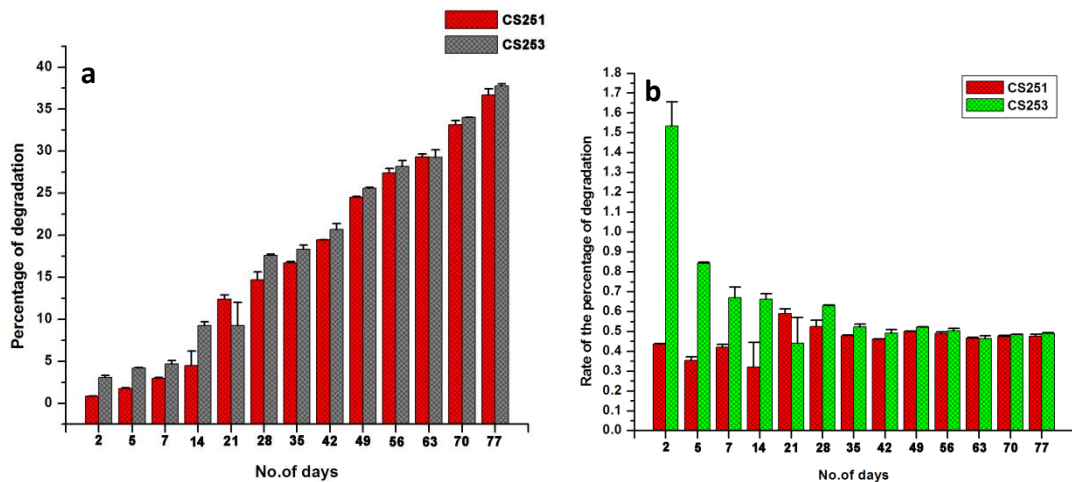


Figure 101: a) the percentage of degradation and b) the rate of percentage of degradation of the CS251 and CS253 bone cement.

4.5.8 In vitro bioactivity of the optimised cement composition

Stacked XRD pattern of the injectable CS253 after immersion in SBF at different time periods has been shown in Figure 102. From 7th day onwards, the XRD pattern

prominently matches with HA which indicates the formation of thick hydroxyapatite layer over the surface of CS253. The ratio of the intensities (raw area under the curve) of the highest peak of hydroxyapatite (at two theta = 31.779°) to that of gypsum (at two theta= 11.634°) at 2, 4 and 7 days of immersion were 0.46, 0.99 and 2.23 respectively.

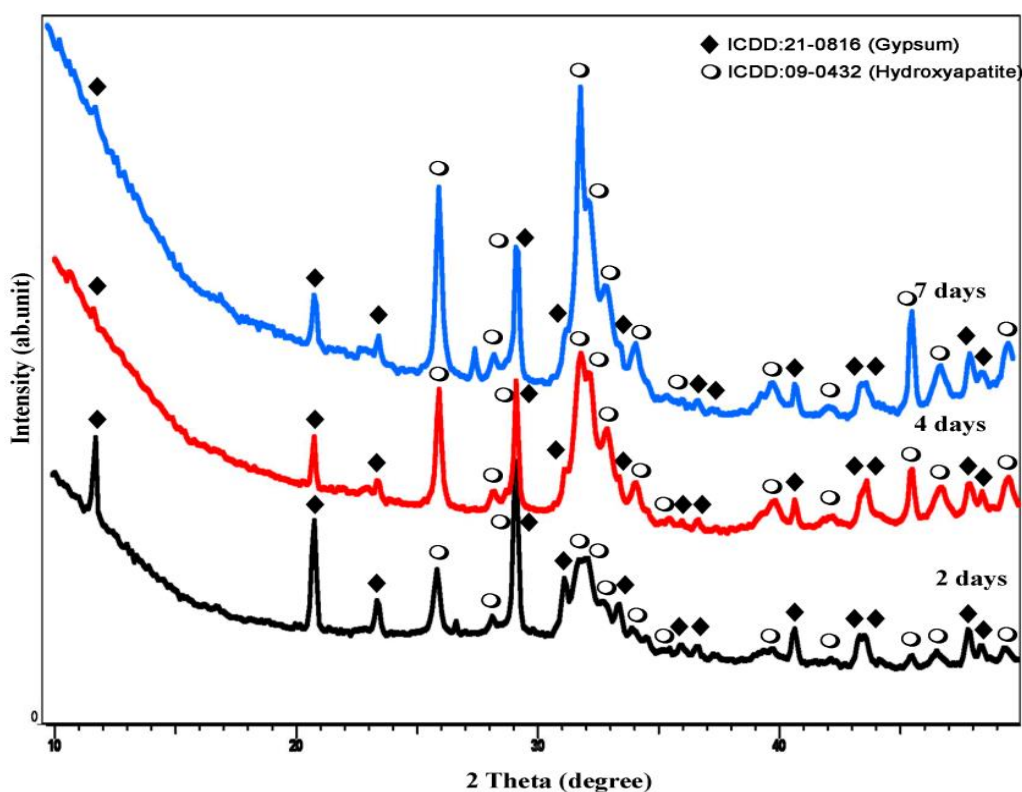


Figure 102: Stacked XRD pattern of CS253 at different immersion periods in SBF

FTIR pattern of the CS253 (figure 103) after 4 days displayed the appearance of characteristic bands of hydroxycarbonated apatite at 954 cm^{-1} and 1033 cm^{-1} corresponds to ν_1 symmetric and ν_3 antisymmetric stretching of P-O and 872 cm^{-1} and doublet at 1457 cm^{-1} and 1416 cm^{-1} attributes to ν_2 out of plane bending mode and ν_3 asymmetric stretching mode of C-O group. However after 7 days of immersion the peaks of HA became prominent. The peaks gave evidence for the formation of

less crystalline carbonated HA (as discussed in section 4.3.1.1). However the thick layer of HA formation got delayed with gelling agent incorporated cement compared to BioCaS.

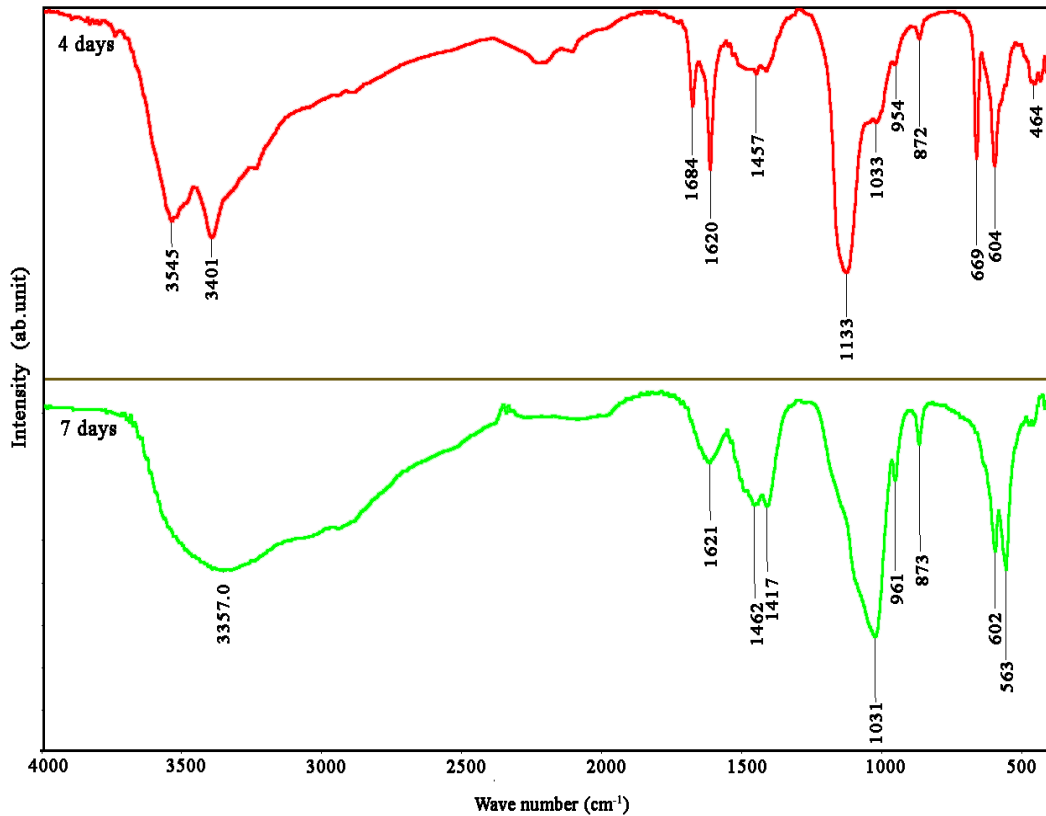


Figure 103: Stacked FTIR pattern of CS253 at different immersion periods in SBF

The ESEM image of CS253 (figure 104) reveals the coating of spherical shaped HA particles on the surface from the 4th day onwards with non-uniform distribution with visible interface. On 7th day onwards, well defined globules of HA with secondary growth features were found uniformly distributed throughout the surface of a thick primary HA layer. The magnified view of the crack shows the different growth layers of HA. It gave evidence for the persistence of higher biomineralisation even after incorporating NOCMC.

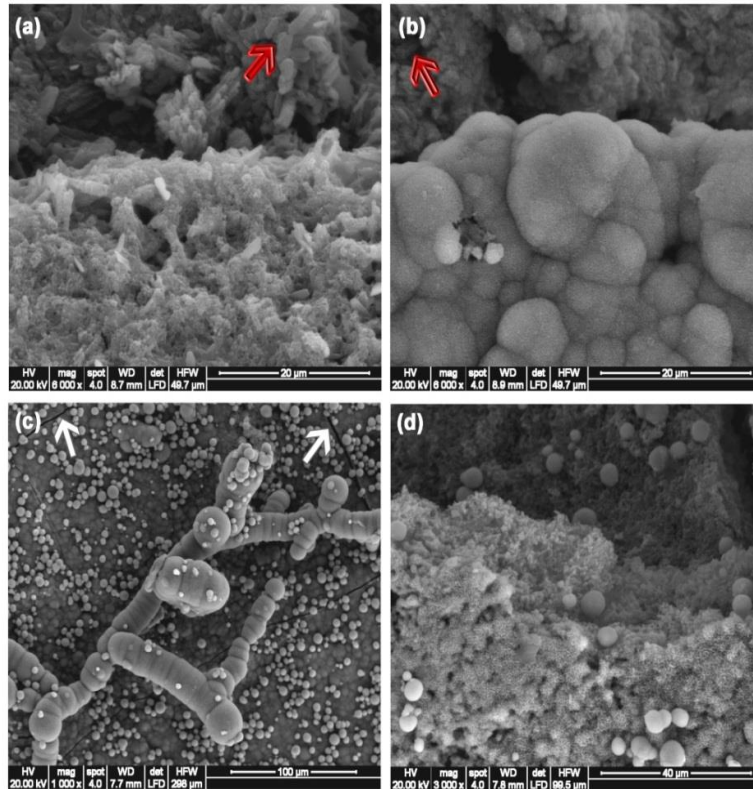


Figure 104: ESEM image of CS253 a) 2 days b) 4 days and c) 7 days immersion in SBF. Red and white arrows show the cement particles and crack at the surface respectively d) shows the magnified view of one of the cracked region.

The pH variation (Figure 105 (a)) shows that initial rate of release of calcium is greater than the consumption and showed an increase from value 7.4 up to 6h, which is due to the exchange with H^+ ions and due to the production of CO_2 (section 4.3.1.1). The precipitation of HA with reduction of pH occurs at lower rate in CS253 than BioCaS and hence uniform HA layer coating was found out only during the 7th day. The pH values of CS253 after 7 days of immersion in SBF was found to be obtained for BioCaS after 4 days. The variation may be due to the difference in the dissolution rate.

The escalation of $[Ca^{2+}]$ and $[S^{6+}]$ and the declining of $[P^{5+}]$ were at a lower rate (Figure 105 (b)-(d)) compared to BioCaS which could explain the higher time

interval required for the formation of thick HA layer over the surface. Concentration of Calcium and sulphur in BioCaS immersed SBF on the 4th day was attained by the CS253 only after a week.

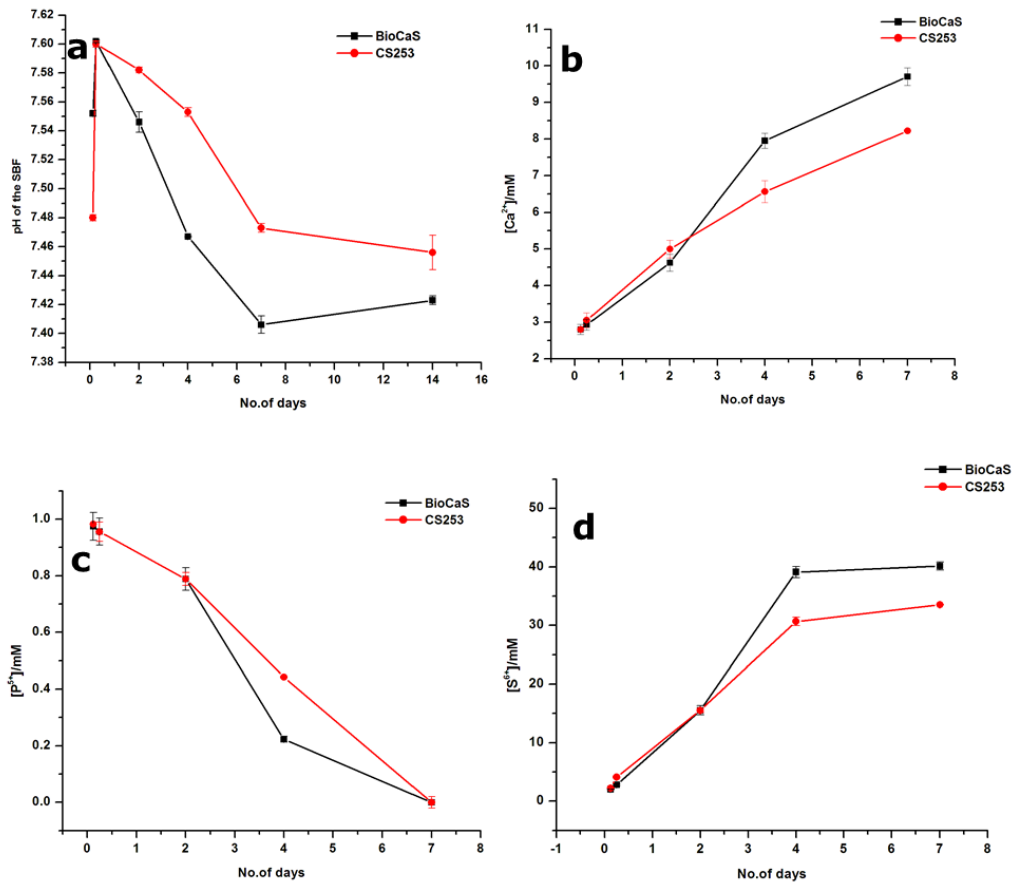


Figure 105: a) pH variation of SBF with immersion time 3 and 6 hours and 2, 4, 7 and 14 days of BioCaS and CS253 b) Elemental concentration profile of a) Ca²⁺ b) P⁵⁺ and c) S⁶⁺ estimated by OES-ICP with the soaking time of CS253 and BioCaS in SBF

4.5.9 Invitro biocompatibility studies

4.5.9.1 Invitro cell culture cytotoxicity by test on extract method

Images of the L929 mouse fibroblast cells after the cell culture cytotoxicity test (using the extracts at 50% dilution) are shown in figure 106. The positive control caused severe damage to the cells (grade 4) and negative and reagent control did not affect the cell morphology (grade 0). Both CS251 and CS253 samples did not evoke lysis of cells or reduction in cell

growth. Discrete intracytoplasmic granules were seen, at a grade value less than 2 and hence non-cytotoxic.

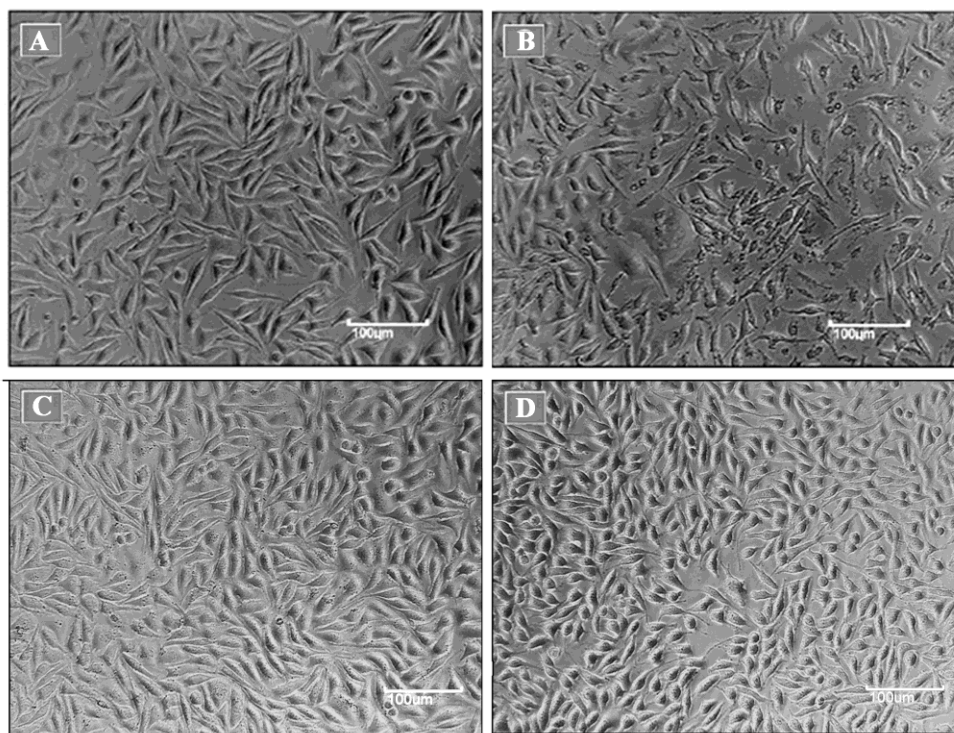


Figure 106: L929 cells after incubating with (a) positive control (b) negative control and 50% extract of (c) CS251 and (d) CS253.

The CS251 and CS253 have showed more than 80 % metabolic activity in all the extracts. Hence the compositions analysed were found out to be non-cytotoxic to L929 mouse fibroblast cells. Negative control gave non-cytotoxic reactivity and positive control gave severe cytotoxic reactivity as expected.

4.5.9.2 MTT assay

The outcomes of the MTT assay are shown in figure 107., where in the metabolic activity values are expressed as mean \pm SD, with n=6. Both CS251 and CS253 have shown greater than 80% metabolic activity directly related to metabolically active cell viability and hence cell compatible as per ISO 10993-5.

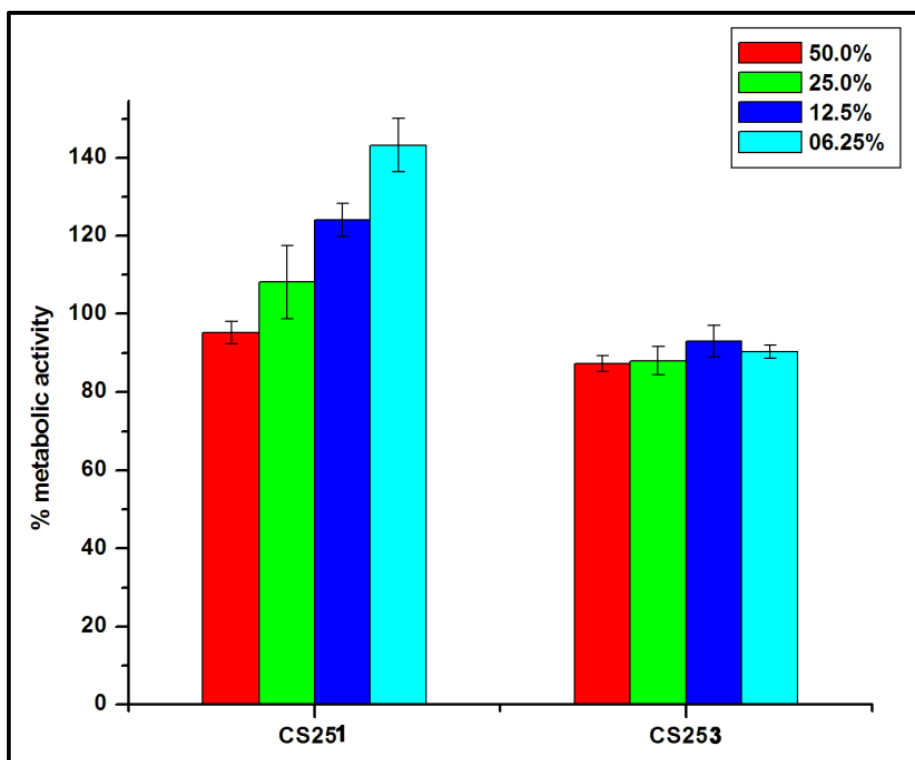


Figure 107: MTT assay for the metabolic activity of viable cells in the physiological saline extract of the CS251 and CS253.

4.5.9.3 Haemolytic assay

The blood sample after exposure to CS253 showed hemolysis value $0.12\% \pm 0.06$ (SD) which is greater than the normal hemolysis value $< 0.1\%$ but within the tolerable limit of $< 5\%$ as stated in [ISO 10993-4:2012 (E)]. The interpretation of the results suggested that the material is safe for *in vivo* experiments.

4.5.10 Human osteoblast cell viability by live dead assay

Most of the cells were found alive in CS251 and CS253 with negligible dead cell distribution which shows the efficiency of the material for bone cell attachment and thereby osteoconductivity (Figure 108). The incorporation of NOCMC has sustained the bone cell compatibility.

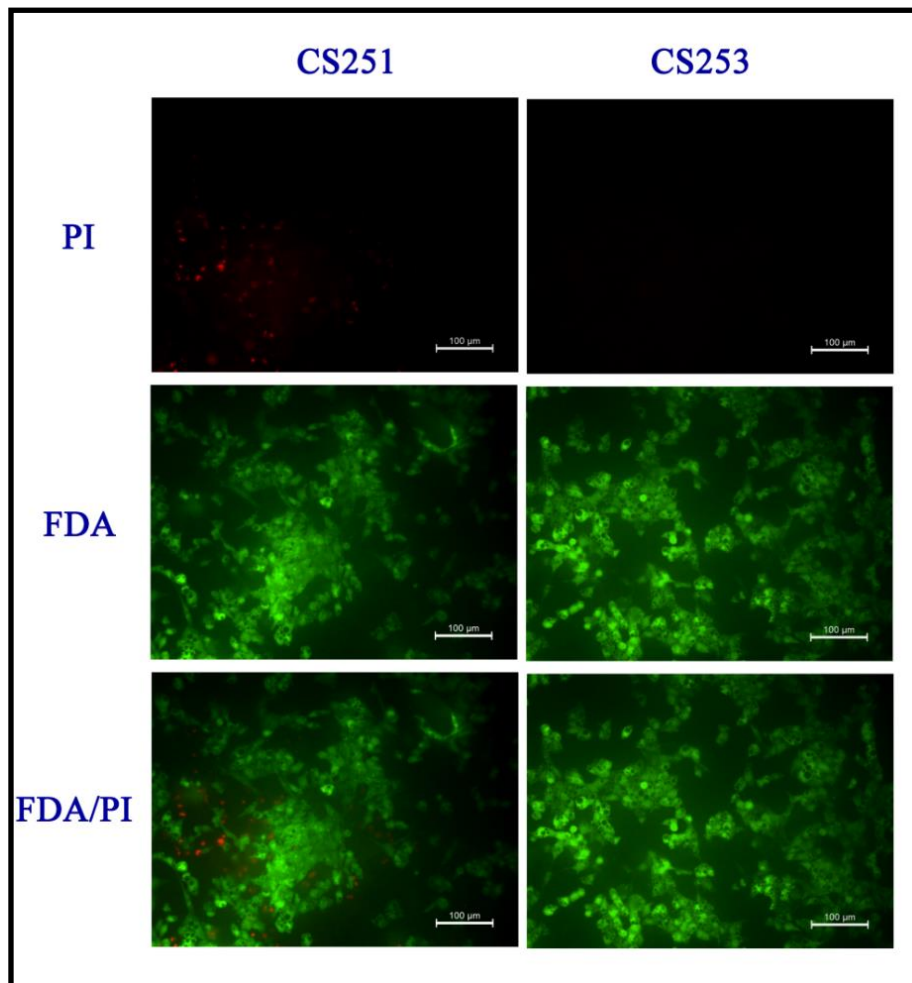


Figure 108: Live–dead double staining of HOS cells adhered on the surface of CS251 and CS253 showing high cell viability: (a) PI signal, (b) FDA signal, and (c) overlay of FDA and PI signal.(scale bar =100µm).

4.5.11 Micromorphology of the HOS cells adhered on the surface of CS 251 and CS253 using Scanning Electron Microscopy

As evident from scanning electron micrographs (Figure 109), HOS cells attached and adhered on the matrix depicted typical flat morphology. Lamellipodium were found directly attached to the cement crystallites and CS253 have shown developed filopodia at higher magnification. Cell activity could be well found out in the pores

and crevices. The cells were found to interact with the material defines the osteoconductive nature and potential tissue healing property.

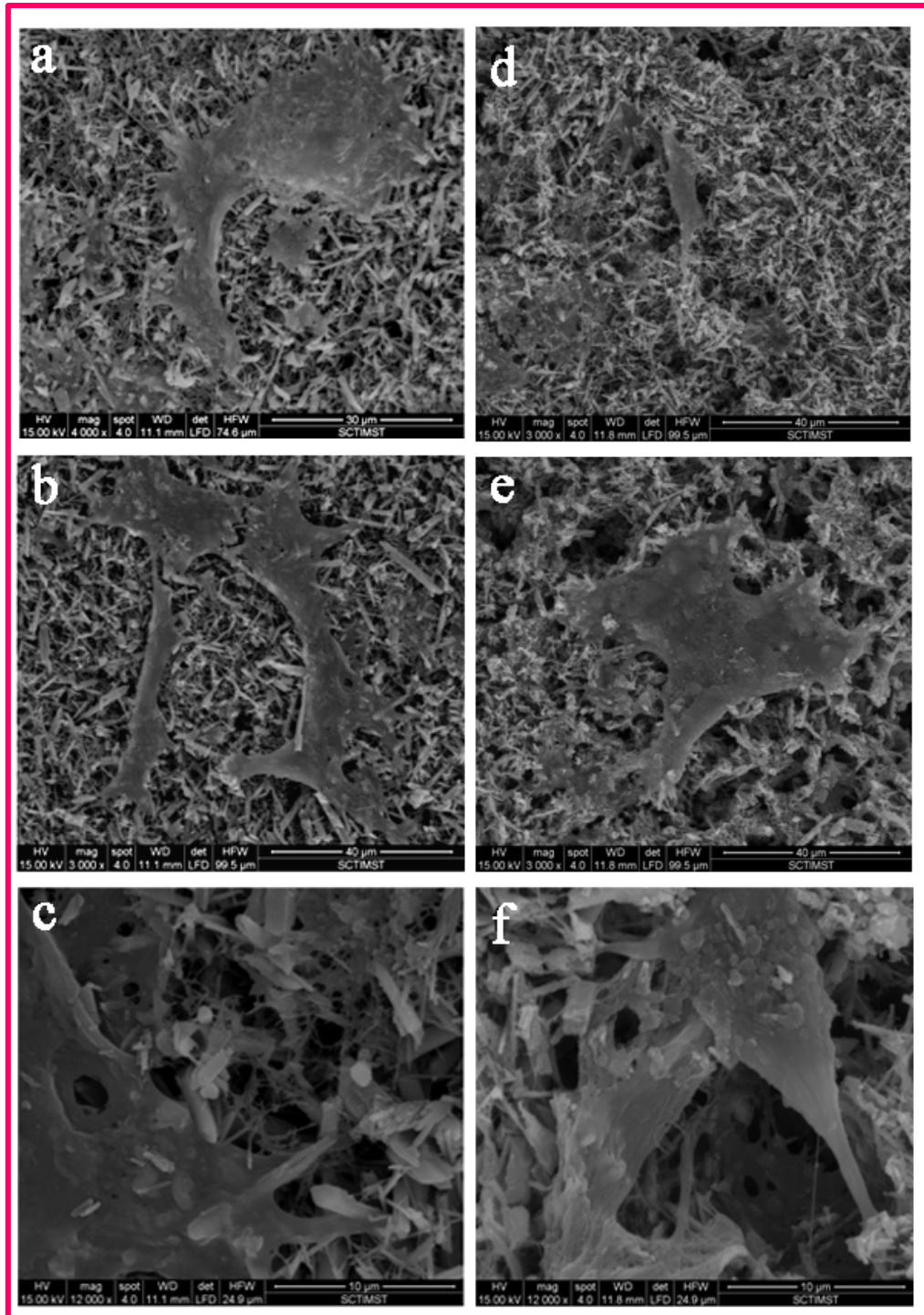


Figure 109: Scanning electron micrographs showing attachment and adhesion of Human osteoblasts like HOS cells on the surface of (a and b) CS251 and (d and e) CS253 and (c) and (f) corresponding magnify

CHAPTER 5

DISCUSSION

This chapter comprises the discussion on the results detailed in the preceding chapter. The prominent outcomes of this study are subsequently correlated with published literature in the relevant field and interpretation is made wherever possible. Finally the limitations of the study are identified and future prospects are outlined.

5.1 Method of synthesis and characterisation of precursor phase for *Injectable Bone Cement (IBC)* formulation

5.1.1 Optimisation of the production of low dimensional medical grade gypsum (smCSD)

Different chemical systems has been reported for the production of gypsum such as $\text{CaCl}_2 \cdot \text{H}_2\text{O}$ and Na_2SO_4 (Wang *et al.*, 2012), CaHPO_4 and H_2SO_4 with cetyltrimethylammonium bromide and sodium dodecyl sulphate as surfactants (Mahmoud *et al.*, 2004), $\text{Ca}(\text{OH})_2$ and H_2SO_4 at 100°C at pH 0.7- 0.8 with NaCl as catalyst, CaCl_2 and Na_2SO_4 in reverse micelle system using n-pentanol, cyclohexane and surfactant polyoxyethylene (9) dodecyl ether (Chen *et al.*, 2007). Most of these methods are developed for industrial application and studies related to nucleation kinetics and precipitation pathway are rare. We have developed a novel method for the synthesis of well crystallised submicron dimensional gypsum (smCSD) rods with monomodal particle size distribution (3-5 μm length and <1 μm width) from calcium nitrate tetrahydrate [$\text{Ca}(\text{NO}_3)_2 \cdot 4\text{H}_2\text{O}$]- sulfuric acid [H_2SO_4] chemical system by ‘drowning out wet chemical method’. Unlike other systems involving sulfuric acid, the precipitate obtained was of phase pure without the co-existence of other

polymorphic forms like bassanite and anhydrite. The current systems were optimised after reconnoitering different methods of synthesis from the chemical system like the cryo-vacuum technique, solvent exchange method for the recovery of gypsum from very dilute aqueous solutions (1g/litre) with different organic solvents, analyzing by changing the concentration ratio of organic solvents and using two miscible solvents and by varying the temperature of aqueous gypsum solutions and the extracting solvent solution. It was possible to produce submicron gypsum whiskers (0.3 to 0.6 μm width) but due to the unfeasibility and low yield the method was not followed.

The yield percentage of gypsum in the new method with respect to the theoretical value was estimated to be $85.89 \pm 1.25\%$. The phase conversion temperature of gypsum is a function of size, shape, crystallinity, and surface area of the particles and degree of lattice perfections. Also it is governed by the procedure adopted for phase transition such as flash drying at high temperature, calcining in rotary kilns, steam or aqueous suspensions, (Bruce *et al.*, 2008). Exploring thermal conversion pathway compiling the simultaneous TG/DTA thermograms and XRD data confirmed the phase conversion to bassanite and orthorhombic anhydrite at 393K (16.12% weight loss) and 613K (23.44% weight loss) respectively. However no evidence for the separate existence of γ -anhydrite alone was obtained and the formation temperature was found out to be from 467.95 K (21.96 wt%).

The current system was developed based on the hypothesis that the control over the particle sizes becomes possible through the suitable selection of nucleation kinetics parameters. The surface free energy may get varied due to the change in the dielectric constant of the medium and carrying out the synthesis in H_2O , $\text{CH}_3\text{-OH}$, $\text{CH}_3\text{-CH}_2\text{-OH}$, $\text{CH}_3\text{-CHOH-CH}_3$, $\text{CH}_3\text{-CO-CH}_3$, $\text{CH}_3\text{-CH}_2\text{-O-CH}_2\text{-CH}_3$ enriched

medium among which the relative polarity with respect to water decreased in the same order. The micromorphology changed from irregular to highly regular with successive descending gradation in particle size. However the relative polarity of $\text{CH}_3\text{-CH}_2\text{-O-CH}_2\text{-CH}_3$ was very low to carry out the synthesis which sediments out the $\text{Ca}(\text{NO}_3)_2 \cdot 4\text{H}_2\text{O}$ and hence excluded. For selecting the medium we have considered the evaporation rate which is in the reverse order of boiling point as H_2O (B.P 373K) < CH_3OH (B.P 337.6 K) < $\text{CH}_3\text{-CH}_2\text{-OH}$ (B.P 351.5 K) < $\text{CH}_3\text{-CHOH-CH}_3$ (B.P 355.4 K). Due to the intermolecular hydrogen bonding the evaporation rate of the $\text{CH}_3\text{-CHOH-CH}_3$ is moderate than the $\text{CH}_3\text{-CO-CH}_3$ and hence selected, which excludes the possibility for creating the polarity gradient in the reaction medium in the large scale production and ensures a wider window for optimization of other parameters during the formulation of bone cements.

The chemical system was analysed further by varying the concentration ratio of 2-propanol with respect to the reaction medium as 1:9, 1:3, 2:3 and 1:1. The highly polar end (1:9) is characterized with irregular flaky particles followed by narrow rods with granular growth features on its surface in the subsequent ratio 1:3. In the 2:3 concentration region the growth features are considerably reduced and in the 1:1 low polar end the regular 3-5 μm length rods were obtained. Hence 2-propanol enriched reaction medium in the 1:1 concentration ratio was selected for the synthesis.

The chemical system was further validated for yield based on the solubility parameter of the Ca^{2+} ions in the supernatant after the completion of the chemical reaction. 2.9 fold decreases in solubility was found out when the reaction media changed from water to methanol. Among the organic compounds the solubility was

found a slow decrease from 6.51 to 5.80 g/l when the relative polarity changed from 0.762 to 0.175. The growth of the particles was effectively controlled by varying the dielectric constant of the medium which decides surface free energy available for growth which will be explained in subsequent sections (Morsy *et al.*, 2014). Even though statistically significant the difference in solubility of synthesised gypsum between acetone and 2-propanol enriched reaction media were only 0.07 g/ml which could be neglected during the up scaling. Hence giving prominence to eliminate the likelihood of polarity gradient at the surface of contact of the two reactant solutions compared to the bulk without compromising the yield, 2-propanol was selected.

Analysing the solubility with change in concentration of the organic solvent at 303K has given unambiguous parameter for the optimization. Introducing 2-propanol in the reaction medium in 1:3 ratio has reduced the loss of 11.18 g/l of gypsum and at 1:1 ratio (maximum workable range) reduced further by 1.69 g/l. The solubility escalated by 2.3 times when the temperature increased by 20K and the particles deviated from homogeneity may be due to the creation of polarity gradient in the reaction media. On the other hand the same trend in reduction of solubility (by only 0.21 times) was not found when the temperature was reduced to 273 K and not shown considerable change in the micromorphology. Considering all the factors, the synthesised system was parameterized with 2-propanol in 1:1 ratio with respect to reaction medium at the reaction temperature of 303K.

BET specific surface area of the synthesised gypsum particles was found to be $12.85 \pm 0.04 \text{ m}^2/\text{g}$ which is significantly higher compared to the reported values of surgical grade calcium sulfate bone void filler $0.6 \text{ m}^2/\text{g}$ (Cooper, US6780391 B1 patent, 2004), $1.94 \text{ m}^2/\text{g}$ (Asadi-Eydivand *et al.*, 2016). Heavy metal analysis in the

lyophilized powder completely exclude the presence of cadmium and lead but contained arsenic and mercury in 6.45 ± 0.60 ppm and 0.60 ± 0.32 ppm level. It is noteworthy that the total concentration of trace elements before and after phase conversion to bassanite (7.049 ± 0.92 ppm and 8.19 ppm respectively) is well below the limiting value of 10 ppm and thus pass the regulatory specification for medical grade gypsum.

Preliminary biocompatibility screening through *in vitro* cell culture cytotoxicity test confirmed the cell compatibility of the material with respect to metabolically active cell viability of L929 mouse fibroblast cells.

Study of nucleation kinetics has been taken up to confirm the insight on the controlled growth mechanisms of new phase formation in this system. The induction time for gypsum particles to appear in the system was determined at homogeneous precipitation conditions through spectroscopic turbidimetry at various millimolar concentrations.

5.1.2 Relevance of CNT in the current chemical system

The data have been analysed using classical nucleation theory for homogeneous nucleation. Typical linear relationship was obtained in the $\log t_{\text{ind}}$ vs $1/\log^2 S$ plot for the supersaturation range between 2.12 and 5.16. Different methods (mainly based on optical and electrochemical techniques) have been used to track the t_{ind} for gypsum. Optical methods include monitoring of scattered and transmitted light, measurement of turbidity and direct observation by naked eye. Electrochemical methods include measuring the conductivity of the feed suspension and evaluating the concentration of free calcium cations in the solution. The value of induction time is specific to the measurement method and is defined operationally (Wang *et al.*,

2010). In the present experiment, turbidimetry using UV-Visible Spectrometer was employed because it is simple and reliable. Essentially the intensity of the beam passing through the sample is measured. Absorption, reflection or scattering due to the nucleated particles can occur, leading to a reduction of intensity. The λ_{\max} of 340 nm was chosen for high sensitivity. As the scattering increases with the inverse fourth power of the wavelength, shorter wavelength will give greater signal difference. Also, the refractive index of the material is greater at shorter wavelength. At the value of 340 nm the detection limit is 40–70 nm. In the present technique, the induction times measured correspond to the presence of particles above 70 nm (Molina-Bolovar and Gonzalez, 2004)

In a study of effects of metallic ions on the crystallization of calcium sulfate dihydrate from calcium hydrogen phosphate - sulfuric acid system (Rashad *et al.*, 2004), the surface energy value reported for bare solution was 8.35 mJ/m². When Al₂O₃ and MgO were added at 1% concentration, the value changed to 9.53 and 8.05 mJ/m² respectively. In another work (Mahmoud *et al.*, 2004), exploring the effects of surfactants on the crystallization of gypsum in the supersaturation ratio range 1.618 to 1.979, a surface energy value of 8.4 mJ/m² was obtained. The addition of 100 ppm concentration of the surfactants cetyl trimethyl ammonium bromide and sodium dodecyl sulfate changed the surface energy values to 8.7 and 6.7 mJ/m² respectively. Alimi and Gadri (Alimi, 2004) studied the kinetics of formation and morphology of gypsum crystals using calcium chloride and sodium sulfate in aqueous system at different supersaturations from 2.5 to 11.0 at a temperature of 30°C. The surface energy obtained for homogeneous nucleation was as high as 13.9 mJ/m². Also with additive 2-phosphonobutane-1,2,4-tricarboxylic acid (PBTC), surface free energy

value of 31.97- 42.23 ($t = 15-35^{\circ}\text{C}$) was reported. Number of fine crystals were found out to increase with the decrease in surface free energy.

At low nucleation rate, size of the nuclei formed was found to be higher due to higher chance of growth using the available concentration and vice versa. On escalating the supersaturation, it was observed that the nucleation rate drastically increased and the calculated critical radius decreased. However, the surface free energy obtained for the present system is 5.6 mJ/m^2 which is the lowest value reported to the best of our knowledge. It could be learnt from the theory that lowering the interfacial tension (or surface free energy) will drastically enhance the rate of nucleation as the exponential relation of J_s is to the 3rd power of γ (equation 23). Increase in the number of nuclei limits the growth of each one in a contained system because the availability molecules through diffusion get exhausted fast due to the very low surface free energy available for growth which inturn contributes to the reduction in particle size.

The particle size of the nanoclusters measured using dynamic light scattering analysis by arresting growth at the t_{ind} gave a distribution centered at 8.079 nm. TEM analysis showed particles in sizes comparable with DLS measurements. It is evident that nano-sized calcium sulfate could be synthesized in the present system by carefully adjusting the nucleation kinetic parameters. The monodispersed nature of particles observed in the particle size analysis could be explained with the help of La Mer Model of growth in a liquid media (Murray *et al.*, 2000). In a supersaturated solution, the nuclei will grow as long as the supersaturation holds, unless properly controlled. After the initial burst, no new nuclei are formed during the growth phase.

If nucleation and growth are separated in time (or, if the growth is slow enough) all growing crystals end up with very similar size since they have a similar history.

5.2 Physicochemical mechanism for the formation of injectable bioactive bone filler cement

The salient outcome of this work is the development of self-setting injectable cement where the preset formulation comprises bassanite obtained from the uniform submicron-sized precursor crystals of gypsum, modified with disodium hydrogen orthophosphate ions and the set cement consists of phosphate integrated gypsum crystal lattices. The effect of induction of injectability in calcium sulfate cement (CSC) paste, by the addition of DHPD has been observed empirically, during the attempts to make calcium sulfate more bioactive by introducing phosphate compounds as additives. The optimised bioactive injectable calcium sulfate cement paste turns out to be highly useful for specific applications like minimally invasive surgery in compression fractures, filling cysts and as a drug delivery medium to treat bone diseases.

The crucial requirement of an injectable bone cement paste is that the viscosity should be in the range of 100–1000 Pa s (Dorozhkin, 2011, Low, 2011). Very thick pastes (with viscosities above 1000 Pa s) demand high injection force which is not achievable practically in hand-operated syringes/applicators. On the otherhand, low viscosities (<100 Pa S) may lead to extravasation of the loose paste from the surgical site to the surrounding tissues (Stephen and Michael, 2008). As per this criterion, the compositions containing DHPD from 2.5 to 3.5 % appear most suited for clinical application, as they provide flowing pastes with low viscosities. The viscosity-time graphs (Figure 34) show that these formulations follow near-

Newtonian behaviour (i.e. the viscosity remains almost independent of the pressure). These CSC formulations were ‘fully injectable’, i.e. the cement paste extruded out throughout the travel distance of the plunger (It is to be noted that even for the ‘full injectable’ cements, a small quantity of the paste will remain at the neck of the syringe. This effect is due to the ‘shear thickening’ of the paste near the neck, which could be minimised with appropriate neck design). The optimum flow with the lowest and constant viscosity throughout the extrusion period was observed for smCHD2 sample.

Interestingly, DHPD is a simple inorganic compound, which basically has no gelling property or any viscous character. This work presents sufficient evidence to conclude that phosphate moiety has played crucial role in imparting flow properties to the (otherwise non-viscous) bare calcium sulfate cement paste. There are several known factors (like temperature, ionic impurities etc.) which affect the setting of CSC and the properties of the set cement (Anusavice, 2008). The enthalpy of hydration determined through Isothermal DSC could be explained based on the theoretical model of hydration of CSH by DeKorte and Brouwers (Korte and Brouwers, 2008). It considers the dissolution and reaction of CSH particles in water which is followed by diffusion and precipitation. The precipitation involves primary nucleation, growth of the nuclei and secondary nucleation, where the energy involved is characterized by the hydration enthalpy, ΔH_{hyd} . The model indicates that the thermal stresses due to the exothermicity of the hydration and the presence of ions introduce lattice and surface defects in beta CSH (bassanite) crystals, resulting in higher grain instability (Fischer *et al.*, 2012). Hence this model implies that ΔH_{hyd} values get enhanced due to defects or ionic modification of the crystal lattice, or in

the event of a new phase formation. The phase analysis using XRD gives indisputable evidence for the inclusion of phosphate (HPO_4^{2-}) in the CSD lattice during crystallization, which gets further supported by FTIR (Sect. 4.3.4) and EDS (Sect. 4.2.5) analyses and also by the ionic elution study (Sect. 4.2.9). The strong molecular interaction observed in Isothermal DSC, presumably, must be between hydrogen orthophosphate and calcium ions. The rehydration reaction and crystal formation of CSD in presence of DHPD might have led to the crystal habit modification and substitution of phosphate in the CSD crystal lattice i.e. the formation of phosphorus enriched microdomains. However, the present data is not sufficient to delineate the nature of the interaction.

The morphological study in SEM showed that the particle sizes get reduced from micron level to sub-micron level on increasing the content of DHPD from 1.5 to 10 % which was corroborated with the surface profile and the particle size peak count histogram from Talysurf CLI 1000. It is clear that the presence of DHPD (or the ions present in it) drastically influence the crystal growth mechanism of CSD (Korte and Brouers, 2008). The interconnecting aggregate structures (containing very small particles as seen in the SEM) also increase with higher concentrations of DHPD, indicating the occurrence of secondary nucleation during the growing of CSD crystals. This gives the advantage of better packing in the cement leading to the increase in compressive strength of the set mass.

The induction of viscosity in calcium sulfate cement paste by the addition of DHPD is an interesting effect, which may have possibly been driven by the interaction between phosphate ions and the precipitating calcium sulfate and due to the inclusion in crystal lattices. It is difficult to provide a clear explanation for the

phenomenon from the present data. The steps in the setting process of CSC are inter-linked with several parameters and hence the practical approach is to deduce conclusions from the available results.

The setting reaction in the calcium sulfate cement could be envisaged to occur in the following steps (Anusavice, 2008) (a) The formation of a workable suspension when the hemihydrate is wetted, (b) The saturation of ions in the water film around the particles of CSH by dissolution, (c) The onset of precipitation of CSD when the supersaturation is achieved, and further dissolution of the remaining CSH as the supersaturation get reduced due to the precipitation, (d) The growth of CSD nuclei to larger crystals on gaining supersaturation in the surrounding water film (secondary nucleation), and (e) The interlocking of growing crystals during growth, leading to the hardening of the mass. The completion of the step (c) marks the initial setting time and the step (e) decides the final setting time (Anusavice, 2008). It is quite likely that the presence of phosphate in the calcium sulfate paste might have been reducing the supersaturation of CSD, thereby slowing down the phase conversion. The proliferation of secondary nucleation and lowering of growth rate of crystals are the consequences. This conclusion is supported by the SEM observation that the crystal sizes get lowered and the aggregates of small particles increase, with the increase in the DHPD content. Also the prolongation of setting times of the corresponding CSC samples is seemingly linked to this process. The initial setting time (t_i) corresponds to the completion of precipitation of CSD in the paste and the final setting time (t_f) refers to the period of growth of crystals. It is to be noted that the t_f is more predominantly affected than the t_i , by the DHPD content.

This is an indication of lowering of the growth rate of CSD crystals in the setting cement by DHPD.

The results show variation in the enthalpy of hydration of CSC powder and inclusion of phosphate in the CSD crystals in the cement matrix. Obviously, HPO_4^{2-} ions are actively involved in the cement conversion process. It could be hypothesized that the Van der Waal's interactions between the molecules impart flow properties to the paste. Ie. The active precipitation process in the cement paste may influence the flow properties. The newly precipitating CSD in the paste will tend to grow uniformly, but in a slow pace. Formation of smaller interconnecting aggregate structures increase the cohesion by reducing interparticle friction leads to homogeneous flowing slurry. However when the particle sizes go down, the non-newtonian behaviour (shear thickening) predominates due to aggregation. This may be the reason for drastic decrease in the viscosity up to smCHD2, and subsequent increase in viscosity after smCHD3.

5.3 preclinical validation of BioCaS

The *in vitro* screening tests of cell culture cytotoxicity and haemolysis tests confirmed the material to be non-cytotoxic to L929 mouse fibroblast cells, with a haemolytic potential well below the acceptable limit. Adhesion and spreading of the osteoblast-like HOS cells points towards the performance of BioCaS as a bioactive scaffold in clinical applications.

The *in vivo* biocompatibility studies done as per ISO 10993, though largely qualitative, help to delineate the toxicological safety profile of BioCaS. In the acute systemic toxicity test, the material extracts in cotton seed oil did not invoke any adverse systemic response in mice. The short transient reduction in motor activity

observed in some mice after intravenous administration of the test extracts may be due to the presence of eluted calcium ions in the extract. Nystrom et al reported the risk management from the experience during the administration of calcium sulfate containing bone substitutes while treating 22 patients with unicameral bone cysts [Nystrom *et al.*, 2008]. The injection of bone substitute has induced acute laryngospasm in 3 patients and tachycardia in one patient. They attributed this effect to the nociceptive stimulus of local tissue damage by the absorption of cement remnants and subsequent acidic and inflammatory environment. Deeper anesthesia with shorter acting agents and highly cognizant of airway management around the time of injection can prevent these complications.

BioCaS samples did not stimulate any erythemic or oedematous reactivity when injected at intracutaneous sites in rabbits. No signs of erythema and oedema nor any adverse skin response was observed in the maximization sensitization study in guinea pigs. Intravenous administration of the physiological saline extract in rabbits in the pyrogen test did not cause any undue rise in body temperature. These results cover the allergic and pyrogenic safety aspects of the material.

The implantation test explored the ability of BioCaS to heal experimental bone defect created in rabbit femora, in comparison with hydroxyapatite porous ceramic. The implantation was done on 12 animals (four each for 12, 26 and 52 weeks) and was uneventful in all cases. The healing of the defects, on macroscopic evaluation, was without any encapsulation, haemorrhage, infection or necrosis. In the histological investigation, healing from the periosteal and endosteal aspects of the cavity was observed at 12 weeks in both test (BioCaS) and control (hydroxyapatite ceramic) samples. New bone formation was observed at the host bone side with good

apposition with the material. These features indicate the osteoconductivity of the materials used for the experiment. The osteoconductive nature of hydroxyapatite ceramic has been established in the literature (Woodard et al., 2007). The present results emphasize that the osteoconductivity of BioCaS cement is on a par with that of hydroxyapatite.

More notable is the resorption of the material and remodelling of the defect site through 52 weeks. BioCaS cement was mixed and applied to the defect formed a solid fill after the setting period. At 12 weeks, considerable material resorption was seen (figures 67(a) and (c)), which is evidently cell mediated. There were no gaps left due to the cement resorption other than some small vacuoles. The deposition of collagen and formation of new bone were observed where resorption had occurred, and rosettes of osteoblasts and osteocytes are present in the region (figure 67(e)). There were no gaps left due to the cement resorption other than some small vacuoles. Most of the cement material filled in the defect had been resorbed by 26 weeks, and was been replaced by new woven bone with early Haversian system formation (figures 68(a), (c) and (e)). The presence of osteocytes in profuse quantity indicates the active resorption of the material and the induced remodelling of the defect. Matured woven bone formation with concentric circular features of the Haversian system is notable in the histological images. The bone remodelling nearing completion (with a lamellar structure) and almost full resorption of the material are evident in the samples at 52 weeks (figures 69(a) and (c)). The remnants of the cement are seen residing as fine particulates in the newly maturing bone at the site, which may disappear with further cell activity (figure 69(e)).

The resorption of the hydroxyapatite ceramic is rather slow, with more than half remaining even after 52 weeks (figure 69(b)). This observation corroborates earlier reports of implantation experiments with hydroxyapatite ceramics (Fernandez and Mohanty M, 2006). All other features of bone remodelling are very similar to those of the test material (figures 68(b) and (d) and 69(b) and (d)). The new bone is in good apposition with the ceramic surface. Though the hard tissue is in biological contact with the material, this kind of healing may not provide adequate strength to the healing site.

On comparing the histological results of the bone defect healing with BioCaS cement through 52 weeks, the phenomenon of progressive material resorption and simultaneous new bone formation is evident (figures 67(a) and (c), 68(a) and (c), and 69(a) and (c)). This property is called ‘*osteotransductivity*’, the ideal requirement for a bone graft substitute [Fernandez et al; 2006, Reardon *et al.*, 2015]. Compared with ceramic granules, BioCaS comprises uniform micron-sized particles entangled together during cement setting. The inter-particle boundaries gradually become weaker during resorption and give way to newly growing bone. The particulate structure of BioCaS offers an enormously large surface area for osteoblasts to act upon and remodel the defect. Such a healing process will provide better strength to the repaired site, as the new bone replaces the material and the remodelling progresses fast.

Osteotransductivity has been reported earlier only for CPC. Comparison with an earlier report on a similar study with CPC [Fernandez *et al*; 2006] shows that the safety and efficacy of BioCaS are on par with those of CPC. The similarities in

mechanical and biological properties are striking, which holds for *osteotransductivity* also.

The bioactivity of BioCaS could be explained through the activity of ions present in the material. Presumably, upon implantation, cement elutes calcium and sulfate ions into the body fluids. The Ca^{2+} ions combine with PO_4^{3-} ions from body fluids and tend to form hydroxyapatite because the surrounding medium is supersaturated with respect to hydroxyapatite. This forms an osteoconductive lattice of biological apatite and stimulates bone growth into the defect (Kumari *et al.*, 2014). Calcium ions, released during the dissolution of CaS, are likely to increase its local concentration there by stimulating the mitogenesis of stem cells and osteoblast differentiation. Also, this high concentration of calcium might inhibit osteoclast-mediated resorption and promote bone remodelling (Ustariz, 2011). Most papers on injectable bone cements are based on the calcium phosphate/CaS composite bone cements with gelling agents to obtain tunable resorption (Larsson and Hannink, 2011, Thai and Lee, 2010). However, BioCaS was developed without the addition of any gelling agent, which means that the biocompatibility of the material is not compromised.

There is sufficient body of evidence to define the *in vivo* resorption period of calcium sulfate implantable material as 4–8 weeks (Thomas and Puleo, 2009, Mirzayan, 2001). Christopher et al reported the degradation period of CSC to be 40–70 days (6–10 weeks) in an ovine model (Peters et al., 2006). Another study in dogs showed substantial resorption of a CaS graft material by 6 weeks (Urbani et al., 2004). These reports in animals almost correlate with data in human clinical trials, wherein a CaS-based graft material was resorbed in 8 weeks (Kelly and Wilkins,

2004, Clayer, 2008). This is a rather short period for new bone to deposit and develop strength through remodeling. In the present study, the BioCaS formulation implanted in rabbit bone took 26 weeks for significant degradation, which seems ideal compared with the resorption data of other CaS formulations. This must be due to the presence of incorporated hydrogen orthophosphate ions in the cement which may be limiting active (cell-mediated) resorption. The resorption rate of BioCaS and its osteoconductive properties make it a promising candidate for bone defect filling in orthopaedics and dentistry.

5.4 Injectable BioCaS as a local drug delivery system for minimally invasive chronic osteomyelitis management

5.4.1 Initial screening of BioCaS for drug holding capability and mechanism of drug loading

In this study we evaluated the potential of the BioCaS as an injectable local therapeutic agents for chronic osteomyelitis. Unlike sintered ceramic blocks and spheres where the drug loading is through vacuum suction based on the porosity, the semisolid consistency of the cement paste helps to incorporate comparatively higher quantity of the drug through wetting medium. It has been suggested that local antibiotic concentration should be above the minimum inhibitory concentration for a period of 14 days for effective prevention of infection which would enable the host immune system to cope more effectively (Howlin *et al.*, 2015).

Initial screening of BioCaS for its drug holding capability with low drug dose was successful with 17 days of GS and 47 days of VH elution. However GS has higher initial burst release compared to VH and almost 42 % release of the initially loaded drug. However more sustained release for the longer duration was found out

for the VH. The GS elution was controlled by quasi-fickian diffusion mechanism in which the surface elution has significant role in the initial 2 days. However previous report mention the desired effect of local drug delivery systems for concentrating the drug locally while simultaneously maintaining low to no detectable serum levels, thus minimising possible systemic toxic levels. For instance., the wound exudate tobramycin concentrations in the animals treated with tobramycin loaded calcium sulfate pellets peaked at 11.9 mg/ml on day 1st and reduced to 2.5 µg/ml on the 7th day, while Serum concentrations were 6 µg/ml at 3 h and non-detectable thereafter (Nelson et al., 2002). Therefore the systemic toxicity based conclusions couldn't be made without *in vivo* experiment.

In VH, elution mechanism was purely diffusion controlled with only $\approx 10\%$ of the loaded drug release where more drug gets entrapped in the matrix which could come out only after the relaxation and degradation of the matrix. The hydrogen bonding interaction between O in SO_4^{2-} and H in $-\text{NH}_2$, $-\text{OH}$ and also Ca^{2+} complexation with drug to an extent may also influence the elution.

Validation of drug release pattern obtained through UV-Visible spectrophotometry was further done with HPLC analysis to exclude the chance of scattering of radiation by the fine particles of the matrix in the eluted medium. Hence further drug elution and kinetics varying concentration and S/V proceeded through UV-Visible spectrophotometry.

5.4.2 Elution kinetics varying the concentration of the drug loaded and S/V ratio of the matrix

Drug elution kinetics and mechanism changed when the concentration of VH loaded in the BioCaS escalated. Increase in drug dose in the matrix contributed to the

cumulative drug release but decreased the efficacy with respect to loading. The diffusion mechanism changes from 'quasi-fickian to fickian to non-fickian controlled' (which is based on the rate of diffusion (R_{diff}) of the drug moiety and rate of relaxation of the cement matrix (R_{relax})) from low to higher drug dose form with corresponding increase in slope of the K-P model graph. Quasi-fickian and fickian diffusion mechanism follows when the PBS medium penetration rate is much below the matrix relaxation rate i.e. the rate of diffusion is much smaller than the rate of relaxation ($R_{diff} \ll R_{relax}$). Non-fickian diffusion mechanism describes the condition in which the diffusion and relaxation rate are comparable ($R_{diff} \approx R_{relax}$) and both contribute to the drug release. Hence BioCaSV3 is both diffusion and relaxation controlled. High rate of release of drug within short interval was expected by varying the surface area to volume ratio. However release was not found to be in direct proportion with S/V ratio and the kinetics followed in all case was quasi-fickian (Gierszewska-Druzynska and Ostrowka-Czubenko., 2012).

Significantly higher elution rate was found out for the GS loaded BioCaS and showed the influence of S/V ratio of the cement cylinder. Percentage cumulative amount of the drug released was found out to be escalated by 31.57 % from cements with low to high S/V ratio. 95% of the loaded drug was found out to be eluted from BioCaSGS3 during the period of 17 days. The kinetics followed were Higuchi model where the concentration of the eluted drug is square root of time dependent where the tortuosity and porosity is the main deciding factor. However with the increase in concentration we got more controlled release pattern. Percentage cumulative amount of the drug released was found out to be higher for the low drug dose forms similar

to BioCaSV1. Nonetheless percentage cumulative release was very high ie.70.78 % for BioCaSG1 against 10.40 % for BioCaSV1.

Comparatively better injectability was found out for BioCaSG3, BioCaSV2 and BioCaSV3. All the compositions except BioCaSG1 have acceptable setting time. Prolonged final setting time of the BioCaSG1 may be due to the decreased solubility of hemihydrate in the basic drug which delays the final phase conversion but may be predominated by the drug-matrix interaction at higher concentration causing the setting time acceleration. In BioCaSV1 the solubility of the hemihydrate (basanite) increases in the acidic drug occupying region and hence precipitation of gypsum becomes faster and setting time decreases. Better compressive strength compared to the BioCaS were found out for the higher drug dosage forms BioCaSG3 and BioCaSV3. Compressive modulus values comparable with BioCaS were obtained for the BioCaSG3 and BioCaSV1 and significantly higher value for BioCaSV3. This may be due to the complex drug-matrix interaction. However in open surgeries all the bone cements discussed above could be used as local drug delivery systems in the form of preformed beads.

5.4.3 Antimicrobial activity of BioCaSG3 and BioCaSV3 against the *E. Coli* and *S. aureus*

Growth inhibition of antimicrobials against the BioCaSG3 and BioCaSV3, tested for the first twenty days after the drug loading gave promising results. From the standard ZOI for the susceptible, intermediate and resistant range of bacteria, GS eluted from the BioCaSG3 has shown antimicrobial activity against both *E.coli* 25922 and *S.aureus* 25923 strain. *S.aureus* has shown antimicrobial susceptibility throughout the study period while the *E.coli* after 15 days were found to develop

intermediate resistance. The eluted VH from the BioCaS was found out to be effective to prevent the growth of even gram positive pathogen E.coli for the first one week. It effectively prevents the growth of S.aureus during the entire period of study with the ZOI value significantly greater than that of positive control and comparable to the susceptibility range.

5.5 Injectable bioactive bone cement with NOCMC integrated Gypsum

Most of the papers on injectable bone cements are based on the calcium phosphate/calcium sulfate composite bone cements with gelling agents for getting tunable resorption (Thai and Lee et al., 2010). However BioCaS is developed without the addition of any gelling agent but by adopting the new method of synthesis for the precursor thereby varying the properties of the resultant cement and by the addition of minor inorganic additive. We hypothesised that the mechanical property and the injectability enhancement of phosphate incorporated cement could be possible with the integration of gelling agent NOCMC through crosslinking with calcium without compromising the bioactivity, cementing properties, degradation rate and cell compatibility. Hence this section includes the verification of the cement systems comprising bassanite and DHPD and N,O-carboxymethyl chitosan. NOCMC was synthesised from chitosan by treating with monochloroacetic acid in alkaline medium and the carboxymethylation was confirmed by FTIR and ¹H NMR. The synthesised NOCMC was imparted to the cement system through wetting medium DD water and a total of nine compositions were tested.

The improved rheology with respect to BioCaS was found out only for CS351 and CS353. The important observations are that irrespective of the DHPD

composition the 0.3 W/V % NOCMC showed better fluidity. The escalation of concentration of DHPD for a constant composition of NOCMC also found to impart better fluidity. Hence the injectability is the compiled effect of interaction of NOCMC and DHPD with β -CSH. However the medium concentration of NOCMC better contributes to fluidity.

Among the tested compositions the CS151 and CS153 is fast setting but the rests are in the clinically acceptable range of 8-14 minutes. The setting of 0.6 wt % incorporated NOCMC was slow due to the increased water holding capacity. Compressive strengths were found to be higher for the CS251 (15.9 MPa) and CS253 (15.6 MPa). CS156, CS356 and the highly injectable compositions CS353 and CS356 with inferior strength < 10 MPa has been excluded.

Based on the analysis we have selected CS251 and CS253 formulations which have higher compressive strength than BioCaS but with higher magnitude of viscosity than BioCaS since the highly injectable compositions doesn't meet the strength requirement. The calcium crosslinking by the -O- of the carboxymethyl group in NOCMC was confirmed from the FTIR spectrum of the CS253 and the higher DHPD and NOCMC containing composition CS356. The high homogeneity of the set CS251 and CS253 cement particles as found in ESEM ensures the tight packing and hence the mechanical strength.

The *in vitro* degradation percentage was found to be 36.66 ± 0.77 and $37.76 \pm 0.25\%$ in CS251 and CS 253 but at a significantly lower rate than BioCaS which is due to the chelating effect of NOCMC. The samples were found to be non-cytotoxic to L929 mouse fibroblast cells and the percentage hemolysis ($0.12 \pm 0.06\%$) within the tolerable limit.

Bioactivity was not hampered by the cross linking of Ca^{2+} in bone cement to NOCMC but the formation of thick HA layer coating gets appeared only after 7 days in SBF while which is after 4 days in BioCaS. This may due to the low rate of ionic dissolution. The XRD gave evidence for the formation of HA layer with less crystallinity and the FTIR shown the presence of carbonated HA, the precursor phase of crystalline HA(Mahamid *et al.*, 2008). The trends in the variation in pH, and the elemental $[\text{Ca}^{2+}]$, $[\text{P}^{5+}]$ and $[\text{S}^{6-}]$ in CS253 and BioCaS at the collected intervals supports the delayed formation of HA in CS253.

The cements were found to be non-cytotoxic to L929 mouse fibroblast cells and non- hemolytic to human blood. The percentage hemolysis value of CS253 (0.12 ± 0.06) was akin to BioCaS (0.14 ± 0.03) with no significant difference. Live dead assay confirmed the human osteoblast like HOS cell compatibility of the material. The spreading of the HOS cells on the surface of the materials were confirmed by the ESEM imaging.

In short, with gelling agent, we could able to develop formulations having higher compressive strength and low degradation rate than BioCaS but with inferior injectability. The gelling agent concentrations were selected without affecting the clinically approved setting time. The cements were bioactive but HA layer formation is slower than BioCaS and passed the invitro screening test for the bone cell compatibility to act as an osteoconductive scaffold.

5.6 Limitations of the study

The explanation for the variation of elution kinetics with concentration of the drug loaded and surface area to volume change could be well depicted only after

correlating with the mechanism of interaction of drug with cement matrix and final phase conversion.

5.7 Future perspectives

The bioactive injectable bone filler cement developed is a viable and affordable product for commercial use in various cases of skeletal repair. BioCaS find attractive applications in the minimally invasive bone defect management and in local delivery of drugs for bone diseases. Osteomyelitic bone defect management of diabetic patients become a serious health concern now adays. Injectability enhancement of drug loaded BioCaS could be addressed and the safety and efficacy assessment of drug carrying matrix should be further studied to develop it as local drug delivery system for the purposes.

CHAPTER 6

SUMMARY AND CONCLUSION

6.1 Summary

Injectable bioactive bone filler cements with calcium sulfate-phosphate system with osteotransductivity with acceptable cementing parameters are the primary concern in this study. A viable method was developed to produce uniform submicron dimensional medical grade gypsum from calcium nitrate-sulphuric acid system possessing reduced surface free energy of 5.6mJ/m^2 by 'drowning out wet chemical method'. Study of nucleation kinetics has been taken up to develop an insight into the mechanisms of new phase formation in this system. The induction time for calcium sulfate particles to appear in the system was determined at homogeneous precipitation conditions through spectroscopic turbidimetry at various millimolar concentrations. The nucleation kinetics parameters were deduced applying classical nucleation theory for homogeneous nucleation. The knowledge of nucleation kinetics parameters were utilized for the synthesis of nanoclusters of gypsum with particle size ≈ 10 nm. However more studies are needed to correlate the nucleation parameters to the growth of crystals in the medium.

A new injectable bioactive bone filler cement named 'BioCaS' has been developed for bone filler applications. This is a self-setting injectable cement where the preset form comprises bassanite obtained from the uniform submicron-sized precursor crystals of gypsum, modified with hydrogen orthophosphate ions. Addition of DHPD to the cement precursor powder in small percentages is found to enhance the rheology of the calcium sulfate cement paste, which basically lacks flow

properties. This phenomenon of induction of viscosity to a mineral paste/slurry by the addition of inorganic compound is a novel part of the study and has not been reported earlier. The phosphate integration imparted higher bioactivity to the cement. With the custom made capillary rheometry model, the paste could be extruded fully from a syringe through an 18 gauge needle. The elevated heat of hydration smCHD2 compared to the control smCHD0 cement indicated certain molecular level interaction. XRD and FTIR analyses indicated the substitution of phosphate ions (without any separate phase formation) in the gypsum crystals of the set cement. This has been reconfirmed through elemental analysis (EDS) and elution test (by quantifying the eluted S, Ca and P using OES-ICP). The quantity of the hydrogen orthophosphate ion substitution in calcium sulfate crystals increased linearly with the DHPD content. This kind of substitution in gypsum crystals has not been reported earlier, though composite of calcium phosphate and calcium sulfate have been tried as bone cements. The presence of phosphate enriched microdomains was seen to affect the crystal morphology of the solidified cement. The crystal habit changed, and the sizes got reduced with the increase in DHPD. The cement mass was seen to be inhabited, more and more, by aggregates of very small crystals. The setting of the cement also got affected, with a considerable change in the final setting time. These effects could be understood as the consequence of the reduction in supersaturation during the calcium sulfate precipitation in the cement paste. The formation of aggregates of small crystals, however, leads to higher compressive strength. The initial and final setting times of the BioCaS are 12.5 and 16.5 min respectively and the compressive strength of the set cement is 12 MPa.

The present study carried out as per ISO 10993 and following international guidelines, demonstrates its safety as well as efficacy in healing bone defects. Set BioCaS cement consisted of phosphate incorporating low-dimensional gypsum crystal lattices, the bioactivity of which has been identified by immersion in simulated body fluid. BioCaS was proved to be non-cytotoxic and non-haemolytic in the screening tests. In the live/dead assay, human osteoblast-like human osteosarcoma cells adhered well and spread on the surface of the material, attaining typical morphology and affirming the bone cell compatibility of the material. The cement has undergone essential biocompatibility tests prescribed for a bone filler, i.e. tests for acute systemic toxicity, intracutaneous reactivity, maximization sensitization and pyrogenicity. The material satisfied all the criteria for passing these tests, indicating that it is toxicologically safe for use *in vivo*. The *in vivo* implantation test was done by filling the material in defects created in rabbit femora as per standard guidelines and analysing these histologically. Hydroxyapatite porous ceramic was used as the control, with observation periods of 12, 26 and 52 weeks. The apposition of BioCaS with host bone at initial periods without any fibrous tissue formation suggested its osteoconductive property, which is comparable with that of hydroxyapatite, the bone mineral. The defects repaired with cement showed almost complete remodeling in a span of 52 weeks with less than 10% material remnants. BioCaS was found to undergo active resorption at a pace matching that of new bone formation, i.e. osteoconductivity. This will help the defect to heal without any discontinuity or weak boundaries and to gain strength faster. Considering its physico-chemical and biological properties, it can be concluded that BioCaS is on a par with other bioactive self-setting cements, particularly CPC.

The drugs GS and VH were integrated in the BioCaS system and analysed the in vitro elution profiles varying the parameters concentration of the drug loaded and the surface area to volume ratio of the cement monolith. The diffusion mechanism for the VH drug release varied from quasi-fickian to non-fickian via fickian from low to high drug dose in the cement monolith. Hence BioCaSV3 followed both diffusion and relaxation controlled diffusion mechanism. The S/V ratio changing always propagated with quasi-fickian diffusion mechanism and not in direct proportion with release rate. The diffusion mechanism for the GS drug release chased the Higuchi model and the percentage cumulative release was effective with the increase in the S/V ratio. With the increase in the initial loading percentage, the efficiency of the release was in reverse trend may be due to the chemical interaction of the drug moiety with the cement matrix or the degradation rate change. The effectiveness of the selected compositions of BioCaSG3 and BioCaSV3 based parameters with in the clinically accepted range shown potential results against E.Coli 25922 and S.aureus 25923 respectively within the 20 days study time period.

The injectable cement compositions were analysed for modification with the synthesised gelling agent N,O-carboxymethyl chitosan. The concentrations of the gelling agents as wetting medium were selected without hampering the final setting time. The improved injectability than BioCaS without compromising the setting time and mechanical property couldn't be successfully achieved; which was found to be combined effect of interaction of DHPD and NOCMC. However the compressive strengths were improved by ≈ 4 MPa in CS251 and CS253 than BioCaS which is due to its Ca cross linking via chelation. The invitro degradation percentages were considerably reduced in CS251 and CS253 compared to BioCaS. However the

bioactivity was not hampered even though HA layer coating was found out to be formed after 7 days of immersion in SBF. In vitro screening test for biocompatibility proved it as an effective osteoconductive scaffold for the bone cell migration and growth.

6.2 Conclusion

The conclusions derived from the present study are as follows :

1. Developed a low cost viable method for the production of high purity gypsum for medical orthopaedic application based on a new 'drowning out' wet chemical method.
2. The new chemical system used for the synthesis of gypsum was analysed theoretically, deducing nucleation kinetics parameters. It was identified that a medium with lower surface free energy will lead to reduction in particle size. Also the theoretical knowledge of nucleation kinetics parameters was extended for the synthesis of nano gypsum.
3. The basic formulation of an aqueous-based self setting cement was designed using the uniform submicron-sized medical grade gypsum after phase conversion to hemihydrate form 'Bassanite'. This was modified with phosphate ions, which imparts injectability and bioactivity to the formulation, as proven in the latter parts of the study.
4. The new cement formulation is found to be fully injectable during the working time of the cement mix, where as the conventional self-setting cements show phase separation before full extrusion. The flow/viscous properties of the cement were studied and optimized using capillary rheometry technique.

5. It was possible to optimize the cement properties to clinically acceptable parameters- setting times (initial setting time = 12.5 min and final setting time = 16.5 min), compressive strength (optimum value of 12 ± 0.15 MPa) and compressive modulus (1094.13 ± 54.98 MPa). The particle size of the set cement was in a narrow range of 2.1- 5.9 μm (with a mean value of 3.65 μm). This optimized cement formulation (consisting phosphate integrated gypsum crystal lattices) was named as 'BioCaS'.
6. BioCaS was proved to be bioactive, non-cytotoxic and non-haemolytic in the screening tests. Human osteoblast-like HOS cells adhered well and spread on the surface of the material, attaining typical morphology and affirming the bone cell compatibility of the material.
7. In the *in vivo* biocompatibility evaluation there were no acute systemic effects and the material proved non-pyrogenic. There was no intracutaneous erythemic or oedematous reactivity and no hypersensitivity observed in the *Magnusson-Kligman* method.
8. Bone implantation study revealed BioCaS to be osteoconductive and its efficacy of healing the experimental bone defects in rabbit femora is on a par with that of hydroxyapatite ceramic.
9. The additional advantage of 'BioCaS' over conventional hydroxyapatite ceramic is the 'osteotransductivity' in which material resorption is at the same rate of new bone formation at the defect site. This will help the defect to heal and gain strength faster.
10. As the 'BioCaS' system sets in water medium without pH change or any vigorous thermal release, it is identified to be a good drug carrier to deliver drugs for bone

diseases. Water dissolving antibiotics like Gentamicin and Vancomycin, which are capable of controlling bone infection (*Osteomyelitis*) were successfully incorporated in BioCaS. High dose drug could be loaded in the cement matrix with out loss of biofunctionality.

11. The *in vitro* elution profiles of Gentamicin and Vancomycin indicated that the drug elution characteristics follow theoretical model representing elution from a porous body. The *in vitro* elution of the drugs incorporated into the cement lasted for more than 14 days, satisfying the essential clinical requirement for *Osteomyelitis* management.
12. Microbiological studies on the potential inhibition of bacterial growth using E.coli and of S.aureus were conducted. Gentamicin sulfate loaded BioCaS cement (8g/40g) showed potential inhibition of E.coli up to 15 days and of S.aureus up to the 20 days study period. Vancomycin hydrochloride loaded BioCaS cement (8g/40g) was effective against S.aureus up to 20 days and it even shows considerable inhibition of E. coli up to 5 days.
13. In order to achieve higher compressive strength, the injectable bone cement formulations was further modified with the gelling agent N,O-carboxymethyl chitosan (NOCMC). It was optimized on the basis of the injectability and cementing parameters. There was improvement in compressive strength, but not in the injectability compared to BioCaS.
14. The *in vitro* degradation percentage of the cements with gelling agent was significantly lower than BioCaS which is due to the chelating effect of NOCMC.

15. Bioactivity was not hampered by the cross-linking of Ca^{2+} in bone cements to NOCMC but the formation of thick HA layer coating appeared only after 7 days in SBF while BioCaS showed this effect after 4 days.
16. The bone cements modified with gelling agents passed the in vitro screening test for biocompatibility and showed good adhesion of human osteoblast like HOS cell indicating the osteoconductive nature.
17. As an overall conclusion, the bioactive injectable bone filler cement 'BioCaS' is a viable and affordable product for commercial use. BioCaS finds attractive applications in the minimally invasive bone defect management and in local delivery of drugs for bone diseases.

BIBLIOGRAPHY

- Aimetti M, Romano F, Griga FB, Godio L (2009) Clinical and histologic healing of human extraction sockets filled with calcium sulfate *Int J Oral Maxillofac Implants*. 24(5): 902-909.
- Alge1 DL, Cruz GS, Goebel WS, Chu TG (2009) Characterization of dicalcium phosphate dihydrate cements prepared using a novel hydroxyapatite-based formulation. *Biomed Mater* 4(2): 025016. doi: 10.1088/1748-6041/4/2/025016. Epub 2009 Apr 6
- Alimi F and Gadri A(2004) Kinetics and morphology of formed gypsum *Desalination* 166: 427–434.
- Alkhraisat MH, Marino FT, Rodriguez CR, Jerez LB, Cabarcos EL (2008) Combined effect of strontium and pyrophosphate on the properties of brushite cements. *Acta Biomater*. 4(3): 664-70.
- An J, Wolke J, Jansen JA, Leeuwenburgh S (2016) Influence of polymeric additives on the cohesion and mechanical properties of calcium phosphate cements *J Mater Sci: Mater Med* 27:58.
- Anitha A, Divya Rani VV , Krishna R , Sreeja V , Selvamurugan N, Nair SV, Tamura H, Jayakumar R (2009) Synthesis, characterization, cytotoxicity and antibacterial studies of chitosan, O-carboxymethyl and N,O-carboxymethyl chitosan nanoparticles *Carbohydr Polym* 78: 672–677.
- Anusavice KJ (2004) *Phillips' science of dental materials* Saunders elsevier, Missouri 25.
- Asadi-Eydivand M, Solati-Hashjin M, Shafiei SS, Mohammadi S, Hafezi M (2016) Structure, properties and In vitro behavior of heat-treated calcium sulfate scaffolds fabricated by 3D printing *PLoS One* 11(3): e0151216.
- Asiri AM, Arshad MN, Marwani HM (2014) Nanohybrid based on antibiotic encapsulated layered double hydroxide as a drug delivery system *Appl Biochem Biotechnol* 175(3): 1412-28.
- ASTM F451-16 (2016) Standard specification for acrylic bone cement (West Conshohocken: ASTM International) <http://dx.doi.org/10.1520/F0451-08>.
- Babo PS, Santo VE, Gomes ME, Reis RL (2016) Development of an injectable calcium phosphate/hyaluronic acid microparticles system for platelet lysate sustained delivery aiming bone regeneration *Macromol Biosci* 16: 1662-1667.
- Bansal R, Patil S, Chaubey KK, Thakur RK, Goyel P (2014) Clinical evaluation of hydroxyapatite and β -tricalcium phosphate composite graft in the treatment of intrabony periodontal defect: a clinico-radiographic study. *J Indian Soc Periodontol*. 18(5): 610-617.
- Barinov SM and Komlev VS (2011) Calcium phosphate bone cements. *J Inorg Mater*. 47(13), pp. 1470–1485.
- Baroli B (2009) From natural bone grafts to tissue engineering therapeutics: brainstorming on pharmaceutical formulative requirements and challenges. *J Pharm Sci*, 98(4): 1317-1325.
- Bayari SH (2012) Applications of vibrational spectroscopy in diagnosis and screening of dental tissues. In: Severcan F, Harris PI (eds) *Vibrational spectroscopy in diagnosis and screening*, Amsterdam, IOS; pp.304
- Bercier A, Gonçalves S, Lignon O and Fitremann J (2010) Calcium phosphate bone cements including sugar surfactants: part one-porosity, setting times and compressive strength *Materials* 3: 4695-4709.
- Beuerlein MJS and McKee MD (2010) Calcium sulfates: what is the evidence? *J Orthop Trauma* 24: S46–51.

- Bishop JL, Lane MD, Dyar MD, King SJ, Brown AJ, Swayze GA (2014) Spectral properties of Ca-sulfates: gypsum, bassanite, and anhydrite *Am mineral*, 10.2138/am-2014-4756.
- Bishop JL, Lane MD, Dyar MD, King SJ, Brown AJ, Swayze GA (2014) What lurks in the martian rocks and soil? investigations of sulfates, phosphates and perchlorates spectral properties of Ca-sulfates: gypsum, bassanite, and anhydrite *Am Mineral* 99: 2105–2115.
- Bohner M (2000) Calcium orthophosphates in medicine: from ceramics to calcium phosphate cements *Injury: Int J Care Injured* 31: S-D37-47.
- Bohner M (2010) Design of ceramic-based cements and putties for bone graft Substitution *Eur Cells Mater* 20: 1-12.
- Bohner M, Baroud G (2005) Injectability of calcium phosphate pastes. *Biomaterials* 26: 1553–1563.
- Bohner M, Landuyt VP, Merkle HP, Lemaitre J (1997) Composition effects on the pH of a hydraulic calcium phosphate cement. *J Mater Sci Mater Med* 8(11): 675-681.
- Boyan BD, Baker MI, Lee CSD, Raines AL, Greenwald AS, Olivares-Navarette R and Schwartz Z (2011) Bone tissue grafting and tissue engineering concepts in: Ducheyne P, Healy KE, Hutmacher DW, Grainger DW, Kirkpatrick CJ (eds) *Comprehensive biomaterials: biomaterials and clinical use*. Elsevier, Amsterdam. pp 237-255.
- Brandel C and Horst J (2015) Measuring induction times and crystal nucleation rates *Faraday Discuss* 179: 199-214.
- Brown CD, Hoffman AS (2006) Modification of natural polymers: chitosan in methods of tissue engineering. in: Atala A, Lanza RP (eds) *Methods of Tissue Engineering*, Elsevier, USA, pp. 565-572 ISBN: 978-81-312-0128-2.
- Brown WE and Chow L C (1987) A new calcium phosphate water setting cement in cements research progress. In: Brown WE (ed), *Ohio: American Ceramics Society*, pp. 352–379
- Bruce RB, Cox DW (2008) Alpha-type calcium sulfate hemihydrate compositions and methods of making same, US 7335254 B2 patent.
- Burguera EF, Xu HH and Weir MD (2006) Injectable and rapid setting calcium phosphate bone cement with dicalcium phosphate dihydrate. *J Biomed Mater Res B* 77(1): 126–134.
- Burguera EF, Xu HHK, Sun L (2008) Injectable calcium phosphate cement: effects of powder-to-liquid ratio and needle size *J Biomed Mater Res B* 84: 493–502.
- Campana V, Milano G, Pagano E, Barba M, Cicione C, Salonna G, Lattanzi W, Logroscino G (2014) Bone substitutes in orthopaedic surgery: from basic science to clinical practice *J Mater Sci Mater Med* 25(10): 2445–2461.
- Carey LE, Xu HHK, Simon CG, Takagi S, Chow LC (2005) Premixed rapid-setting calcium phosphate composites for bone repair *Biomaterials* 26: 5002–5014.
- Chang Y, Chen WC, Hsieh PH, Chen DW, Lee MS, Shih H, Ueng SWN (2011) In vitro activities of daptomycin, vancomycin and teicoplanin loaded polymethyl methacrylate against methicillin susceptible, methicillin resistant and vancomycin-intermediate strains of staphylococcus aureus *Antimicrob agents chemother* 55(12): 5480-5484.
- Chen SC, Wu YC, Mi FL, Lin YH, Yu LC, Sung HW (2004) *J Control Release* 96: 285–300.
- Chen Y, Wu Q, Ding Y (2007) Stepwise assembly of nanoparticles, tubes, rods, and wires in reverse micelle systems *Eur J Inorg Chem* 31: 4906–4910.
- Chernousova S and Epple M (2014) Bioactive Bone Substitution Materials. *Advanced Biomaterials and Devices in Medicine* 1: 74-87.

- Chow LC (2009) Next generation calcium phosphate-based biomaterials *Dent Mater J* 28(1): 1–10.
- Chow LC, Takagi S (2001) A natural bone cement ? a laboratory novelty led to the development of revolutionary new biomaterials. *J Res Natl Inst Stand Technol* 106: 1029–1033.
- Class II special controls guidance document: Resorbable calcium salt bone void filler device; guidance for industry and FDA (Silver Spring, MD: US Department of Health and Human Services, Food and Drug Administration, Center for Devices and Radiological Health) <http://www.fda.gov/MedicalDevices/ucm072704.htm>.
- Clayer M (2008) Injectable form of calcium sulphate as treatment of aneurysmal bone cysts. *ANZ j Surg* 78: 366–370.
- Constantz BR, Ison IC, Fulmer MT, Poser RD, Smith ST, Wagoner MV, Ross J, Goldstein SA, Jupiter JB, Rosenthal DI (1995) Skeletal repair by in situ formation of the mineral phase of bone *Science* 267: 1796-1799.
- Cooper JJ (2004), Method of producing surgical grade calcium sulphate, US6780391 B1 patent.
- Dadkhah M, Pontiroli L, Fiorilli S, Manca A, Tallia F, Tcacencue I and Vitale-Brovarone C (2017) Preparation and characterisation of an innovative injectable calcium sulphate based bone cement for vertebroplasty application *J Mater Chem B* 5: 102-115.
- Datta S and Grant DJW (2005) Effect of supersaturation on the crystallization of phenylbutazone polymorphs *Cryst Res Technol* 40: 233-242.
- DeAza PN (2007) Bioactive glasses and glass-ceramics. *Bol Soc Esp Ceram V.* 46(2):45-55.
- DeKorte ACJ, Brouwers HJH (2008) Hydration modeling of calcium sulphates *ICCBT 2008 A* 39: 433–444.
- Desai TR, Bhaduri SB, Tas AC (2007) A Self-setting, monetite (CaHPO₄) cement for skeletal repair in: Mizuno M, Wereszczak A, Lara-Curzio E (eds) *Advances in bioceramics and Biocomposites II, Ceramic Engineering and Science Proceedings*, John Wiley & Sons Inc, Hoboken. doi: 10.1002/9780470291351.ch6.
- DeYoreo JJ and Vekilov PG (2003) Biomineralization. In: Dove PM, DeYoreo JJ, Weiner S (eds) *Reviews in mineralogy and geochemistry*, The Mineralogical Society of America, Washington DC, 2003, pp. 57-94.
- Ding H, Zhao C, Cui X, Gu Y, Jia W, Rahaman MN, Wang Y, Huang W, Zhang C (2014) A novel injectable borate bioactive glass cement as an antibiotic delivery vehicle for treating osteomyelitis *Plos One* 9(1): e85472.
- Ding T, Xue Y, Lu H, Huang Z, Sun J (2012) Effect of particle size of hydroxyapatite nanoparticles on its biocompatibility *IEEE Trans Nanobiosci* 11: 336–40.
- Dixit NM, Kulkarni AM, Zukoski CF (2001) Comparison of experimental estimates and model predictions of protein crystal nucleation rates *Colloid Surf A* 190: 47-60.
- Dorozhkin SV (2010) Calcium orthophosphates as bioceramics: state of the art. *J Funct Biomater* 1: 22-107.
- Dorozhkin SV (2011) Self-setting calcium orthophosphate formulations: cements, concretes, pastes and putties *Int J Mater Chem.* 1:1–48.
- Dorozhkin SV (2013) Review: self-Setting calcium orthophosphate formulations *J Funct Biomater* 4: 209-311.
- Eichert D, Combes C, Drouet C, Rey C (2005) Formation and evolution of hydrated surface layers of apatites *Key Eng Mater* 3: 284–6.
- Engstrand J, Persson C, Engqvist H (2013) Influence of polymer addition on the mechanical properties of a premixed calcium phosphate cement, *Biomater* 2013 3(4): e27249, doi:10.4161/biom.27249.
- Eun HT and Ko YS (2003) Preparation of gypsum using STS sludge and waste sulfuric acid produced in iron & steel industry *J Ind Eng Chem* 9(5): 614-688.

- Farag RK and Mohamed RR (2013) Synthesis and characterization of carboxymethyl chitosan nanogels for swelling studies and antimicrobial activity *Molecules* 18: 190-20 doi:10.3390/molecules18010190.
- Ferguson JY, Dudareva M, Riley ND, Stubbs D, Atkins BL, McNally MA (2014) The use of a biodegradable antibiotic-loaded calcium sulphate carrier containing tobramycin for the treatment of chronic osteomyelitis a series of 195 cases *Bone Joint J* 96(6) :829-36.
- Fernández E, Gil FJ, Best S.M, Ginebra MP, Driessens FCM, Planell, JA (1998) The cement setting reaction in the $\text{CaHPO}_4\text{-}\alpha\text{-Ca}_3(\text{PO}_4)_2$ system: An X-ray diffraction study. *J Biomed Mater Res* 42: 403–406.
- Fischer HB, Nowak S, Hartman M, Riechert C (2012) About the reactivity of calcium sulfate binders *UPB Sci Bull.* 74(B):1–22.
- Flautre B, Maynou C, Lematre J, Landuyt VP, Hardouin P (2002) Bone colonization of β -TCP granules incorporated in brushite cements *J Biomed Mater Res Appl Biomater* 63: 413–417.
- Gantenbein-Ritter B, Sprecher CM, Chan S, Illien-Junger S, Grad S (2011) Confocal imaging protocols for live/dead staining in three-dimensional carriers *Methods Mol Biol* 740: 127–140.
- Gbureck U, Barralet JE, Spatz K, Grover LM, Thull R (2004) Ionic modification of calcium phosphate cement viscosity. Part I: Hypodermic injection and strength improvement of apatite cement *Biomaterials* 25: 2187–2195.
- Ghaly M, Kerns DG, Hallmon WW, Solomon ES, Nagy WW, Al-Hashimi I, Rossmann JA (2013) Comparison of guided bone regeneration using a bovine collagen membrane vs a calcium sulfate barrier *J Contemp Dent* 3(3):138-143.
- Gierszewska-Druzynska M, Ostrowska-Czubenko J (2012) Mechanism of water diffusion into non-crosslinked and ionically crosslinked chitosan membranes *Prog Che Appl Chitin and Deriv* 17: 59-66.
- Graham S, Leonidou A, Aslam-Pervez N, Hamza A, Panteliadis P, Heliotis M, Mantalaris A, Tsiroidis E (2010) Biological therapy of bone defects: the immunology of bone allo-transplantation. *Expert Opin Biol Ther.* 10: 885.
- Grover LM, Hofmann MP, Gbureck U, Kumarasami B, Barralet JE (2008) Frozen delivery of brushite calcium phosphate cements. *Acta Biomater* 4(6): 1916-1923.
- Guan B, Yang L, Wu Z (2010) Effect of Mg^{2+} ions on the nucleation kinetics of calcium sulfate in concentrated calcium chloride solutions *Ind Eng Chem Res* 49 (12): 5569-5574.
- Guarnieri R, Grassi R, Ripari M, Pecora G (2006) Maxillary sinus augmentation using granular calcium sulfate (surgiplaster sinus): radiographic and histologic study at 2 years *Int J Periodontics Restorative Dent* 26: 79-85.
- Guarnieri R, Bovi M (2002) Maxillary sinus augmentation using prehardened calcium sulfate: a case report *Int J Periodontics Restorative Dent* 22(5): 503-507.
- Gupta K, Singh S, Rao MSR (2016) Direct and facile room-temperature synthesis of nanocrystalline calcium sulfate dihydrate (Gypsum) *Cryst Growth Des* 16: 3256–3261.
- Harris RJ (2004) Clinical evaluation of a composite bone graft with a calcium sulfate barrier *J Periodont* 75 (5): 685-92.
- Harrison, R (2016) Mechanical properties of α -tricalcium phosphate-based bone cements incorporating regenerative biomaterials for filling bone defects exposed to low mechanical loads *J Biomed Mater Res - Part B: Appl Biomater* 104(1): 149-157
- Hawthorne FC, Krivovichev SV, Burns PC 2000 The crystal chemistry of sulfate minerals, *Rev Mineral Geochem* 40(1): 1-112.

- Hill RG (2011) Bioactive glass ceramics in: Ducheyne P, Healy KE, Hutmacher DW, Grainer DW, Kirkpatrick CJ, *Comprehensive biomaterials-metallic, ceramic and comprehensive biomaterial*, Elsevier, Amsterdam. pp. 181-186.
- Horowitz RA, Rohrer MD, Tovar H and Mazor Z (2012) Enhancing extraction socket therapy with a biphasic calcium sulfate *Compendium* 33 (6): 1-7.
- Horsch M, Vrabec J and Hasse H (2008) Modification of the classical nucleation theory based on molecular simulation data for surface tension, critical nucleus size, and nucleation rate *Phys Rev E* 78: 011603.
- Howlin RP, Brayford MJ, Webb JS, Cooper JJ, Aiken SS, Stoodley P (2015) Antibiotic-loaded synthetic calcium sulfate beads for prevention of bacterial colonization and biofilm formation in periprosthetic infections *Antimicrob Agents Chemother* 59(1): 111-120.
- Hughes E, Gianni T, Jamshidi P and Grover LM (2015) Inorganic cements for biomedical application: calcium phosphate, calcium sulfate and calcium silicate. *Adv Appl Ceram* 114: 65-76.
- Humm G, Noor S, Bridgeman P, David M, Bose D (2014) Adjuvant treatment of chronic osteomyelitis of the tibia following exogenous trauma using OSTEOSET-T: a review of 21 patients in a regional trauma centre *Strat Traum Limb Recon* 9:157–161.
- Ikpeme IA, Ngim NE, Ikpeme AA (2010) Diagnosis and treatment of pyogenic bone infections *Afr Health Sci* 10 (1):82-88).
- International Standard ISO 10993-1 (2009) Biological evaluation of medical devices: Evaluation and Testing Within a Risk Management Process (Geneva: International Organization for Standardization).
- International Standard ISO 10993-10 (2010) Biological evaluation of medical devices: X. tests for irritation and skin sensitization (Geneva: International Organization for Standardization).
- International Standard ISO 10993-11 Annex F document (2006) Information on material mediated pyrogen (Geneva: International Organization for Standardization).
- International Standard ISO 10993-4 document (2002) Biological evaluation of medical devices: IV. selection of tests for interaction with blood (Geneva: International Organization for Standardization).
- International Standard ISO 10993-6 (2007) Biological evaluation of medical devices: VI. Tests for local effects after implantation (Geneva: International Organization for Standardization).
- International Standard ISO Standard 23317:2014 (E) Implants for surgery - In vitro evaluation for apatite-forming ability of implant materials, pp: 1-12 (*International Organisation for Standardisation*).
- Ishikawa K (2014) Calcium phosphate cements in: Nissam BB (ed) *Advances in calcium Phosphate biomaterials, Springer series in Biomaterials Science and Engineering* 2, Springer Verlag, Berlin.
- Ishikawa K, Takagi S, Chow LC, Ishikawa Y (1995) Properties and mechanisms of fast-setting calcium phosphate cements, *J Mater Sci Mater Med* 6(9): 528–533.
- Jia W, Luo S, Zhang C, Wang J (2010) *In vitro* and *In vivo* efficacies of teicoplanin-loaded calcium sulfate for treatment of chronic methicillin-resistant staphylococcus aureus osteomyelitis *Antimicrob Agents Chemother* 54(1): 170–176.
- Kai D, Li D, Zhu X, Zhang L, Fan H, Zhang X (2009) Addition of sodium hyaluronate and the effect on performance of the injectable calcium phosphate cement, *J Mater Sci Mater Med* 20: 1595-602.
- Kapanen A, Knen JR, Danilov A, Tuukkanen J (2001) Effect of nickel titanium shape memory metal alloy on bone formation. *Biomaterials* 22: 2475- 2480.

- Kasuya A, Sobajima S, Kinoshita M (2012) In vivo degradation and new bone formation of calcium phosphate cement–gelatin powder composite related to macroporosity after in situ gelatin degradation *J orthop res* 30(7): 1103-1111.
- Katz JL (1992) Homogeneous nucleation theory and experiment: a survey *Pure & Appl Chem* 64(11): 1661-66.
- Kelly CM, Wilkins RM (2004) Treatment of benign bone lesions with an injectable calcium sulfate-based bone graft substitute. *Orthopedics*. 27:s131-5.
- Khan SB, Alamry KA, Alyahyawi NA, Asiri AM, Arshad MN, Marwani HM (2015) Nanohybrid Based on Antibiotic Encapsulated Layered Double Hydroxide as a Drug Delivery System, *Appl Biochem Biotechnol* 175(3): 1412-1428. DOI 10.1007/s12010-014-1211-9.
- Khashaba RM, Moussa MM, Mettenburg DJ (2010) Polymeric-calcium phosphates cement composites-material properties: in vitro and in vivo investigations *Int J Biomater* (8): 2863–73.
- Kheirallah M, Almeshaly H (2016) Bone graft substitutes for bone defect regeneration a collective review, *Int J Dentistry Oral Sci*. 3(5): 247-257.
- Kim CK, Kim HY, Chai JK, Cho KS, Moon IS, Choi SH, Sottosanti JS, Wikesjo UM, (1998) Effect of a calcium sulfate implant with calcium sulfate barrier on periodontal healing in 3-wall intrabony defects in dogs *J Periodontol* 69(9):982-8.
- Kim H, Knowles JC, Kim H (2005) Hydroxyapatite porous scaffold engineered with biological polymer hybrid coating for antibiotic Vancomycin release *J Mater sci: Mater Med* 16: 189– 195.
- Kokubo T (2006) How useful is SBF in predicting in vivo bone bioactivity *Biomaterials* 27: 2907–2915.
- Kokubo T (2008) *Bioceramics and their clinical applications*. Wood head publishing limited, USA.
- Komath M and Varma H K (2004) Fully injectable calcium phosphate cement-a promise to dentistry *Indian J Dent Res* 1: 89–95.
- Komath M and Varma H K (2005) Fully injectable calcium phosphate cement-a promise to dentistry. *Indian J Dent Res* 1: 89–95.
- Komlev VS, Fadeeva IV, Barinov SM, Rau JV, Fosca M, Gurin AN, Gurin NA (2012) Phase development during setting and hardening of a bone cement based on a tricalcium and octacalcium phosphates *J Biomater Appl*, 26: 1051-1067.
- Kulkarni SA, Kadam SS, Meekes H, Stankiewicz AI, Horst JH (2013) Crystal nucleation kinetics from induction times and metastable zone widths *Cryst Growth Des* 13: 2435–2440.
- Laino L, Troiano G, Giannatempo G, Graziani U, Ciavarella D, Dioguardi M, Lo Muzio L, Lauritano F and M. Ciccio (2015) Sinus lift augmentation by using calcium sulphate. A retrospective 12 months radiographic evaluation over 25 treated Italian patients *Open Dent J* 9:414-419.
- Lane MD (2007) Mid-infrared emission spectroscopy of sulfate and sulfate-bearing minerals *Am Mineral* 92: 1-18.
- Larsson S (2011) Injectable bone-graft substitutes: current products, their characteristics and indications and new developments. *Int J Care Injured* 42: S30–S34.
- Lee GH, Khoury JG, Bell J, Buckwalter JA (2002) Adverse reactions to osteoset bone graft substitute *The Iowa Orthop J* 22: 35-38.
- Lewis G (2011) Viscoelastic properties of injectable bone cements for orthopaedic applications: state-of-the-art review. *J Biomed Mater Res B: App Biomater* 98: 171-191.
- Li YW (2000) A novel injectable bioactive bone cement for spinal surgery: a developmental and preclinical study, *J Biomed Mater Res* 52: 164-170.

- Lian X, Liu H, Wang X, Xu S, Cui F, Bai X (2013) Antibacterial and biocompatible properties of vancomycin-loaded nano-hydroxyapatite/collagen/poly (lactic acid) bone substitute. *Prog Nat sci Mater* 23:549-556.
- Lin M, Zhang L, Wang J, Chen X, Yang X, Cui W, Zhang W, Yang G, Liu M, Zhao Y, Gao C, Gou Z (2014) Novel highly bioactive and biodegradable gypsum/calcium silicate composite bone cements: from physicochemical characteristics to in vivo aspects. *J Mater Chem B* 2: 2030-2038.
- Ling Y and Demopoulos GP (2005) Preparation of α -calcium sulfate hemihydrate by reaction of sulfuric acid with lime *Ind Eng Chem Res* 44: 715-724.
- Liu HY, Liu X, Zhang LP, Ai HJ, Cui FZ (2010) Improvement on the performance of bone regeneration of calcium sulfate hemihydrate by adding mineralized collagen *Tissue Eng Part A* 16(6): 2075–2084.
- Liu W, Zhang J, Weiss P, Tancret F, Bouler J (2013) The influence of different cellulose ethers on both the handling and mechanical properties of calcium phosphate cements for bone substitution *Acta Biomater* 9: 5740–5750.
- Liu WC, Wong CT, Fong MK, Cheung WS, Kao RYT, Luk KDK, Lu WW (2010) Gentamicin loaded strontium containing hydroxyapatite bioactive bone cement-an efficient antibiotic drug delivery system *J of Biomed Mater Res B: Appl biomater* 95(2):397-405.
- Liu Y, Wang A, Freeman JJ (2009) ‘Raman, MIR and NIR spectroscopic study of calcium Sulfates: gypsum, bassanite, and anhydrite’ *Proceedings of the 40 th Lunar and Planetary Science Conference*, Houston.
- Liu Z, Jiao Y, Zhang Z (2007) Calcium-carboxymethyl chitosan hydrogel beads for protein drug delivery *J Appl Polym Sci* 103: 3164–3168.
- Lokhandwala H, Deshpande A, Deshpande S (2013) Kinetic modeling and dissolution profiles comparison: an overview *Int J Pharm Bio Sci* 4(1): 728-737.
- Maeyer EAP, Verbeeck RMH, Verduyck CWJ (2000) Conversion of octacalcium phosphate in calcium phosphate cements, *J Biomed Mater Res* 52(1): 95-106.
- Mahamid J, Sharir A, Addadi L, Weiner S (2008) Amorphous calcium phosphate is a major component of the forming fin bones of zebrafish: indications for an amorphous precursor phase *PNAS* 105(35): 12748-53.
- Mahmoud MHH, Rashad MM, Ibrahim IA, Abdel-Aal EA (2004) Crystal modification of calcium sulfate dihydrate in the presence of some surface-active agents *J colloid interface sci* 270: 99-105.
- Majekodunmi AO, Deb S, Nicholson JW (2003) Effect of molecular weight and concentration of poly(acrylic acid) on the formation of a polymeric calcium phosphate cement. *J Mater Sci Mater Med* 14: 747.
- McConoughey S, Howlin RP, Wiseman J, Stoodley P, Calhoun JH (2015) Comparing PMMA and calcium sulfate as carriers for the local delivery of antibiotics to infected surgical sites *J Biomed Mater Res B: Appl Biomater* 103(4): 870-877.
- McManamon, Silva JP, Delaney P, Morris MA, Cross GLW (2016) Characteristics, interactions and coating adherence of heterogeneous polymer/drug coatings for biomedical devices *Mater Sci Eng C* 59: 102–108.
- Menon KV and Varma HK (2005) Radiological outcome of tibial plateau fractures treated with percutaneously introduced synthetic porous hydroxyapatite granules *Eur J Orthop Surg Trauma* 15: 205–13.
- Mirtchi AA, Lemaitre J, Munting E (1989) Calcium phosphate cements: action of setting regulators on the properties of the beta-tricalcium phosphate-monocalcium phosphate cements *Biomaterials*. 10(9): 634-8.
- Mirzayan R, Panossian V, Avedian R, Forester DM, Menendez L R (2001) The use of calcium sulfate in the treatment of benign bone lesions. *J Bone Joint Surg Am* 83: 355–8.

- Mohan BG, Sureshababu S, Varma HK, John A (2013) In vitro evaluation of bioactive strontium-based ceramic with rabbit adipose-derived stem cells for bone tissue regeneration *J Mater Sci Mater Med* 24: 2831–44.
- Molina-Bolovar JA, Galisteo-Gonzalez F (2004) Latex immune agglutination assays. in: Elaissari A (ed) *Colloidal biomolecules, biomaterials and biomedical applications* Marcel Dekker, New York, pp. 53.
- Monma H, Kanazawa T (1976) “The hydration of α -tricalcium phosphate, *J Ceram Assoc Jap* 84: 209–213.
- Monma H, Makishima A, Mitomo M and Ikegami T (1988) Hydraulic properties of the tricalcium phosphate –dicalcium phosphate mixture, *J Ceram Soc Jap* 96(8): 878–80.
- Montazerian M and Zanotto ED (2016) History and trends of bioactive glass-ceramics. *J Biomed Mater Res Part A* 104A: 1231–1249.
- Montufar EB, Traykova T, Schacht E, Ambrosio L, Santin M, Planell JA, Ginebra M (2010) Self-hardening calcium deficient hydroxyapatite/gelatine foams *J Mater Sci: Mater Med* 21:863–869.
- Moroni D, Wolde PR, Bolhuis PG (2005) Interplay between structure and size in a critical crystal nucleus *Phys Rev Lett* 94: 235703.
- Morsy SMI (2014) Role of surfactants in nanotechnology and applications *Int J curr microbial appl sci* 3(5): 237-260.
- Mourya VK, Inamdara NN, Tiwari A (2010) Carboxymethyl chitosan and its applications *Adv Mat Lett* 1(1): 11-33.
- Mullin JW (2001) *Crystallisation*, Butterworth- Heinemann, London. ISBN:0750648333.
- Murray CB, Kagan CR, Bawendi MG (2000) Synthesis and characterization of monodisperse nanocrystals and close-packed nanocrystal assemblies *Ann Rev Mater Sci*, 30: 545-610, DOI: 10.1146/annurev.matsci.30.1.545.
- Nelson CL, McLaren SG, Skinner RA, Smeltzer MS, Thomas JR, Olsen KM (2002) The treatment of experimental osteomyelitis by surgical debridement and the implantation of calcium sulfate tobramycin pellets *J Orthop Res* 20: 643-647.
- Neut D, Kluin OS, Thompson J, Mei H, Busscher HJ Gentamicin release from commercially-available gentamicin-loaded PMMA bone cements in a prosthesis-related interfacial gap model and their antibacterial efficacy *BMC Musculoskelet Disord* 10: (11): 258.
- Newman ES, Wells LS (1938) Heats of hydration and transition of calcium sulfate. *J Res Nat Bur Stand* 20: 825-36.
- Nich C, Hamadouche M (2011) Synthetic bone Grafts: clinical use in: Ducheyne P (ed) *Comprehensive Biomaterials-metallic, ceramic and comprehensive biomaterial*. Elsevier, Amsterdam. pp-335-346.
- Nien Y and Chen J (2006) Studies of the mechanical and thermal properties of cross-linked poly(methylmethacrylate-acrylic acid-allylmethacrylate)-modified bone cement, *J Appl Polym Sci* 100: 3727–3732.
- Nyan M, Sato D, Oda M, Machida T, Kobayashi H, Nakamura T and Kasugai S (2007) Bone Formation With the Combination of Simvastatin and Calcium Sulfate in Critical-Sized Rat Calvarial Defect *J Pharmacol Sci* 104:384 – 386.
- Omidirad R, Rajabi HF, Farahani BV (2013) Preparation and in vitro drug delivery response of doxorubicin loaded poly(acrylic acid) coated magnetite nanoparticles *J Serb Chem Soc* 78(10): 1609–1616.
- Osterwalde N (2007) Preparation of nano-gypsum from anhydrite nanoparticles: strongly increased vickers hardness and formation of calcium sulfate nano-needles *J Nanopart Res* 9: 275–28.
- Osterwalder N, Loher S, Grass RN, Brunner TJ, Limbach LK, Halim SC, Stark WJ (2007) Preparation of nano-gypsum from anhydrite nanoparticles: strongly increased

- vickers hardness and formation of calcium sulfate nano-needles *J Nanopart Res* 9: 275–281, DOI 10.1007/s11051-006-9149-7.
- Oudadesse H, Bui X, Gal Y, Mostafa A, Cathelineau G (2011) Chitosan effects on bioactive glass for application as biocomposite biomaterial *Int J Biology Biomed Eng* 2(5): 49-56.
- Park Y, Mohan K, Al-Sanousi A, Almaghrabi B, Genco R, Swihart M, Dziak R (2011) Synthesis and characterization of nanocrystalline calcium sulfate for use in osseous regeneration *Biomed Mater* 6: 055007.
- Paz A, Guadarrama D, Lopez M, Gonzalez JE, Brizuela N, Aragon J (2012) A comparative study of hydroxyapatite nanoparticles synthesised by different routes *Quim Nova* 35(9): 1724-1727
- Perez RA, Kim HW, Ginebra M (2012) Polymeric additives to enhance the functional properties of calcium phosphate cements. *J Tissue Eng* 3(1): 1-20.
- Perut F, Montufar EB, Ciapetti G, Santin M, Salvage J, Traykova T, Planell JA, Ginebra MP, Baldini N (2011) Novel soybean/gelatine-based bioactive and injectable hydroxyapatite foam: material properties and cell response *Acta Biomater.* 7:1780–1787.
- Peters CL, Hines JL, Bachus KN, Craig MA, Bloebaum RD (2006) Biological effects of calcium sulfate as a bone graft substitute in ovine metaphyseal defects *J Biomed Mater Res A.* 76(3): 456-62.
- Pinto AJ, Carneiro J, Katsikopoulos D, Jimenez A, Prieto M (2012) The link between brushite and gypsum: miscibility, dehydration, and crystallo chemical behaviour in the $\text{CaHPO}_4 \cdot 2\text{H}_2\text{O} - \text{CaSO}_4 \cdot 2\text{H}_2\text{O}$ System, *Cryst Growth Des* 12: 445–455.
- Pishbin F, Mourinno V, Flor S, Kreppel S, Salih V, Ryan MP, Boccaccini AR (2014) Electrophoretic deposition of gentamicin-loaded bioactive glass/ chitosan composite coatings for orthopaedic implants *Appl Mater Interfaces* 6: 8796–8806.
- Prisciandaro M, Lancia A, Musmarra D (2003) The retarding effect of citric acid on calcium sulfate nucleation kinetics *Ind Eng Chem Res* 42: 6647-6652.
- Prisciandaro M, Olivieri E, Lancia A, Musmarra D (2006) Gypsum precipitation from an Aqueous Solution in the Presence of Nitrotrimethylenephosphonic Acid, *Industrial & engineering chemistry research* 45 (6): 2070-2076.
- Prisciandaro M, Lancia A, Musmarra D, Celso G (2014) Gypsum scale inhibition on process equipment surfaces: a review *Chem Eng Transactions* 39: 775-780.
- Purvi PSD (2008) Compressive properties of commercially available polyurethane foams as mechanical models for osteoporotic human cancellous bone *BMC Musculoskelet Disord*, 9: 137–44.
- Qi X, Li H, Qiao B, Weichao Li, Xinyan Hao, Jun Wu, Bao Su, Dianming Jiang (2013) Development and characterization of an injectable cement of nano calcium-deficient hydroxyapatite/ multi(amino acid) copolymer/calcium sulfate hemihydrate for bone repair *Int J Nano Med* 8: 4441-4452.
- Qi X, Pei P, Zhu M, Du X, Xin C, Zhao S, Li X & Zhu Y (2017) Three dimensional printing of calcium sulfate and mesoporous bioactive glass scaffolds for improving bone regeneration in vitro and in vivo *Sci Reports* 7: 1-12.
- Rabizadeh T, Stawski TM, Morgan DJ, Peacock CL, Benning LG (2017) The effects of inorganic additives on the nucleation and growth kinetics of calcium sulfate dihydrate crystals *Cryst Growth Des* 17: 582–589.
- Rahaman MN (2011) Bioactive glass in tissue engineering *Acta Biomater* 7: 2355-3
- Rahman CV, Saeed A, White LJ, Gould TWA, Kirby GTS, Sawkins MJ, Alexander C, Rose FRAJ, Shakesheff KM (2012) Chemistry of polymer and ceramic-based injectable scaffolds and their applications in regenerative medicine. *Chem Mater* 24: 781–795.

- Ramteke KH, Dighe PA, Kharat AR, Patil SV (2014) Tortuosity, mathematical models of drug dissolution: a review *Sch Acad J Pharm* 3(5): 388-396.
- Rapacz-kmita A, Stodolak-zych E, Ziabka M, Rozycka A, Dudek M (2015) Instrumental characterization of the smectite clay–gentamicin hybrids *Bull Mater Sci.* 38(4) pp.1069–1078.
- Rashad MM, Mahmoud MHH, Ibrahim IA, Abdel-Aal EA (2004) Crystallization of calcium sulfate dihydrate under simulated conditions of phosphoric acid production in the presence of aluminum and magnesium ions *J Cryst Growth* 267: 372–379]
- Rees GD, Evans-Gowing R, Hammond SJ, Robinson BH (1999) Formation and morphology of calcium sulfate nanoparticles and nanowires in water-in-oil microemulsions *Langmuir* 15: 1993-2002.
- Reichardt C (2003) *Solvents and solvent effects in organic chemistry* Wiley-VCH Publishers, Weinheim.
- Ribeiro M, Monteiro FJ, Ferraz MP (2012) Infection of orthopedic implants with emphasis on bacterial adhesion process and techniques used in studying bacterial-material interactions *Biomatter* 2(4): 176–194.
- Rietveld IB, Kobayashi K, Yamada H, Matsushigea K (2006) Morphology control of poly(vinylidene fluoride) thin film made with electrospray *J Colloid Interface Sci* 298 (2): 639-651.
- Sabareeswaran A, Basu B, Shenoy SJ, Jaffer Z, Saha N, Stamboulis A (2013) Early osseointegration of a strontium containing glass ceramic in a rabbit model *Biomaterials* 34: 9278–86.
- Salvadori B, Capitani G, Mellini M, Dei L G (2006) A novel method to prepare inorganic water-soluble nanocrystals *J Colloid Interface Sci* 298: 487–90.
- Sanginario V, Ginebra MP, Tanner KE (2006) Biodegradable and semi-biodegradable composite hydrogels as bone substitutes: morphology and mechanical characterization *J Mater Sci Mater Med* 17(5): 447–454.
- Sasidharan S, Bahadur D, Srivastava R (2016) Protein-poly (amino acid) nanocore–shell mediated synthesis of branched gold nanostructures for computed tomographic imaging and photothermal therapy of cancer *ACS Appl Mater Interfaces* 8: 15889–903.
- Sear RP (2006) Heterogeneous and homogeneous nucleation compared: rapid nucleation on microscopic impurities *J Phys Chem B* 110: 4985-4989.
- Shi B, Zhou Y, Wang YN, Cheng XR (2007) Alveolar ridge preservation prior to implant placement with surgical-grade calcium sulfate and platelet-rich plasma: a pilot study in a canine model *Int J Oral Maxillofac Implants* 22(4): 656-65.
- Sohnel O and Mullin JW (1988) Interpretation of crystallization induction periods *J Colloid Interface Sci* 123(1): 43-50.
- Song X, Zhang L, Zhao J, Xu Y, Sun Y, Li P, Yu J (2011) Preparation of calcium sulfate whiskers using waste calcium chloride by reactive crystallization *Cryst Res Technol* 46(2): 166 – 172. DOI\10.1002/crat.201000420.
- Sottosanti J (1992) Calcium sulfate: A biodegradable and biocompatible barrier for guided tissue regeneration *Compendium* 13: 226-228, 230, 232-234.
- Stephan B and Michael O, Injectable cements for vertebroplasty and kyphoplasty. In: Bohner M (ed) *Ballon kyphoplasty*, Springer, Vienna pp. 143–148.
- Stubbs D, Deakin M, Chapman-Sheath P, Bruce W, Debes J, Gillies RM, Walsh WR (2004) In vivo evaluation of resorbable bone graft substitutes in a rabbit tibial defect model *Biomaterials* 25: 5037–5044.
- Sun L, Xu HHK, Takagi S, Chow LC (2007) Fast setting calcium phosphate cement–chitosan composite: mechanical properties and dissolution rates *J Biomater Appl* 21 (3): 299-315.

- Szpalski C, McRae M, Rogers GF, Bumgardener JD, Warren SM (2011) Biomaterials and their applications in craniomaxillofacial surgery in: Ducheyne P, Healy KE, Hutmacher DW, Grainger DW, Kirkpatrick CJ (eds) *Comprehensive biomaterials: biomaterials and clinical use*, Elsevier, Amsterdam. pp: 325-327.
- Tamimi F, Sheikh Z, Barralet J (2012) Dicalcium phosphate cements: Brushite and monetite *Acta Biomater* 8: 474–487.
- Teller M, Gopp U, Neumann HG, Kuhn KD (2006) Release of gentamicin from bone regenerative materials an invitro study *J Biomed Mater Research Part B Appl Biomater* 81(1), 23-29.
- Thai VV and Lee B (2010) Fabrication of calcium phosphate–calcium sulfate injectable bone substitute using hydroxy-propyl-methyl-cellulose and citric acid *J Mater Sci Mater Med*. 21(6): 1867–1874.
- Thomas MV, Puleo DA (2008) Review: calcium sulfate: properties and clinical applications. *J Biomed Mater Res B* 88: 597–610.
- Tiwari A, Ramalingam M, Kobayashi, Turner APF (2012) *Biomedical Materials and Diagnostic Devices*. John Wiley & Sons.
- Toloue SM, Chesnoiu-Matei I and Blanchard SB (2012) A clinical and histomorphometric study of calcium sulfate compared with freeze-dried bone allograft for alveolar ridge preservation *J Periodont* 83(7): 847-855.
- Tritschler U, Kellermeier M, Debus C, Kempter A, Colfen H (2015) A simple strategy for the synthesis of well-defined bassanite nanorods *Cryst Eng Comm* 17: 3772-3776.
- Ujang Z, Diah M, Hazri A, Rashid A, Halim AS (2011) The development, characterization and application of water soluble chitosan in: Elnashar M (ed), *Biotechnology Biopolym InTech*, pp. 110, DOI: 10.5772/16771.
- Upman P (1999) Handbook of biomaterials evaluation, scientific techniques and clinical testing of implant materials ed A F Von Recuum 2nd edn (Philadelphia, PA: Taylor and Francis) pp 275–89.
- Urban RM, Turner TM, Hall DJ, Infanger SI, Cheema N, Lim TH, Moseley J, Carroll M, Roark M (2004) Effects of altered crystalline structure and increased initial compressive strength of calcium sulfate bone graft substitute pellets on new bone formation, *Orthopedics*. 27:s113-8.
- Urban RM, Turner TM, Hall DJ, Inoue N, Steven Gitelis (2007) Increased Bone Formation Using a Calcium Sulfate and Calcium Phosphate Composite Graft *Clinic orthop Rel Res* 459: 1-8.
- USP 34 NF 29 (2011) United States Pharmacopeia and National Formulary Vol.3, p. 4565.
- USP 38 NF 33 (2015) United states pharmacopeia and national formulary 2:3662.
- Vekilov PG (2010) Nucleation *Cryst Growth Des* 10(12): 5007–5019.
- Virto M R, Frutos P, Torrado S, Frutos G (2003) Gentamicin release from modified acrylic bone cements with lactose and hydroxylpropylmethyl cellulose *Biomaterials* 24: 79-87.
- Vorndran E (2013) Ready-to-use injectable calcium phosphate bone cement paste as drug carrier, *Acta Biomater* 9(12): 9558–9567.
- Wang F, Davis TE, Tarabara VV (2010) Crystallization of calcium sulfate dihydrate in the presence of colloidal silica *Indus Eng Chem Res* 49 (22): 11344-11350 DOI: 10.1021/ie100309b.
- Wang P, Lee EJ, Park CS, Yoon B, Shin D, Kim H, Koh YH, Park SH (2008) Calcium sulfate hemihydrate powders with a controlled morphology for use as bone cement *J Am Ceram Soc* 91: 2039-2042.
- Wang X, Chen L, Xiang H, Ye J (2007) Influence of anti-washout agents on the rheological properties and injectability of a calcium phosphate cement *J Biomed Mater Res Part B: Appl Biomater* 81(2): 410-418.

- Wang X, Ye J, Wang Y (2007) Influence of a novel radio pacifier on the properties of an injectable calcium phosphate cement *Acta Biomater* 3(5): 757–763.
- Wang Y and Meldrum FC (2012) Additives stabilize calcium sulfate hemihydrate (bassanite) in solution *J Mater Chem* 22: 22055-22062.
- Wang Y, Kim Y, Christensonb HK, Meldrum FC (2012) A new precipitation pathway for calcium sulfate dihydrate (gypsum) via amorphous and hemihydrate intermediates *Chem Commun* 48: 504–506.
- Wang Z, Wang F, Peng Y, Han Y (2015) Direct observation of liquid nucleus growth in homogeneous melting of colloidal crystals *Nat Commun* 21(6): 6942.
- Weir MD and Xu HHK (2010) Osteoblastic Induction on Calcium Phosphate Cement-chitosan constructs for bone tissue engineering *J Biomed Mater Res A* 94(1): 223–233.
- Weiss H, Brau MF (2009) How much water does calcined gypsum contain *Angew Chem* 48:3520–4.
- World Health Organization (2001) *Model prescribing information. Drugs used for bacterial infections* WHO, Geneva, Switzerland.
- Wu F, Su J, Wei J, Liu C (2009) Injectable bioactive calcium-magnesium phosphate cement for bone regeneration *Biomed Mater* 3(4):0441050.
- Xu LX, Shi XT, Wang YP, Shi ZL (2008) Performance of calcium phosphate bone cement using chitosan and gelatin as well as citric acid as hardening liquid. *J Clin Rehabil Tissue Eng Res* 12: 6381–6384.
- Yan C, Nishida J, Yuan R, Fayer MD (2016) Water of hydration dynamics in minerals gypsum and bassanite: ultrafast 2D IR spectroscopy of rocks *J Am Chem Soc* 138: 9694–9703.
- Yang L, Meng Y, Yin P, Yang Y, Tang Y, Qin L (2011) Shape control synthesis of low-dimensional calcium sulfate *Bull Mater Sci* 34(2): 233–237.
- Yoreo JJ, Vekilov PG (2003) Principles of crystal nucleation and growth, *Rev. Mineral. Geochem.*, 2003, 54, 57-93.
- Yu B, Han K, Ma H, Zhang C, Su J, Zhao J, Li J, Bai Y, Tang H (2009) Treatment of tibial plateau fractures with high strength injectable calcium sulphate. *International Orthopaedics (SICOT)*33:1127-1133.
- Yu L, Li Y, Zhao K, Tang Y, Cheng Z, Chen J, Zang Y, Wu J, Kong L, Liu S, Lei W, Wu Z (2013) A novel injectable calcium phosphate cement-bioactive glass composite for bone regeneration *Plos One* 8(4): e62570.
- Yu L, Li Y, Zhao K, Tang Y, Cheng Z, Chen J, Zang Y, Wu J, Kong L, Liu S, Lei W, Wu Z (2013) A novel injectable calcium phosphate cement-bioactive glass composite for bone regeneration *Plos One* 8(4): e62570.
- Yu T, Ye J, Gao C (2010) Effect of biomedical organic compounds on the setting reaction of calcium phosphates *Colloids Surf B Biointerfaces* 75(1): 363–369.
- Zaiss S, Brown TD, Reichert JC, Berner A (2016) Poly (ϵ -caprolactone) scaffolds fabricated by melt electrospinning for bone tissue engineering *Materials* 9: 232.
- Zhang J, Liu W, Gauthier O, Sourice S, Pilet P, Rethore G, Khairoun K, Bouler J, Tancret F, Weiss P A (2016) simple and effective approach to prepare injectable macroporous calcium phosphate cement for bone repair: Syringe-foaming using a viscous hydrophilic polymeric solution. *Acta Biomater* 31: 326-338.
- Zhang J, Liu W, Schnitzler V, Tancret F, Bouler J (2014) Calcium phosphate cements for bone substitution: Chemistry, handling and mechanical properties. *Acta Biomater* 10: 1035–1049.
- Zhao L, Weir MD, Xu HHK (2010) An injectable calcium phosphate-alginate hydrogel-umbilical cord mesenchymal stem cell paste for bone tissue engineering. *Biomaterials* 31: 6502-6510.

LIST OF PUBLICATIONS

ORIGINAL PAPERS

1. **Sony Sandhya**, Parayanthala Valappil Mohanan, Arumugan Sabareeswaran, Hari Krishna Varma and Manoj Komath, Preclinical safety and efficacy evaluation of 'BioCaS' bioactive calcium sulfate bone cement, *Biomedical Materials : Materials for tissue engineering and regenerative medicine*, 12(1), 2017; 015022. doi: 10.1088/1748-605X/aa5522 (Impact factor – 3.361).
2. **Sony Sandhya**, Suresh Babu S, Nishad KV, Varma H and Komath M, Development of an injectable bioactive bone filler cement with hydrogen orthophosphate incorporated calcium sulfate, *Journal of Materials Science: Materials in Medicine*, 26(1), 201; 5355. doi: 10.1007/s10856-014-5355-5. (Impact Factor- 2.587).
3. **Sandhya S**, Sureshbabu S, Varma HK, Komath M. Nucleation kinetics of the formation of low dimensional calcium sulfate dihydrate crystals in isopropyl alcohol medium, *Crystal Research and Technology*, 47(7), 2012; 780–92. doi:10.1002/crat.201200098. (Impact Factor- 1.120).

PAPER PRESENTATIONS AND CONFERENCE PROCEEDINGS

1. **Sandhya S**, Sureshababu S, Varma HK and Manoj Komath, “Nucleation kinetics study as a tool for making nanoparticles”, National Conference on ‘Recent Trends in Material Science and Technology’ (NCMST 2013), Indian Institute of Science and Technology (IIST Thiruvananthapuram), July 10-12, 2013.
2. **Sandhya S**, Sureshababu S, Varma HK and Manoj Komath, “Development of a versatile drug eluting bioactive bone filler cement”, International Union of Material Research Societies - International Conference in Asia 2013 (IUMRS-ICA 2013), Indian Institute of Science (IISc Bangalore), December 16-20, 2013.
3. **Sandhya Sony**, S. Sureshababu, Harikrishna Varma, Manoj Komath “A novel bone cement for local delivery of antibiotics in bone infections”, International Symposium for Research Scholars on Metallurgy, Material Science and Engineering (ISRS-2014), Indian Institute of Technology (IIT Chennai), December 11-13, 2014.

CURRICULUM VITAE

Education

Ph.D. Scholar (June 2012- present) at Sree Chitra Tirunal Institute for Medical Sciences and Technology, Biomedical Technology Wing, Thiruvananthapuram, Kerala, India.

Master of Science in Analytical Chemistry (2005-2007), Department of Chemistry, S.N College, Sivagiri, Kerala, India (Passed with **First rank (83.28%)** from Kerala University).

Bachelor of Science in Chemistry (2002-2005), Department of Chemistry, S.N College, Sivagiri, Kerala (Passed with First class and Distinction (**87.70%**) from Kerala University).

Bachelor of Education in Physical Science (2007-2008), S.N. Training College, Nedunganda, Kerala, India (Passed with First class with Distinction (**82.21%**) from Kerala University).

State Level Eligibility Test (SET – 2008)

Plus Two (Biology Science) (2000-2002), Govt. H.S.S Palayamkunnu, Kerala, India (Passed with First Class with Distinction (**78.11%**)).

S.S.L.C (2000) Govt.V.H.S.S, Njekkad, Kerala, India (Passed with First class with Distinction (**90.33%**)).

Achievements

1. **SCTIMST Institute Fellowship Scheme 2012.**
2. **Best poster award** on “Development of a versatile drug eluting bioactive bone filler cement” by **Sandhya S**, Sureshababu S, Varma HK and Manoj Komath in International Conference: **Interbnational Union of Materials Research Societies- International Conference in Asia 2013** (IUMRS-ICA 2013 organized by **Indian Institute of Science (IISc, Bangalore)** 16-20 December 2013.